Department of Computer Science, Bioengineering, Robotics and Systems Engineering

---

Data Assimilation in high resolution Numerical Weather Prediction models to improve forecast skill of extreme hydrometeorological events.

by

Martina Lagasio

DIBRIS, Università di Genova

Via Opera Pia, 13 16145 Genova, Italy

http://www.dibris.unige.it/

Università degli Studi di Genova

Dipartimento di Informatica, Bioingegneria,

Robotica ed Ingegneria dei Sistemi

Ph.D. Thesis in Computer Science and Systems Engineering

System Engineering Curriculum

Data Assimilation in high resolution Numerical Weather Prediction models to improve forecast skill of extreme hydrometeorological events.

by

Martina Lagasio

May, 2019

Dottorato di Ricerca in Informatica ed Ingegneria dei Sistemi
Indirizzo Ingegneria dei Sistemi
Dipartimento di Informatica, Bioingegneria, Robotica ed Ingegneria dei Sistemi
Università degli Studi di Genova

DIBRIS, Univ. di Genova
Via Opera Pia, 13
I-16145 Genova, Italy
http://www.dibris.unige.it/

Ph.D. Thesis in Computer Science and Systems Engineering
Systems Engineering Curriculum
(S.S.D. GEO/12)

Submitted by Martina Lagasio
DIBRIS, Univ. di Genova

Date of submission: January 2019

Title: *Data Assimilation in high resolution Numerical Weather Prediction models to improve forecast skill of extreme hydrometeorological events.*

Advisors: Antonio Parodi, Giorgio Boni

Ext. Reviewers: Olivier Caumont, Maria Carmen Llasat

Abstract

The complex orography typical of the Mediterranean area supports the formation, mainly during the fall season, of the so-called back-building Mesoscale Convective Systems (MCS) producing torrential rainfall often resulting into flash floods. These events are hardly predictable from a hydro-meteorological standpoint and may cause significant amount of fatalities and socio-economic damages. Liguria region is characterized by small catchments with very short hydrological response time, and it has been proven to be very exposed to back-building MCSs occurrence. Indeed this region between 2011 and 2014 has been hit by three intense back-building MCSs causing a total death toll of 20 people and several hundred million of euros of damages.

Building on the existing relationship between significant lightning activity and deep convection and precipitation, the first part of this work assesses the performance of the Lightning Potential Index, as a measure of the potential for charge generation and separation that leads to lightning occurrence in clouds, for the back-building Mesoscale Convective System which hit Genoa city (Italy) in 2014. An ensemble of Weather Research and Forecasting simulations at cloud-permitting grid spacing (1 km) with different microphysical parameterizations is performed and compared to the available observational radar and lightning data. The results allow gaining a deeper understanding of the role of lightning phenomena in the predictability of back-building Mesoscale Convective Systems often producing flash flood over western Mediterranean complex topography areas. Despite these positive and promising outcomes for the understanding highly-impacting MCS, the main forecasting issue, namely the uncertainty in the correct reproduction of the convective field (location,

timing, and intensity) for this kind of events still remains open. Thus, the second part of the work assesses the predictive capability, for a set of back-building Liguria MCS episodes (including Genoa 2014), of a hydro-meteorological forecasting chain composed by a km-scale cloud resolving WRF model, including a 6 hour cycling 3DVAR assimilation of radar reflectivity and conventional ground sensors data, by the Rainfall Filtered Autoregressive Model (RainFARM) and the fully distributed hydrological model Continuum. A rich portfolio of WRF 3DVAR direct and indirect reflectivity operators, has been explored to drive the meteorological component of the proposed forecasting chain. The results confirm the importance of rapidly refreshing and data intensive 3DVAR for improving first quantitative precipitation forecast, and, subsequently flash-floods occurrence prediction in case of back-building MCSs events. The third part of this work devoted the improvement of severe hydro-meteorological events prediction has been undertaken in the framework of the European Space Agency (ESA) STEAM (SaTellite Earth observation for Atmospheric Modelling) project aiming at investigating, new areas of synergy between high-resolution numerical atmosphere models and data from spaceborne remote sensing sensors, with focus on Copernicus Sentinels 1, 2 and 3 satellites and Global Positioning System stations. In this context, the Copernicus Sentinel satellites represent an important source of data, because they provide a set of high-resolution observations of physical variables (e.g. soil moisture, land/sea surface temperature, wind speed, columnar water vapor) to be used in NWP models runs operated at cloud resolving grid spacing . For this project two different use cases are analyzed: the Livorno flash flood of 9 Sept 2017, with a death tool of 9 people, and the Silvi Marina flood of 15 November 2017. Overall the results show an improvement of the forecast accuracy by

assimilating the Sentinel-1 derived wind and soil moisture products as well as the Zenith Total Delay assimilation both from GPS stations and SAR Interferometry technique applied to Sentinel-1 data.

Table of Contents

List of Figures

List of Tables

1. Introduction

The Mediterranean region is frequently struck by severe floods and flash floods causing impressive losses of lives and several millions of euros of damages every year. The western Mediterranean area is characterized by a complex orography (Alps, Apennines, Massif Central, Pyrenees) often sitting close to the coastline, potentially able to enhance or even to trigger the deep convective processes originating over the warm sea in the rainfall season [Rebora et al. (2013), Ducrocq et al. (2014), Fiori et al. (2017)]. According to the Molini et al (2011) criterion severe rainfall events in the Mediterranean area can be classified as: type I –long-lived (duration d ≥ 12 hours) and spatially distributed (more than AS = 50 × 50 km^2). These events correspond to the equilibrium convection, where it is assumed that production of CAPE by large-scale processes is nearly balanced by its consumption by convective phenomena, and thus CAPE values stay small; type II –brief and localized, having a shorter duration (*d* <= 12 h) and a spatial extent smaller than AS = 50 × 50 km2, in this case a larger amount of CAPE is available, as a result of building up from large-scale processes over long time-scales, but the extent to which it produces convection and precipitation is restricted by the need for a trigger sufficient to overcome the convective inhibition energy (CIN). The most severe events in this area, corresponding to type II, are due to a particular type of mesoscale configuration featuring a continuous redevelopment of storm cells persisting for hours over the same area, the so called back-building Mesoscale Convective Systems MCSs [Rebora et al. (2013); Ducrocq et al. (2014); Cassola et al. (2015), Fiori et al. (2017), Lagasio et al. (2017)].

A considerable effort has been made in last few years to develop cloud resolving NWP systems, possibly in combination with ensemble and multi-physics approaches, to improve the short term Quantitative Precipitation Forecast (QPF) of such severe convective events [Ducrocq et al. (2014), Hally et al. (2015), Clark et al. (2016), Davolio et al. (2017), Fiori et al. (2017), Lagasio et al. (2017)]. However, a reliable forecast of these events in terms of rainfall amount, location and timing is still an open issue [Ducrocq et al. (2014)] that cannot be tackled only through the increase of the NWP models space-time resolution.

The main goal of this thesis is to provide a significant contribution to the aforementioned open issue, namely the meteorological forecast of such extreme events. The thesis work is divided in three different but complementing activities using the WRF meteorological model.

The first activity aims is to identify a tool helping in the forecasting phase to discriminate between scenarios leading to (very) deep moist convective, heavily precipitating, and persistent storms and ones resulting in shallower and more disorganized convective situations, thus not producing significant ground effects.

Along complementing lines, the second and the third thesis activities aim to reduce the uncertainty in the forecasting of high impact weather events with the use of different data assimilation techniques using conventional (second activity) and non-conventional (third activity) observations.

Concerning the first research line, many studies performed around the globe and corresponding to different weather regimes [Carter and Kidder (1976), Tapia et al. (1998), Soula and Chauzy (2001), Adamo et al. (2009)] confirmed a

strong interplay between lightning phenomena and severe rainfall process evolution in thunderstorms.

Although several real-time lightning detection systems are nowadays able to determine the impact location of lightning with high accuracy, short-range meteorological forecasting is still affected by many sources of uncertainty when trying to predict them [McCaul et al. (2009), Dahl et al. (2011)]. Different algorithms for the prediction of the total lightning spatio-temporal evolution in case of severe weather events have been considered so far, resulting in the development of valuable tools for the warning decision-making process of forecasters. Some of them are nowcasting methods based on observed data [Schultz et al. (2009), Gatlin and Goodman (2010), Stough et al. (2014)], others built on outputs from numerical weather prediction models [Lynn and Yair, (2008, 2010), McCaul et al. (2009); Barthe et al. (2010), Wong et al. (2013), Giannaros et al. (2015)]. Within this context, the first research activity proposes a novel methodological approach for the assessment of the predictive ability of a microphysics driven ensemble of km-scale mesoscale numerical model simulations in case of back-building MCSs, concurrently producing extreme rainfall and lightning activity: it emerges that the use of a Lightning Potential Index is helpful both in forecasting and hindcast phase, allowing to individuate the scenarios leading to deep moist convection and enabling the investigation of the physical parameters that determine lightning activity and which are essential for the reproduction of this kind of high impact weather events. However, the main source of uncertainty in the forecast of severe rainfall phenomena remains linked to the correct reproduction of the deep moist convective field.

These predictive ability challenges can derive from the poor knowledge of the initial state of the atmosphere at small spatio-temporal scales leading to an inevitable model spin-up that often results in an inaccurate simulation of the convective system in terms of timing, location and intensity [Sugimoto et al. (2009)]. This challenge becomes even more relevant when the model grid spacing is approaching the kilometric scale, mainly as a consequence of the lack of high spatio-temporal resolution observations. Consequently, the second research activity aims to gain a further insight on the hydro-meteorological prediction of back-building MCSs through the combination of a high resolution WRF model instance including a 3DVAR data assimilation cycle - with the fully distributed Continuum hydrological model, via the RainFARM stochastic downscaling procedure [Rebora et al. (2006b)]. A rich portfolio of WRF 3DVAR indirect and direct reflectivity assimilations, including an innovative reflectivity forward operator properly dealing with mixed-phase clouds, has been explored to drive the meteorological component of the proposed forecasting framework. From this activity it stands out that the use of such hydro-meteorological framework can help to obtain more timely and accurate streamflow forecasts for back-building MCSs.

The third research activity is fully integrated with the STEAM (SaTellite Earth observation for Atmospheric Modeling) research project, and it aims to respond to a specific question asked by the European Space Agency (ESA), namely if Sentinel satellites constellation weather observation data can be used to better understand and predict with at higher spatial-temporal resolution the atmospheric phenomena resulting in severe weather events and intense atmospheric turbulence phenomena. To tackle this research topic, the thesis has fed for the first time, to the best of the author knowledge, a cloud-resolving

model, namely WRF, with observational data provided by Sentinel satellites constellation, such as humidity, soil and sea temperature, wind on the sea, the amount of water vapour in the atmospheric band closest to the earth. All these data are not normally used in atmospheric forecasting models, but they are rather taken into account mainly for hydrological and marine modelling. The outcomes of the third research activity strongly support the synergy between high resolution numerical weather modelling and the ESA Sentinel satellites products for the forecast of highly precipitating severe weather events.

The structure of the thesis manuscript is organized as it follows. Chapter 1 provides a general overview on Numerical Weather Prediction (NWP) modelling. Chapter 2 and 3 describe the WRF-ARW meteorological model and the WRFDA package for data assimilation respectively. In Chapter 4 the Method for Object baseD Evaluation (MODE) used to validate the forecasts of all the activities is described with the method applied in each work to find the best simulations performance. Chapter 5 presents the first research activity on the evaluation of Lightning Potential Index performances in multi-microphysical cloud-resolving simulations applied to the Genoa 2014 back-building MCS. In Chapter 6 are described analysis and results about the predictive capability of a high-resolution hydro-meteorological forecasting framework coupling WRF cycling 3dvar and Continuum applied to three back-building MCSs happened over Liguria region (Cinqueterre 2011, Genoa 2011, Genoa 2014). The effect of the ingestion in the WRF model of different Sentinel-derived and GNSS-derived products during the STEAM projects is discussed in Chapter 7 considering two different test cases: the Livorno flash flood and the Silvi Marina flood happened in autumn 2017. Finally, concluding considerations of the results achieved in the different activities are summarized in Chapter 8.

2. Numerical Weather Prediction

2.1 History and development

The numerical weather prediction is a technique used to obtain an objective forecast of the future weather by solving a set of governing equations, called also primitive equations, that describe the evolution of atmosphere in time and its motion in space. The complexity of these equations forces the researcher to use computers to resolve them. However, the basic ideas of numerical forecasting and climate modelling were developed about a century ago, long before the first electronic computer was invented.

There were several major practical obstacles to overcome before numerical prediction could be put into practice. A better understanding of the atmospheric dynamics allowed the development of simplified systems of equations; regular radiosonde observations of the free atmosphere and, later, satellite data, provided the initial conditions; stable finite difference schemes were developed; and powerful electronic computers provided a practical means of carrying out the calculations required to predict the changes in the weather [Lynch (2008)].

The numerical weather prediction was invented in the 19th century when the development of thermodynamics resulted in a completion of the set of fundamental physical principles governing the flow of the atmosphere. By about 1890, the great American meteorologist Cleveland Abbe recognized that ‘‘meteorology is essentially the application of hydrodynamics and thermodynamics to the atmosphere’’ [Willis and Hooke (2006)]. He proposed a mathematical approach to forecasting.

In 1904 Vilhem Bjerknes proposed a more explicit analysis of the weather prediction problem. He recognized the importance of a good knowledge of the

initial state of the atmosphere and found a two-steps plan for rational forecasting, the diagnostic and prognostic step. In the first case, the initial state of the atmosphere is determined by observation. Whereas in the second case, the state of the atmosphere and his changing over time is calculated by laws of motion [Bjerknes (1904)] the prognostic step was to be taken by assembling a set of equations, one for each dependent variable describing the atmosphere. He then identified seven independent equations and developed a qualitative, graphical method for solving the equations.

In 1913 Lewis Fry Richardson attempted a direct solution of these equations of motion using two simplifications. The first simplification is the hydrostatic assumption, and the second was the adoption of an approximate solution. The fundamental idea is that atmospheric pressures, velocities, etc., are tabulated at certain latitudes, longitudes and heights so as to give a general description of the state of the atmosphere an instant. Therefore the idea of grid was born. Richardson estimated that 64,000 people, the well-know “forecast factory”, would be needed to keep pace with the atmosphere.

Between 1946 and 1953 were built the first machines to resolve numerically equations. They were used for different projects, among which numerical weather prediction. John von Neumann, one of the leading mathematicians of the 20th century, contributed to assemble those machines. He recognized weather forecasting a problem of both great practical significance and intrinsic scientific interest, as an ideal problem for an automatic computer. With Neumann ends what is called Prelude of Numerical Weather Prediction.

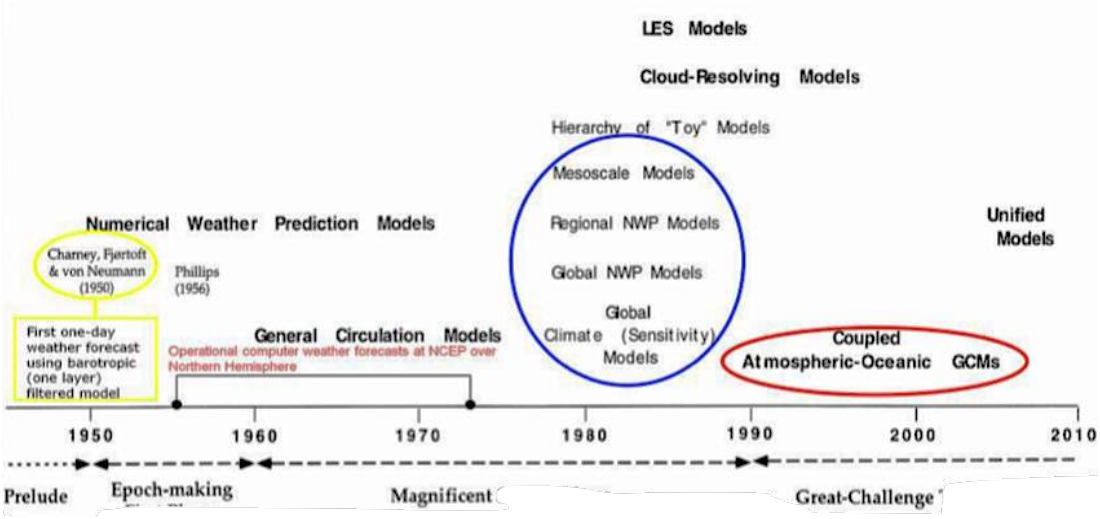

Figure 1: History of numerical modeling of the atmosphere (Arakawa, 2001)

The history of numerical modelling of the atmosphere can be divided in 4 phases: the first phase is the *Prelude*, analysed above. The second phase is the *Epoch-making* during this phase, it is possible see a rapid development of theories on large-scale motion, the coming of supercomputer age and the development of early simple numerical weather prediction model (GCM phase). The third phase is the *Magnificent* in 1980, due to increased computer power, higher resolution models were developed and LAM becomes operational. The fourth phase is the *Great-Challenge*, in the new millennium the researcher are moving from purely atmospheric models to coupled ocean-atmosphere models and higher attention has been given to the estimation of uncertain of numerical model predictions.

The beginnings of the second, third and fourth phases roughly correspond to the development of the early numerical weather prediction (NWP) models, that of the early general circulation model (GCMs), and that of the recent coupled atmosphere-ocean GCMs, respectively.

2.2 NWP features

Numerical weather prediction models based on the same physical principles can be used to generate either short-term weather forecasts or longer-term climate predictions; the latter are widely applied for understanding and projecting climate change.

One of the main problems we encounter with numerical modelling of atmospheric motions and processes is the difficulty to describe accurately several phenomena at different spatial and temporal scales. In fact, in order to describe phenomena at planetary or synoptic scale, it is needed a general circulation model with relatively low space and time resolution. However due to their low resolution, these models are not able to catch the dynamics of mesoscale phenomena (as tropical storm, tornado or thunderstorms, ranging from spatial scale of 1000 km down to 10 km) and a finer spatio-temporal scales numerical model become necessary.

There are several component of a Numerical Weather Prediction model. First of all there is the Dynamical Core, which has inside the Governing Equation and Numerical Procedures, secondly there is the Physical Process Parameterization, thirdly, the Initial Condition, fourth, the Boundary Condition, and finally Post-Processing and Verification.

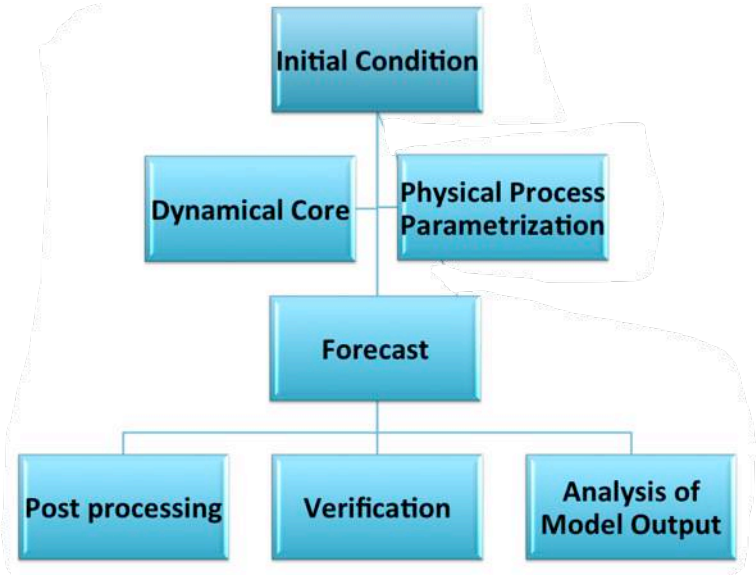

Figure 2: Scheme of Numerical Weather Prediction Model

Below every box of the presented schematization will be analysed.

2.2.1 Initial and boundary Condition

The numerical weather prediction is an initial-boundary value problem therefore given an estimate of the present state of the atmosphere (initial conditions), and appropriate surface and lateral boundary conditions, the model simulates (forecasts) the atmospheric evolution.

The more accurate the estimate of the initial conditions, the better the quality of the forecasts. The process of combining observations and short-range forecasts to obtain an initial condition for NWP is called (atmospheric) data assimilation. The purpose of data assimilation is to determine as accurately as possible the state of the atmospheric flow by using all available information. In other words the data assimilation is an analysis technique in which the observed information is accumulated into the model state by taking advantage of consistency constraints with laws of time evolution and physical properties.

In this work two global circulation models are used, namely the Integrated Forecasting System (IFS) developed and operated by ECMWF (European Center Medium Weather Forecast) and, the Global Forecasting System (GFS) developed and operated by NCEP (National Centers for Environmental Prediction).

2.2.1.1 IFS model

The ECMWF forecasting system (the IFS) consists of several components: an atmospheric general circulation model, an ocean wave model, a land surface model, an ocean general circulation model and perturbation models for the data assimilation (EDA) producing forecasts from days to weeks and months ahead.

The atmospheric general circulation model

The atmospheric general circulation model describes the dynamical evolution on the resolved scale and is augmented by the physical parameterization, describing the mean effect of subgrid processes and the land-surface model. Coupled to this is an ocean wave model [Bechtold et al (2008)]. The higher the numerical resolution, the more accurate the calculations become. A high spatial resolution also enables a better representation of topographical fields, such as mountains and coastlines, and the effect they have on the large-scale flow. It also produces a more accurate description of horizontal and vertical structures, which facilitates the assimilation of observations.

The smallest atmospheric features, which can be resolved by high-resolution forecasts, have wave lengths four or five times the numerical resolution. Although these atmospheric systems have a predictability of only some hours, which is about the time it takes to disseminate the forecasts, their representation is nevertheless important for energetic exchanges between different atmospheric scales. Increasing the resolution not only benefits the

analyses and forecasts of the small-scale systems associated with severe weather but also those of large-scale systems. On march 2016, the horizontal grid spacing for IFS high-resolution forecasts has been increased from 16 km to just 9 km. The IFS high-resolution forecasting system provides twice a day (00 and 12UTC) weather predictions up to 10 days ahead for free and fourth a day (00, 06, 12 and 18 UTC) for a fee.

The ocean wave model

The wave model at ECMWF is called the “WAM”. It describes the rate of change of the 2- dimensional wave spectrum, in any water depth, caused by advection, wind input, dissipation due to white capping and bottom friction and non-linear wave interactions. It is set up so as to allow the two-way interaction of wind and waves with the atmospheric model. Radar altimeter wave-height data are assimilated from satellites. Buoy wave data are not assimilated; instead, they serve as an independent check on the quality of modelled wave parameters.

The land surface model

In the H-TESSEL scheme (Hydrology-Tiled ECMWF Scheme for Surface Exchange over Land) the main types of natural surfaces found over land are represented by a "mosaic" approach. In other words, each atmospheric model grid-box is in contact and exchanges energy and water with up to 6 different types of parcel or "tile" on the ground. These are: bare soil, low and high vegetation, water intercepted by leaves, and shaded and exposed snow. Each land-surface tile has its own properties, describing the heat, water and momentum exchanges with the atmosphere; particular attention is paid to evaporation, as near-surface temperature and humidity are very closely related to this process. The soil (with its four layers) and the snow-pack (with one layer)

have dedicated physical parameterizations, since they represent the main land reservoirs that can store water and energy and release them into the atmosphere in lagged mode.

Finally, the vegetation seasonality is described by the leaf area index (LAI) from climatological data. The LAI describes the growing, mature, senescent and dormant phases of several vegetation types in H-TESSEL (four types of forests and ten types of low vegetation).

The dynamic ocean model

The three-dimensional general circulation ocean model can reproduce the general features of the circulation and the thermal structure of the upper layers of the ocean and its seasonal and inter-annual variations. It has, however, systematic errors, some of which are caused by the coarse vertical and horizontal resolution: the model thermocline is too diffuse; the Gulf Stream does not separate at the right location. The ocean analysis is performed every 10 days, down to a depth of 2000 m. Observational input comes from all around the globe, but mostly from the tropical Pacific, the tropical Atlantic and, to an increasing degree, from the Indian Ocean. The ocean-atmosphere coupling is achieved by a two-way interaction: the atmosphere affects the ocean through its wind, heat and net precipitation (precipitation-evaporation), whilst the ocean affects the atmosphere through its sea surface temperature.

The four-dimensional data assimilation (4D-Var)

The increasing availability of asynoptic data and non-conventional observations has necessitated the use of advanced analysis procedures, such as four-dimensional variational data assimilation (4D-Var), where the concept of a continuous feedback between observations and model data is put on a firm mathematical foundation (Andersson and Thépaut, 2008). The 4D-Var analysis

uses observations from a 12-hour time window, either 21 - 09 UTC (for the 00 and 06 UTC analyses) or 09 - 21 UTC (for the 12 and 18 UTC analyses). To provide the best initial condition for the next analysis a full resolution 3-hour forecast is run, based on the previous 4D-Var analysis.

2.2.1.2 The GFS model

The NCEP's Global Forecast System (GFS) is the cornerstone of NCEP's operational production suite of numerical guidance. NCEP's global forecasts provide deterministic and probabilistic guidance out to 16 days. The GFS provides initial and/or boundary conditions for NCEP's other models for regional, ocean and wave prediction systems. The Global Data Assimilation System (GDAS) uses maximum amounts of satellite and conventional observations from global sources and generates initial conditions for the global forecasts. The global data assimilation and forecasts are made four times daily at 0000, 0600, 1200 and 1800 UTC. The Global Forecast System (GFS) component is a weather forecast model produced by the National Centers for Environmental Prediction (NCEP). Dozens of atmospheric and land-soil variables are available through this dataset, from temperatures, winds, and precipitation to soil moisture and atmospheric ozone concentration. The entire globe is covered by the GFS at a base horizontal resolution of 13 kilometers (distributed to 25 km grid spacing) between grid points, which is used by the operational forecasters who predict weather out to 16 days in the future. Horizontal resolution drops to 44 miles (70 kilometers) between grid point for forecasts between one week and two weeks. The GFS model is a coupled model, composed of four separate models (an atmosphere model, an ocean model, a land/soil model, and a sea ice model), which work together to provide an accurate picture of weather conditions. Changes are regularly made to the

GFS model to improve its performance and forecast accuracy. It is a constantly evolving and improving weather model. Gridded data are available for download through the NOAA National Operational Model Archive and Distribution System (NOMADS). Forecast products and more information on GFS are available at the GFS home page. Prior to January 2003, the GFS was known as the GFS Aviation (AVN) model and the GFS Medium Range Forecast (MRF) model. GFS-AVN and MRF products are a collection from NCEP's NOAAPort. Grids, domains, run frequencies, and output frequencies have changed over the years.

2.2.2 Dynamical Core

The Dynamical Core refers to the Governing Equations and the Numerical Procedure to solve them. NWP models represent the behaviour of the atmosphere which is described by the primitive equations or governing equations. These equations can be derived from various conservation principles and related approximations. The conservation principle here adopted are: conservation of motion (momentum), conservation of mass, conservation of heat (thermodynamic energy), conservation of water (mixing ratio/ specific humidity) in different forms and conservation of other gaseous and aerosol material.

They are written in the Eulerian framework in which values and their derivatives are evaluated at fixed locations on the earth. They are also written in pressure (x-y-p) coordinates and contain all of the essential physics and dynamics needed for NWP models, except that terms considering the earth's curvature have been left out and physical processes, such as friction and adiabatic heating, are represented as one term rather than many.

It is possible to divide the equation in two groups: Prognostic equation and diagnostic equations. A prognostic equation is an equation that predicts the value of variables for some time in the future on the basis of the values at the current or previous times. A diagnostic equation is an equation that links the values of these variables simultaneously, either because the equation is time-independent, or because the variables all refer to the values they have at the identical time. This is by opposition to a prognostic equation.

Another important classification is the difference between Hydrostatic and Non-Hydrostatic model. The Hydrostatic models assume hydrostatic equilibrium, in which the downward weight of the atmosphere balances the upward-directed pressure gradient force. This hydrostatic assumption is valid for synoptic and global-scale systems and for some mesoscale phenomena. Non-hydrostatic processes and their effects become important when the horizontal wavelength of atmospheric phenomena is approximately equal to its height. Since the heights of most weather phenomena are limited by the height of the troposphere, this becomes an issue for features approximately 10 km and less in size.

Important weather examples with significant non-hydrostatic processes include convective storms, gust fronts and other convergence lines, and gravity waves, including mountain waves and turbulence.

For numerical weather prediction, non-hydrostatic models include equations for vertical motion that hydrostatic models lack. As a result, non-hydrostatic models directly forecast weather resulting from vertical motion due to buoyancy changes and other vertical accelerations. In contrast, hydrostatic models can only infer the weather phenomena resulting from such vertical motions. In

succession it is listed the main advantage and disadvantage for both numerical modelling approaches.

The advantage of a hydrostatic model are that it can run fast over limited area-domains, providing forecast in time for operational use. It is important remember that the hydrostatic assumption is valid for many synoptic and sub-synoptic scale phenomena. The main disadvantages are that, firstly it cannot predict the vertical acceleration, and secondly, it cannot predict details of small-scale processes associated with buoyancy.

The advantage for non hydrostatic model are that, firstly, it can calculate the vertical motion explicitly, secondly, it accounts for cloud and precipitation processes and their contribution to vertical motion, thirdly, it is able to predict convection and mountain wave. The disadvantage of this model is, first of all the time needed to run. It is longer to run than hydrostatic model with same resolution and domain size.

2.2.2.1 Governing equations

The set of the equations used in a numerical weather prediction model is ample. The principal equations are:

The Momentum Equation: Newton's second law of motion stated as the force balance for acceleration relative to a rotating coordinate frame. The momentum equation can be stated as:

$$\frac{D\vec{U}}{Dt} = 2\vec{\Omega}\times\vec{\mathbf{U}} - \frac{1}{\rho}\nabla p + \vec{g} + \overrightarrow{F_r} \qquad \textbf{(Eq 2.1)}$$

Where:

- $\overrightarrow{U}$ is the velocity vector [ms^{-1}]
- t is time [s]
- p is pressure [Pa]

- $\boldsymbol{\Omega}$ is the angular velocity [ms^{-1}]
- ρ is the density [kg m^{-3}]
- g is the sum of gravitational and centrifugal forces [m s^{-2}]
- F_r is friction and turbulent mixing
- $\frac{D}{Dt}$ represents the sum of the local rate of change plus advection terms.

For synoptic and planetary circulations the acceleration of the horizontal wind is on the order of 10^{-4} [m s^{-2}] compared with 10^{-7} [m s^{-2}] for the vertical acceleration:

$$\frac{Dw}{Dt} = -\frac{1}{\rho}\frac{\partial p}{\partial z} - g \qquad \textbf{(Eq 2.2)}$$

The vertical momentum equation is replaced by the hydrostatic approximation, in which the weight of the atmosphere balances the vertical pressure gradient. No vertical accelerations are calculated explicitly

$$\frac{Dw}{Dt} \approx 0 \qquad \textbf{(Eq 2.3)}$$

$$\frac{\partial p}{\partial z} = -\rho g \qquad \textbf{(Eq 2.4)}$$

However, the hydrostatic assumption does not hold when the length and depth are similar (typically ≤ 10 km). Deep convection, which is common in the tropics, is non-hydrostatic. Therefore, the rate of change of vertical motion is calculated as the sum of the advection, local buoyancy, and non-hydrostatic vertical pressure gradient minus the precipitation drag. These models can reproduce mesoscale convection in realistic detail but they are subject to error in timing and placement of convection. Non-hydrostatic models have the disadvantage of being computationally intensive.

The Continuity Equation: A fundamental principle in meteorology is that mass is conserved except for external sources and sinks, as described by the equation below:

$$\frac{\partial p}{\partial t} + \nabla \cdot (\rho \vec{U}) = 0 \quad \textbf{(Eq 2.5)}$$

Which can be rewritten as

$$\frac{1}{\rho}\frac{Dp}{Dt} + \nabla \cdot \vec{U} = 0 \quad \textbf{(Eq 2.6)}$$

Where:

- $\vec{U}$ is the velocity
- t is time
- ρ is density

The second form of the equation is useful for forecasting as it relates the rate of density increase, following an air parcel, to the velocity divergence.

The Thermodynamic Equation or First Law of Thermodynamics: This equation describes the conservation of energy applied to a moving fluid element. For a system in thermodynamic equilibrium, the change in internal energy is due to the difference between work done by the system and heat added to the system, written as:

$$c_v \frac{DT}{Dt} + p\frac{D\alpha}{Dt} = Q \quad \textbf{(Eq 2.7)}$$

where:

- $c_v \frac{DT}{Dt}$ is the change in internal energy per unit mass. c_v is the specific heat at constant volume (717 [J kg^{-1} K^{-1}]). T is temperature [K].
- $\frac{D\alpha}{Dt}$ is the rate of work by the fluid system per unit mass, *α is* specific volume ($\frac{1}{\rho}$) [m^3], *p* is pressure [Pa].

- Q is heating rate

It is possible rewrite the thermodynamic equation as

$$c_p \frac{DT}{Dt} - \alpha \frac{Dp}{Dt} = Q \quad \textbf{(Eq 2.8)}$$

Where:

- c_p is the specific heat at constant pressure.

For adiabatic processes no heat is exchanged with surroundings. Therefore any work done in the system is taken from the internal energy and the temperature decreases.

2.2.2.2 Numerical Procedures

The Numerical procedures are the way that the numerical weather prediction uses to calculate the variables. They are approximations used to estimate each term, to integrate model forward in time and boundary condition.

There are four different modelling frameworks for dealing with the space dependence in the nonlinear difference equation of atmospheric dynamics and thermodynamics: grid point or finite difference, spectral, finite element and finite volume.

The choice of which method to be used in a particular modelling application depends on a variety of factor including whether the model has a limited or global computational area, and the degree to which the code needs to be easy to modify for research purpose. Most NWP models solve the forecast equations using data represented as gridded values or in spectral form. Grid Point and spectral models are based on the same set of primitive equations. However, each type formulates and solves the equations differently.

The differences in the basic mathematical formulations contribute to different characteristic errors in model guidance. The differences in the basic mathematical formulations lead to different methods for representing data.

The Grid Point method is one of the oldest methods to solve differential equation. From over the past half-century, atmospheric scientists and oceanographers have developed numerous approaches for applying this method to the solution of the equations of fluid flow over part or the entire sphere. This method includes the use of map projections latitude-longitude grids and spherical geodesic grids. The procedure is defined for organizing grid points in a systematic way over the area of the sphere for which the atmosphere is to be modelled. The models perform their calculations on a fixed array of spatially disconnected grid points. The values at the grid points actually represent an area average over a grid box. This model represents the atmosphere in three-dimensional grid cube.

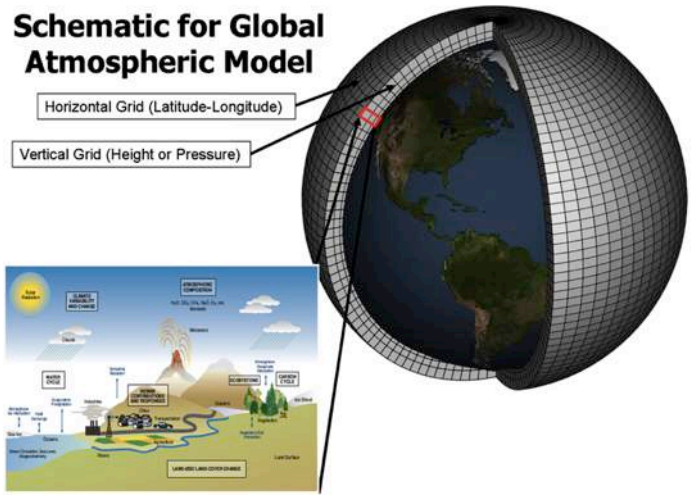

Figure 3: A scheme of three-dimensional grid cube (courtesy of the COMET program).

The arrangement of variables within and around the grid cube has advantages when calculating derivatives. It is also physically intuitive; average thermodynamic properties inside the grid cube are represented at the centre, for example, the temperature, pressure and moisture, are shown in the centre of the cube because they represent the average condition throughout the cube, while the winds on the faces are associated with fluxes into and out of the cube.

The east-west wind and north-south wind are located at the side of the box because they represent the average of the wind components between the centre of this cube and the adjacent cubes.

The vertical motion is represented on the upper and lower faces of the cube. So different variable are show in different part of the cube. Therefore when it is necessary to calculate a variable this variable is calculated in all point of the grid in the region of interest.

The number of point depends on the grid interval Δx over which the region of study is divided. It is also important remember that there are global model and limited area model, so the number of point depend either grid interval or type of numerical model. The main difference, other the dimension of the domain, between a global model and limited area model is that in a global model it is necessary only initial condition and upper and bottom layer condition, whilst in a limited area model it is necessary initial condition, upper and bottom layer condition and boundary condition. For this region a limited area model is a model insert in a global model.

The domain of an NWP model can be viewed as a three-dimensional array of cubes.

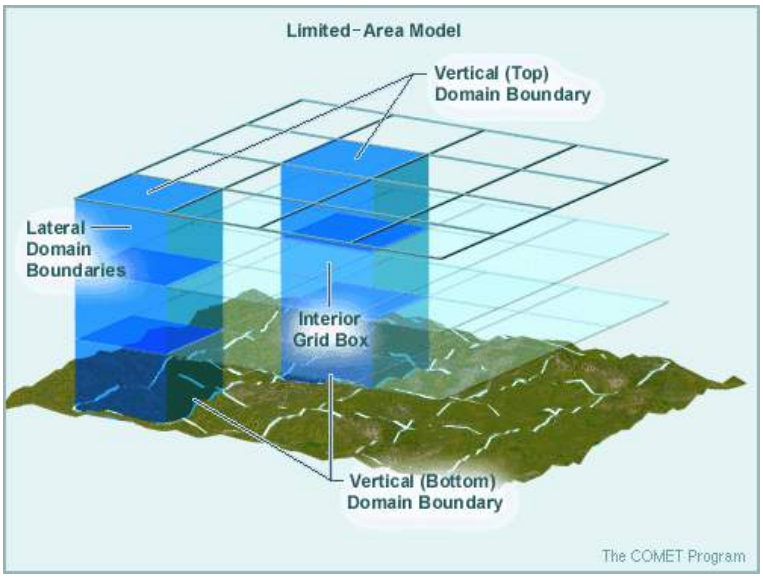

Figure 4: Scheme of cube that creates the Limited area model domain (courtesy of the COMET program)

Each cube encompasses a volume of the atmosphere corresponding to a model grid point. Forecast values for the meteorological variables in each cube are derived from the current values within the cube plus those from the surrounding cubes. As the cubes on the boundaries are not surrounded by other cubes on all sides, the information needed to provide forecast values for the meteorological parameters cannot be determined using only the data contained in the model.

The information for the outside boundaries must be supplied from another source. Ideally, boundary conditions should be based on observed data. However, the best that can be done in weather prediction is to use boundary conditions based on another forecast model. This happens in the case analysed in this thesis.

Another method to study the variable is the spectral model, it represent the atmospheric spatial variability as a finite series of sine and cosine waves of differing wavelengths. Model resolution is a function of the number of waves that are used to represent variability in the model. Several types of wave

orientation are possible in spectral models. The wavelength of the smallest number in a spectral model is represented as:

$$Minimum\ wavelenght = \frac{360°}{Total\ number\ of\ waves\ or\ \mathrm{T}\ number} \quad \textbf{(Eq 2.9)}$$

The T170 configuration is commonly used in operational models because its resolution in the zonal and meridional directions is almost the same around the globe. Although horizontal gradients are calculated exactly from the wave solution, grids are still used for non-linear and physical calculations. Spectral models are the primary models at operational forecast centers such as ECMWF and NCEP, while grid point models are used for smaller, regional models.

Another thing analysed by numerical procedure is the way in which the vertical coordinate is treated. The vertical coordinate is very important. Depicting properly the vertical structure of the atmosphere leads to better forecast. To successfully understand this vertical structure, the model must have an appropriate vertical coordinate to lead to better resolution and thus better forecast. The equations of motion have their simplest form in pressure coordinate, but, unfortunately, pressure coordinate system are not particularly suited to solving the forecast equations because, like height surface, they can intersect the orography an consequently disappear over parts of the forecast domain. The principal vertical coordinate types are: Sigma Coordinate, Eta Vertical Coordinate and Hybrid Coordinate.

In a numerical model, it is important that the vertical coordinate exhibits monotonic behaviour with height. For example, continuously decrease (pressure coordinates) or continuously increase in the vertical (isentropic coordinates). Second a coordinate should preserve conservative atmospheric

properties and treat important dynamical processes accurately, such as adiabatic and adiabatic motions and flow over terrain. Third it should accurately represent the pressure gradient force (PGF, used for calculating the geostrophic wind) over both flat and sloping terrain. Most hydrostatic models use relatively straightforward configurations for their vertical coordinates. It is important remember that no one vertical coordinate system is ideal; each has its strengths and limitations.

The first vertical coordinate analysed is the Sigma Coordinate, the equations of motion, which form the basis for all NWP models, have their simplest form in pressure coordinates. Unfortunately, pressure coordinate systems are not particularly suited to solving the forecast equations how explained above. To solve the problem of discontinuous forecast surfaces, Phillips in 1957 developed a terrain-following coordinate called the sigma (σ) coordinate. This coordinate traditionally has been used in most NWP models. Nowadays, many models use a sigma coordinate to follow the terrain, but aloft it blends into some other type of coordinate system. In its simplest form, the sigma coordinate is defined by:

$$\sigma = \frac{p}{p_s} \qquad \textbf{(Eq 2.10)}$$

Where:

- p is the pressure on a forecast level within the model.
- p_s is the pressure at the earth's surface, not mean sea level pressure.

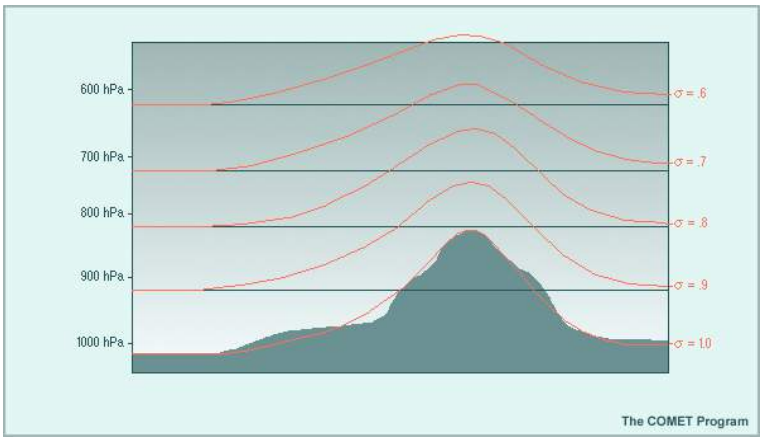

Figure 5: Scheme of Sigma Coordinate (courtesy of the COMET program)

The lowest coordinate surface (usually labelled σ = 1) follows a smoothed version of the actual terrain. The other sigma surfaces gradually transition from being nearly parallel to the smoothed terrain at the bottom of the model (σ = 1) to being nearly horizontal to the constant pressure surface at the top of the model (σ = 0). The top layer of the model is typically placed well above the tropopause, usually between 25 and 1 hPa. The sigma vertical coordinate can also be formulated with respect to height (z), rather than pressure.

The second vertical coordinate analysed is the Eta Coordinate (η). It was created in the early 1980s in an effort to reduce the errors incurred in calculating the pressure gradient force using sigma coordinate models. The eta coordinate is, in fact, another form of the sigma coordinate, but uses mean sea level pressure instead of surface pressure as a bottom reference level. As such, eta is defined as

$$\eta = \frac{p_{r|z_s} - p_t}{p_{r|z=0} - p_t} \qquad \textbf{(Eq 2.11)}$$

Where

. p_t is pressure at the model top

- $p_r|_{z=0}$ is the standard atmosphere MSL pressure (1013 hPa)
- $p_r|_{z_s}$ is the standard atmosphere pressure at the model terrain level z_s

Eta usually is labelled from 0 to 1 from the top of the model domain to mean sea level. Unlike sigma models, where all grid cubes are considered to be above the earth's surface, in eta models, some of the model's grid cubes are located underground in areas where the surface elevation is notably above sea level. This requires special numerical formulations to model flow near the earth's surface.

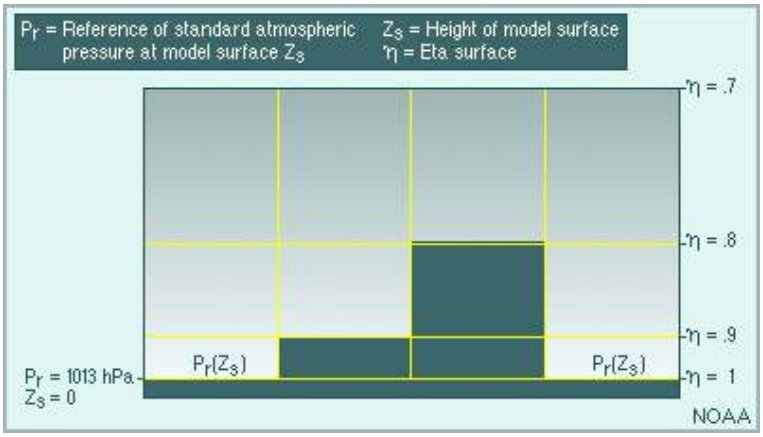

Figure 6: Scheme of Eta Coordinate (courtesy of the COMET program)

The difference between the definitions of the sigma and eta coordinate systems allows the bottom atmospheric layer of the model to be represented within each grid box as a flat "step," rather than sloping like sigma in steep terrain. For this reason, the eta coordinate is sometimes referred to as the step-mountain coordinate. This configuration eliminates nearly all errors in the PGF calculation and allows models using the eta coordinate to have extreme differences in elevation from one grid point to its neighbour. Eta coordinate models can therefore develop strong vertical motions in areas of steep terrain and thus more accurately represent many of the blocking effects that mountains can have on stable air masses.

Even when the step-like eta is used as the vertical coordinate, model terrain is still much coarser than real terrain, but the topographic gradients are less smoothed than in sigma models. Although this representation of terrain is a source of error in areas strongly affected by small-scale terrain features, it is still necessary to depict the average elevation within the entire grid box area. Representing terrain in this manner impacts the scale of features that can be preserved in the model's forecast, making the forecast representative of the average conditions in the grid box.

The Eta coordinate was used in the primary NCEP mesoscale model from 1993 to 2006. As of 2009, it is still in use in regional models run by public or private forecast operations in several countries in Europe and Central and South America, though not those of Canada, Western Europe, or Japan.

The last vertical coordinate analysed is the Hybrid Vertical Coordinate in particular the Hybrid sigma-pressure coordinate. This type has a combination of sigma layers at the bottom that shift to isobaric layers above. This takes advantage of the terrain-following sigma in the boundary layer while utilizing flatter coordinates which have better numerical properties aloft and improves the efficiency and accuracy of radiative transfer calculations used in assimilating satellite radiance observations.

The upper troposphere and stratosphere are crucial for the assimilation of satellite radiance observations, and these observations now play a dominant role in the data assimilation due to their overwhelming abundance.

Some models, such as GFS, have a blend, so that the coordinate gradually transitions from sigma at the bottom to isobaric at the top. The blended method

avoids numerical artefacts at the transition level seen in some forecasts using the type which abruptly shifts from sigma to pressure.

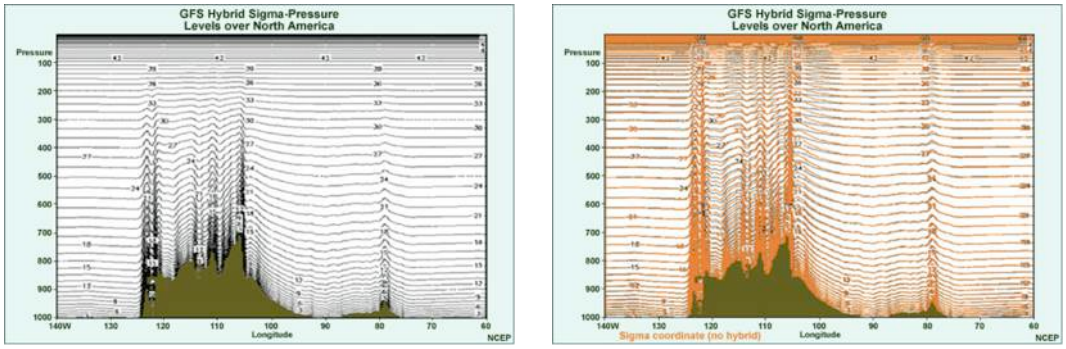

Figure 7: The two images show the difference between Sigma and Hybrid coordinate. The image on the left side shows the Sigma Coordinate, while the image on the right side shows the Hybrid Coordinate in grey and the Sigma Coordinate in Orange (courtesy of the COMET program)

Figure 7 show the sigma coordinate in orange while the hybrid in grey. It is possible to notice the difference over complex (sloping) terrain of any height, even the low mountains at 80° W the hybrid is much flatter in the upper troposphere. Over relatively flat areas, the two coordinates nearly coincide.

Uccellini et al introduced the Hybrid Coordinates in 1979. He introduced important advancements that improved the feasibility of using hybrid isentropic-sigma vertical coordinates.

2.2.3 Physical process parameterization

The Physical Process parameterization represent what the model cannot calculate at the grid point. In Figure 8 there is an example of that a numerical model cannot calculate:

Figure 8: An example of what numerical cannot calculate (courtesy of the COMET program)

It is important remember that a numerical weather prediction models cannot resolve weather features and/or processes that occur within a single model grid box. In fact a model cannot resolve any of local flows, swirls, or obstacles if they exist within a grid box. However, the model must account for the aggregate effect of these surfaces on the low-level flow with a single number that goes into the friction term in the forecast wind equation.

The method of accounting for such effects without directly forecasting them is called parameterization. The atmospheric processes that need to parameterize sub grid-scale are: Convective processes and Microphysical processes.

The Convective parameterization is the method by which models account for convective effects through the redistribution of temperature and moisture in a grid column, that reduces atmospheric instability. By reducing thermodynamic instability, Convective parameterization prevents the grid-scale microphysics scheme from creating unrealistic large-scale convection and overly active low-level cyclogenesis.

Usually, the convective parameterizations are used in current operational hydrostatic models to account for the effects of convection since the model cannot resolve convective motions explicitly. However, high-resolution (5 km or less) non-hydrostatic models can be run without CP schemes because the grid spacing are small enough to begin to resolve convective motions. For example, the resolution can be fine enough that entire grid boxes can be filled with updraft air and condensate while others are filled with downdrafts.

The explicit convection is able to calculate explicitly simulated updrafts strong enough to lift hydrometeors up to the equilibrium level and explicitly simulated downdrafts and their accompanying gust fronts. This allows a more realistic redistribution of heat and moisture than when a convection parameterization scheme is used. It also enables the winds and vertical motion to be modified directly by the convection. The explicit convection ultimately provides a direct prediction of convective precipitation, whilst the convective parameterization schemes can only indirectly predict convective precipitation as a by-product of removing instability.

3. WRF-ARW model

The Weather Research and Forecasting (WRF) Model is a next-generation mesoscale numerical weather prediction system designed to serve both operational forecasting and atmospheric research needs.

At the end of the last century, circa 1995, the National Centers for Environmental Prediction (NCEP) had interest in developing a nonhydrostatic model for operational forecasting on finer scales. This idea arose on the premise that a NWP model shared between research and operational sector could have lead to a beneficial synergy for both communities since the model could be a common platform on which an extensive research community develop capabilities that operatives could really exploit.

The original partners to build WRF were NCAR, the National Oceanic and Atmospheric Administration (NOAA), the U.S. Air Force, the Naval Research Laboratory, the University of Oklahoma, and the Federal Aviation Administration. The first model release at the end of December 2000 emerged from the partners efforts was a model with a higher-order numerical accuracy and scalar conservation properties than the previous models such as the fifth-generation Pennsylvania State University–NCAR Mesoscale Model (MM5; Grell et al. 1994) developed during the 1990s. The model contained a preprocessor for domain and input preparation, an evolution of an initial physical packages ported from the MM5 and two alternative atmospheric fluid flow solvers or cores. The two WRF variants were called the Advanced Research version of WRF (ARW) WRF-ARW and the NCEP's Nonhydrostatic Mesoscale Model (NMM) WRF-NMM. Oversight of the WRF enterprise has evolved over time. Through the early years, the partners coordinated the various efforts and at the developmental level, various working groups focused on narrower areas, such

as numerics, data assimilation, and physics. From the late 2000s, the original top-down direction of WRF has transitioned to a mode of community-driven input, with the responsibility for basic system and community support led by NCAR.

The WRF simulations are produced by two phases, the first to configure the model domain(s), ingest the input data, and prepare the initial conditions, and the second to run the forecast model and this is done by the forecast component that contains the dynamical solver and physics packages for atmospheric processes (e.g., microphysics, radiation, planetary boundary layer). Figure 9 shows the flowchart for the WRF Modelling System:

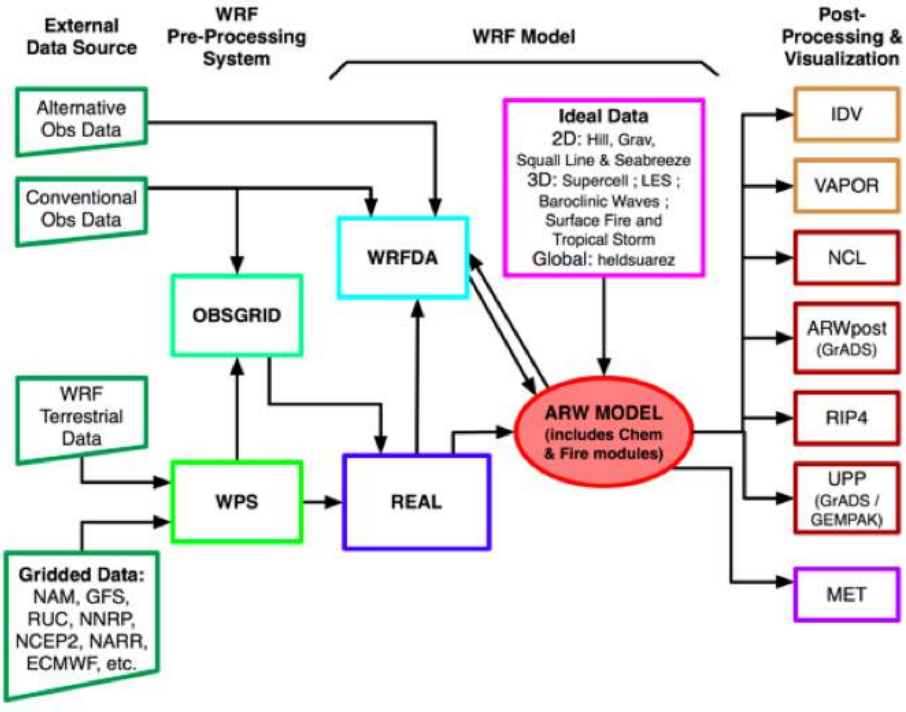

Figure 9: WRF Modelling System Flow Chart

The forecast model components operate within WRF's software framework, which handles I/O and parallel-computing communications. WRF is written

primarily in Fortran, can be built with a number of compilers, and runs predominately on platforms with UNIX-like operating systems, from laptops to supercomputers. WRF's architecture has allowed it to be ported to virtually every type of platform in the world's top 500 supercomputers. WRF model is applied extensively under both real-data and idealized configuration for research activity but also it is used operationally at governmental centers around the word as well as by private companies (Figure 10).

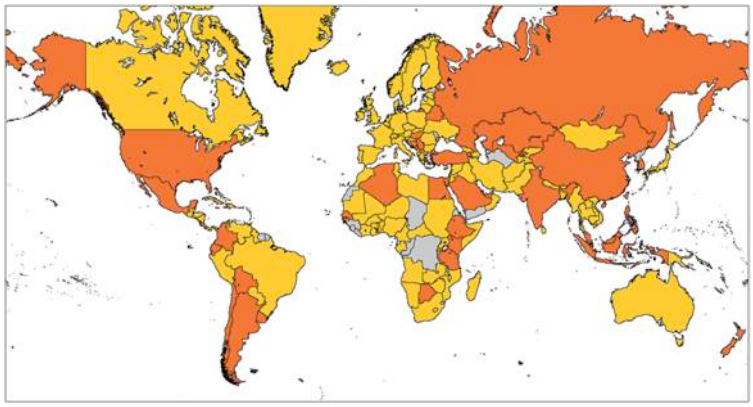

Figure 10: Countries that have logged registered WRF users (gold) and that have logged users and have run WRF operationally (orange). In some countries, the WRF operation has been in regional meteorological centers in selected cities. Note also that operational centers may have run multiple NWP models, with WRF not being the exclusive model (courtesy of Powers et al. 2017).

WRF is suitable for a broad spectrum of applications across scales ranging from meters to thousands of kilometres, and has been widely used at CIMA Research Foundation for hydro-meteorological research applications [Parodi and Emanuel (2009), Parodi and Tanelli (2010), Parodi, Foufoula-Georgiou and Emanuel 2(011), Fiori et al. (2014, 2017) and Pieri et al. (2015), Parodi et al. (2017a), Parodi et al. (2017b)].

The WRF model represents the atmosphere as a number of variables of state discretized over regular Cartesian grids. The model solution is computed using an explicit high-order Runge-Kutta timesplit integration scheme in the two horizontal dimensions with an implicit solver in the vertical. Since WRF domains

are decomposed over processors in the two horizontal dimensions only, interprocess communication is between neighbours on most supercomputer topologies.

3.1 Analysis of the surface parameterizations

This paragraph presents the available WRF surface schemes for NWM applications, including planetary boundary layer, atmospheric surface layer, and land surface model components (Figure 11).

The planetary boundary layer (PBL) is the lowest part of the atmosphere. Its behavior is directly influenced by its contact with a planetary surface. On Earth it usually responds to changes in surface radiative forcing in an hour or less. In this layer physical quantity such as flow velocity, temperature, moisture, etc., displays rapid fluctuations (turbulence) and vertical mixing is strong. Above the PBL is the "free atmosphere" where the wind is approximately geostrophic (parallel to the isobars) while within the PBL the wind is affected by surface drag and turns across the isobars. The free atmosphere is usually nonturbulent, or only intermittently turbulent.

The atmospheric surface layer is the lowest part of the planetary boundary layer (typically about a tenth of the height of the PBL) where mechanical (shear) generation of turbulence exceeds buoyant generation or consumption. Turbulent fluxes and stress are nearly constant with height in this layer.

The earth/land (land hereafter) surface layer involves a number of crucial processes for “free” atmosphere and planetary boundary layer namely infiltration, internal soil moisture fluxes, internal soil heat fluxes, and gravitational flow.

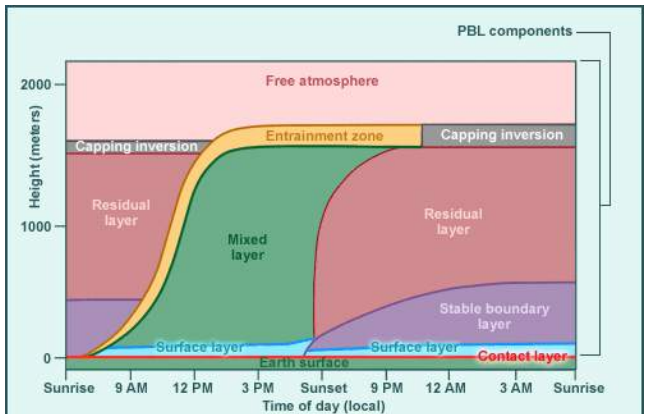

Figure 11: planetary boundary layer, and atmospheric surface layer daily cycle (courtesy of the COMET Program).

The planetary boundary layer, the atmospheric surface layer and the land surface layer interact through some key processes (Figure 12): the atmospheric surface layer provides exchange coefficients for heat and moisture to the land surface layer, while the land surface layer provides land-surface fluxes of heat and moisture to the planetary boundary layer, and finally the atmospheric surface layer supplies friction stress and water-surface fluxes of heat and moisture to the planetary boundary layer.

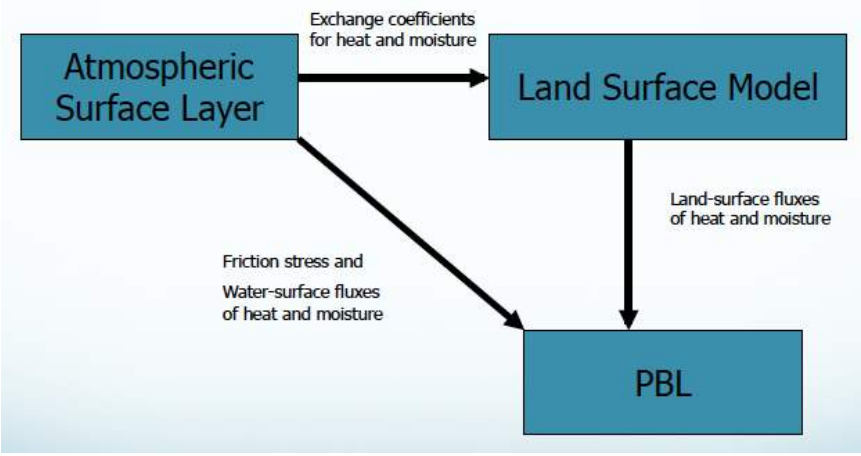

Figure 12: main interactions between planetary boundary layer, the atmospheric surface layer and the land surface layer (courtesy of WRF-ARW tutorials).

Surface processes are dealt in WRF model through a set of physics categories which are summarized as planetary boundary layer and land-surface parameterizations, discussed hereafter.

3.1.1 The surface Layer

The surface layer schemes calculate friction velocities and exchange coefficients that enable the calculation of surface heat and moisture fluxes by the land-surface models and surface stress in the planetary boundary layer scheme. Over water surfaces, the surface fluxes and surface diagnostic fields are computed in the surface layer scheme itself. The schemes provide no tendencies, only the stability-dependent information about the surface layer for the land-surface and PBL schemes. Some boundary layer schemes require the thickness of the surface layer in the model to be representative of the actual surface layer (e.g. 50-100 meters).

3.1.1.1 MM5 scheme

This scheme uses stability functions from Paulson (1970), Dyer and Hicks (1970), and Webb (1970) to compute surface exchange coefficients for heat, moisture, and momentum. A convective velocity following Beljaars (1994) is used to enhance surface fluxes of heat and moisture. No thermal roughness length parameterization is included in the current version of this scheme. A Charnock relation relates roughness length to friction velocity over water. There are four stability regimes following Zhang and Anthes (1982). This surface layer scheme must be run in conjunction with the MRF or YSU PBL schemes.

3.1.1.2 Eta scheme

The Eta surface layer scheme [Janjic (1996, 2002)] is based on similarity theory [Monin and Obukhov (1954)]. The scheme includes parameterizations of a viscous sub-layer. Over water surfaces, the viscous sub-layer is parameterized explicitly following Janjic (1994). Over land, the effects of the viscous sub-layer are taken into account through variable roughness height for temperature and humidity as proposed by Zilitinkevich (1995). The Beljaars (1994) correction is

applied in order to avoid singularities in the case of an unstable surface layer and vanishing wind speed. The surface fluxes are computed by an iterative method. This surface layer scheme must be run in conjunction with the Eta (Mellor-Yamada-Janjic) PBL scheme, and is therefore sometimes referred to as the MYJ surface scheme.

3.1.1.3 Pleim scheme

The Pleim surface layer scheme [Pleim (2006)] was developed as part of the Pleim-Xiu land surface model (LSM) but can be used with any LSM or PBL model. This scheme is based on similarity theory and includes parameterizations of a viscous sub-layer in the form of a quasi-laminar boundary layer resistance accounting for differences in the diffusivity of heat, water vapor, and trace chemical species. The surface layer similarity functions are estimated by analytical approximations from state variables.

3.1.2 The Land-Surface Model

The land-surface models (LSMs) use atmospheric information (Figure 13) from the surface layer scheme, radiative forcing from the radiation scheme, precipitation forcing from the microphysics and convective schemes, surface temperature, water vapour and wind from the PBL scheme, together with internal information on the land's state variables and land-surface properties, to provide heat and moisture fluxes over land points and sea-ice points.

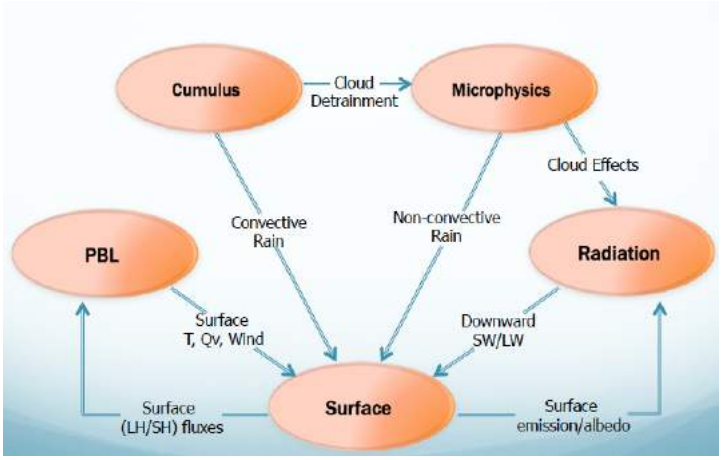

Figure 13: direct interactions of parameterizations, with special focus on surface related ones (courtesy of WRF-ARW tutorials).

These fluxes provide a lower boundary condition for the vertical transport done in the PBL schemes (or the vertical diffusion scheme in the case where a PBL scheme is not run, such as in large-eddy mode). The land-surface models have various degrees of sophistication in dealing with thermal and moisture fluxes in multiple layers of the soil and also may handle vegetation, root, and canopy effects and surface snow-cover prediction. The land-surface model provides no tendencies, but does update the land's state variables which include the ground (skin) temperature, soil temperature profile, soil moisture profile, snow cover, and possibly canopy properties. There is no horizontal interaction between neighbouring points in the LSM, so it can be regarded as a one-dimensional column model for each WRF land grid-point, and many LSMs can be run in a stand-alone mode.

Scheme	Vegetation processes	Soil variables (Layers)	Snow scheme
5-layer	No	Temperature (5)	None
Noah	Yes	Temperature, Water+Ice, Water (4)	1-layer, fractional
Noah-MP	Yes	Temperature, Water+Ice, Water (4)	multi-layer
RUC	Yes	Temperature, Ice, Water + Ice (6-9)	multi-layer
Pleim-Xiu	Yes	Temperature, Moisture (2)	input only
CLM	Yes	Temperature, Water+Ice, Water (10)	multi-layer
SSiB	Yes	Temperature, Water+Ice, Water (3)	multi-layer

3.1.2.1 5-layer thermal diffusion

This simple LSM is based on the MM5 5-layer soil temperature model. Layers are 1, 2, 4, 8, and 16 cm thick. Below these layers, the temperature is fixed at a deep-layer average. The energy budget includes radiation, sensible, and latent heat flux. It also allows for a snow-cover flag, but the snow cover is fixed in time. Soil moisture is also fixed with a landuse- and season-dependent constant value, and there are no explicit vegetation effects.

3.1.2.2 Noah

This is a 4-layer soil temperature and moisture model with canopy moisture and snow cover prediction. The layer thicknesses are 10, 30, 60 and 100 cm from

the top down. It includes root zone, evapotranspiration, soil drainage, and runoff, taking into account vegetation categories, monthly vegetation fraction, and soil texture. The scheme provides sensible and latent heat fluxes to the boundary-layer scheme. The Noah LSM additionally predicts soil ice, and fractional snow cover effects, has an improved urban treatment, and considers surface emissivity properties.

3.1.2.3 Noah-MP

Noah-MP is a land surface model using multiple options for key land-atmosphere interaction processes [Niu et al. (2011)]. Noah-MP contains a separate vegetation canopy defined by a canopy top and bottom, crown radius, and leaves with prescribed dimensions, orientation, density, and radiometric properties. The canopy employs a two-stream radiation transfer approach along with shading effects necessary to achieve proper surface energy and water transfer processes including under-canopy snow processes [Dickinson (1983), Niu and Yang (2004)]. Noah-MP contains a multi-layer snow pack with liquid water storage and melt/refreeze capability and a snow-interception model describing loading/unloading, melt/refreeze capability, and sublimation of canopy-intercepted snow [Yang and Niu (2003), Niu and Yang (2004)]. Multiple options are available for surface water infiltration and runoff and groundwater transfer and storage including water table depth to an unconfined aquifer [Niu et al. (2007)]. The Noah-MP model can be executed by prescribing both the horizontal and vertical density of vegetation using either ground- or satellite-based observations. Another available option is for prognostic vegetation growth that combines a Ball-Berry photosynthesis-based stomatal resistance [Ball et al. (1987)] with a dynamic vegetation model [Dickinson et al. (1998)] that allocates carbon to various parts of vegetation (leaf, stem, wood and root) and

soil carbon pools (fast and slow). The model is capable of distinguishing between C3 and C4 photosynthesis pathways and defines vegetation-specific parameters for plant photosynthesis and respiration.

3.1.2.4 Rapid Update Cycle (RUC)

The RUC LSM has a multi-level soil model (6 levels is default but it could 9) with higher resolution in the top part of soil domain (0, 5, 20, 40, 160, 300 cm is default). The soil model solves heat diffusion and Richards moisture transfer equations, and in the cold season takes into account phase changes of soil water [Smirnova et al. (2004, 2007)]. The RUC LSM also has a multi-layer snow model with changing snow density, refreezing liquid water percolating through the snow pack, snow depth and temperature dependent albedo, melting algorithms applied at both snow-atmosphere interface and snow-soil interface, and simple parameterization of fractional snow cover with possibility of grid averaged skin temperature going above freezing. It also includes vegetation effects and canopy water. The RUC LSM has a layer approach to the solution of energy and moisture budgets. The layer spans the ground surface and includes half of the first atmospheric layer and half of the top soil layer with the corresponding properties (density, heat capacity, etc.) The residual of the incoming fluxes (net radiation, latent and sensible heat fluxes, soil heat flux, precipitation contribution into heat storage, etc.) modify the heat storage of this layer. An implicit technique is applied to the solution of these equations. Prognostic variables include soil temperature, volumetric liquid, frozen and total soil moisture contents, surface and sub-surface runoff, canopy moisture, evapotranspiration, latent, sensible and soil heat fluxes, heat of snow-water

phase change, skin temperature, snow depth and density, and snow temperature.

3.1.2.5 Pleim-Xiu (PX)

The PX LSM [Pleim and Xiu (1995), Xiu and Pleim (2001)] includes a 2-layer force-restore soil temperature and moisture model. The top layer is taken to be 1 cm thick, and the lower layer is 99 cm. The PX LSM features three pathways for moisture fluxes: evapotranspiration, soil evaporation, and evaporation from wet canopies. Evapotranspiration is controlled by bulk stomatal resistance, that is dependent on root zone soil moisture, photosynthetically active radiation, air temperature, and the relative humidity at the leaf surface. Grid aggregate vegetation and soil parameters are derived from fractional coverages of land use categories and soil texture types.

3.1.2.6 Community Land Model (CLM)

The Community Land Model is the land component of the Community Climate System Model.

Its version 4 is extended with a carbon-nitrogen (CN) biogeochemical model that is prognostic with respect to vegetation, litter, and soil carbon and nitrogen states and vegetation phenology. An urban canyon model is added and a transient land cover and land use change (LCLUC) capability, including wood harvest, is introduced, enabling study of historic and future LCLUC on energy, water, momentum, carbon, and nitrogen fluxes. The hydrology scheme is modified with a revised numerical solution of the Richards equation and a revised ground evaporation parameterization that accounts for litter and within-canopy stability. The new snow model incorporates the SNow and Ice Aerosol Radiation model (SNICAR) - which includes aerosol deposition, grain-size

dependent snow aging, and vertically-resolved snowpack heating – as well as new snow cover and snow burial fraction parameterizations.

The thermal and hydrologic properties of organic soil are accounted for and the ground column is extended to, 50-m depth. Several other minor modifications to the land surface types dataset, grass and crop optical properties, surface layer thickness, roughness length and displacement height, and the disposition of snow-capped runoff are also incorporated

3.1.2.7 Simplified Simple Biosphere Model (SSiB)

The Simple Biosphere Model (SiB) is a bio-physically based model of land surface-atmosphere interaction. For some general circulation model (GCM) climate studies, further simplifications are desirable to have greater computation efficiency, and more important, to consolidate the parametric representation. The diurnal variation of surface albedo is computed in SiB by means of a comprehensive yet complex calculation. Since the diurnal cycle is quite regular for each vegetation type, this calculation can be simplified considerably. The effect of root zone soil moisture on stomatal resistance is substantial, but the computation in SiB is complicated and expensive.

The surface stress and the fluxes of heat and moisture between the top of the vegetation canopy and an atmospheric reference level have been parameterized in an off-line version of SiB.

3.1.3 The Planetary boundary layer Model

In the set of equation for turbulent flow the number of unknowns is larger than the number of equations, therefore there are unknown turbulence terms, which must be parameterized as a function of known quantities and parameters. Much of the problem in numerical modeling of the turbulent atmosphere is related to

the numerical representation (or parameterization as a function of known quantities and parameters) of these fluxes. This problem is known as closure problem. Closure can be local and non-local: for local closure, an unknown quantity in any point in space is parameterized by values and/or gradients of known quantities at the same point; for non-local closure, an unknown quantity at one point in space is parameterized by values and/or gradients of known quantities at many points in space; additionally the use of first-order closure schemes for evaluating turbulent fluxes is common in many boundary layer, mesoscale, and general circulation models of the atmosphere.

In this framework, the planetary boundary layer (PBL) model/parameterization is responsible for vertical sub-grid-scale fluxes due to eddy transports in the whole atmospheric column, not just the boundary layer. Thus, when a PBL scheme is activated, explicit vertical diffusion is de-activated with the assumption that the PBL scheme will handle this process. The most appropriate horizontal diffusion choices are those based on horizontal deformation or constant Kh values where horizontal and vertical mixing are treated independently. The surface fluxes are provided by the surface layer and land-surface schemes. The PBL schemes determine the flux profiles within the well-mixed boundary layer and the stable layer, and thus provide atmospheric tendencies of temperature, moisture (including clouds), and horizontal momentum in the entire atmospheric column. Most PBL schemes consider dry mixing, but can also include saturation effects in the vertical stability that determines the mixing. The schemes are one-dimensional, and assume that there is a clear scale separation between sub-grid eddies and resolved eddies. This assumption will become less clear at grid sizes below a few hundred meters (LES mode), where boundary layer eddies may start to be resolved, and

in these situations the scheme should be replaced by a fully three-dimensional local sub-grid turbulence scheme such as the TKE diffusion scheme.

WRF PBL schemes can be:

- based on turbulent kinetic energy prediction
- diagnostic non local

Scheme	Unstable PBL	Entrainment PBL	Top Mixing
MYJ	K from prognostic TKE	part of PBL mixing	multi-layer
QNSE	K from prognostic TKE	part of PBL mixing	multi-layer
BouLac	K from prognostic TKE	part of PBL mixing	multi-layer
MYNN2	K from prognostic TKE	part of PBL mixing	multi-layer
TEMF	K from prognostic TKE	part of PBL mixing	multi-layer
UW	K from prognostic TKE	part of PBL mixing	multi-layer
Shin-Hong	K from prognostic TKE	part of PBL mixing	multi-layer
MRF	K profile + countergradient term	part of PBL mixing	None
YSU	K profile + countergradient term	explicit term	1-layer, fractional
ACM2	transilient mixing up, local K down	part of PBL mixing	input only

3.1.3.1 Turbulent kinetic energy predictions schemes

Mellor-Yamada-Janjic (MYJ) scheme

This parameterization of turbulence in the PBL and in the free atmosphere [Janjic (1990, 1996, 2002)] represents a non-singular implementation of the Mellor-Yamada Level 2.5 turbulence closure model [Mellor and Yamada (1982)] through the full range of atmospheric turbulent regimes. In this implementation, an upper limit is imposed on the master length scale. This upper limit depends on the TKE as well as the buoyancy and shear of the driving flow. In the unstable range, the functional form of the upper limit is derived from the requirement that the TKE production be non-singular in the case of growing turbulence. In the stable range, the upper limit is derived from the requirement

that the ratio of the variance of the vertical velocity deviation and TKE cannot be smaller than that corresponding to the regime of vanishing turbulence.

Quasi-Normal Scale Elimination (QNSE) scheme

The QNSE scheme is a one-and-a-half order, local closure scheme and has a TKE prediction option that uses a new theory for stably stratified regions [Sukoriansky et al. (2005)]. The PBL height is defined as where the TKE profile decreases to a prescribed low value (0.01 m^2 s^{-2}), similar to the MYJ scheme. QNSE Provides realistic depiction of potential temperature profiles, PBL height, and kinematic profiles based on observational data and corresponding large eddy simulations [Kosovic and Curry (2000)] for its designed environment (stable conditions). Conversely, as with the MYJ scheme, in the case of the less-stable PBL, QNSE depicts too cool, moist, and shallow of a PBL for simulations of springtime convective environments.

Bougeault–Lacarrère (BouLac) scheme

The BouLac scheme is a one-and-a-half order, local closure scheme and has a TKE prediction option designed for use with the BEP (Building Environment Parametrization) multi-layer, urban canopy model. BouLac diagnoses PBL height as the height where the prognostic TKE reaches a sufficiently small value (in the current version of WRF is 0.005 m^2s^{-2}). It is found to better represent the PBL in regimes of higher static stability compared to nonlocal schemes in similar regimes [Shin and Hong (2011)].

Mellor–Yamada–Nakanishi–Niino Level 2.5 (MYNN2) scheme

The MYNN2 scheme is tuned to a database of large eddy simulations (LES) in order to overcome the typical biases associated with other MY-type schemes, such as insufficient growth of convective boundary layer and under-estimated

TKE. The MYNN2 scheme is a one-and-a-half order, local closure scheme and predicts sub-grid TKE terms.

Total Energy–Mass Flux (TEMF) scheme

The Total Energy–Mass Flux (TEMF) scheme [Angevine et al. (2010)] is a one-and-a-half order, non-local closure scheme and has a sub-gridscale total energy prognostic variable, in addition to mass-flux-type shallow convection. TEMF uses eddy diffusivity and mass flux concepts to determine vertical mixing. It compares favorably with large eddy simulation results for observations from the 2006 Texas Air Quality and Gulf of Mexico Atmospheric Composition and Climate Study (TexAQS II/GoMACCS) around Houston, Texas [Angevine et al. (2010)]; it yields PBL profiles more accurately depicting scenarios supporting shallow cumulus clouds than other schemes [Angevine et al. (2010)]. It Indicates greater drying beneath stratocumulus clouds and higher moisture content within the lower cloud layer compared to results from the large eddy simulations, indicating too much moisture flux across the lower cloud boundary in the TEMF scheme [Angevine et al. (2010)].

University of Washington (UW) scheme

The University of Washington (UW) scheme [Bretherton and Park (2009)] is a one-and-a-half order, local TKE closure scheme from the Community Earth System Model (CESM), climate model [Gent et al. (2011)].

Shin-Hong Scale–aware scheme

The Shin-Hong PBL is based on YSU and it is designed for subkilometer transition scales (200 m – 1 km). It attempts to represent the subgrid-scale (SGS) turbulent transport in convective boundary layers (CBLs) at gray-zone resolutions by investigating the effects of grid-size dependency in the vertical heat transport parameterization for CBL simulations.

First, nonlocal transport via strong updrafts and local transport via the remaining small-scale eddies are separately calculated. Second, the SGS nonlocal transport is formulated by multiplying a grid-size dependency function with the total nonlocal transport profile fit to the large-eddy simulation (LES) output. Finally, the SGS local transport is formulated by multiplying a grid-size dependency function with the total local transport profile, which is calculated using an eddy-diffusivity formula [Shin and Dudhia (2016)].

3.1.3.2 Diagnostic non local schemes

Medium Range Forecast (MRF) scheme

The scheme is described by Hong and Pan (1996). This PBL scheme employs a so-called counter-gradient flux for heat and moisture in unstable conditions. It uses enhanced vertical flux coefficients in the PBL, and the PBL height is determined from a critical bulk Richardson number. It handles vertical diffusion with an implicit local scheme, and it is based on local Ri in the free atmosphere. Compared to local PBL schemes, MRF more accurately simulates the deeper mixing within an unstable PBL where larger eddies entrain higher potential temperatures above the PBL into the PBL.

Yonsei University (YSU) scheme

The Yonsei University PBL [Hong et al. (2006)] is the next generation of the MRF PBL, also using the countergradient terms to represent fluxes due to non-local gradients. This adds to the MRF PBL [Hong and Pan (1996)] an explicit treatment of the entrainment layer at the PBL top. The entrainment is made proportional to the surface buoyancy flux in line with results from studies with large-eddy models [Noh et al. (2003)]. The PBL top is defined using a critical bulk Richardson number of zero (compared to 0.5 in the MRF PBL), so is effectively dependent on the buoyancy profile, in which the PBL top is defined

at the maximum entrainment layer (compared to the layer at which the diffusivity becomes zero). A smaller magnitude of the counter-gradient mixing in the YSU PBL produces a well-mixed boundary-layer profile, whereas there is a pronounced over-stable structure in the upper part of the mixed layer in the case of the MRF PBL. Details are available in Hong et al. (2006), including the analysis of the interaction between the boundary layer and precipitation physics. In version 3.0, an enhanced stable boundary-layer diffusion algorithm [Hong (2007)] is also devised that allows deeper mixing in windier conditions. YSU more accurately simulates deeper vertical mixing in buoyancy-driven PBLs with shallower mixing in strong-wind regimes compared to MRF [Hong et al. (2006)], however it has still been found to overdeep the PBL for springtime deep convective environments, resulting in too much dry air near the surface and underestimation of MLCAPE related to environments of deep convection [Coniglio et al. (2013)].

Asymmetrical Convective Model version 2 scheme

The ACM2 [Pleim (2007)] is a combination of the ACM, which is a simple transilient model that was originally a modification of the Blackadar convective model, and an eddy diffusion model. Thus, in convective conditions the ACM2 can simulate rapid upward transport in buoyant plumes and local shear induced turbulent diffusion. The partitioning between the local and nonlocal transport components is derived from the fraction of non-local heat flux according to the model of Holtslag and Boville (1993). The algorithm transitions smoothly from eddy diffusion in stable conditions to the combined local and non-local transport in unstable conditions. The ACM2 is particularly well suited for consistent PBL transport of any atmospheric quantity including both meteorological (u, v,θ , qv) and chemical trace species.

The scheme predicts changes in water vapor and condensate in the forms of cloud water, rain, cloud ice, and precipitation ice (snow/graupel/sleet). The individual hydrometeor fields are combined into total condensate, and it is the water vapor and total condensate that are advected in the model. Local storage arrays retain first-guess information that extract contributions of cloud water, rain, cloud ice, and precipitation ice of variable density in the form of snow, graupel, or sleet. The density of precipitation ice is estimated from a local array that stores information on the total growth of ice by vapor deposition and accretion of liquid water. Sedimentation is treated by partitioning the time-averaged flux of precipitation into a grid box between local storage in the box and fall out through the bottom of the box. This approach, together with modifications in the treatment of rapid microphysical processes, permits large time steps to be used with stable results.

3.2 Analysis of the atmospheric parameterizations

This paragraph is devoted to the analysis of available WRF atmosphere schemes for NWM and LES applications, including microphysics and radiation model components.

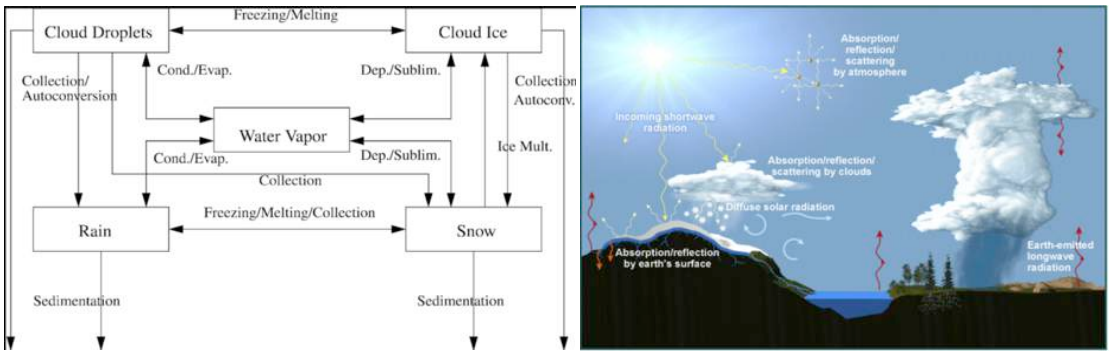

Figure 14: key microphysics and radiation processes

3.2.1 Microphysics parameterizations

Microphysics includes explicitly resolved water vapor, cloud, and precipitation processes. The model is general enough to accommodate any number of mass mixing-ratio variables, and other quantities such as number concentrations. Four-dimensional arrays with three spatial indices and one species index are used to carry such scalars. Memory, i.e., the size of the fourth dimension in these arrays, is allocated depending on the needs of the scheme chosen, and advection of the species also applies to all those required by the microphysics option. WRF offers microphysics parameterization options with different level of sophistication:

- Warm rain (i.e. no ice) – Kessler (idealized)
- Simple ice (3 arrays) – WSM3
- Mesoscale (5 arrays, no graupel) – WSM5
- Cloud-scale single-moment (6 arrays, graupel) – WSM6, Lin, Goddard, Eta-Ferrier
- Double-moment (8-13 arrays) – Thompson, Morrison, WDM5, WDM6, NSSL

Single-moment schemes have one prediction equation for mass (kg/kg) per species with particle size distribution being derived from fixed parameters.

Double-moment (DM) schemes add a prediction equation for number concentration (#/kg) per DM species, bearing in mind that DM schemes may only be double-moment for a few species and that they allow for additional processes such as size-sorting during fall-out and sometimes aerosol (CCN) effects.

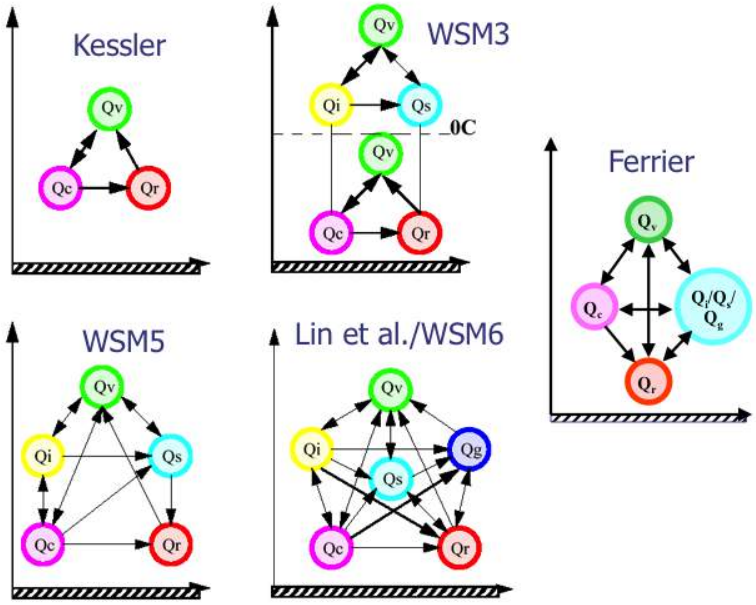

Figure 15: illustration of microphysics interactions for schemes with different level of sophistication, where Qv stands for water vapour, Qc for cloud water, Qr for rain water, Qi for cloud ice, Qs for snow, and Qg for graupel (courtesy of WRF-ARW tutorials).

3.2.1.1 Kessler scheme

This scheme (Kessler, 1969), which was taken from the COMMAS model (Wicker and Wilhelmson, 1995), is a simple warm cloud scheme that includes water vapor, cloud water, and rain. The microphysical processes included are: the production, fall, and evaporation of rain; the accretion and autoconversion of cloud water; and the production of cloud water from condensation.

3.2.1.2 Purdue Lin scheme

Six classes of hydrometeors are included: water vapor, cloud water, rain, cloud ice, snow, and graupel. All parameterization production terms are based on Lin et al. (1983) and Rutledge and Hobbs (1984) with some modifications, including saturation adjustment following Tao et al. (1989) and ice sedimentation. This is a relatively sophisticated microphysics scheme in WRF, and it is most suitable for use in research studies. The scheme is taken from the Purdue cloud model, and the details can be found in Chen and Sun (2002).

3.2.1.3 WRF Single-Moment 3-class (WSM3) scheme

The WRF single-moment microphysics scheme follows Hong et al. (2004) including ice sedimentation and other new ice-phase parameterizations. A major difference from other approaches is that a diagnostic relation is used for ice number concentration that is based on ice mass content rather than temperature. The computational procedures are described in Hong and Lim (2006).

As with WSM5 and WSM6, the freezing/melting processes are computed during the fall-term sub-steps to increase accuracy in the vertical heating profile of these processes. The order of the processes is also optimized to decrease the sensitivity of the scheme to the time step of the model. The WSM3 scheme predicts three categories of hydrometers: vapor, cloud water/ice, and rain/snow, which is a so-called simple-ice scheme. It follows Dudhia (1989) in assuming cloud water and rain for temperatures above freezing, and cloud ice and snow for temperatures below freezing. This scheme is computationally efficient for the inclusion of ice processes, but lacks supercooled water and gradual melting rates.

3.2.1.4 WSM5 scheme

This scheme is similar to the WSM3 simple ice scheme. However, vapor, rain, snow, cloud ice, and cloud water are held in five different arrays. Thus, it allows supercooled water to exist, and a gradual melting of snow falling below the melting layer. Details can be found in Hong et al. (2004), and Hong and Lim (2006). As with WSM6, the saturation adjustment follows Dudhia (1989) and Hong et al. (1998) in separately treating ice and water saturation processes, rather than a combined saturation such as the Purdue Lin (above) and Goddard

[Tao et al. (1989)] schemes. This scheme is efficient in intermediate grids between the mesoscale and cloud-resolving grids.

3.2.1.5 WSM6 scheme

The six-class scheme extends the WSM5 scheme to include graupel and its associated processes. Some of the graupel-related terms follow Lin et al. (1983), but its ice-phase behavior is much different due to the changes of Hong et al. (2004). A new method for representing mixed-phase particle fall speeds for the snow and graupel particles by assigning a single fallspeed to both that is weighted by the mixing ratios, and applying that fallspeed to both sedimentation and accretion processes is introduced [Dudhia et al. (2008)]. The behavior of the WSM3, WSM5, and WSM6 schemes differ little for coarser mesoscale grids, but they work much differently on cloud-resolving grids. Of the three WSM schemes, the WSM6 scheme is the most suitable for cloud-resolving grids, considering the efficiency and theoretical backgrounds [Hong and Lim (2006)]. As a further step towards high-resolution applications WRF also supplies a double-moment version (WDM6) of this scheme for warm rain processes, so that cloud condensation nuclei, and number concentrations of cloud and rain are also predicted.

3.2.1.6 Eta Ferrier scheme

The scheme (NOAA 2001) predicts changes in water vapor and condensate in the forms of cloud water, rain, cloud ice, and precipitation ice (snow/graupel/sleet). The individual hydrometeor fields are combined into total condensate, and it is the water vapor and total condensate that are advected in the model. Local storage arrays retain first-guess information that extract contributions of cloud water, rain, cloud ice, and precipitation ice of variable

density in the form of snow, graupel, or sleet. The density of precipitation ice is estimated from a local array that stores information on the total growth of ice by vapor deposition and accretion of liquid water. Sedimentation is treated by partitioning the time-averaged flux of precipitation into a grid box between local storage in the box and fall out through the bottom of the box. This approach, together with modifications in the treatment of rapid microphysical processes, permits large time steps to be used with stable results.

3.2.1.7 Thompson scheme

Compared to earlier single-moment schemes, the new scheme incorporates a large number of improvements to both physical processes and computer coding plus employs many techniques found in far more sophisticated spectral/bin schemes using look-up tables.

Furthermore, the assumed snow size distribution depends on both ice water content and temperature and is represented as a sum of exponential and gamma distributions. Furthermore, snow assumes a non-spherical shape with a bulk density that varies inversely with diameter as found in observations and in contrast to nearly all other BMPs that assume spherical snow with constant density. New features specific to this version of the bulk scheme compared to the Thompson et al. (2004) paper description include:

- generalized gamma distribution shape for each hydrometeor species
- non-spherical, variable density snow, and size distribution matching observations
- y-intercept of rain depends on rain mixing ratio and whether apparent source is melted ice
- y-intercept of graupel depends on graupel mixing ratio, and a more accurate saturation adjustment scheme
- variable gamma distribution shape parameter for cloud water droplets based on observations

- look-up table for freezing of water drops
- look-up table for transferring cloud ice into snow category
- improved vapor deposition/sublimation and evaporation
- variable collection efficiency for rain, snow, and graupel collecting cloud droplets
- improved rain collecting snow and graupel.

3.2.1.8 Goddard Cumulus Ensemble Model scheme

The Goddard Cumulus Ensemble (GCE) models [Tao and Simpson (1993)] one-moment bulk microphysical schemes are mainly based on Lin et al. (1983) with additional processes from Rutledge and Hobbs (1984). However, the Goddard microphysics schemes have several modifications.

First, there is an option to choose either graupel or hail as the third class of ice [McCumber et al. (1991)]. Graupel has a relatively low density and a high intercept value (i.e., more numerous small particles). In contrast, hail has a relative high density and a low intercept value (i.e., more numerous large particles). These differences can affect not only the description of the hydrometeor population and formation of the anvil-stratiform region but also the relative importance of the microphysical-dynamical-radiative processes. Second, new saturation techniques [Tao et al. (1989, 2003)] were added. These saturation techniques are basically designed to ensure that super saturation (sub-saturation) cannot exist at a grid point that is clear (cloudy). Third, all microphysical processes that do not involve melting, evaporation or sublimation (i.e., transfer rates from one type of hydrometeor to another) are calculated based on one thermodynamic state. This ensures that all of these processes are treated equally. Fourth, the sum of all sink processes associated with one species will not exceed its mass. This ensures that the water budget will be balanced in the microphysical calculations . The Goddard microphysics has a

third option, which is equivalent to a two-ice (2ICE) scheme having only cloud ice and snow. This option may be needed for coarse resolution simulations (i.e., > 5 km grid size). The two-class ice scheme could be applied for winter and frontal convection.

3.2.1.9 Morrison et al. double-moment scheme

The Morrison et al. (2009) scheme is based on the two-moment bulk microphysics scheme of Morrison et al. (2005) and Morrison and Pinto (2006). Six species of water are included: vapor, cloud droplets, cloud ice, rain, snow, and graupel/hail. The code has a user-specified switch to include either graupel or hail. Prognostic variables include number concentrations and mixing ratios of cloud ice, rain, snow, and graupel/hail, and mixing ratios of cloud droplets and water vapor (total of 10 variables). The prediction of two-moments (i.e., both number concentration and mixing ratio) allows for a more robust treatment of the particle size distributions, which are a key for calculating the microphysical process rates and cloud/precipitation evolution. Several liquid, ice, and mixed-phase processes are included. Particle size distributions are treated using gamma functions, with the associated intercept and slope parameters derived from the predicted mixing ratio and number concentration. The scheme has been extensively tested and compared with both idealized and real case studies covering a wide range of conditions.

3.2.1.10 NSSL double-moment scheme

This two-moment microphysics scheme predicts mass mixing ratio and number concentration of cloud droplets, rain, ice crystals, snow, graupel, and hail. Bulk particle density of graupel was also predicted, which allows a single category to represent a greater range of particle characteristics. The scheme is intended for

cloud-resolving simulations (dx <= 2km) in research applications [Mansell et al.(2010)].

3.3 Radiation parameterization

The radiation schemes provide atmospheric heating due to radiative flux divergence and surface downward longwave and shortwave radiation for the ground heat budget. Longwave radiation includes infrared or thermal radiation absorbed and emitted by gases and surfaces. Upward longwave radiative flux from the ground is determined by the surface emissivity that in turn depends upon land-use type, as well as the ground (skin) temperature. Shortwave radiation includes visible and surrounding wavelengths that make up the solar spectrum. Hence, the only source is the Sun, but processes include absorption, reflection, and scattering in the atmosphere and at surfaces. For shortwave radiation, the upward flux is the reflection due to surface albedo. Within the atmosphere the radiation responds to model-predicted cloud and water vapor distributions, as well as specified carbon dioxide, ozone, and (optionally) trace gas concentrations. All the radiation schemes in WRF currently are column (one-dimensional) schemes, so each column is treated independently, and the fluxes correspond to those in infinite horizontally uniform planes, which is a good approximation if the vertical thickness of the model layers is much less than the horizontal grid length. This assumption would become less accurate at high horizontal resolution.

3.3.1 Longwave schemes

They compute clear-sky and cloud upward and downward radiation fluxes:

- consider IR emission from layers
- Surface emissivity based on land-type
- Flux divergence leads to cooling in a layer

- Downward flux at surface important in land energy budget
- IR radiation generally leads to cooling in clear air (~2K/day),
- stronger cooling at cloud tops and warming at cloud base

3.3.1.1 Rapid Radiative Transfer Model (RRTM) Longwave

This RRTM, which is taken from MM5, is based on Mlawer et al. (1997) and is a spectral-band scheme using the correlated-k method. It uses pre-set tables to accurately represent longwave processes due to water vapor, ozone, CO2, and trace gases (if present), as well as accounting for cloud optical depth.

3.3.1.2 Eta Geophysical Fluid Dynamics Laboratory (GFDL) Longwave

This longwave radiation scheme is from GFDL. It follows the simplified exchange method of Fels and Schwarzkopf (1975) and Schwarzkopf and Fels (1991), with calculation over spectral bands associated with carbon dioxide, water vapor, and ozone. Included are Schwarzkopf and Fels (1985) transmission coefficients for carbon dioxide, a Roberts et al. (1976) water vapor continuum, and the effects of water vapor-carbon dioxide overlap and of a Voigt line-shape correction. The Rodgers (1968) formulation is adopted for ozone absorption. Clouds are randomly overlapped. This scheme is implemented to conduct comparisons with the operational Eta model.

3.3.1.3 CAM Longwave

A spectral-band scheme used in the NCAR Community Atmosphere Model (CAM 3.0) for climate simulations. It has the potential to handle several trace gases. It interacts with resolved clouds and cloud fractions, and is documented fully by Collins et al. (2004).

3.3.2 Shortwave schemes

They compute clear-sky and cloudy solar fluxes by including annual and diurnal solar cycles. Most schemes consider downward and upward (reflected) fluxes,

even if Dudhia scheme only has downward flux. They have primarily a warming effect in clear sky, as an important component of surface energy balance.

3.3.2.1 Eta Geophysical Fluid Dynamics Laboratory (GFDL) Shortwave

This shortwave radiation is a GFDL version of the Lacis and Hansen (1974) parameterization. Effects of atmospheric water vapor, ozone (both from Lacis and Hansen, 1974), and carbon dioxide [Sasamori et al. (1972)] are employed. Clouds are randomly overlapped. Shortwave calculations are made using a daylight-mean cosine solar zenith angle over the time interval (given by the radiation call frequency).

3.3.2.2 MM5 (Dudhia) Shortwave

This scheme is base on Dudhia (1989) and is taken from MM5. It has a simple downward integration of solar flux, accounting for clear-air scattering, water vapor absorption [Lacis and Hansen (1974)], and cloud albedo and absorption. It uses look-up tables for clouds from Stephens (1978).

3.3.2.3 Goddard Shortwave

This scheme is based on Chou and Suarez (1994). It has a total of 11 spectral bands and considers diffuse and direct solar radiation components in a two-stream approach that accounts for scattered and reflected components. Ozone is considered with several climatological profiles available.

3.3.2.4 CAM Longwave

A spectral-band scheme used in the NCAR Community Atmosphere Model (CAM 3.0) for climate simulations. It has the ability to handle optical properties of several aerosol types and trace gases. It uses cloud fractions and overlaps assumptions in unsaturated regions, and has monthly zonal ozone climatology.

It is documented fully by Collins et al. (2004). The CAM radiation scheme is especially suited for regional climate simulations by having a ozone distribution that varies during the simulation according to monthly zonal-mean climatological data.

3.4 Analysis of the forecast skill limitations

Since 1960, the meteorological modelling has been characterized by two main broad classes of models: *mesoscale modelling*, including nowadays cloud permitting and cloud resolving applications, and the *large eddy simulation (*LES*)*, whose range of applicability has been largely independent for many years. LES have been generally used to study turbulence processes in boundary layer (in particular in dry boundary layer), even though atmospheric turbulence ranges in nature from the typical large eddies production scales to the turbulent kinetic energy (TKE) dissipative scales.

Literature on turbulence studies shows as it is well represented by LES models at very fine grid meshes (10-100 m). In the early 1970s LES were developed for high Reynolds number in a channel [Lilly (1967); Deardorff (1970)], and then applied to meteorological flows [Deardorff (1972), Sommeria (1976)]. These simulations are based on a fundamental assumption: the chosen resolution Δ must be adapted as the most energetic eddies of typical scale L are resolved by the model and the mean effect of the smallest eddies on the mean flow is parameterized.

The concepts of resolved and unresolved scales of the atmospheric motion in NWM are strictly related to the spatial and temporal discretization used to solve numerically the primitive differential equations whose integration provides future state of the atmosphere.

Typical physical processes which operate on unresolved scales and need to be parameterized in terms of their interaction with the resolved scales are originated from friction, moist processes such as evaporation and condensation and radiative cooling and heating. The effects in atmosphere of these unresolved processes are captured by parameterizations which play the role of interconnection between atmosphere and surface since these processes drive the momentum and heat budgets at the grid scale and influence the skill of NMW in weather and climate prediction. For radiation and microphysical processes the formulation in global model is similar to that used in high resolution models while for deep convection and boundary layer processes their degree of formulation in parameterization is strictly related to the resolution used.

Over the last decades, the increase in computing power and resources has yielded a NWM with horizontal grid spacings (Δ) of the order of a few kilometers not only for pure scientific or idealized studies but allowing to most operational forecast centres to make in plan to use non hydrostatic models at kilometer scale. For example, the operative WRF model [Janjic (2003), Skamarock and Klemp (2008)] at the National Centers for Environmental Prediction (NCEP), the Air Force Weather Agency (AFWA) and at other centres used a 4 km resolution. At the same time, many sensitivities studies performed high resolution experiments with NWM have been conducted to try to reproduce extreme rainfall events and to evaluate the sources of uncertainty which limit the forecast skills of the models. In particular, combination of different grid resolutions and different timing in the initialization of the experiments that conducted to support the value added to use initialization as much as possible closer to the analyzed event. The combination of different grid resolutions and

different microphysical parameterizations stressed the importance of the role of cloud physics in simulation of the spatial distribution of rainfall.

However, even these high resolution simulations imply additional coast of maintenance, many modelers have avoided simulations in the so-called "gray zone" where some assumptions in parameterizations are violated but at the same time the physical process is not sufficiently resolved to be modeled explicitly. This is the case for deep convection representation: it is an open discussion the limit of horizontal resolution for which convection parameterization is no longer necessary [Dirmeyer et al.(2012)].

Some studies in the last years have reported improved model behavior at 4 km and less grid spacing without convection parameterization schemes [Done et al. (2004) Weisman et al. (2008), Schwartz et al. (2009), Fiori et al. (2014, 2017), Prein et al. (2013b)] with considerable increasing in quantitative precipitation forecasts [Benoit et al. (2002), Richard et al. (2007), Lean et al. (2008), Skamarock and Klemp (2008), Weusthoff et al. (2010), Baldauf et al. (2011)]. Switching off the convection parameterization (convection-resolving modeling) are thus attractive approaches since leads to more realistic precipitation patterns, especially in cases of moist convection and/or over mountainous regions [Grell et al. (2000), Mass et al. (2002)]. Additional advantages by applying high resolution and such convection-resolving models (CRMs) are a better representation of topography, surface fields, and boundary layer processes.

In regions with complex orography, when resolution is in the order of 1-2 km so that steep slopes can be resolved, studies have demonstrated that the distribution of rainfall is strongly influenced [Foresti et al. (2013), Foresti and Seed (2015)].

The influence on boundary layer processes development in relation to run numerical weather and climate model with grid sizes as small as 2 km is also related on how turbulence is represented. If such models treat turbulence as an entirely sub-grid processes (Δ larger than 2 km) or the three-dimensional turbulence providing energy to the inertial sub-range is explicitly resolved in LES mode (Δ 10-100m), turbulence is well represented. At intermediate scales, the so called "terra incognita" (Wyngaard, 2004), the turbulent structures are neither entirely subgrid scale (as in global and mesoscale models) nor largely resolved (as in LES).

Several studies have shown that grid spacing of *O*(1) km is insufficient to resolve turbulent eddies and cloud-scale motions [Bryan et al. (2003), Rotunno et al. (2009), Dawson et al. (2010), Bryan and Morrison (2012)] while several other studies have found convergence in various bulk quantities as horizontal grid spacing is reduced to 500-200 m [Fiori et al. (2010, 2011), Langhans et al. (2012), Verelle et al. (2014)] and LES is used not only for idealized cases but also for isolated convective system [Ricard et al. (2013)] and simulations of the Hector thunderstorm [Dauhut et al. (2015)].

3.5 WRF Preprocessing System (WPS)

The initial and boundary conditions for the WRF real-data cases are pre-processed through a separate package called the WRF Preprocessing System (WPS). The WPS is a set of programs that takes terrestrial and meteorological data (typically in GriB format) and transforms them for input to the ARW pre-processor program for real-data cases (real). Figure 16 shows the flow of data into and out of the WPS system:

- The purpose of geogrid is to define the simulation domains, and

interpolate various terrestrial data sets to the model grids. The simulation domains are defined using information specified by the user in the “geogrid” namelist record of the WPS namelist file, namelist.wps. In addition to computing the latitude, longitude, and map scale factors at every grid point, geogrid will interpolate soil categories, land use category, terrain height, annual mean deep soil temperature, monthly vegetation fraction, monthly albedo, maximum snow albedo, and slope category to the model grids by default. Global data sets for each of these fields are provided through the WRF download page, and, because these data are time-invariant, they only need to be downloaded once. Several of the data sets are available in only one resolution, but others are made available in resolutions of 30", 2', 5', and 10'; here, " denotes arc seconds and ' denotes arc minutes;

- The ungrib program reads GRIB files, "degribs" the data, and writes the data in a simple format, called the intermediate format (see the section on writing data to the intermediate format for details of the format). The GRIB files contain time-varying meteorological fields and are typically from another regional or global model, such as IFS-ECMWF, or GFS models. The ungrib program can read GRIB Edition 1 and, if compiled with a "GRIB2" option, GRIB Edition 2 files;
- The metgrid program horizontally interpolates the intermediate-format meteorological data that are extracted by the ungrib program onto the simulation domains defined by the geogrid program. The interpolated metgrid output can then be ingested by the WRF real program. The range of dates that will be interpolated by metgrid are defined in the “share” namelist record of the WPS namelist file, and date ranges must

be specified individually in the namelist for each simulation domain. Since the work of the metgrid program, like that of the ungrib program, is time-dependent, metgrid is run every time a new simulation is initialized.

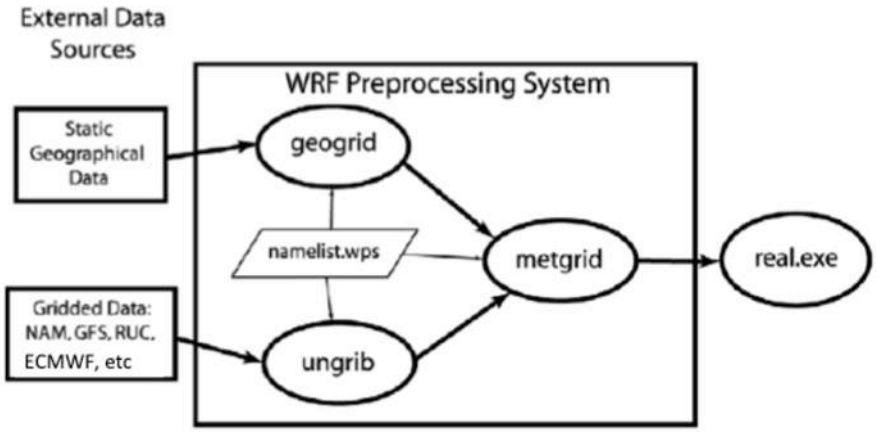

Figure 16: WPS rationale (courtesy of WRF-ARW tutorials).

The inputs a to the ARW real-data processor (real. Exe) from WPS contains 3-dimensional fields (including the surface) of temperature (K), relative humidity (and the horizontal components of momentum (m/s, already rotated to the model projection). The 2-dimensional static terrestrial fields include: albedo, Coriolis parameters, terrain elevation, vegetation/land-use type, land/water mask, map scale factors, map rotation angle, soil texture category, vegetation greenness fraction, annual mean temperature, and latitude/longitude. The 2-dimensional time-dependent fields from the external model, after processing by WPS, include: surface pressure and sea-level pressure (Pa), layers of soil temperature (K) and soil moisture (kg/kg, either total moisture, or binned into total and liquid content), snow depth (m), skin temperature (K), sea surface temperature (K), and a sea ice flag.

4. The WRF data assimilation system: WRFDA

4.1 WRFDA structure and observational capability

The data assimilation is the techniques that combines a Numerical Weather Prediction (NWP) output (first guess or background forecast) with observations and their respective error statistics providing as product an improved state of the atmosphere (analysis). The improvement of the forecast skill through the use of data assimilation techniques became in the last few years an increasingly important topic of research. WRFDA is a freely available data assimilation software allowing the NWP community to perform both research and operational implementation in the same framework [Barker et al. (2012)].

The WRF model had a significant data assimilation component from the beginning of its development. After an initial discussion between major partners (NCAR, National Oceanic and Atmospheric Administration (NOAA), the U.S. Air Force Weather Agency (AFWA), Oklahoma University, and the U.S. Naval Research Laboratory) in 1999-2000 the basic requirements of the data assimilation system were defined to satisfy both operational and research communities. The key idea at the base of the system is that WRFDA has to be robust and efficient, accurate, computational efficient, portable, well documented and ease of use. In this framework WRFDA features three-dimensional and four-dimensional data assimilation (3DVAR, 4DVAR) as well as an hybrid variational ensemble technique (ensemble transform Kalman filter (ETKF) – 3DVAR). The first version of this data assimilation system was distributed in 2003 with only 3DVAR implemented (named WRF 3DVAR), and subsequently updated in two steps: WRF 2.0 (2004) and WRF 3.0 [Barker et al. (2004), Skamarock et al. (2008)]. Furthermore in 2004 the 4DVAR has been

released [Huang et al. (2009)] and the system's name was changed in WRF-VAR. Finally, in 2008 the release of the ETKF-3DVAR hybrid variational/ensemble system led to the final name WRFDA.

All the techniques can assimilate a wide range of observations ranging from the more traditional ones (surface, rawinsonde, aircraft, wind profiler, and atmospheric motion vectors) to the newer ones (radar radial velocity and reflectivity, satellite-based observations such as radiance, GPS radio occultation measurements etc) as reported in Table 1 [Powers et al. (2017)].

Conventional surface and upper-air, radar, and precipitation data	Satellite and related ground-based retrievals	Satellite radiances
SYNOP, METAR, SHIP, BUOY, mesonet (surface pressure, 2-m temperature *T* and specific humidity *q*, 10-m wind speed *U*/wind direction *V*)	Atmospheric motion vectors	HIRS, AMSU-A, AMSU-B, MHS from NOAA and MetOp series
Radiosonde (*U*, *V*, *T*, *q*)	SATEM thicknesses	SSMIS from DMSP series
Pibal (upper-air *U*, *V*)	Scatterometer oceanic surface winds	ATMS from *SNPP*
AIREP/ACARS/AMDAR/TAMDAR (*U*, *V*, *T*, *q*)	Wind profiler (*U*, *V*)	AIRS from *Aqua*
Radar derived: Reflectivity, radial velocity, retrieved rainwater, retrieved humidity within cloud	Ground-based GPS total precipitable water and zenith total delay	IASI from MetOp series
Stage IV precipitation (for 4DVAR only)	GPS refractivity	SEVIRI from Meteosat series
	AIRS-retrieved *T* and *q* profiles	MWTS/MWHS from FY-3 series
		AMSR-2 from GCOM-WI

Table 1: The WRFDA Observation Catalog (Powers et al. 2017)

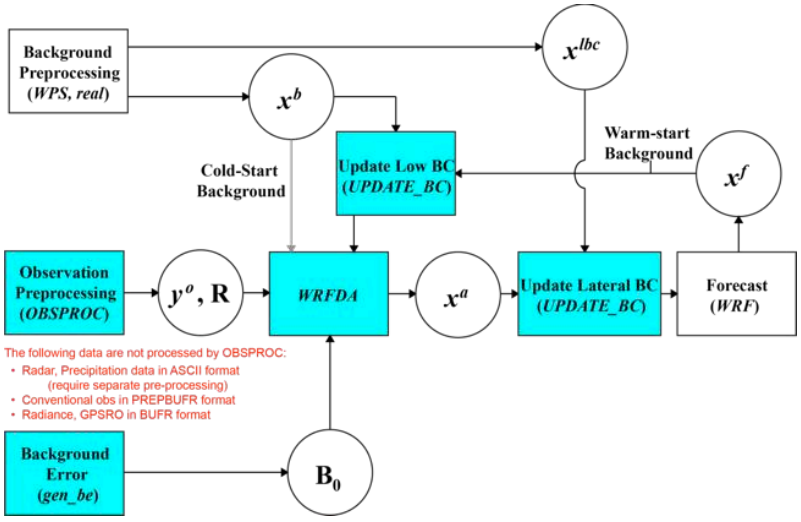

Figure 17: WRFDA in the WRF modelling system. In blue the WRFDA components are reported with the relation of the rest of the WRF system (white boxes). Where: x^b: first guess, either from a previous WRF forecast or from WPS/real.exe output. x^{lbc}: lateral boundary from WPS/real.exe output. x^a: analysis from the WRFDA data assimilation system. x^f :WRF forecast output. y^o: observations processed by OBSPROC (note: PREPBUFR input, radar, radiance, and rainfall data do not go through OBSPROC). B_0: background error statistics from generic BE data (CV3) or gen_be utility. R: observational and representative error statistics.

One of the main advantages of WRFDA is that it is built directly within the WRF modelling system (Figure 17) providing a direct interface with the other WRF components.

The inputs for WRFDA are three (Figure 17):

- The background forecast (x^b): in cold-start mode it is a forecast or analysis from another model interpolated to ARW grid through the use of WPS and Real programs of WRF system, in warm-start mode (cycling mode) it is the output of a short range forecast (typically 1-6 hours) run with WRF-ARW system.
- Observations (y^0): they can be provided in PREBUFR or LITTLE_R format, and an observation preprocessor (OBSPROC) is designed to reform and quality check observations that after can be directly read in WRFDA.
- Background error covariances matrix (B): necessary to define the spatial and multivariance response of the analysis to observations. It is calculated off-line through the use of gen_be utility.

When the data assimilation of all observations ends, the analysis state (x^a) must be merged with the existing boundary conditions (x^{lbc}) using the UPDATE_BC utility.

Summarizing, together with WRFDA there are three main utilities helpful for efficient data assimilation: OBSPROC for observation preprocessing, gen_be for background error estimation and UPDATE_BC to merge the analysis product of data assimilation with the existing boundary condition file.

4.1.1 Observation Preprocessing (OBSPROC)

OBSPROC provides observations (y^0) for ingest in WRFDA. The program reads LITTLE_R format (a text-based format) and its functions are:

- Read the observations from LITTLE_R file and the run time and space coverage from a namelist file.
- Remove observations that are outside the temporal window and the spatial domain.
- Through the hydrostatic pressure assumption retrieve pressure or height based on observed information.
- Check multi-level observations for vertical consistency and superadiabatic conditions.
- Estimate the error for each observation from a pre-specified error file
- Write an output file in ASCII or BUFR format to be direct ingested in WRFDA.

4.1.2 Background Error Calculation (gen_be)

The background error covariance statistics are necessary in WRFDA cost function minimization to weight errors in features of background forecast field. The WRFDA's gen_be utility estimates domain-specific climatological background error covariance matrix based on input training data that could be time series of forecast differences (the so called "NMC method", Parrish an Derber (1992)) or perturbations from an ensemble prediction system [Skamarock et al. (2008), chapter 9].

The NMC-method estimates climatological background error covariances using a process that assume background errors to be well approximated by averaged forecast difference statistics (Eq 4.1):

$$\mathbf{B} = \overline{\left(\mathbf{x}'^{b} - \mathbf{x}'^{t}\right)\left(\mathbf{x}'^{b} - \mathbf{x}'^{t}\right)^{T}} = \overline{\varepsilon_b \varepsilon_b^{T}} \approx \overline{\left(\mathbf{x}'^{T+24} - \mathbf{x}'^{T+12}\right)\left(\mathbf{x}'^{T+24} - \mathbf{x}'^{T+12}\right)^{T}} \qquad \textbf{Eq 4.1}$$

where $\mathbf{x}'^{t}$ is the true state of the atmosphere and ε_b is the background error. The overbar means an average over time and/or space. Alternatively, for an ensemble based statistics the vectors are $\mathbf{x}_k' = \mathbf{x}_k - \overline{\mathbf{x}}$, where the overbar is the average of ensemble members and K=1,ne (number of ensemble members).

However, the background error covariance matrix is computed not in the model space x' (u,v,T,q,p_s) but in a control variable space (**v**) related to the model space through the control variable transform (**U**):

$$\mathbf{x}' = \mathbf{U}\mathbf{v} = \mathbf{U}_p \mathbf{U}_v \mathbf{U}_h \mathbf{v} \qquad \textbf{Eq 4.2}$$

The expansion $\mathbf{U}=\mathbf{U}_p\,\mathbf{U}_v\,\mathbf{U}_h$ in Eq. 4.2 represents a series of operations (Lorenc et al. 2000) implemented in different stages of covariance modelling: horizontal correlations ($\mathbf{U}_h$), vertical covariances ($\mathbf{U}_v$) and multivariate covariances ($\mathbf{U}_p$). The **v** components are chosen so that their error cross-correlation are negligible, so the B matrix will be block-diagonalized.

Gen_be calculates the background error covariance matrix through 4 stages:

- *Stage_0*: stage_0 converters transforms model-specific data (alternative models use different grids, variables, data format, etc.) to standard perturbation fields and metadata and output them in a standard binary format. The standard fields are:

- Perturbations: streamfunction /'(i,j,k), velocity potential |' (i,j,k), temperature T'(i,j,k), relative humidity RH'(i,j,k), surface pressure $p'_s(i,j)$.
- Full-fields: height z(i,j,k), latitude \(i,j) (required to produce error statistics stored in terms of physics variables rather than tied to a grid).

- *Stage_1*: remove the time-mean in order to calculate covariance between fields.
- *Stage_2*: In this stage is provided a statistics for the unbalanced fields ($|_u$,T_u, P_{su}) used as control variables in WRFDA. The unbalanced control variables are the difference between the full and balanced components of the field. In Stage_2 the balanced component of particular fields is modelled through a regression analysis of the fields using specific predictor fields (see Wu et al. 2002). The regression coefficients obtained are output to be used in WRFDA U_p transform. The regression analysis results in three sets of regression coefficients:
  - *Velocity potential* – streamfunction regression: $\chi_b(k) = c(k)\psi(k)$
  - *Temperature* – streamfunction regression: $T_b(k) = \sum_{k1} G(k1,k)\psi(k1)$
  - *Surface pressure* – streamfunction regression: $p_{sb} = \sum_{k1} W(k1)\psi(k1)$

  Note: perturbation notation dropped for clarity.

The sum over k1 relates to integral relationship between mass fields and the wind field. The regression coefficient c, G and W do not vary horizontally by default. Once computed the regression coefficients, the unbalanced components of fields will be:

- $\chi_u(k) = \chi(k) - c(k)\psi(k)$
- $T_u(k) = T(k) - \sum_{k1} G(k1,k)\psi(k1)$
- $p_{su} = p_s - \sum_{k1} W(k1)\psi(k1)$

The fields calculated in this way will be the input for the next stage (spatial covariances).

- *Stage_3*: calculates statistics necessary for the vertical component of the control variable transform. The vertical transform $\mathbf{U}_v$ is applied using an empirical orthogonal function (EOF) decomposition of background error covariances (Barker et al. 2004). The vertical component of **B** ($\mathbf{B}_v$) is calculated for each 3D control variable and eigenvector decomposition is calculated on model levels k. $\mathbf{B}_v$ considering K model levels will be a KxK positive-definite, symmetric matrix and given an estimate of $\mathbf{B}_v$ (through NMC method), the eigendecomposition $\mathbf{B}_v = \mathbf{E}\Lambda\mathbf{E}^T$ of the matrix is performed to obtain eigenvectors **E** and eigenvalues Λ. After this calculation, the entire sequence of 3D control variables is projected into EOF space (vertical transform $\mathbf{U}_v$): $\mathbf{v}_p = \mathbf{U}_v\mathbf{v}_v = \mathbf{E}\Lambda^{1/2}\mathbf{v}_v$.
- *Stage_4*: computes the last requirement of background error covariance, the horizontal error correlations, through the use of recursive filters (Hayden and Purser 1995; Purser et al. 2003a) in case of regional applications and power spectra for global mode. In regional applications the horizontal correlations are computed between each 2D field grid points, binned as a function of distance. A Gaussian curve is fitted to the data to provide the length scales of correlation that is used in the recursive filter algorithm (refer to Barker et al. 2004 for further details). In

contrast, in global applications power spectra are computed for each vertical modes (K) control variables $/$, $|_u$, T_u, RH_u and p_{su}.

From a more practical point of view, in gen_be utility the users have four choices to define the B matrix, called CV3, CV5, CV6 and CV7. Each of them has different properties and considers different control variables as it is reported in Table 2.

CV option	***Control Variables***
CV3	ψ, χ_u, T_u, q, p_{su}
CV5	ψ, χ_u, T_u, RH_s, p_{su}
CV6	ψ, χ_u, T_u, RH_{su}, p_{su}
CV7	u, v, T, RH_s, p_s

Table 2: Background error covariances matrix options where: $/$ is the streamfunction, $|_u$ is the unbalanced velocity potential, T_u is the unbalanced temperature, p_{su} is the unbalanced surface pressure, RH_s is the pseudo relative humidity, RH_{su} is the unbalanced pseudo relative humidity and p_s is the surface pressure.

The CV3 option is provided in WRFDA and the control variables are in physical space while CV5, CV6 and CV7 are obtained through the use of gen_be and the control variables are in eigenvector space. The main difference between CV3 and others is linked to the vertical covariance: CV3 uses the vertical recursive filter, while others uses EOF to model the vertical covariance. Also the recursive filters to model horizontal covariance are different. In general, CV3 is a global B matrix that could be used in any regional domain, while CV5, CV6 and CV7 are domain-dependent B matrices and should be generated on forecasts or ensemble data from the same domain that will be used for data assimilation. Furthermore, the difference between CV5, CV6 and CV7 is only linked to the control variables they use.

4.1.3 Update boundary conditions (UPDATE_BC)

Using the analysis state (output of WRFDA) as initial conditions, it is necessary to first update the lateral boundary conditions to reflect differences between background and analysis state. Only boundary conditions of domain 1 must be updated because boundary conditions for nests domains are calculated from domain 1. To pursue this aim the script update_bc.csh is provided and it works with the following input:

- The analysis state (initial conditions after data assimilation)
- Original lateral boundary conditions of 1 domain (wrfbdy_d01)
- A namelist called parame.in

After running the executable update_bc.exe the old boundary conditions will be overwritten with the updated one.

4.2 WRFDA variational data assimilation

In general, variational system can be classified as those techniques that provide an analysis state of the atmosphere through the minimization of a cost function given two source of data: a background forecast (first guess) and observations. The main advantages related to the variational data assimilation technique are the possibility to assimilate a wide range of observations related nontrivially to standard atmospheric variables (e.g. radiance) and the imposition of a dynamic balance that can be implicit in the forecast model itself (in case of 4DVAR) or explicit using some balance equations (in case of 3DVAR). In WRFDA both 3DVAR and 4DVAR are available from WRF 3.0 [Skamarock et al. (2008)] release. Prior to WRF 3.0 only 3DVAR was available and the cost function minimization used a modified version of limited memory Quasi-Newton Method (QNM), starting from WRF 3.0 the alternative Conjugate Gradient Method (CGM) is implemented. This update imply the complete linearization of

WRFVAR's inner loop that was a limitation overcame through the introduction of multiple outer loops with the purpose of iterate over nonlinear solutions (like observation operators, balance constraints in 3DVAR and the forecast itself in 4DVAR) through the use of the WRFDA's analysis state from the previous iteration as new first guess (Figure 18). The use of multiple outer loops can be also very useful in variational quality control because usually observations are rejected if the magnitude of the observation minus the background forecast differences are larger than a given threshold (typically a multiple of the observation error standard deviation). This choice implicitly assumes that the first guess is accurate, but in case of areas with large forecast errors, there was the danger that good observations could be rejected. The outer loops allow observations rejected in previous iteration to be accepted in the following iteration if the observation minus the updated first guess (the analysis from the previus outer loop) became smaller than the specified threshold.

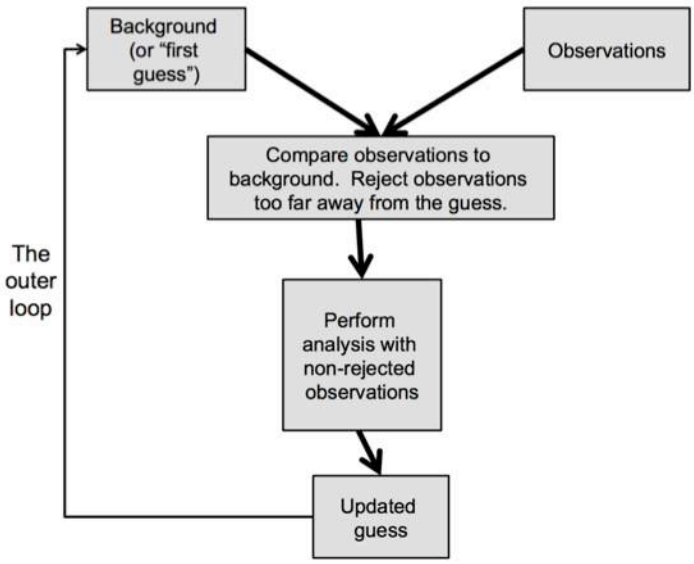

Figure 18: Outer loop schematization.

4.2.1 3DVAR implementation

The 3DVAR was the first data assimilation technique released in WRF model, the basic goal of this technique is to provide an optimal estimate of the true state of the atmosphere through the minimization of the cost function reported in Eq. 4.3 [Ide et al. (1997)].

$$J(x) = J^b + J^0 = \frac{1}{2}(\mathbf{x} - \mathbf{x}^b)^T B^{-1}(\mathbf{x} - \mathbf{x}^b) + \frac{1}{2}(\mathbf{y} - \mathbf{y}^0)^T(\mathbf{E} + \mathbf{F})^{-1}(\mathbf{y} - \mathbf{y}^0). \quad \textbf{Eq 4.3}$$

In summary, the 3DVAR problem is the iterative solution of Eq. 4.3 to find the analysis state (**x**) that minimizes the cost function J(**x**) which represents the a posteriori maximum likelihood estimate of the true state of the atmosphere, combining the two sources of data: observations ($\mathbf{y}^0$) and background ($\mathbf{x}^0$). **B**, **E** and **F** are the background, observation (instrumental) and representivity error covariance matrices respectively used as weight to fit the two sources of data. The representitivity error is introduced from the use of an observation operator (H) to transform the gridded analysis to the observation space: **y**=H(**x**).

Eq. 4.3 assumes that the error covariances are described by a Gaussian PDF with 0 mean error, but can be also used alternative costs functions that relax this constraint (e.g. Dharssi et al. 1992). Furthermore Eq. 4.3 neglects correlations between observation and background errors, as it is usually done in variational approach [Parrish and Derber (1992), Zou et al. (1997), Lorenc et al. (2000)].

The multidimensional cost function is efficiently solved through the use of adjoint operations (like multidimensional application of the chain-rule for partial differentiation). Considering a model state x with n degrees of freedom (grid

points number times independent variables number), the calculation of the J^b term of Eq. 4.3 requires ~$O(n^2)$ calculations. In a typical NWP problem n^2~10^{12}-10^{14}, then a direct solution is not feasible in the time window necessary for data assimilation in operational issues. A solution to reduce the computational cost of J^b calculation is to calculate it in terms of *control variables* defined as **x**'=**Uv**, where **x**' is the analysis increment (**x**-$\mathbf{x}^b$) and **U** transform is designed to nondimensionalize the problem and to allow the use of efficient filtering techniques that approximate the full background error covariance matrix. With a U transform well designed, the condition numbers will be small and the product $\mathbf{UU}^T$ will quite match the **B** matrix. In terms of analysis increments, the Eq. 4.3 can be rewritten as:

$$J(v) = J^b + J^0 = \frac{1}{2}\mathbf{v}^T\mathbf{v} + \frac{1}{2}(\mathbf{y}^{0'} - \mathbf{HUv})^T(\mathbf{E}+\mathbf{F})^{-1}(\mathbf{y}^{0'} - \mathbf{HUv}). \qquad \textbf{Eq 4.4}$$

Where $\mathbf{y}^{0'}$=$\mathbf{y}^0$-H($\mathbf{x}^b$) is the innovation vector and H is the linearization of *H.*

4.2.2 4DVAR algorithm

The main advantages of 4DVAR technique with respect to 3DVAR are:

- The ability of using observations at the time of their measurements.
- The implicit definition of flow dependent forecast error covariances.
- The ability of use the forecast model itself as a constraint enhancing the analysis in terms of dynamical balance.

Instead, the main disadvantage is related to the higher computational cost.

The WRFDA 4DVAR implementation algorithm takes the incremental formulation from commonly used in operational systems [Courtier et al. (1994), Veersé and Thépaut (1998), Lorenc (2003)]. This approach finds the analysis

increment that minimizes a cost function that is a function of the analysis increment instead the analysis itself. Usually in this incremental 4DVAR the tangent linear and adjoint models are derived from a simplified forward model used in the inner loop minimization, while the background evolution is predicted with the full forward model.

From a mathematical point of view, the 4DVAR minimizes a cost function (J) that includes a quadratic measure of the distance to background (J_b), observation (J_o) and balanced solution (J_c):

$$J = J_b + J_0 + J_c \qquad \textbf{Eq 4.5}$$

Where:

- The background cost function (J_b) is:

$$\begin{aligned} J_b &= \frac{1}{2}(\mathbf{x}^n - \mathbf{x}^b)^T \mathbf{B}^{-1}(\mathbf{x}^n - \mathbf{x}^b) \\ &= \frac{1}{2}[(\mathbf{x}^n - \mathbf{x}^{n-1}) + (\mathbf{x}^{n-1} - \mathbf{x}^b)]^T \mathbf{B}^{-1}[(\mathbf{x}^n - \mathbf{x}^{n-1}) + (\mathbf{x}^{n-1} - \mathbf{x}^b)] \\ &= \frac{1}{2}\left[(\mathbf{x}^n - \mathbf{x}^{n-1}) + \sum_{i=1}^{n-1}(\mathbf{x}^i - \mathbf{x}^{i-1})\right]^T \mathbf{B}^{-1}\left[(\mathbf{x}^n - \mathbf{x}^{n-1}) + \sum_{i=1}^{n-1}(\mathbf{x}^i - \mathbf{x}^{i-1})\right] \end{aligned} \qquad \textbf{Eq 4.6}$$

in which superscripts -1 and T indicate the inverse and adjoint of a matrix or a linear operator, **B** is the background error covariance matrix, $\mathbf{x}^b$ is the background state (usually is a short range forecast), the notation x^i denotes an intermittent analysis after the *i*th outer loop and the final analysis is denoted as $\mathbf{x}^n$ (or $\mathbf{x}^a$).

- The observation cost function (J_0) is the quadratic measure of distance between the final analysis ($\mathbf{x}^n$) and the observations ($\mathbf{y}_k$) through the forecast model (M_k) and the observation operator (H_k):

$$
\begin{aligned}
J_0 &= \frac{1}{2}\sum_{k=1}^{K}\left\{H_k[M_k(\mathbf{x}^n)]-\mathbf{y}_k\right\}^T \mathbf{R}^{-1}\left\{H_k[M_k(\mathbf{x}^n)]-\mathbf{y}_k\right\} \\
&\approx \frac{1}{2}\sum_{k=1}^{K}\left\{H_k[M_k(\mathbf{x}^{n-1})]+\mathbf{H_k}\mathbf{M_k}(\mathbf{x}^n-\mathbf{x}^{n-1})-\mathbf{y}_k\right\}^T \mathbf{R}^{-1}\left\{H_k[M_k(\mathbf{x}^{n-1})]+\mathbf{H_k}\mathbf{M_k}(\mathbf{x}^n-\mathbf{x}^{n-1})-\mathbf{y}_k\right\} \quad \textbf{Eq 4.7} \\
&= \frac{1}{2}\sum_{k=1}^{K}\left\{\mathbf{H_k}\mathbf{M_k}(\mathbf{x}^n-\mathbf{x}^{n-1})-\mathbf{d}_k\right\}^T \mathbf{R}^{-1}\left\{\mathbf{H_k}\mathbf{M_k}(\mathbf{x}^n-\mathbf{x}^{n-1})-\mathbf{d}_k\right\}
\end{aligned}
$$

The assimilation time window is here split into K observation windows. H_k and $\mathbf{H}_k$ are the nonlinear and tangent linear observation operators over the observation window necessary to transform the variables from the gridded model space to the observation space. M_k and $\mathbf{M}_k$ are the nonlinear and tangent linear models used to propagate respectively the first guess vector $\mathbf{x}^{n-1}$ and the analysis increment $\mathbf{x}^n$ - $\mathbf{x}^{n-1}$. $\mathbf{R}$ is the observation error covariance matrix. Finally, $\mathbf{d}_k$ is the innovation vector for observation vector for observation window:

$$\mathbf{d}_k = \mathbf{y}_k - H_k[M_k(\mathbf{x}^{n-1})] \qquad \textbf{Eq. 4.8}$$

- The balancing cost function (J_c) measures the quadratic distance between analysis state and a balanced state. To do this, a digital filter is included in 4DVAR to remove high-frequency waves and its implementation is similar to the forms in Gustafsson (1992), Gauthier and Thépaut (2001), and Wee and Kuo (2004):

$$J_c = \frac{1}{2}\gamma_{df}\left[\mathbf{M}_{N/2}(\mathbf{x}^n - \mathbf{x}^{n-1}) - \sum_{i=0}^{N} f_i \mathbf{M}_i(\mathbf{x}^n - \mathbf{x}^{n-1})\right]^T \mathbf{C}^{-1}\left[\mathbf{M}_{N/2}(\mathbf{x}^n - \mathbf{x}^{n-1}) - \sum_{i=0}^{N} f_i \mathbf{M}_i(\mathbf{x}^n - \mathbf{x}^{n-1})\right] \quad \textbf{Eq 4.9}$$
$$= \frac{1}{2}\gamma_{df}\left[\sum_{i=0}^{N} g_i \mathbf{M}_i(\mathbf{x}^n - \mathbf{x}^{n-1})\right]^T \mathbf{C}^{-1}\left[\sum_{i=0}^{N} g_i \mathbf{M}_i(\mathbf{x}^n - \mathbf{x}^{n-1})\right]$$

  where f_i is the digital filter coefficient (Lynch and Huang 1992; Gauthier and Thépaut 2001), g_i is the modified coefficient ($g_i = -f_i$ if $i \neq N/2$ and $g_{N/2} = 1 - f_{N/2}$), N is the total integration steps over the assimilation window, γ_{df} is the weight assigned to J_c, and **C** is a diagonal matrix that contains variances of wind (3 m/s)^2, temperature (1 K)^2 and dry surface pressure (10 hPa)^2.

As previously explained for 3DVAR, also in this case the preconditioning of the background cost function is implemented through the use of a control variable transform:

$$\mathbf{v}^n = \mathbf{U}^{-1}(\mathbf{x}^n - \mathbf{x}^{n-1}) \quad \textbf{Eq 4.10}$$

Thus, the cost function gradient J' becomes:

$$J'(\mathbf{v}^n) = \sum_{i=1}^{n-1} \mathbf{v}^i + \mathbf{v}^n + \mathbf{U}^T \sum_{k=1}^{K} \mathbf{M}_k^T \mathbf{H}_k^T \mathbf{R}^{-1} \left\{ \mathbf{H}_k \mathbf{M}_k \mathbf{U}\mathbf{v}^n - \mathbf{d}_k \right\} + \mathbf{U}^T \sum_{i=0}^{N} \mathbf{M}_i^T f_i \gamma_{df} \mathbf{C}^{-1} \left(\sum_{i=0}^{N} f_i \mathbf{M}_i \mathbf{U}\mathbf{v}^n \right) \quad \textbf{Eq 4.11}$$

Where $\mathbf{H}_k^T$ is the adjoint observation operation on observation window (k), $\mathbf{M}_k^T$ is the adjoint model used to propagate the analysis residuals (contained in {} parenthesis) and the digital filter forcing (contained in () parenthesis) backward in time from the time indicated from i or k indices to 0. Note that setting K=1 and removing the model-related components it is possible to find the 3DVAR solution.

4.3 Hybrid ETKF-Variational data assimilation

The hybrid data assimilation techniques aim to combine the benefits of the variational data assimilation (dynamical and physical constraints, simultaneous treatment of observations, quality control, the use of outer loops to treat nonlinearities) with those of ensemble technique (flow dependence and flexibility).

The use of WRFDA coupled with an ensemble prediction system is shown in Figure 19. There are two main steps, the first is a forecast step where and an ensemble of N WRF forecast members ($\mathbf{x}^f_n$) is integrated forward until the next data assimilation window. The second step is the update step where the ensemble mean is used as background for WRFDA, here the flow-dependent forecast errors is supplied by ensemble perturbations (member minus mean) reported in Figure 19 as a blue dashed line. The main difference between hybrid and pure 3DVAR is that the 3DVAR relies on a static error covariance of background, while the hybrid system uses a combination of the 3DVAR static

error covariances and an ensemble estimated error covariance incorporating a flow-dependent estimate of background error statistics.

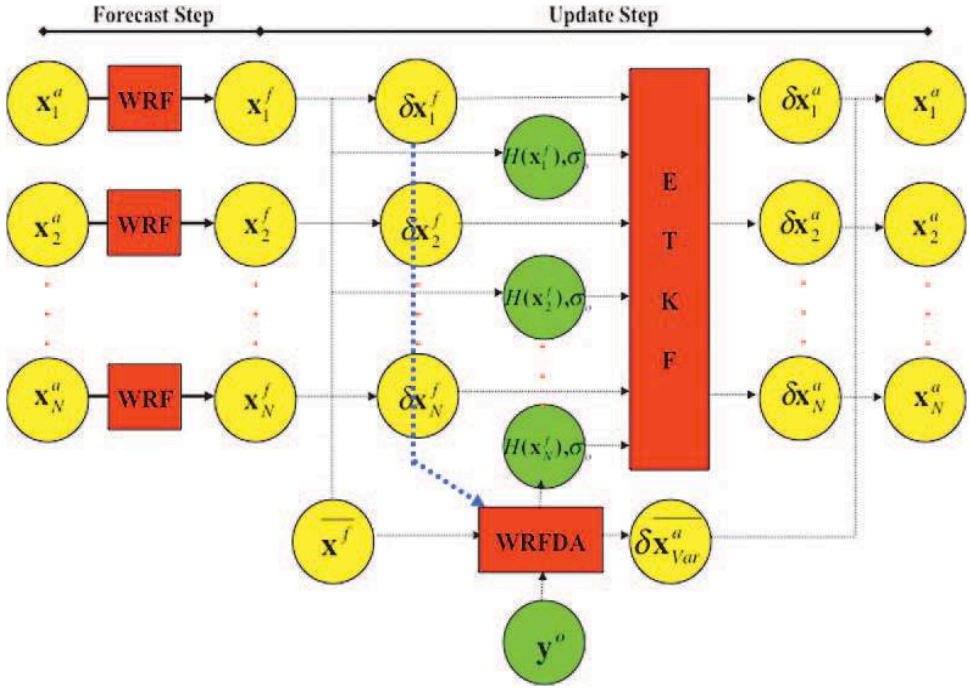

Figure 19: Operating scheme of WRFDA within a coupled ensemble prediction system

From a mathematical point of view the analysis increment in the hybrid ETKF-3DVAR approach is obtained by minimizing the following cost function:

$$J(\mathbf{x}'_1,\mathbf{a}) = \beta_1 J_1 + \beta_2 J_e + J_0$$
$$= \beta_1 \frac{1}{2}(\mathbf{x}'_1)^T \mathbf{B}^{-1}(\mathbf{x}'_1) + \beta_2 \frac{1}{2}(\mathbf{a})^T \mathbf{A}^{-1}(\mathbf{a}) + \frac{1}{2}(\mathbf{y}^{0'} - \mathbf{H}\mathbf{x}')^T \mathbf{R}^{-1}(\mathbf{y}^{0'} - \mathbf{H}\mathbf{x}') \quad \textbf{Eq 4.12}$$

The usual background term used in a normal 3DVAR is replaced by a weighted sum of J_1 and J_e . J_1 is the WRFDA term associated with the static covariance matrix (**B**), while in J_e **a** is a vector composed of K concatenated vectors $\mathbf{a}_k$ with k=1,…,K that is like assume $\mathbf{a}^T=(\mathbf{a}^T_1,\ldots,\mathbf{a}^T_K)$. Similar to Eq. 17 of Lorenc (2003) the extended control variables are constrained by a diagonal matrix **A** composed of K blocks:

$$\mathbf{A} = \begin{pmatrix} \mathbf{S} & & & \\ & \mathbf{S} & & \\ & & \mathbf{...} & \\ & & & \mathbf{S} \end{pmatrix} \qquad \textbf{Eq 4.13}$$

Each block contains the same correlation matrix S that contains the spatial variation of $\mathbf{a}_k$. Thus, the aim of **A** is to define the spatial covariance (in this case spatial correlation since variance is equal to 1) of **a** in the same way as **B** define the spatial covariance of $\mathbf{x}'_1$. Also in Eq 4.12 J_0 is the observation term and like previously explained for the traditional 3DVAR $\mathbf{y}^{0'} = \mathbf{y}^0 - \mathrm{H}(\mathbf{x}^b)$ is the innovation vector, in this case $\mathbf{x}^b$ is the ETKF ensemble mean forecast that is used as background forecast for WRFDA.

4.4 Reflectivity assimilation operators

WRFDA includes different reflectivity operator options allowing the use of different techniques for reflectivity assimilation.

The first method is the direct technique [Xiao et al. (2007)] that assimilates reflectivity by converting the model rainwater mixing ratio into reflectivity using the total mixing ratio as control variable. This method follows Sun and Crook (1997) relation for the observation operator (Eq. 4.14):

$$\boldsymbol{Z(q_r) = 43.1 + 17.5 log_{10}(\rho q_r)} \qquad \textbf{Eq 4.14}$$

where Z is the reflectivity in dBZ unit, ρ is the atmospheric density in kg/m^3, and q_r is the rainwater mixing ratio in kg/kg (refer to Xiao et al. 2007 for further information about direct reflectivity data assimilation methods using 3DVAR technique).

The second method is the indirect assimilation [Wang et al. (2013); Gao et al. (2012) which assimilates hydrometeors mixing ratio estimated from radar reflectivity. The forward reflectivity operator is obtained adjusting the formulation of Lin et al. (1983) Gilmore et al. (2004) and Dowell et al. (2011), and it is represented in Eq. 4.15.

$$Z_e = \begin{cases} Z(q_r) & T_b > 5\ °C \\ Z(q_s) + Z(q_h) & T_b < -5\ °C \\ \alpha Z(q_r) + (1-\alpha)[Z(q_s) + Z(q_h)] & -5\ °C < T_b < 5\ °C \end{cases} \quad \textbf{Eq 4.15}$$

where Z_e is the equivalent reflectivity α varies linearly between 0 at T_b= -5 °C and 1 at T_b= 5 °C, T_b is the background temperature from a NWP model and:

$$\boldsymbol{Z}(q_r) = 3.63 \times 10^9 (\rho q_r)^{1.75} \quad \textbf{Eq 4.16}$$

is the rain component of reflectivity (Smith et al. 1975),

$$\boldsymbol{Z}(q_s) = 9.80 \times 10^8 (\rho q_s)^{1.75} \qquad T_b < 0\ °C \quad \textbf{Eq 4.17}$$

$$\boldsymbol{Z}(q_s) = 4.26 \times 10^{11} (\rho q_s)^{1.75} \qquad T_b > 0\ °C \quad \textbf{Eq 4.18}$$

are the snow component operators. If the temperature is lower than 0 °C the dry snow operator is used (Eq. 4.17) otherwise the wet snow operator (Eq. 4.18) is applied. Finally, Eq. 4.19 represents the hail component of reflectivity [Lin et al. (1983); Gilmore et al. (2004)]:

$$\boldsymbol{Z}(q_h) = 4.33 \times 10^{10} (\rho q_h)^{1.75} \quad \textbf{Eq 4.19}$$

It is worth to notice that in the formulation it is mentioned the hail component (q_h), that it is predicted only by a subset of microphysics parameterizations in the WRF model; however, in the WRFDA code uses for the retrieval the graupel species (q_g). The last step needed is the conversion of the equivalent reflectivity (Ze) in dBZ unit (Eq. 4.20)

$$\mathbf{Z} = 10 log_{10}(\boldsymbol{Z_e}) \quad \textbf{Eq 4.20}$$

Furthermore, it is available an additional option of the indirect assimilation that allows the assimilation also of the in-cloud humidity estimated from reflectivity [Wang et al. (2013)]. In this case, the observation operator is defined by Eq. 4.21.

$$\boldsymbol{q_v} = rh \times q_s \qquad \textbf{Eq 4.21}$$

where $\mathbf{q_v}$ is the specific humidity, rh the relative humidity and q_s is the saturated specific humidity of water vapor. Thus, in this experiment, it is retrieved for the assimilation the in-cloud humidity in addition to the hydrometeors species retrieved with the indirect method alone.

All these reflectivity operators are available in the standard WRFDA-3DVAR package. In this work, an additional experiment has been performed by modifying the direct assimilation operator. In fact, the direct reflectivity operator (Eq. 4.14) that uses a warm rain scheme is substituted with the indirect operator (Eq. 4.15). The model reflectivity is computed using the different microphysics species and subsequently compared to the observed one for the innovation vector calculation. Thus, the moisture and hydrometeors partitioning is done exactly in the same way as it is done in the indirect method, but the operation is performed on the models variables and not on the observed reflectivity (the indirect method uses an inverted form of Eq. 4.15 to obtain hydrometeors species from observed reflectivity). Therefore, the modified operator allows obtaining a direct data assimilation of reflectivity that takes into account all the hydrometeors (snow, hail/graupel) and not only the rainwater.

5. The validation tool: MODE

To validate all the modeling experiments and identify the most convenient WRF-3DVAR setup for each case study, the Method for Object-Based Evaluation (MODE, Davis et al. (2006a and 2006b)) is applied by comparing the Quantitative Precipitation Forecast (QPF) of WRF with the QPE offered by raingauges or radar. MODE identifies precipitation structures in both forecast and observed fields and performs a spatial evaluation of the model capability of reproducing the identified observed objects. The evaluation of MODE is summarized as output indices such as centroid distance, angle difference, area ratio, symmetric difference and percentile intensity (in this work above the 90th percentile threshold); for a complete description of the indices used for this part of the validation refer to Table 3.

MODE provides also some classical statistical score. In this work each meteorological simulation has been validated using:

- Frequency BIAS (FBIAS), measuring the ratio of the frequency of forecast events to the frequency of observed events, indicates whether the forecast system has a tendency to underforecast (FBias <1) or overforecast (FBias >1) events. FBIAS does not measure how well the forecast corresponds to the observations, only measures relative frequencies;
- Probability of Detection Yes (PODY), is the fraction of events that were correctly forecasted to occur (range:0-1, perfect value=1);
- False Alarm Ratio (FAR), is the proportion of forecasts of the event occurring for which the event did not occur (range:0-1, perfect value=0);

- Critical Success Index (CSI), is the ratio of the number of times the event was correctly forecasted to occur to the number of times it was either forecasted or occurred (range:0-1, perfect value=1);
- Hanssen and Kuipers discriminant (HK), it measures the ability of the forecast to discriminate between (or correctly classify) events and non-events (range:-1 -1, perfect value=1);
- Heidke Skill Score (HSS), it is a skill score based on Accuracy, where the Accuracy is corrected by the number of correct forecasts that would be expected by chance (range: -∞ 1, perfect value=1).

The aforementioned statistical parameters were derived from a contingency table that shows the frequency of "yes" and "no" rain forecasts and occurrences. The four combinations of forecasts (yes or no) and observations (yes or no) generate four different output of the table:

1) hit: rain forecasted and occurred;

2) miss: rain not forecasted and occurred;

3) false alarm: rain forecasted and not occurred;

4) correct negative: rain not forecasted and not occurred.

From this output it is possible to compute the statistical scores with the following formulations:

- $FBIAS = \frac{\text{hits+false alarms}}{\text{hits+misses}}$
- $PODY = \frac{hits}{hits+misses}$
- $FAR = \frac{\text{false alarms}}{\text{hits+false alrms}}$
- $CSI = \frac{\text{hits}}{\text{hits+misses+false alrms}}$

- $HK = \frac{\text{hits}}{\text{hits+misses}} - \frac{\text{false alarms}}{\text{false alarms+correct negative}}$

- $HSS = \frac{(\text{hits+correct negatives}) - (expected\ correct)_{random}}{\text{total} - (expected\ correct)_{random}}$

where:

$$(expected\ correct)_{random} =$$

$$\frac{1}{total}\left[\begin{matrix}(hits + misses)(hits + false\ alarm) + \\ (correct\ negatives + misses)(correct\ negatives + false\ alarms)\end{matrix}\right]$$

All the meteorological validations of this work are performed to select the best forecast out of the set of the sensitivity experiments performed in each research activity. The most reliable meteorological forecast was selected in agreement with Lagasio et al. (2017): all the indices and statistical scores described above are calculated for each sensitivity experiment, then it is counted the times in which a simulation has been the best for each score or index.

Index	Description
CEN DIST	Centroid Distance: Provides a quantitative sense of spatial displacement of forecast (Best score 0).
ANG DIFF	For non-circular object gives measure of orientation errors (Best score 0)
AREA RATIO	Provides an objective measure of whether there is an over- or under-prediction of areal extent of forecast (Best score 1).
INT AREA	Area of intersection between corresponding objects (Best value equal to observed area).
UNION AREA	Total area of two corresponding objects summed together (Best value equal to observed area).
SYMM DIFF	Provides a good summary statistic for how well Forecast and Observed objects match (Best value small).
P90 INT	Provides objective measures of near-Peak (90th percentile) intensities found in objects (Best score 1).

Table 3: MODE indices description.

6. First activity - lightning prediction

Most of the work presented hereafter is taken from the following publication:
Lagasio, M., Parodi, A., Procopio, R., Rachidi, F., & Fiori, E. (2017). Lightning Potential Index performances in multimicrophysical cloud-resolving simulations of a back-building mesoscale convective system: The Genoa 2014 event. *Journal of Geophysical Research: Atmospheres*, *122*(8), 4238-4257.

6.1 Introduction

Many studies performed around the globe and corresponding to different weather regimes [Carter and Kidder (1976), Tapia et al. (1998), Soula and Chauzy (2001), Adamo et al. (2009), Price et al. (2011a,b)] have confirmed that there is a strong interplay between lightning phenomena and severe rainfall process evolution in thunderstorms. The improvement of the so-called total lightning observation (i.e., cloud-to-ground and intra-cloud) systems in the last decades has allowed investigating the relationship between lightning flash rate and the kinematic and microphysical properties of severe hydro-meteorological events characterized by strong convection and significant ground effects [Gatlin and Goodman (2010), Pineda et al. (2011), Schultz et al. (2011)]. Deep convective processes are characterized by very intense vertical velocities, able to reach the zone of the atmosphere between the 0°C and -20° isotherms (the so-called lightning charging zone, according to Latham et al. (2004)) where lightning phenomena occurs [Petersen et al. (1996, 1999)].

According to last decades studies [Deierling and Petersen (2008)] strong updrafts produce large amount of hydrometeors in the mixed ice phase region and the presence of ice particles is a necessary component for electrification processes that lead to lightning occurrence [Rakov and Uman (2003)].

As convective processes are one of necessary ingredients for the occurrence of lighting phenomena, lightning activity can be used to map the location of

thunderstorms convective core where normally is located the heaviest rainfall [Defer et al. (2005), Price (2013)].

Since lightning can be monitored from great distances from the storms themselves, lightning may allow us to provide early warnings for severe weather phenomena such as hail storms, flash floods, tornadoes, and even hurricanes. FP6 FLASH focused on 23 case studies over the Mediterranean region using lightning data together with rainfall estimates in order to understand the storms' development and electrification processes [Price et al. (2011b)] and developed tools for short-term predictions (nowcasts) of intense convection across the Mediterranean and Europe, and long-term forecasts (a few days) of the likelihood of intense convection. The project found that real-time lightning observations on a regional basis are very useful in detecting, monitoring and tracking intense thunderstorm activity on large spatial scales [Price et al. (2011a)].

Due to this relationship, the relevance of lightning prediction is becoming in the last decades more clear, however, despite many real-time lightning detection systems are now able to determine with high accuracy the impact location of lightning, there is a much lower capability to forecast the potential for lightning occurrence in short-range forecast [Lynn and Yair (2010)].

Recent advanced in lightning prediction have occurred. The National Severe Storm Laboratory (NSSL) produces near-real-time hourly total lightning forecasting with 36 hours lead times basing his prediction on the model-derived graupel flux in convective clouds with the total ice content to obtain a statistical relationship between this parameters and the total lightning flash density [McCaul et al. (2009)]. Dahl et al. (2011) formulated a forecasting methodology, allowing the identification of convective cells and related lightning phenomena

in their early stages, when the “critical electric field strength” reaches a certain threshold value. Furthermore, the EXploiting new Atmospheric Electricity Data for Research and the Environment (EXAEDRE) project started in 2016 and founded by the French National Research Agency (ANR) contributes to the HyMeX (HYdrological cycle in the Mediterranean Experiment) trying to reach two different scientific objects (https://www.hymex.org/exaedre/?page=publications): 1) an observational- and modeling-based characterization of the electrical activity in Northwestern Mediterranean storms; 2) an assessment of the potential of lightning information for a better monitoring of thunderstorms.

This first thesis activity is then inspired by some recent studies [Lynn and Yair (2008), Lynn and Yair (2010)] that described the development and utilization of a Lightning Potential Index (LPI). In this research LPI is used to evaluate the potential of lightning activity from weather forecast model output data (Advanced Research Weather Research and Forecast model (WRF-ARW) is used) during a High Impact Weather Event (HIWE).

The LPI uses the direct correlation of lightning activity with the microphysical and the dynamical process within the cloud: it is an empirical equation consisting of cloud-physical parameters and it is calculated within the charge separation region of clouds where the non-inductive mechanism of collision of ice and graupel particle is most effective [Saunders (2008)]. It is derived from the model simulated updraft velocity and the mass mixing ratio of liquid water, cloud ice, snow and graupel.

Within this context, the present activity proposes a novel methodological approach for the assessment of the predictive ability of a microphysics driven

ensemble of km-scale mesoscale numerical model simulations in case of back-building MCSs, concurrently producing extreme rainfall and lightning activity.

The first step concerns the evaluation of the ensemble quantitative precipitation forecast (QPF) performances through a comparison with the quantitative precipitation estimation (QPE) provided by in situ sensors, such as the km-scale radar data adopted for this work. Subsequently the same analysis is performed by comparing the observed lightning occurrence with the flashes prediction provided by the ensemble of km-scale mesoscale numerical model simulations, adopting a lightning parameterization based on updraft velocity [Price and Rind (1992)]: the lightning parameterization choice is consistent with Giannaros et al. (2015). As final step, the Lightning Potential Index (LPI) as formulated by Lynn and Yair (2008, 2010) and Yair et al. (2010) is computed to understand its value-added in the predictive ability of back-building MCSs. The proposed methodological approach is described and assessed for the event occurred over Genoa, Liguria, on 9th October 2014 [Fiori et.al. (2017)].

6.2 Charging mechanism in thunderstorms

A major difficulty in identifying the causes of electricity in clouds has been our inability to obtain adequate measurements within clouds. These problems are now being remedied by modern technologies and many quantitative theories of charging have become available.

Wilson [Wilson (1916)] assumed a vertical charge dipole within thunderstorms and determined that the charge regions are usually positive above negative: he measured electric field changes at the ground caused by intra-cloud lightning in which the dipole charges neutralised each other. This picture was confirmed with extensive electric field change measurements made by a study [Krehbiel et

al. (1979)] in New Mexico, in which the locations and values of charges in thunderstorms charge centres were determined. More complicated charge centre distributions have been reported in other studies (i.e. Stolzenburg et al. (1998)).

The generally accepted concept for the development of the thunderstorm charge dipole is the physical separation of oppositely charged particles within the cloud. Larger cloud particles fall under gravity while smaller particles are transported in the updraught; if these particles carry negative and positive charges respectively then the normal charge dipole will result [Saunders (2008)].

There are two main categories of charging mechanism: The micro-scale separators, which lead to charged cloud and precipitation particles, and the cloud-scale separators, which can result in field intensification and lightning. These mechanisms are coupled with other micro-scale separators to produce net charges on cloud and precipitation particles, for example the attachment of ions by diffusion to cloud drops and the charging that results from particle collisions. Once the cloud and precipitation particles become appreciably charged, a larger scale separator such as differential sedimentation is needed to create electrification on the cloud scale. Convection can also act as a cloud-scale separator by redistributing ions and particles.

It is difficult to find a “typical” storm with which all models could be compared because of the natural variability of processes that lead thunderclouds. However, it is possible to find some common observed features and list them to have general criteria that can be used as comparison. Mason (1953, 1971) used thunderstorm observations to list some requirements of the basic thunderstorm observations that still appears to be valid:

1. From a single cell, the average duration of electric field generation and precipitation is about 30 minutes.
2. The average charge generation produces 20 to 30 Coulomb per flash.
3. In large cumulonimbus, the charge is separated in a volume bounded by the 0°C and -40°C in a region of radius about 2 to 3 km.
4. The negative charge centre is between the -5°C and -25°C levels depending on cloud physics. A study (Krehbiel et al. 1979) observed that negative charge originates from regions between -10°C to -17°C, and is not depending on the height above ground. Main positive charges generate several kilometres higher, instead lower positive charges are closed to the 0°C level.
5. Charge-separation processes are associated with the development of precipitation in form of graupel.
6. The fist lightning occurs within 12 to 20 minutes from the appearance of precipitation particles of a radar-detectable size (with a diameter less than 200 μm.
7. Charge mechanisms must generate 5 to 30 C Km^{-3} leading to a charge generation rate of order 1 C $km^{-1}min^{-1}$.

6.3 The Genoa 2014 event description

6.3.1 Synoptic background

The high impact weather event which hit the Genoa city centre on 9th October 2014 had a dynamics similar to previous back-building MCSs observed during the events happened over the Ligurian Sea (North-West of Italy) on October 2010, October and November 2011 [Parodi et al. (2012), Rebora et al. (2013), Cassola et al. (2015), Davolio et al. (2015)]. All these events in fact showed three main ingredients: an area of intense precipitation sweeping an arc of a few degrees around the warm conveyor belt originating about 50-60 km from the Liguria coastline, thus assuming a V-shape pattern as shown in Figure 20 by the cloud top temperature and height (CTTH), developed within the SAF NWC (Nowcasting Satellite Application Facilities by EUMETSAT) context, on 9

October 2014 at 12 UTC. A second main ingredient was the presence of a convergence line, which supported the development, and the maintenance of the aforementioned back-building process. Other common features were the persistence of such geometric configuration for many hours [Parodi et al. (2012), Rebora et al. (2013)] with an associated strong lightning activity.

From a synoptic point of view, the presence of an upper-level trough over the Atlantic Ocean led to a diffluent flow over the Genoa area resulting in the Genoa 2014 event. The situation was similar to the Genoa 2011 event, but in 2014 the upper-level trough over the Atlantic Ocean was less marked and the mid-tropospheric flow was more west-south-westerly than in 2011 when it was south-westerly. Fiori et al. (2017), taking advantage of the availability of both observational data and modelling results at the micro-α meteorological scale, provides insights about the triggering mechanism and the subsequent spatio-temporal evolution of the 2014 back-building Mesoscale Convective System. The major finding concerns the identification of the physical process responsible for convective cells development over the Ligurian sea, primarily at large distance (≈ 40-50 km) from the Apennines divide as shallow convection, then getting closer to the coastline (≈ 5-10 km) as towering cumulonimbus up to 10-12 km, and why the vertex of the persists over the same area for quite a long time. It is shown in fact that within the Planetary Boundary Layer (PBL), a cold and dry jet outflowing from the Po valley and reaching the Liguria sea acts as a virtual mountain forcing the incident more unstable warm and moist low level south-easterly jet to rise up over it triggering convection over the sea. The reader is referred for further insight also to the available media material (https://vimeo.com/195611161).

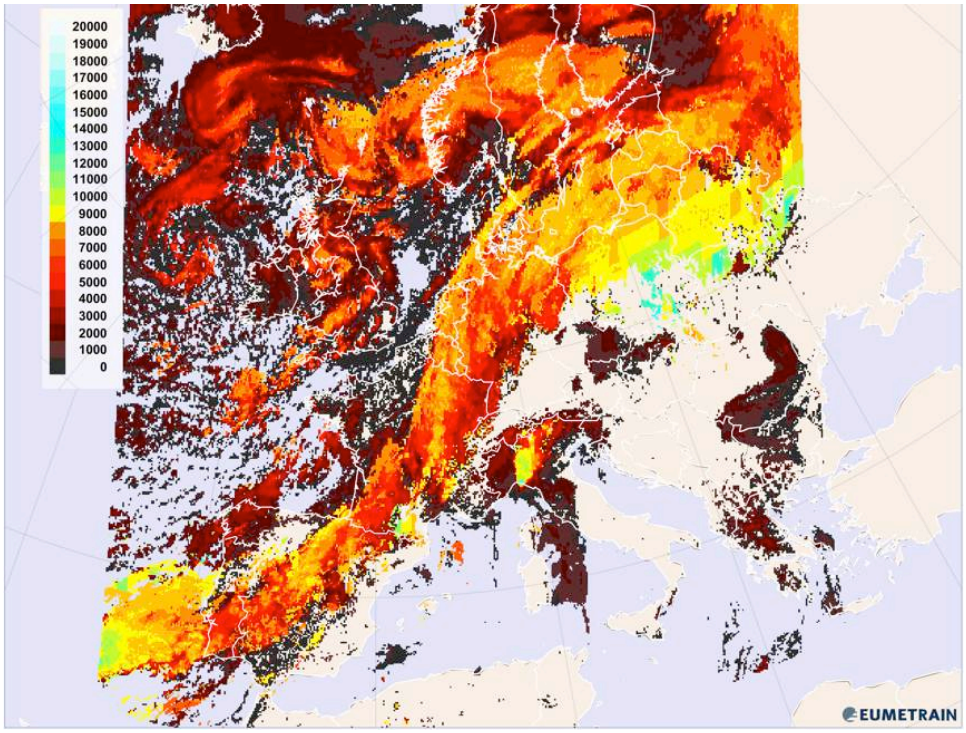

Figure 20: The cloud top temperature and height (CTTH), developed within the SAF NWC context, on 9th October 2014 at 12 UTC.

6.3.2 Observational data

Rainfall is presented in the methodological approach as first metric to evaluate the performances of the microphysics driven ensemble of km-scale WRF simulations for this event. The Liguria territory is monitored by an elevate number of rain gauges (on average 1 sensor every 25 km^2). However, given the very localized and intense nature of this event (with hourly peak around 130 mm, 3 hourly around 200 mm and 24 hours above 400 mm), the coexistence of deep moist convective phenomena over the Liguria sea and the coastal Apennines mountains as well as the availability of km-scale WRF outputs, radar data are used as main Quantitative Precipitation Estimate (QPE) sources. The preference is given to the C-band polarimetric radar located at Monte Settepani (about 1400 m amsl) in Savona (Italy) (Figure 21) installed in 2002 by Liguria and Piemonte regions and currently managed by the Piemonte and Liguria

regions Meteorological Weather Services and by the Italian Civil Protection Department [Silvestro et al. (2009)].

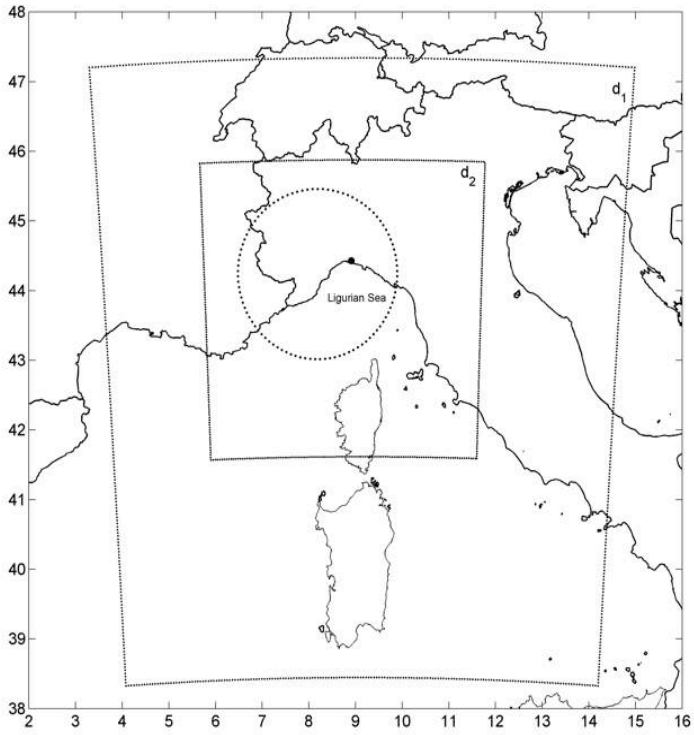

Figure 21: Nested domains d_1 at 5 km grid resolution and d_2 at 1 km grid resolution adopted for WRF simulations (rectangles). Area monitored by the C-band polarimetric radar at Monte Settepani represented by the dotted circle. The black dot indicates the location of Genoa city in the Ligurian region.

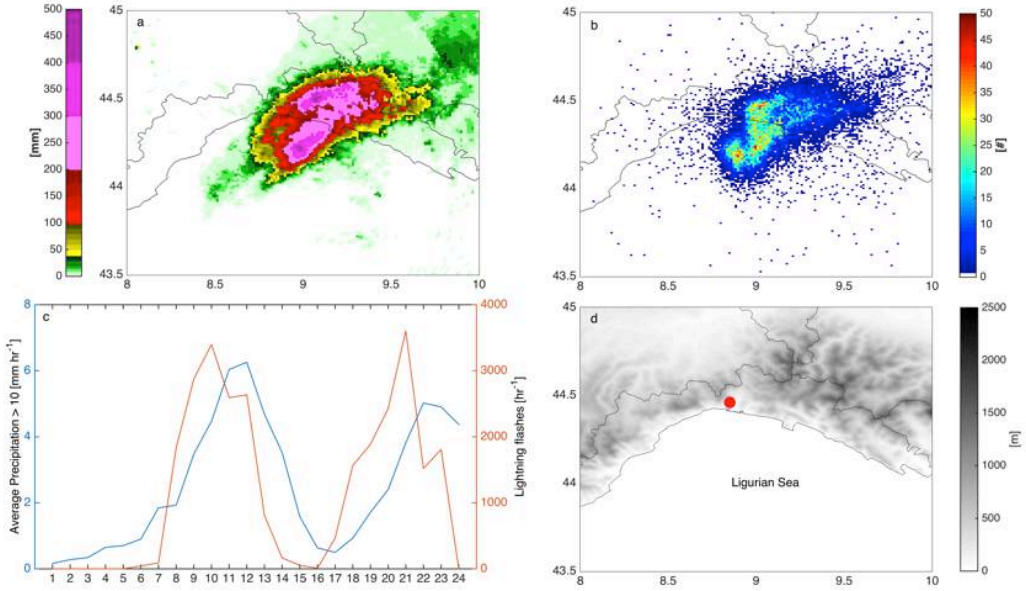

Figure 22: First row: comparison between QPE radar (Panel a) and observed lightning activity (Panel b) from 00 to 24 UTC on Oct. 9th, 2014. The colorbar in Panel b) indicates the number of observed lightning. Second row: comparison between the number of total lightning flashes and the average QPE from RADAR where rainfall > 10 [mmhr-1] (Panel c). Ligurian topography (Panel d) with the red dot indicating the Genoa city location.

The 24 hours radar QPE map for the Genoa 2014 event is provided in Figure 22a. As well as rainfall data, lightning data are used as a further metric to assess the predictive ability of the microphysics driven ensemble of km-scale WRF simulations. To this aim, SFLOC (term derived from the words spheric and location) data are used. They consist of the position (longitude and latitude), the estimated current peak (in kA) and the polarity (positive or negative) of the lightning flash acquired by the LAMPINET lightning network of the Aeronautic Meteorological Service based on VAISALA technology [De Leonibus et al. (2010)]. The LAMPINET network is composed of 15 IMPACT ESP sensors uniformly distributed over the Italian national territory (Figure 23). The LAMPINET detection efficiency is estimated to be 90% for lightning intensity over 50 kA while the localization accuracy is about 500 meters.

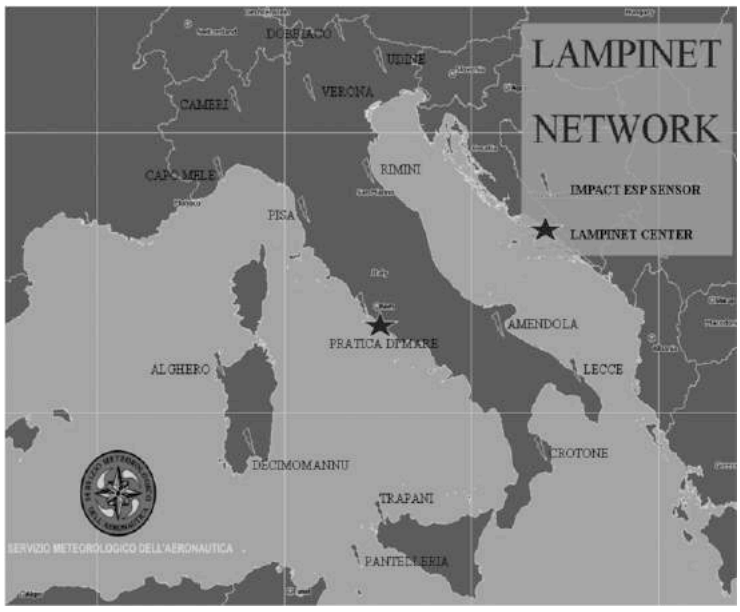

Figure 23: LAMPINET lightning location network (De Leonibus et al. 2010).

The paper leading idea that lightning and rainfall have a strong spatio-temporal correlation in case of back-building MCSs, like the Genoa 2014 event, is shown in Figure 22. Figure 22a-b support the high degree of spatial correlation between the rain depth pattern (Figure 22a) and the SFLOC (Figure 22b) cumulated on the 00-24 UTC time window. The highest number of lightning flashes was measured over the precipitation area corresponding to 24 hours cumulated rainfall depth peaking up to 200 mm or higher (pink shaded regions). Furthermore, Figure 22c shows the temporal evolution of the lightning with respect to the convection development of the MCS. In the first hours of the day no lightning activity is observed even if the average precipitation rate due to warm rain process slowly increases in time. As shown in Fiori et al. (2017, Figures 17 and 18), the V-shape needs up to 6-7 UTC before reaching vertical depth that overcame the 0 °C level. At this time of the convective evolution, lightning activity increases rapidly following the increasing trend of the QPE and reaching the maximum observed value about 2 hours in advance the precipitation peak.

This correlation supports the theoretical idea that lightning activity can represent a further element for the prediction (in forecasting operational phase) and tracking (in nowcasting operational phase) of this category of flash flood producing storms.

6.4 Model setup and verification approach

The WRF setup for this case study is based on the modeling results achieved for another extreme autumnal event happened in Liguria Region in November 2011 [Fiori et.al. (2014)]. Two nested domains (Figure 21) with respectively 5 km (179x200 grid points) and 1 km (475x475 grid points) grid spacing are used

to cover the upper and lower limit of the cloud-permitting range [Arakawa (2004)]. The number of vertical levels, over the 20 km atmosphere depth, is equal to 83, since the sensitivity analysis performed in Fiori et al. (2014) demonstrated the importance of fine grid spacing also in the vertical direction. All the analyses presented hereafter refer to the innermost domain at 1 km grid spacing.

Both adopted grid spacing (5 and 1 km) allow to solve explicitly, albeit crudely, many convective processes [Kain et al. (2006, 2008)] so an explicit treatment of convection is chosen for this case supported also by the results of sensitivity tests done for the Genoa event in 2011 [Fiori et al. (2014)]. A large eddy simulation (LES) like turbulence closure is adopted [Parodi and Tanelli (2010)]. Regarding the microphysics parameterization, an ensemble approach of ten different microphysics parameterizations is adopted for WRF simulations, in which ice species processes are taken into account since the presence of solid hydrometeors in atmosphere is relevant for lightning activation.

The chosen microphysics, with related predicted mass and number variables, are reported in Table 4: Lin et al. scheme [Lin et al. (1983)], WRF single moment 6-class scheme (WSM6) [Hong and Lim, (2006)], Goddard scheme [Tao et al. (1989)], Thompson scheme [Thompson et al. (2008)], WRF double moment 6-class scheme [Lim and Hong (2010)], NSSL 2-moment scheme and 2-moment scheme with CCN Prediction [Mansell et al. (2010)], NSSL 1-moment 7-class scheme (single moment version of the NSSL 2-moment scheme above presented), NSSL 1-moment 6-class scheme [Gilmore et al. (2004)], NSSL double-moment without hail [Mansell et al. (2010)]. They range from single moment schemes to double moment ones, aiming at reducing the uncertainty in

predicting the key microphysics processes responsible for the extreme rainfall and lightning deep moist convective storms [Parodi et al. (2011)].

Member	Microphysics	Mass Variables	Number Variables
LIN	Lin	Qc Qr Qi Qs Qg	-
WSM6	WRF single moment 6-class	Qc Qr Qi Qs Qg	-
GODD	Goddard	Qc Qr Qi Qs Qg	-
THOM	Thompson	Qc Qr Qi Qs Qg	Ni Nr
WDM6	WRF double moment 6-class	Qc Qr Qi Qs Qg	Nn Nc Nr
NSSL2	NSSL double-moment	Qc Qr Qi Qs Qg Qh	Nc Nr Ni Ns Ng Nh
NSSL2C	NSSL double-moment With CCN Prediction	Qc Qr Qi Qs Qg Qh	Nc Nr Ni Ns Ng Nh Nn
NSSL17	NSSL single-moment 7-class	Qc Qr Qi Qs Qg Qh	VOLg
NSSL16	NSSL single-moment 6-class	Qc Qr Qi Qs Qg	-
NSSL2G	NSSL double-moment without hail	Qc Qr Qi Qs Qg	Nc Nr Ni Ns Ng Nn VOLg

Table 4: Microphysics settings chosen for the domains d_1 (5Km grid spacing) and d_2 (1Km grid spacing) where Qr= rain water, Qc=cloud water, Qi= cloud ice, Qs= snow,Qg=graupel, Qh= hail, N r= concentration number for rain water, Nc= concentration number for cloud water, Ni= concentration number for cloud ice, Ns= concentration number for snow, Ng= concentration number for graupel, Nh= concentration number for hail, Nn= cloud condensation nuclei concentration number, VOLg= graupel volume.

Concerning the lightning flashes occurrence, among the lightning parameterizations available in WRF, in this study an updraft based lightning scheme [Price and Rind (1992), Wong et al. (2013)] is adopted: the flash rate is assumed to be proportional to the maximum vertical updraft velocity and the to fourth power of cloud dimension. Then by imposing a linear relation between the maximum vertical updraft velocity and the cloud dimension, the flash rate becomes directly proportional to the fifth power of the cloud-top height [Williams (1985)].

Finally, the WRF version used in this work has an implementation of the Lightning Potential Index based on the Lynn and Yair (2010) and Yair et al. (2010) formulation and it is already applied in a single case study by Pytharoulis et al. (2016). The LPI is defined as a volume integral of the total mass flux of ice and liquid water within a zone between 0 and -20 °C isotherms (charging zone), where the non-inductive mechanism (collisions of ice and graupel particles in the presence of supercooled water) is most effective [Saunders (2008), Mansell et al. (2010)]. According to recent studies in which a correlation between deep convection and lightning is demonstrated [Van Den Broeke et al. (2005)], the LPI has its largest values in the presence of strong vertical velocities, when graupel exists in equal ratios relative to snow, ice and water.

The LPI [Jkg^{-1}] is defined by:

$$\mathrm{LPI} = \frac{1}{V} \iiint \varepsilon w^2 \, dx \, dy \, dz \qquad \textbf{Eq 6.1}$$

where V is the model unit volume, w is the vertical velocity in [ms^{-1}], ε is a dimensionless number, which assumes values between 0 and 1and is defined as:

$$\varepsilon = 2(Q_i Q_l)^{0.5} / (Q_i + Q_l) \qquad \textbf{Eq 6.2}$$

in which Q_l is the total liquid water mass mixing ratio in [kgkg^{-1}], given by the sum of cloud water (q_c) and rain water (q_r) both in [kgkg^{-1}]. Q_i is the ice fractional mixing ratio in [kgkg^{-1}] function of graupel (q_g), snow (q_s) and cloud ice (q_i) and defined by:

$$Q_i = q_g[((q_s q_g)^{0.5} / (q_s + q_g)) + ((q_i q_g)^{0.5} / (q_i + q_g))] \qquad \textbf{Eq 6.3}$$

ε is a scaling factor for the cloud updraft, and attains its maximal value when the mixing ratios of super-cooled liquid water (Q_l) and of the combined ice species (Q_i) are equal. The maximum value of ε occurs when the ratio between species is equal in accordance with laboratory experiments summarized by Saunders (2008) indicating that the charge separation requires all the species to operate synergistically within the charging zone.

Initial and boundary conditions are provided by the European Centre for Medium-Range Weather Forecast (ECMWF) Integrated Forecast System (IFS) with a spatial resolution of 0.25x0.25 degrees. All the ten simulations are initialized at 00UTC on October 9th, and the boundary is updated every 3 hours, as already performed in Fiori et al. (2014) and Cassola et al. (2015) for similar back-building MCS.

The proposed methodological approach for the extreme rainfall and lightning predictive ability verification of a microphysics driven ensemble of WRF simulations at cloud-permitting grid spacing (1 km) is based on two sequential phases of analysis. In both phases, MODE is used (see Chapter 5). Since this event is characterized by both heavy precipitation and very intense lightning activity, MODE analysis is applied on the rainfall and the lightning fields respectively, and for each of two target atmospheric fields the three best runs

and the worst one are chosen to gain a comprehensive understanding of the overall ensemble members performances.

6.5 Result discussion

6.5.1 Rainfall results

The first step of the methodological approach consists of the comparison between the QPFs ensemble members and the QPE radar. The comparison refers to the time period from 00 UTC to 24 UTC on Oct. 9th, 2014 (Figure 24). QPF panels in Figure 24 suggest a general good agreement in the representation of the precipitation pattern by all members with respect to the QPE (panel a) since spatial pattern both over the sea and over the ground seem correctly reproduced. However, it is possible to guess that all the members underestimate the 24 hours cumulated precipitation. This is confirmed by comparing the rainfall volumes of all the members with the observed radar rainfall volume (Table 5): for this preliminary metric, the WSM6 and THOM microphysics results outperform other microphysics in line with Fiori et al. (2014, 2017). To gain a deeper and more quantitative understanding of the QPF ensemble members performances, a MODE analysis is performed. MODE spatial and statistical scores and indices are computed by applying three different rainfall depth thresholds, namely 24 mm, 48 mm and 72mm, for each member of the microphysics driven ensemble (Table 6, Table 7 and Table 8). At the end of each tables two columns, named GOOD and BAD, are added as summary of each member performances: they count the times each microphysics has been the best and the worst in each score and index estimation. Total interest values higher than 90% confirm the preliminary visual inspection of Figure 24: all the members QPFs have a high degree of

agreement with the radar based QPE. Narrowing down towards a ranking of the ensemble members, the best performances in terms of total interest are provided by WSM6 and THOM, while the worst is given by WDM6. Additionally in terms of the traditional indices (accuracy, BIAS, POD, FAR, HK and HSS) the two best ensemble members are THOM and the NSSL2C, while the worst is again the WDM6. All in all, given that this event is characterized by very high values of cumulated precipitation, the identification of the best three members and the worst one from a QPF standpoint is done by comparing the GOOD (BAD) column in Table 7 for threshold of 48 mm of rainfall with the GOOD (BAD) in Table 8 for the 72 mm rainfall threshold. The three best runs results WSM6, THOM and NSSL2C and the worst one results the WDM6. Interestingly enough, single and double-moment microphysics coexist among the best performing QPF members not revealing the prevalence of either of the two approaches for this event metric. Furthermore, WDM6 member does not outperform WSM6 QPF performances differently from Hong et al. (2010). These intermediate results already suggest that uncertainty in microphysical schemes could still be a productive area of future research from perspective of both model improvements and observations [Pu and Lin (2015)]: further understanding of these results is gained in section 6.6.

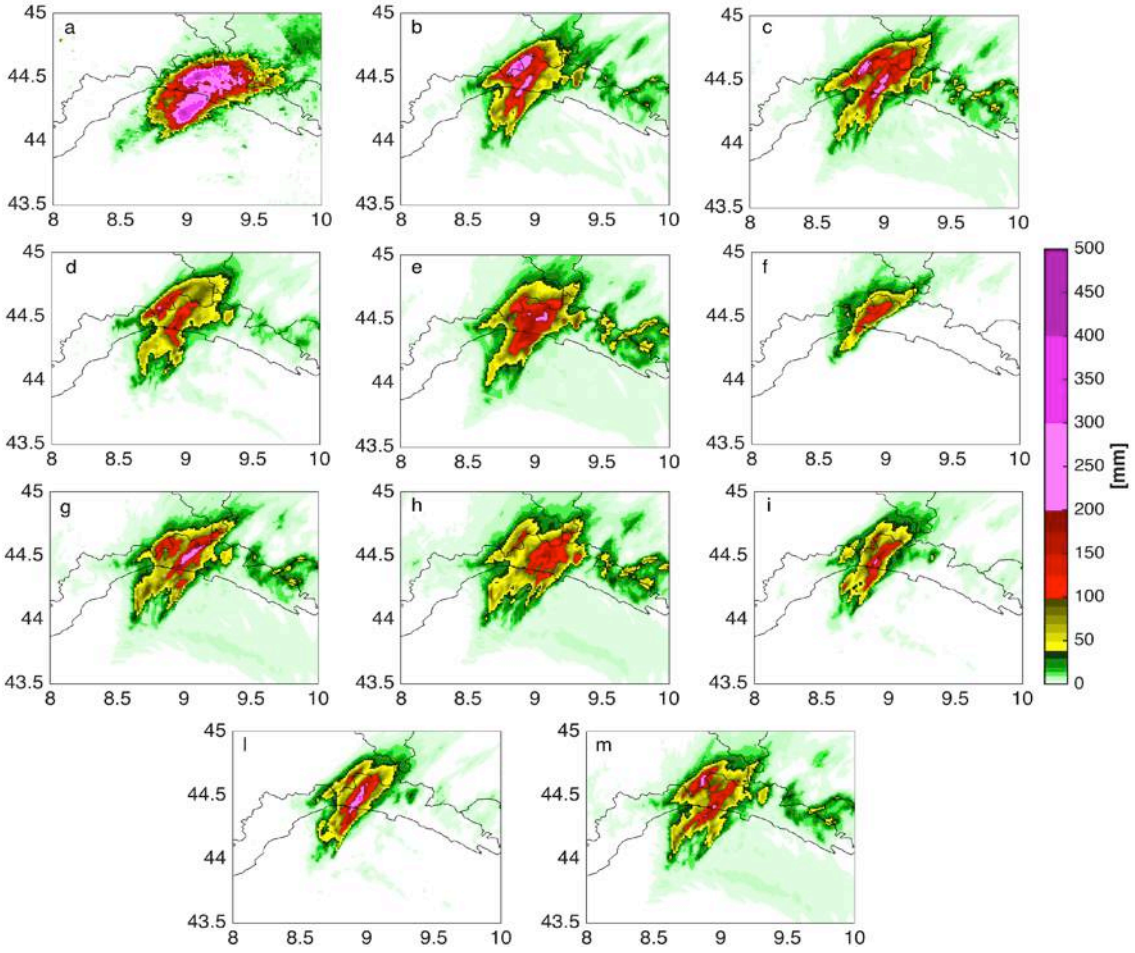

Figure 24: Comparison among QPE from RADAR (panel a) and the QPF obtained from the 10 microphysical ensemble members in the time window from 00 UTC to 24 UTC on 9th October 2014: LIN (panel b), WSM6 (panel c), GODD (panel d), THOM (panel e), WDM6 (panel f), NSSL2 (panel g), NSSL2C (panel h), NSSL17 (panel i), NSSL16 (panel l) and NSSL2G (panel m).

mp	Volumes 24h [Mm^3]
LIN	247
WSM6	270
GODD	186
THOM	275
WDM6	73
NSSL2	218
NSSL2C	247
NSSL17	117
NSSL16	148
NSSL2G	200
RADAR	462

Table 5: Rainfall volumes between 00 and 24 UTC. Comparison among the different microphysical parameterizations adopted for WRF simulations and rainfall volumes from radar data.

MP	CEN DIST	ANG DIFF	AREA RATIO	SYMM DIFF	P50 INT	P90 INT	TOT INTR	FBIAS	POD	FAR	HK	HSS	GOOD	*BAD*
LIN	16.72	19.34	0.82	**2689**	**0.60**	**0.64**	**1**	0.84	0.48	**0.43**	0.48	0.52	**5**	0
WSM6	10.48	19.21	**0.97**	3195	0.57	**0.56**	**1**	**1.01**	0.51	0.49	0.50	0.50	4	0
GODD	17.26	26.14	0.83	2824	0.54	0.41	**1**	0.81	0.47	**0.42**	0.46	0.51	2	0
THOM	**6.48**	*30.59*	**1.10**	3167	0.51	0.53	0.9995	1.13	**0.55**	0.51	**0.54**	0.50	4	1
WDM6	*24.75*	**16.19**	*0.35*	*3372*	0.49	0.40	*0.9332*	*0.35*	*0.16*	*0.55*	*0.15*	*0.22*	1	*9*
NSSL2	14.73	**17.46**	0.84	**2545**	0.57	0.48	**1**	**0.91**	0.52	**0.43**	0.51	**0.53**	**6**	0
NSSL2C	**5.27**	28.72	1.15	2868	0.47	0.41	**1**	1.18	**0.62**	0.48	**0.61**	**0.56**	**5**	0
NSSL17	22.24	28.59	0.57	3154	*0.46*	*0.39*	0.967	0.55	0.29	0.47	0.29	0.37	2	2
NSSL16	21.13	26.47	0.60	3067	0.52	0.50	0.971	0.58	0.32	0.45	0.31	0.39	0	0
NSSL2G	17.18	22.11	0.81	2740	0.54	0.46	**1**	0.86	0.47	0.46	0.46	0.49	1	0
Best	*Small*	*Small*	*1*	*Small*	*1*	*1*	*1*	*1*	*1*	*0*	*1*	*1*		

Table 6: Rainfall MODE scores and indices for 24 mm threshold. The best and the worst performances for each index are highlighted in bold underlined and in italic underlined respectively. Last two columns refer to the sum of times each microphysics has been the best and the worst in one index. The last raw reports the desirable values for each index.

MP	CEN DIST	ANG DIFF	AREA RATIO	SYMM DIFF	P50 INT	P90 INT	TOT INTR	FBIAS	PODY	FAR	HK	HSS	GOOD	BAD
LIN	17.99	27.56	0.67	2395	0.69	**0.70**	0.9813	0.67	0.38	0.44	0.37	0.44	1	0
WSM6	17.46	21.94	**0.71**	2567	**0.71**	**0.59**	**0.988**	**0.73**	0.37	0.50	0.36	0.42	**5**	0
GODD	18.29	26.31	0.64	2578	*0.53*	0.44	0.9777	0.64	0.33	0.49	0.32	0.39	0	1
THOM	15.37	22.14	**0.71**	2187	**0.68**	0.57	**0.9878**	**0.76**	**0.44**	0.42	**0.43**	0.49	**6**	0
WDM6	*21.9*	**13.33**	*0.22*	*2657*	0.57	*0.42*	*0.9109*	*0.23*	*0.10*	*0.55*	*0.10*	0.17	1	*9*
NSSL2	**15.09**	22.1	0.65	**2152**	0.59	0.52	0.979	0.65	0.41	**0.36**	0.41	0.50	3	0
NSSL2C	**13.09**	**19.41**	**0.71**	**1927**	0.57	0.43	0.9869	**0.74**	**0.49**	**0.34**	**0.48**	0.55	**8**	0
NSSL17	20.38	*35.33*	0.31	2477	0.58	0.48	0.9195	0.36	0.18	0.48	0.18	0.27	0	1
NSSL16	20.25	31.85	0.43	2428	0.59	0.60	0.9433	0.43	0.25	0.42	0.25	0.35	0	0
NSSL2G	18.49	29.66	0.59	2404	0.59	0.51	0.9706	0.60	0.34	0.43	0.33	0.42	0	0
Best	*Small*	*Small*	*1*	*Small*	*1*	*1*	*1*	*1*	*1*	*0*	*1*	*1*		

Table 7: Rainfall MODE scores and indices for 48 mm threshold. The best and the worst performances for each index are highlighted in bold underlined and in italic underlined respectively. Last two columns refer to the sum of times each microphysics has been the best and the worst in one index. The last raw reports the desirable values for each index.

MP	CEN DIST	ANG DIFF	AREA RATIO	SYMM DIFF	P50 INT	P90 INT	TOT INTR	FBIAS	PODY	FAR	HK	HSS	GOOD	*BAD*
LIN	19.15	30.69	0.54	2205	**0.74**	**0.75**	0.9612	0.54	0.25	0.53	0.25	0.32	2	0
WSM6	18.69	**19.86**	**0.60**	*2248*	**0.71**	0.62	**0.972**	**0.60**	0.27	0.55	0.27	0.33	**5**	1
GODD	15.18	28.9	0.25	1936	*0.55*	0.45	0.9155	0.38	0.17	0.56	0.17	0.24	0	1
THOM	14.83	24.62	**0.59**	**1809**	0.67	0.58	**0.9692**	**0.59**	**0.37**	**0.38**	**0.37**	**0.46**	**8**	0
WDM6	*21.11*	**12.69**	*0.15*	2221	0.60	*0.44*	*0.8976*	*0.15*	*0.05*	*0.64*	*0.05*	*0.09*	1	*9*
NSSL2	**14.8**	23.2	0.46	1963	0.60	0.61	0.9509	0.47	0.27	0.42	0.27	0.36	1	0
NSSL2C	**14.8**	23.2	0.40	**1439**	0.63	0.47	0.9404	0.47	**0.36**	**0.22**	**0.36**	**0.49**	**6**	0
NSSL17	19.07	*36.02*	0.23	2041	0.58	0.53	0.9033	0.23	0.13	0.43	0.13	0.21	0	1
NSSL16	16.61	26.04	0.27	1882	0.69	**0.69**	0.9196	0.31	0.19	**0.38**	0.19	0.29	2	0
NSSL2G	19.04	34.82	0.43	2036	0.60	0.55	0.9393	0.43	0.24	0.45	0.23	0.32	0	0
Best	*Small*	*Small*	*1*	*Small*	*1*	*1*	*1*	*1*	*1*	*0*	*1*	*1*		

Table 8: Rainfall MODE scores and indices for 72 mm threshold. The best and the worst performances for each index are highlighted in bold underlined and in italic underlined respectively. Last two columns refer to the sum of times each microphysics has been the best and the worst in one index. The last raw reports the desirable values for each index.

6.5.2 Lightning flashes results

As said above, the second step for the evaluation of the ensemble members is based on the comparison between modelled and observed lightning flashes. Figure 25 shows the results of the total lightning prediction obtained by the PR92 parameterization application: all the ensemble members are compared with the observed lighting gridded on the model grid on the same time windows used for precipitation comparison (00 UTC – 24 UTC). In terms of spatial distribution of lightning, all the microphysics are able to capture the lightning activity over the sea as well as the typical V shape feature with the well fixed vertex. The lightning prediction over the ground instead is quite different from member to member. This result suggests that the lightning parameterization adopted has a good response over the sea independently by the microphysics adopted and suggests how the cloud condensation nuclei (CCN) concentration plays crucial role in this MCS.

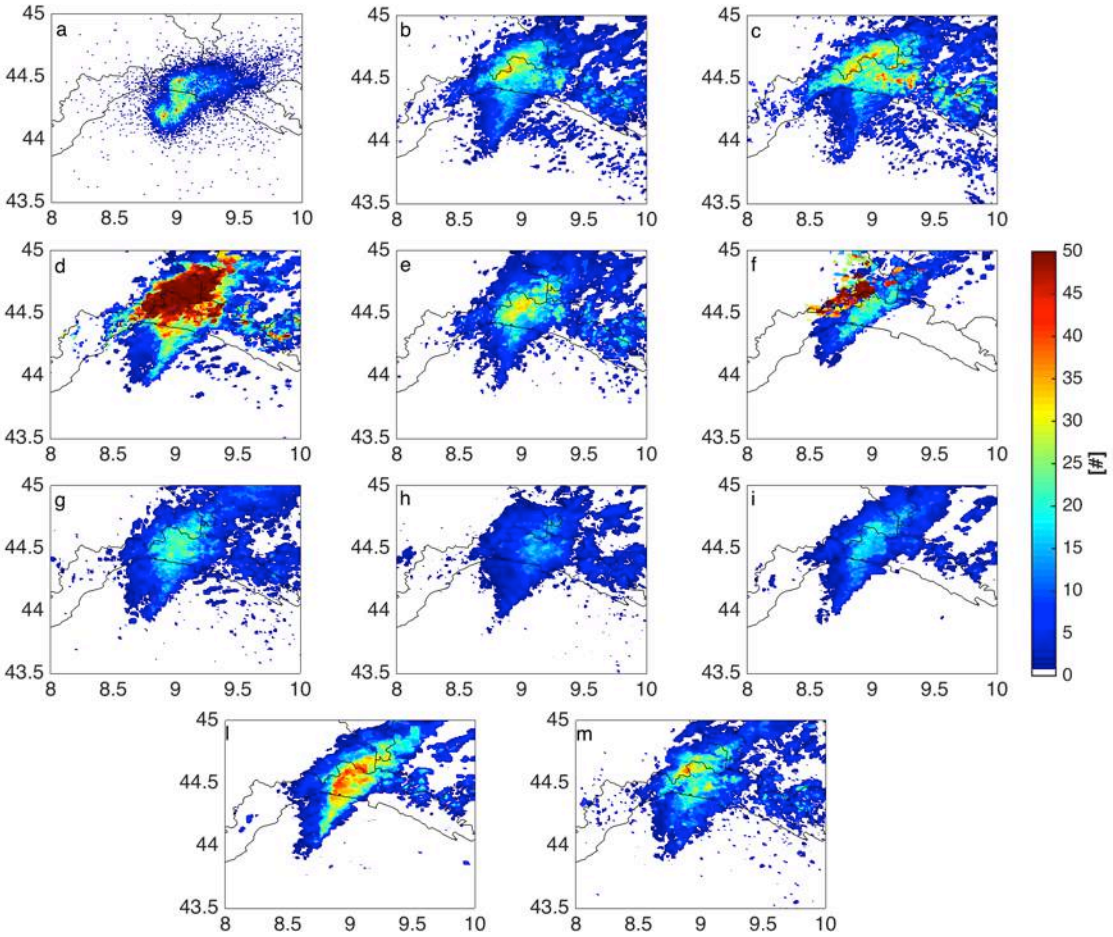

Figure 25: Comparison among observed total lightning (panel a) and parameterized lightning with PR92 scheme obtained from the 10 microphysical ensemble members in the time window from 00 UTC to 24 UTC on 9th October 2014: LIN (panel b), WSM6 (panel c), GODD (panel d), THOM (panel e), WDM6 (panel f), NSSL2 (panel g), NSSL2C (panel h), NSSL17 (panel i), NSSL16 (panel l) and NSSL2G (panel m).

MODE scores and indices have been computed by using a threshold of 5 flashes for grid point to identify the most active lightning area within the back-building MCS here investigated (Table 9). The adopted threshold corresponds to the minimum daily amount of observed lightning strokes, obtained by the data in Figure 22 b. As for rainfall analysis, the total interest score reveals a strong overall agreement between the forecast ensemble members and observations with values over the 90%, except for the worst forecast, namely the WDM6 member. A general overestimation of all the member forecasts in terms of area extension is revealed both by the area ratio score and Figure 25. In terms of total interest, the two best members are NSSL2C and NSSL17, not

surprisingly, given their specific formulation for convective thunderstorms electrification [Mansell et al. (2010)], while the worst one is again the WDM6 member. Conversely, in terms of the statistical indices, there isn't a real predominance of any member while the worst is confirmed to be the WDM6. By considering all together the results of the MODE analysis for rainfall and lightning fields, a final evaluation on the performances of all the 10 members of the microphysics driven ensemble of km-scale WRF simulations is possible.

Table 10 reports, for every index, the GOOD (BAD) column from Table 7, corresponding to the rainfall index analysis with intermediate rain depth threshold of 48 mm, together with the GOOD (BAD) column from Table 9 for the lightning MODE analysis. The TOTAL GOOD and TOTAL BAD columns summarize the times in which a given member of the microphysical driven ensemble is the best one and the times in which is the worst as appears from the MODE indices analysis for both rainfall and lightning fields. From this calculation it results that the three best members are WSM6, THOM and NSSL2C, while the worst one is the WDM6. These findings for the Genoa 2014 back-building MCS confirms that WSM6, THOM and NSSL2C microphysics are mostly recommended for the WRF km-scale (cloud-resolving) simulation of flash-flood producing storms associated with strong lightning phenomena, further strengthening previous results of Rajeevan et al. (2010), Giannaros et al. (2015, 2016), Pytharoulis et al. (2016) obtained with WRF at cloud-permitting grid-spacing (around 2 km or above). The LPI as formulated by Lynn and Yair (2008, 2010) and Yair et al. (2010) is then computed and analyzed for WSM6, THOM, NSSL2C, and WDM6 members to gain further physical insight into the deep moist convective processes, and to understand its predictive ability, for this Genoa 2014 back-building MCS.

MP	CEN DIST	ANG DIFF	AREA RATIO	SYMM DIFF	P50 INT	P90 INT	TOT INTR	ACC	FBIAS	PODY	FAR	HK	HSS	GOOD	*BAD*
LIN	**12.63**	46.79	2.79	3796	**0.99**	0.84	0.9162	0.97	3.48	0.65	0.81	0.62	**0.28**	**3**	0
WSM6	**16.46**	42.03	3.77	4850	**1.11**	**1.03**	0.9045	0.95	5.43	**0.79**	0.85	**0.75**	0.23	**5**	0
GODD	25.43	9.62	*4.57*	5726	*1.66*	2.47	0.9072	0.95	*6.39*	**0.90**	0.86	**0.85**	0.23	2	3
THOM	17.56	*51.21*	2.66	3576	**0.93**	**0.93**	0.9153	0.97	3.55	0.66	0.82	0.63	**0.28**	**3**	1
WDM6	*79.53*	19.72	4.19	*7535*	1.20	*1.44*	*0.8054*	*0.94*	5.51	*0.12*	*0.98*	*0.07*	*0.02*	0	*9*
NSSL2	49.01	**4.94**	3.55	4689	0.71	0.70	0.9211	0.97	4.03	0.73	0.82	0.70	**0.28**	2	0
NSSL2C	19.38	22.14	**1.35**	**1846**	0.71	0.53	**0.992**	**0.99**	**1.70**	0.58	**0.66**	0.56	0.42	**6**	0
NSSL17	24.02	14.03	1.83	3144	0.79	0.62	**0.9634**	**0.98**	**1.97**	0.38	0.81	0.37	0.25	**3**	0
NSSL16	23.93	**8.98**	**2.41**	3596	1.28	1.27	0.9428	0.97	2.98	0.52	0.82	0.50	0.25	2	0
NSSL2G	21.67	14.75	2.53	**3115**	**0.93**	0.89	0.9384	0.97	3.52	0.74	**0.79**	0.72	0.32	**3**	0
Best	*Small*	*Small*	*1*	*Small*	*1*	*1*	*1*	*1*	*1*	*0*	*1*	*1*			

Table 9: Lightning MODE analysis results for 5 flashes for pixel threshold. The best and the worst performances for each index are highlighted in bold underlined and in italic underlined respectively. Last two columns refer to the sum of times each microphysics has been the best and the worst in one index. The last raw reports the desirable values for each index.

MP	**RAIN GOOD**	*RAIN BAD*	**FLASH GOOD**	*FLASH BAD*	**TOT GOOD**	*TOT BAD*
LIN	1	0	**3**	0	4	0
WSM6	**5**	0	**5**	0	**10**	0
GODD	0	1	2	3	2	4
THOM	**6**	0	**3**	1	**9**	1
WDM6	1	*9*	0	*9*	1	*18*
NSSL2	3	0	2	0	5	0
NSSL2C	**8**	0	**6**	0	**14**	0
NSSL17	0	1	**3**	0	3	1
NSSL16	0	0	2	0	2	0
NSSL2G	0	0	**3**	0	3	0

Table 10: Sum of GOOD and BAD scores/indices analysis for cumulated rainfall (48mm threshold) and lightning (5 lightning threshold). The best and the worst performances for each index are highlighted in bold underlined and in italic underlined respectively. Last two columns refer to the sum of times each microphysics has been the best and the worst in one score/index.

6.5.1 *Lightning predictive capability – LPI*

The LPI analysis is performed over the same time window adopted for the rainfall and lightning flashes analysis, namely cumulating 30 minutes LPI values over 00-24 UTC interval (Figure 26). To allow a comparison between the LPI maps and the lightning flashes spatial distribution, the observed flashes have been gridded on the same grid of the model data.

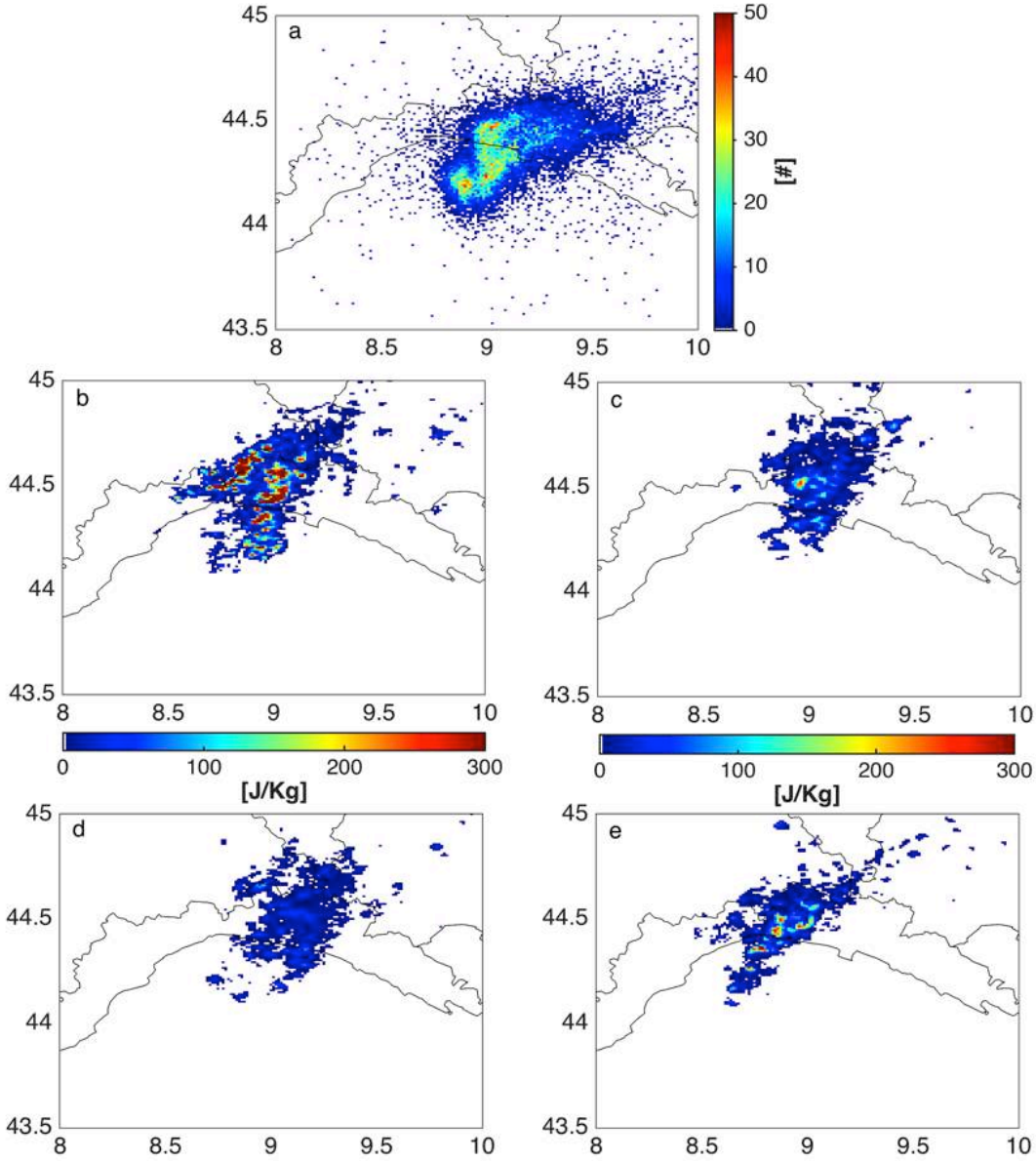

Figure 26: Observed total lightning (panel a), application of LPI to WSM6 (panel b), THOM (panel c), NSSL2C (panel d) and WDM6 (panel e) in the time window between 00 and 24 UTC on 9th October 2014

Figure 26 shows that the WSM6 experiment provides the highest LPI cumulated values with a spatial pattern in remarkable agreement with the observed lightning area: both the sea and ground are potentially subjected to lightning activity. The THOM and NSSL2C experiments provide lower cumulated LPI values with respect to WSM6 especially over the sea area, which is the most hit area by lightning (Figure 26a). Furthermore, not surprisingly, the WDM6 shows the worst LPI performances both in terms of cumulated values and spatial pattern.

These considerations are confirmed also from the MODE analysis performed to investigate the correlations between the observed lightning flashes and the modelled LPI patterns for each of the four selected members (Table 11). This time only the paired clusters orientation and collocation will be considered, while the percentile intensity within object above a fixed threshold (50 and 90) is not meaningful for this comparison between LPI and lightning flashes occurrence. The MODE analysis is undertaken considering a threshold of 2 J/kg for LPI and 5 flashes for pixel for observed lightning, in agreement with section 6.5.2.

MP	CEN DIST	ANG DIFF	AREA RATIO	SYMM DIFF	TOT INTR	ACC	FBIAS	PODY	FAR	HK	HSS
WSM6	**18.41**	**9.97**	**1.16**	2884	**1**	0.98	*1.29*	**0.42**	0.68	**0.41**	0.36
THOM	18.63	32.34	0.79	**2194**	0.9957	0.98	0.88	0.38	**0.56**	0.38	**0.40**
WDM6	*24.38*	**12.26**	*0.65*	*2983*	*0.9673*	0.98	**1.00**	*0.15*	*0.85*	*0.13*	*0.13*
NSSL2C	**16.58**	*32.54*	**0.88**	**1935**	**0.9976**	**0.99**	**0.89**	**0.49**	**0.45**	**0.49**	**0.51**
Best	*Small*	*Small*	*1*	*Small*	*1*	*1*	*1*	*1*	*0*	*0*	*1*

Table 11: LPI MODE analysis. The best and the worst performances for each index are highlighted in bold underlined and in italic underlined respectively. The last raw reports the desirable values for each index

Once more the overall high values of total interest (over 95%) for all the selected members (WSM6, THOM, NSSL2C, and WDM6) suggest a good spatial correlation between the observed lightning flashes and the LPI patterns. The worst performance in terms of total interest is provided by WDM6, while the best one is offered by WSM6 then confirming the considerations valid for Figure 26. The traditional statistical analysis (accuracy, BIAS, POD, FAR, HK and HSS) suggests that a good performance in all indices is reached by the NSSL2C, while WDM6 provides the worst performances with a FAR of 85% and a POD of only 15%. Since the LPI formulation is strictly related to the presence of ice species, the observed (Settepani radar) and predicted reflectivity fields at the bottom (0 °C isotherm) and in the middle (-10 °C isotherm) of the lightning charging zone are compared (Figure 27) at 11 UTC, one of the most intense phase of the observed morning lightning activity as shown in Figure 22b.

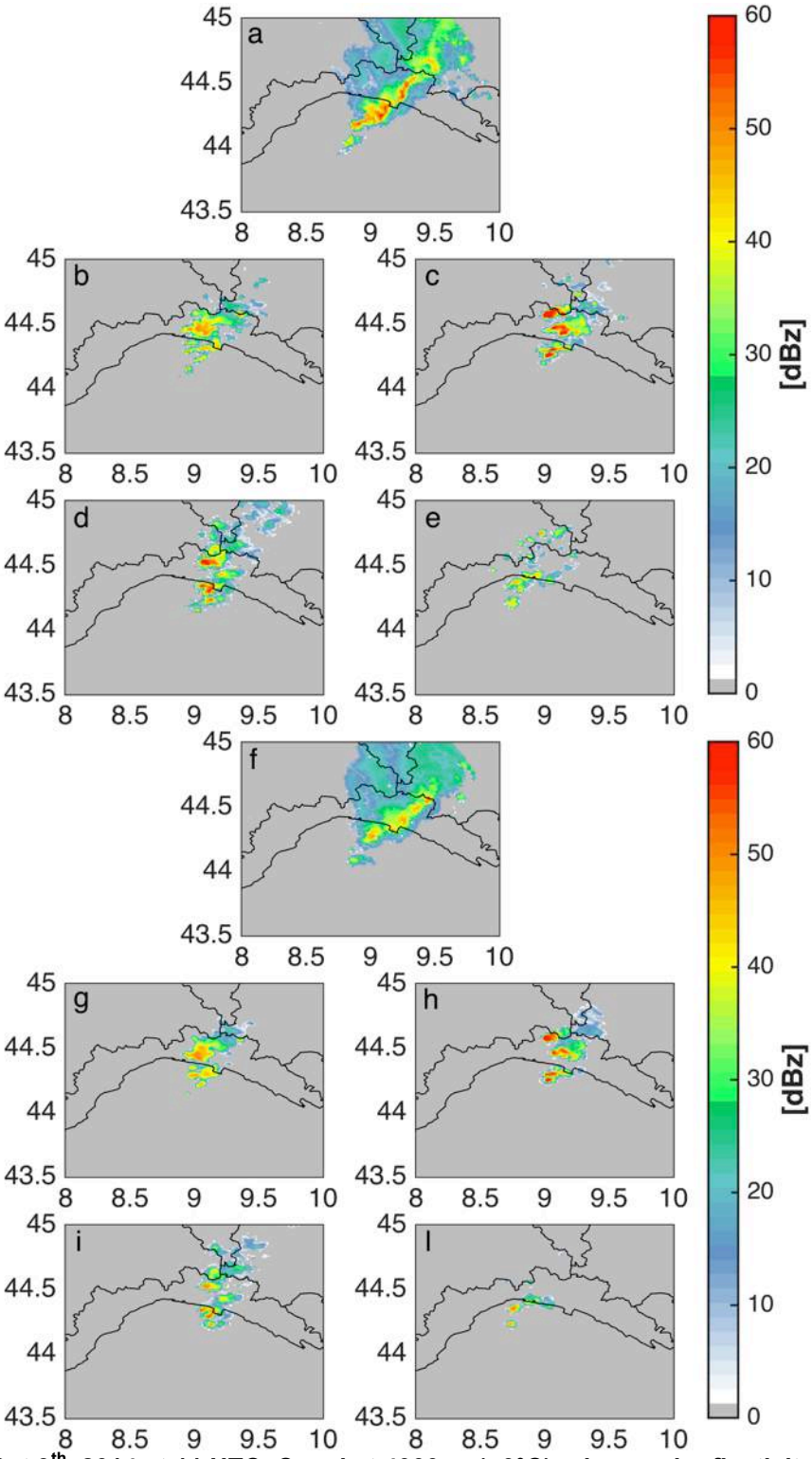

Figure 27: Oct.9th, 2014 at 11 UTC. Cappi at 4000 m (~0°C): observed reflectivity (panel a), WSM6 reflectively (panel b), THOM reflectively (panel c), NSSL2C (panel d), WDM6 reflectivity (panel e). Cappi at 6000 m (~-10°C): observed reflectivity (panel f), WSM6 reflectively (panel g), THOM reflectively (panel h), NSSL2C (panel i), WDM6 reflectivity (panel l).

The panels show that WSM6, THOM and NSSL2C members produce much more coherent and organized reflectivity fields both at the -0 and -10 °C levels, corresponding to a considerable ice-species production, thus resulting in a more active lightning charging layer. Conversely, WDM6 reflectivity field is definitely more scattered and disorganized, thus resulting in lower values of cumulated LPI. A possible explanation for these WDM6 findings is provided by the fact that has a default CCN (cloud condensation nuclei) concentration of 100 cm^{-3}, corresponding mostly to continental conditions. This results in the production of smaller raindrops, with weaker updrafts (in agreement with theoretical arguments of Parodi and Emanuel (2009, 2011)), and consequently in predominant warm rain process, such that rain falls out before reaching the freezing level. However, fine-tuning of each microphysics scheme of the adopted ensemble is beyond the scope of this work, since the different parameterizations have been adopted purposely as they are.

Moreover, as the inspection of the LPI equation (Eq. 1.9) suggests, the vertical velocity field and the graupel mixing ratio play a fundamental role in the LPI formulation, thus vertical cross sections for these two quantities (crossing the respective convective cells core at 10.30 UTC and 11UTC) are depicted in Figure 28 and Figure 29. Figure 28 shows a strong difference in the updrafts and downdraft fields among the WSM6, THOM, NSSL2C and WDM6 members. WSM6 and THOM produce stronger and widerspread updrafts than WDM6, thus resulting in towering (above 10000 m) cumulus nimbus clouds, in agreement with CTTH observational data (Figure 20). NSSL2C produces stronger updraft at 10.30 UTC while at 11.00 UTC it is less intense than WSM6 and THOM but it remains more organized than WDM6. The observed lightning

activity (Figure 22b) suggests very strong updrafts during the entire event, so the stronger the updrafts, the higher the altitude at which particles can be transported, and consequently the higher the number of ice particles collisions leading to larger LPI values. However, towering (above 10000 m) cumulus nimbus clouds are missing in WDM6 results, thus vertical sections in panel g and h provide in both figures a possible explanation of the significant underestimation of the Genoa 2014 event by the WDM6 member both in terms of rainfall and in lightning activity. This can also suggest why the NSSL2C-LPI doesn't reach high value as the other considered members even if in term of cumulated rainfall is one of the member with better scores/indices. The NSSL2C-QPF in fact shows rainfall activity not completely convective as it has been observed. Only the application of the LPI to this member of the ensemble has allowed counting the performance not among the best ones.

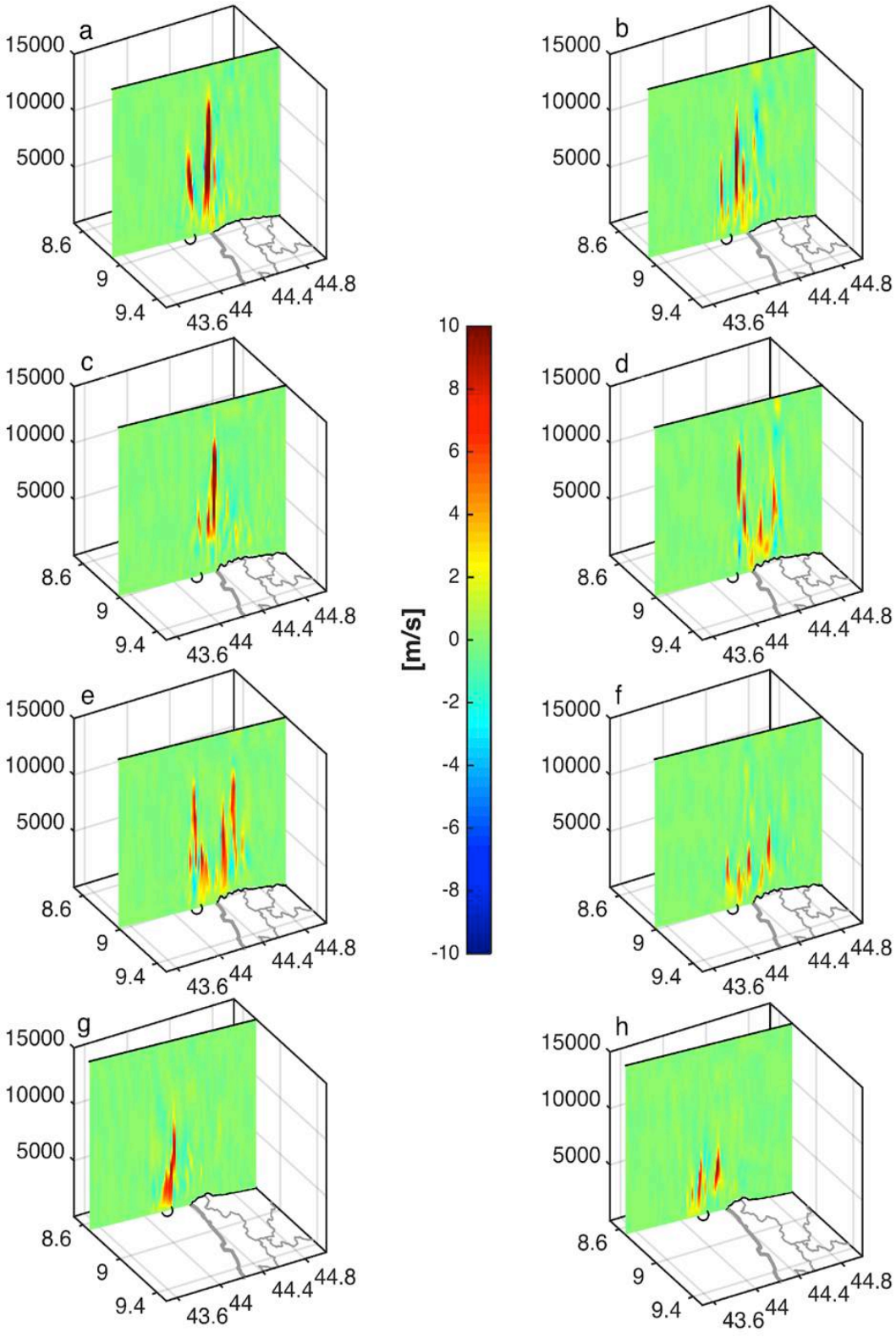

Figure 28: Vertical sections of vertical velocity field [ms^{-1}]. Left column refers to 10.30UTC, right column to 11UTC on 9th October 2014: WSM6 in Panel a-b, THOM in Panels c -d, NSSL2C in Panels e -f and WDM6 in Panels g -h.

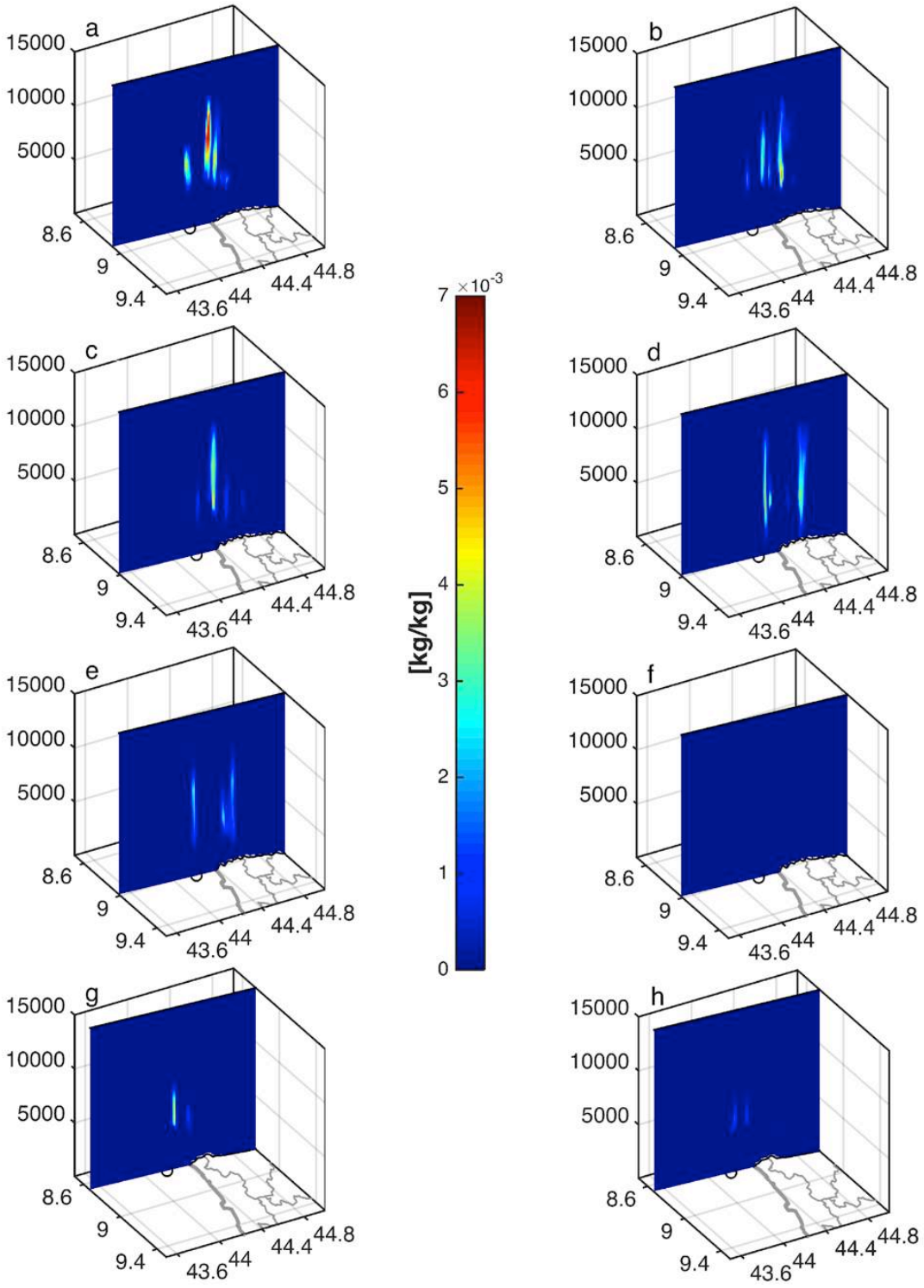

Figure 29: Vertical sections of graupel mixing ratio [kgkg^{-1}]. Left column refers to 10:30UTC, right column to 11UTC on 9th October 2014: WSM6 in Panel a-b, THOM in Panels c -d, NSSL2C in Panels e -f and WDM6 in Panels g -h.

Figure 29 confirms this statement, the WDM6 (both at 10.30 UTC and 11.00 UTC) and, to some extent, the NSSL2C (at 11.00 UTC) members show much lower graupel mass fraction values than what WSM6 and THOM members do. Furthermore, WSM6 shows higher graupel mass fraction values compared to THOM that explains finally why WSM6 gives higher LPI values. Fiori et al. (2017) classified this back-building MCS as a non-equilibrium regime, since a significant amount of CAPE was available over the Ligurian sea (between 1000 and 1500 Jkg-1 in the morning), but the extent to which it could produce convection and precipitation has been conditioned by the presence of a sufficient trigger to overcome any thermodynamical “barrier”, such as the convective inhibition energy. The trigger was provided by the aforementioned virtual topography over the Liguria sea, enabling the rapid adiabatic ascension of plumes of warm and almost saturated air above the level of free convection (around 700 m), generating very strong updrafts, thus fully exploiting the available CAPE, available in the lower to middle troposphere. Along similar lines, LPI shows a significant capability of providing further insight into the vertical thermodynamical structure of the predicted convective flow field in the upper troposphere portion, allowing to discriminate in the forecasting phase between scenarios leading to (very) deep moist convective and persistent storms, with very strong updrafts, and ones resulting in shallower and more disorganized convective situations, thus not producing significant ground effects, such as flash-floods. This important finding complements and supports research results about the relevance of total lightning activity, as an indicator of updraft and turbulence convection processes characteristics [Deierling and Petersen (2008), Al-Momar et al. (2015), Sakurai et al. (2015)], using LPI as a physical based tool for their prediction.

6.6 Concluding remarks

The back-building MCS, which affected the Genoa city center on 9th October 2014, was extremely challenging from a predictive ability standpoint if following a purely deterministic approach. Thus, using the WRF model at 1 km grid spacing, a microphysics driven ensemble of 10 members has been adopted to get a better understanding of this severe hydro-meteorological event predictability.

This work has been developed to exploit the interplay between extreme convective rainfall phenomena and severe lightning activity for back-building MCSs occurring in north-western Mediterranean (Varazze, 4th October 2010, Cinqueterre, 25th October 2011, Genoa, 4th November 2011 and Genoa, 9th October 2014, Nice, 3rd October 2015 and so forth) and to use the LPI to provide further insight into the vertical thermodynamical structure of the predicted convective flow field in the upper troposphere portion.

An effective methodology for the rainfall and lightning activity forecasting and evaluation is here presented to improve the probability of predicting events like the one occurred in Genoa.

In this work a numerical modelling of a back-building MCS is performed by applying the Price and Rind (1992) lightning parameterization and the Lightning Potential Index (LPI) approaches to a microphysics driven ensemble modelling approach, at cloud-resolving grid spacing (1 km).

Along these lines, the first part of this research activity focuses on a methodological approach for the evaluation of extreme rainfall and lightning predictive ability of the 10 ensemble members by applying the Method for Object-Based Evaluation (MODE) to assess their performances.

From a rainfall forecast point of view, the convective event is quite well captured by about half of the adopted microphysics parameterizations, when referring to rainfall amounts and spatial distribution as confirmed by the MODE total interest scores. Still there is a general QPF underestimation highlighted by different statistical indices (POD, FAR, etc) allowing then to identify a group of three as the best QPFs performance members and a worst one. Since these events are characterized by a high correlation between heavy rainfall and intense lightning activity, the second analysis is performed by comparing, again via the MODE scores and indices, the parameterized (PR92 scheme) and the observed lightning activities. All together QPF and the lightning predictions scores and indices results are summarized and the three best run and the worst one are chosen: THOM, WSM6 and NSSL2C are the best performing members, while WDM6 one gives the worst results both in terms of spatial and statistical analysis.

On these selected members the LPI performances have been then solely analysed. The results show a significant agreement and consistency both between the predicted rainfall patterns and the LPI versus the corresponding observed data, which confirms the initial idea of strong connection between rainfall and lightning activity. The vertical sections of the vertical velocity field and graupel mixing ratio, representing the main ingredients for lightning occurrence [Saunders (2008)], reveal that the main difference between the best microphysics driven ensemble members and the worst one is in the representation of the convective flow field resulting in significantly different graupel mixing ratios patterns and peaks. In particular, the WDM6 has weaker updrafts and consequently less graupel particles and lower LPI values. Also NSSL2C reveals a weaker vertical velocity field and lower graupel mixing ratio

with respect to the WSM6 and THOM members, as highlighted by lower LPI. As a consequence, it is possible to conclude that the use of the LPI can be helpful for real-time forecasting aims (by coupling rainfall and LPI predictions) allowing as aforementioned to discriminate in the forecasting phase between scenarios leading to (very) deep moist convective and persistent storms and ones resulting in shallower and more disorganized convective situations, thus not producing significant ground effects. It could be also an instrument for hindcast studies by enabling the investigation of the physical parameters that determine lightning activity and which are essential for the reproduction of this kind of high impact weather events, over complex topography areas [Fiori et al. (2016)]. However, the main source of uncertainty in the forecast of these back-building MCSs remains linked to the correct reproduction of the convective field that is a fundamental ingredient for this kind of events. Thus, in the next chapters the use of data assimilation to reduce the uncertainty in the reproduction of this kind of events is investigated.

The LPI prediction is currently active in the operational WRF model run at CIMA Research Foundation executed on behalf of the Liguria Region Environment Protection Agency (ARPAL hereafter). The model outputs have been also provided during the HyMeX EXAEDRE measurement field campaign that took place in September 2018 in Corsica. In this framework future work will be devoted to the impact evaluation of reflectivity assimilation on LPI forecasts considering the 8 intensive observation periods (IOP) selected during EXAEDRE.

7. Second activity - data assimilation with operational purpose

Most of the work presented hereafter is taken from the following paper currently under review: Lagasio, M, Silvestro, F, Campo, L, & Parodi, A. Predictive capability of a high-resolution hydrometeorological forecasting framework coupling WRF cycling 3dvar and Continuum. Journal of Hydrometeorology.

7.1 Data assimilation development overview

Nowadays, the skill of the Numerical Weather Prediction (NWP) models is certainly being improved thanks to the increasing model resolution [Clark et al. (2016)]. However, quantitative precipitation NWP models predictive ability challenges can derive from the poor knowledge of the initial state of the atmosphere at small scales leading to an inevitable model spin-up that often results in an inaccurate simulation of the convective system in terms of timing, location and intensity [Sugimoto et al. (2009)]. So, the knowledge of the initial (and boundary) conditions is affected by significant uncertainties and are the first sources of error in the weather modelling.

In the last decade, the observational hydro-meteorological data sources have increased benefiting from conventional telemetered observations, from land, ships and sounding balloons, from satellites, meteorological radars and nonconventional platforms (such as airplanes), thus helping to better reconstruct the spatio-temporal evolution of variables such as temperature, wind speed and direction, relative humidity, reflectivity, rainfall and other microphysics related variables.

As explained in Chapter 2, starting from an approximation of the state of the atmosphere in terms of initial and boundary (in case of limited area modelling) conditions (IC and BC hereafter), a NWP model simulates the atmospheric evolution. The forecast quality strongly depends on IC and BC estimation accuracy, that can be significantly improved through a proper combination of

the observational data and the short-range forecasts: this approach is called “data assimilation” and its purpose is defined as “using all the available information, to determine as accurately as possible the state of the atmospheric (or oceanic) flow” [Talagrand (1997)].

The early NWP data assimilation experiments consisted in hand grid interpolations of the observations to a regular grid, resulting in IC fields manually digitized [Richardson (1922), Charney et al. (1950)]. The need of an automatic procedure for preparing an objective analysis field emerged since the early days of NWP, so different interpolation algorithms were developed during the next period [Charney (1951), Panofsky (1949)].

Despite the automation of objective analysis preparation was a step forward in NWP, the spatial interpolation of observations over a regular grid does not improve, alone, sufficiently the operational NWP predictive ability, since a modern NWP model has a number of degree of freedom of the order of 10^7, while the available conventional observations are of the order of 10^4. The main problem related to the observations is that their distribution is usually not homogeneous neither in space nor in time.

To overcome this problem, it became clear that a “first guess” estimate of the atmosphere in all grid points of the considered domain was necessary in addition to observational data to obtain the necessary initial conditions to solve the NWP equations [Bergthorsson and Döös, (1955)]. The “first guess”, also called “background field” or “prior estimation”, is the best state of the atmosphere representation without the use of observations data. In the NWP infancy, it was estimated from climatology or a combination of climatology and a short range forecast [Bergthorsson and Döös, (1955)]. Nowadays, as NWP became better, it is universally adopted the use of short-range forecast as first

guess in a context of operational analysis cycle system that typically uses a 6-h cycle performed four times a days and, for each cycle, uses as background field the last state of the previous forecast cycle [Kalnay (2002)].

In this respect, a key consideration is that both the model that provides the first guess and the observations taken from different instruments are affected by uncertainty. The data assimilation aims to merge these different datasets, taking adequately into account their respective degree of uncertainty, thus, producing a new state with desirable statistical properties (e.g. unbiased, minimum variance, etc).

Furthermore, besides measurements errors, observations can have various resolutions in time and space resulting in an inhomogeneous distribution. To overcome this problem, models can be used both to impose physical constraints reducing the freedom in the observations data interpretation and to retrieve information on unobserved areas or time instants exploiting the model dynamical and spatial dependencies.

Therefore, different approaches of data assimilation have been developed in the last years to take into account the variability (in space and time) of observations and their measurements error and the model errors. There are many classifications of data assimilation techniques. In terms of assimilation procedures, the methods can be divided in: sequential assimilation where real-time observations are available and they are considered in the past until the analysis time and non-sequential data assimilation when information from the future (with respect to the analysis date) are used in reanalysis procedures. Another subdivision can be applied by considering the time period of the data assimilation: intermittent methods, in which observations are assimilated in

small batches iteratively in time, or continuous methods where longer periods are considered [Bouttier and Courtier (1999)].

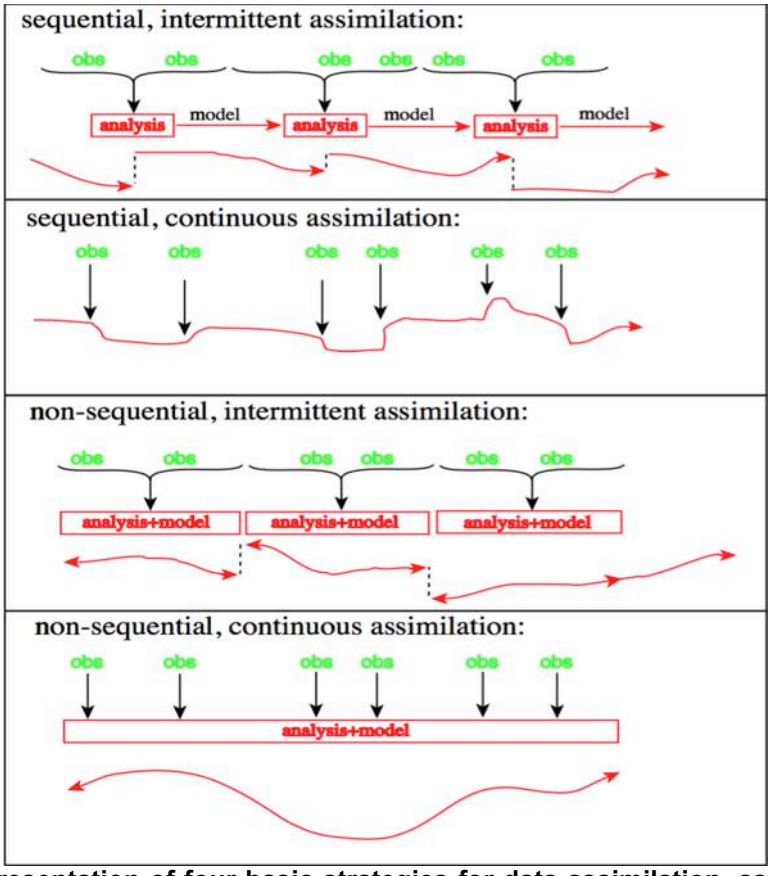

Figure 30: Representation of four basic strategies for data assimilation, as a function of time. [Bouttier and Courtier,1999]

Compromises of different approaches are also possible. Figure 30 shows a schematization of the assimilation approaches here presented.

Starting from the basic strategies, many assimilation techniques have been developed with different numerical cost, optimality and suitability for real-time data assimilation [Lorenz (1986); Daley (1991)] and some of them are still under development.

From a mathematical point of view, data assimilation techniques can be divided in two main categories: variational techniques (3DVAR, 4DVAR) and ensemble stochastic filtering techniques (derived Kalman Filter, Particle Filters and other smoother methods). A general view of these approaches is presented hereafter.

7.2 Predictive capability of a high-resolution hydrometeorological forecasting framework coupling WRF cycling 3dvar and Continuum.

The western Mediterranean area is characterized by a complex orography (Alps, Apennines, Massif Central, Pyrenees) often sitting close to the coastline, potentially able to enhance or even to trigger the deep convective processes originating over the warm sea in the fall season [Rebora et al. (2013), Ducrocq et al. (2014), Fiori et al. (2017)]. The most severe events in this area are due to a particular type of mesoscale configuration featuring a continuous redevelopment of storm cells persisting for hours over the same area, the so called back-building Mesoscale Convective Systems MCSs [Rebora et al. (2013); Ducrocq et al. (2014); Cassola et al. (2015), Fiori et al. (2017), Lagasio et al. (2017)].

Having a very steep coastal orography, mostly drained by very small-sized catchments (1-10 km^2), the Liguria region (N-W Italy) is particularly prone to flash-floods induced by back building MCSs: in the period between October 2010 and October 2014 alone, four events (Varazze, 4 October 2010; Cinqueterre, 25 October 2011; Genoa, 4 November 2011; and Genoa, 9 October 2014) accounted for 30 casualties and hundreds of millions of euros of damages. Consequently, the use of high-resolution hydro-meteorological forecasting frameworks combining Numerical Weather Prediction (NWP) models and rainfall-runoff models is recognized essential to provide timely and accurate streamflow forecasts [Silvestro et al. (2015b)]. A considerable effort has been made in the last few years to develop cloud resolving NWP systems, possibly in combination with ensemble and multi-physics approaches, to improve the short term Quantitative Precipitation Forecast (QPF) of convective

extreme events [Ducrocq et al. (2014), Hally et al. (2015), Clark et al. (2016), Davolio et al. (2017), Fiori et al. (2017)]; an example is reported in the first research activity (Chapter 6 and Lagasio et al. (2017)) However, a reliable forecast of these events in terms of rainfall amount, location and timing is still an open issue [Ducrocq et al. (2014)] that cannot be tackled only through the increase of the NWP models space-time resolution.

As already discussed, NWP is a mathematical problem determined by its initial and boundary (in case of limited area modelling) conditions. QPF challenges often derive from the uncertainty related to the initial state of the atmosphere at small spatio-temporal scales [Bauer et al. (2015)]. This challenge becomes even more relevant when the model grid spacing is approaching the kilometric scale, mainly as a consequence of the lack of high spatio-temporal resolution observations. In last few years, significant advances in forecasting heavy rainfall events have been achieved thanks to the combination of high resolution meteorological models with the data assimilation of both in situ and radar observations [Davolio et al. (2017), Maiello et al. (2017), Mazzarella et al. (2017)]. More specifically, some studies investigated the influence of reflectivity data assimilation combined with conventional surface observations for heavy rainfall events in southwest England, Korea and Bangladesh [Lee et al. (2010); Liu et al. (2013), Ha et al. (2011); Das et al. (2015)] as well as over central Italy area [Maiello et al. (2014), Maiello et al. (2017), Mazzarella et al. (2017)]. In the case of the Liguria region the effect of the nudging of radar-derived rainfall data on hydro-meteorological predictive capability has been evaluated through the coupling of the meteorological forecast with the Continuum hydrological model [Davolio et al. (2015), Davolio et al. (2017)] for some events of the autumn 2014. Their main result is that the contribution of the nudging of radar rainfall

data observations is large during the assimilation period and still relevant in the following 3 hours of the free forecasts, but rapidly decreases after 6 hours.

This research activity aims further insights into the hydro-meteorological prediction of back-building MCSs through the combination of a high resolution WRF model instance including a 3DVAR data assimilation cycle - with the fully distributed Continuum hydrological model, via the RainFARM stochastic downscaling procedure [Rebora et al. (2006)]. In previous works, the e-Science environment developed in the framework of the EU-funded DRIHM project was used to demonstrate its ability to provide relevant, meaningful hydrometeorological forecasts [Hally et al. (2015), Parodi et al. (2017)], but without the use of data assimilation in the meteorological model. The specific novelty of this research resides in driving the flash-flood forecasting framework with a rich portfolio of direct and indirect radar reflectivity WRFDA-3DVAR operators as well as in situ weather stations data fed into a cloud resolving NWP model in a cycling mode.

7.2.1 Test cases: back-building MCSs over Liguria region

This study will focus on three extreme meteo-hydrological events that hit the Liguria region (located in northwestern part of Italy) in 2011 and 2014. The first event occurred on 25 October 2011 when a very intense back-building MCS (470 mm of rain in 6 hours) produced widespread flash-flood phenomena in Cinque Terre (the red dot in Figure 31), causing the death of thirteen people and several millions of euros of damages. Ten days after, on 4th November, another back-building MCS of the same intensity (450 mm of rain in 5 hours) affected Genoa's city centre (black dot in Figure 31) resulting again in a large amount of damages and the death of six people. Three years later (9 October 2014), a third flash flood struck again the very same part of Genoa. This time

the meteorological event was characterized by two phases: the first one happened in the morning (between 08 UTC and 12 UTC) recording rainfall amounts between 50 and 130 mm over the Bisagno catchment, while the second one occurred after few hours and although a rather similar meteorological dynamics, was even more intense pounding again the same catchment with other 150 and 260mm in 2 hours (20-22 UTC). Locally the daily maximum cumulated rainfall reached 400 mm with an average of 200 mm over the entire basin area (about 90 km^2). The main ingredients of these kind of events are reported in Chapter 6.5.1, where the third flash flood (Genoa 2014) was investigated in terms of Lightning Potential Index (LPI).

The three selected test cases will allow for evaluating the impact of a cycling 3DVAR and different assimilation operators for in situ stations and weather radar data.

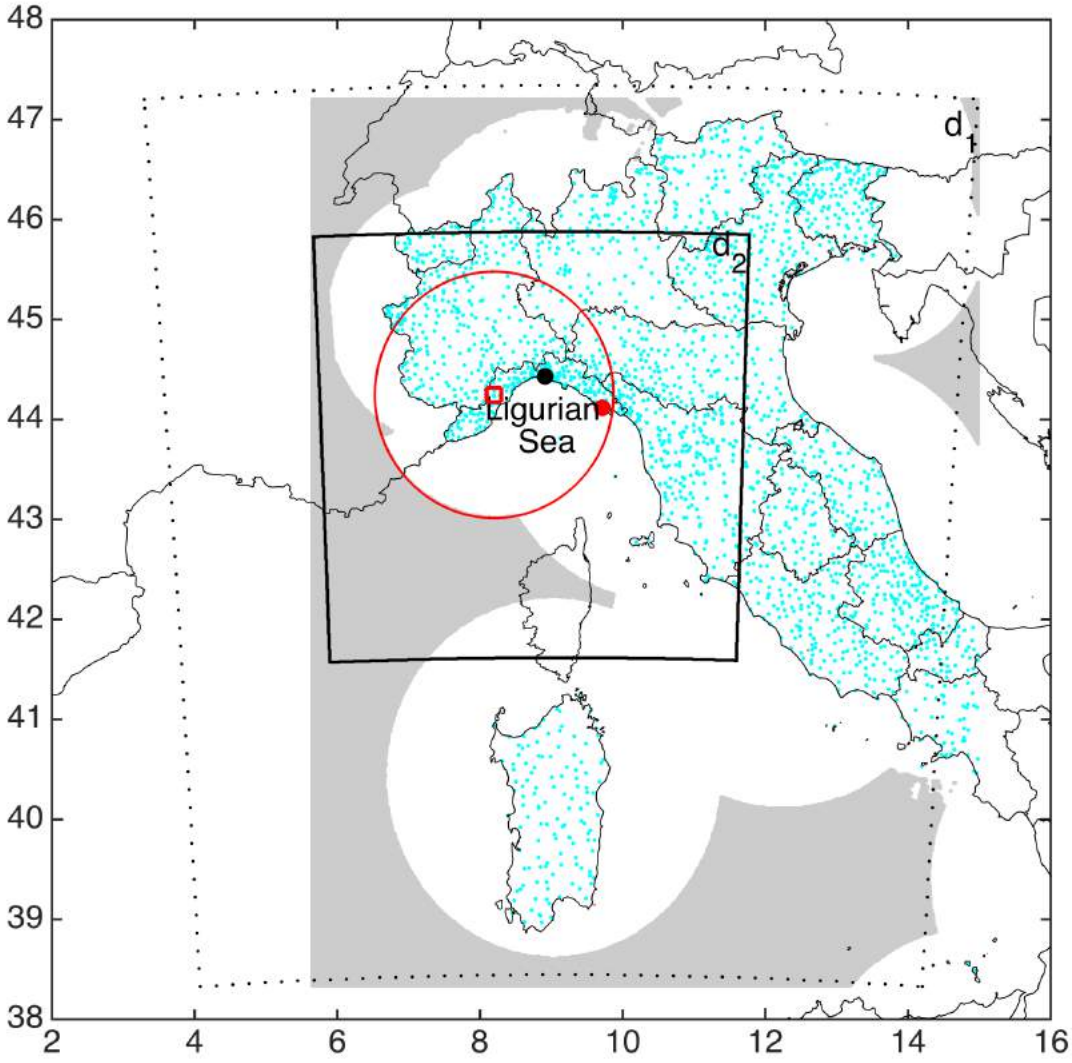

Figure 31: Data available for the assimilation. The red circle represents the area covered by the Settepani radar with the red small square indicating the radar location. Cyan dots are all the available SYNOP stations recording wind speed and direction, temperature and humidity. The grey shadow isolates the area covered by the Italian Radar Network (white circles mosaic) inside the WRF domains. The dotted and solid black lines represent WRF nested domains with spatial resolutions of 5 km (d_1) and 1 km (d_2) adopted for simulations, while the black dot indicates the Genoa city location (interested by two of the three extreme events simulated) and the red dot locates the Cinque Terre area (hit by one extreme event considered) in the Liguria region.

7.2.2 Observations available for data assimilation and validation

The observational data to be assimilated via 3DVAR in WRF experiments are: reflectivity from weather radars and temperature, wind speed and direction and relative humidity from surface observations.

For the radar reflectivity, the observational data are provided by Meteorological Radar national mosaic operated by the Italian Civil Protection (Vulpiani et al. (2006), CAPPI data on 3 levels: 2000, 3000 and 5000 m a.s.l.) covering the whole italian territory (Figure 31, grey shadow) and by the 8 levels (CAPPI data at 1500, 2000, 3000, 4000, 5000, 6000, 8000, 10000 m a.s.l.) of the C-band polarimetric radar located on Mount Settepani (Figure 31, red square) covering the Liguria region [Silvestro et al. (2009)]. The Settepani radar is already integrated in the national mosaic, however the idea of using its data separately when available (for instance, during the Genoa 2014 flood) is justified by their higher vertical resolution with respect to the national mosaic. The ground sensors data are provided by the Italian Civil Protection hydrometeorological network. This operational network, employed for the hydrometeorological monitoring of the Italian territory, is composed by thermometers, rain gauges, hygrometers and anemometers and it is particularly dense (about 1 station every 10 km^2) on the the Ligurian coast (Figure 31, cyan dots).

Concerning the quantitative precipitation estimate (QPE), the 2011 case studies rely purely on raingauge data, while the rainfall retrieval from the Settepani radar [Silvestro et al. (2009)] was only possible for the Genoa 2014 flash flood. The Settepani radar therefore allowed for obtaining accurate data over the sea, a key element for the prediction of the onset of these kinds of events [Lagasio et al. (2017)].

7.2.3 Model setup and methodology

7.2.3.1 Hydrometeorological framework

To assess the impact of the atmospheric 3DVAR data assimilation on streamflow prediction, a hydro-meteorological forecasting framework was employed. The framework is composed by the cascade of the WRF-ARW with WRFDA for cyclic 3DVAR data assimilation, a stochastic downscaling model (RainFARM) and a hydrological model (Continuum).

7.2.3.2 WRF-ARW and WRFDA setup and validation

The WRF model setup is based on the previous results for back-building MCSs occurred in Liguria [Fiori et al. (2014), Fiori et al. (2017), Lagasio et al. (2017)]. Two nested domains (Figure 1) with respectively 5 km (179 x 200 grid points) and 1 km (475 x 475 grid points) grid spacing, covering the upper and lower limits of the cloud-permitting range [Arakawa (2004)], have been used for all the experiments.

The number of vertical level is set to 50 with a higher density in the first 1000 m layer of atmosphere. Both grid spacings (5 and 1 km) allow solving explicitly many convective processes [Kain et al. (2006, 2008)] so an explicit treatment of convection is chosen. Given the observed presence of solid hydrometeors in atmosphere due to the strong convection that characterizes all these events [Fiori et al. (2017), Lagasio et al. (2017)] the microphysics parameterization corresponding to the WRF single-moment six-class scheme (WSM6) [Hong and Lim (2006)] is applied. The Yonsei University Scheme (YSU) is used for the Planetary Boundary Layer (PBL) because it accurately simulates deeper vertical mixing in buoyancy-driven PBLs with shallower mixing in strong-wind regimes with respect to the older MRF scheme [Hong et al. (2006)]. Shortwave and longwave parameterization are taken into account through the Rapid

Radiative Transfer Model (RRTMG, Iacono et al. (2008)). Furthermore, land surface is parameterized by the Rapid Update Cycle (RUC) land surface model [Benjamin et al. (2004)] that is a multi-level soil model with higher resolution in the top part of soil domain (0, 5, 20, 40, 160, 300 cm as in the default configuration).

Regarding the data assimilation, a sensitivity analysis has been performed for each test case using all the available reflectivity operators plus the modified direct operator (Chapter 4.4), both stand-alone and coupled with surface observations data. Table 12 describes the 9 sensitivity experiments. The run with the modified direct reflectivity operator is implemented only for the assimilation of reflectivity alone (Table 12) due to the fact that, on one side, the main aim is to compare its behavior with the other operators and, on the other one, because the best results for the other operators have been achieved with the assimilation of reflectivity alone.

A 3DVAR assimilation technique is applied every 6 hours in a cycling mode and for each cycle the forecast lead-time is the end of the day of interest (Figure 32). Referring to Chapter 4, the **B** matrix plays a fundamental role for the good quality of data assimilation results. In this work The Control Variable option 5 (CV5) of the WRFDA package is used in this work (for more details refer to WRFDA User Guide) for the **B** matrix calculation using the National Meteorological Center (NMC) method [Wang et al. (2014)] over the entire month of October 2013 with a 24-hour lead time for the forecasts starting at 00:00 UTC and a 12-hour lead time for the ones initialized at 12:00 UTC of the same day. The differences between the two forecasts (t+24 and t+12) valid for the same reference time are used to calculate the domains specific error statistics.

Run abbreviation	Run description
Open Loop	Run without data assimilation
ALL-direct	Assimilation of reflectivity and SYNOP with direct method
ALL-indirect	Assimilation of reflectivity and SYNOP with indirect method
ALL-indirect-rqv	Assimilation of reflectivity and SYNOP with indirect method adding the in-cloud humidity estimation
Radar-direct	Assimilation of reflectivity only with direct method
Radar-direct-modif	Assimilation of reflectivity only with direct method using the modified reflectivity operator
Radar-indirect	Assimilation of reflectivity only with indirect method
Radar-indirect-rqv	Assimilation of reflectivity only with indirect method adding the in-cloud humidity estimation
Stations-only	Assimilation of SYNOP stations only

Table 12: List of simulations that compose the sensitivity for each test case and corresponding abbreviation that will be used in the text.

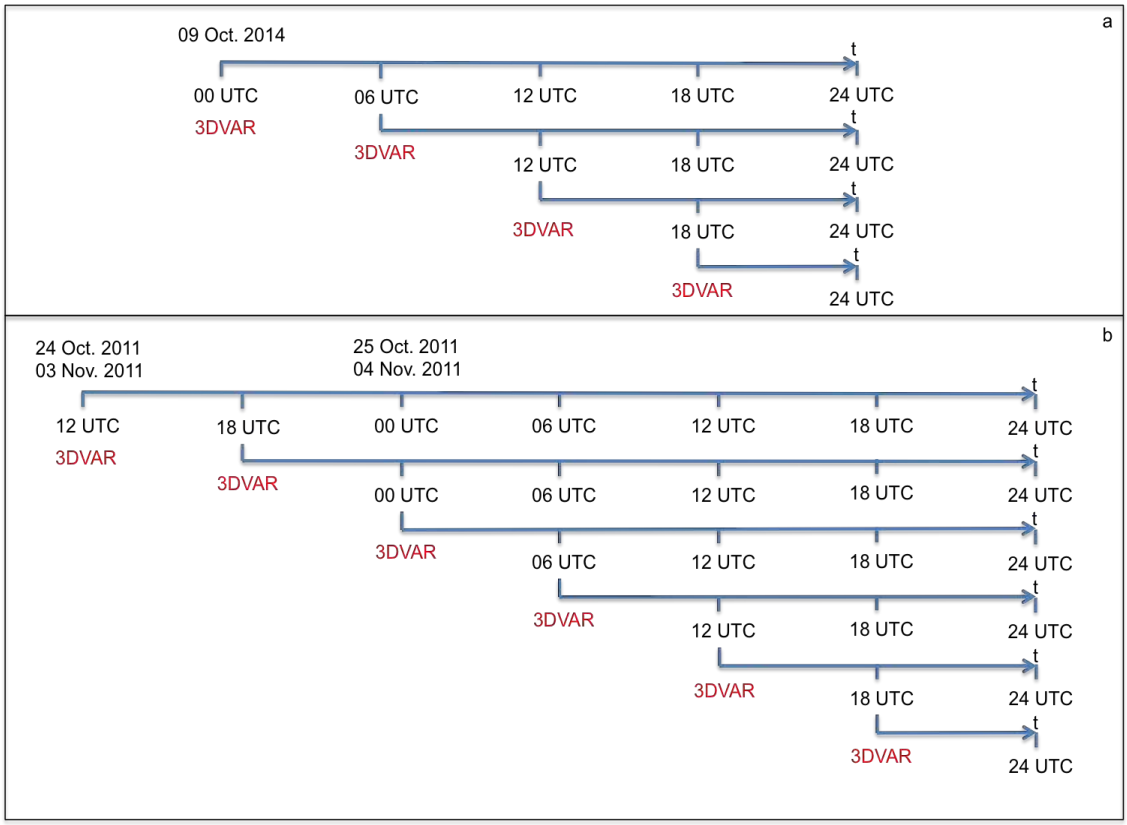

Figure 32: Six hour cycling 3DVAR assimilation scheme for the selected test cases: Genoa 2014 in Panel a, Cinqueterre 2011 and Genoa 2011 in Panel b.

When coming to the test cases, the initialization time depends on the timing of each event (see section 2): for the two episodes of 2011 the runs are initialized at 12 UTC of the day before (24 October and 03 November) while the 2014 case is initialized at 00 UTC of the same day (09 October). Initial and boundary conditions for all the simulations are provided by the European Centre for Medium-Range Weather Forecasts Integrated Forecast System (ECMWF - IFS) with a spatial resolution of 0.125 x 0.125° and the boundary are updated every 3 hours. In terms of operational framework IFS analysis are available 6 hours and 5 hours after the initialization time in the cases happened during October and November respectively. The main advantage of maintaining the same IFS analysis over all the forecasting period, while updating the model with a 6 hour cycling 3DVAR of observations, is that the corresponding forecast is available 4 or 5 hours in advance with respect to the forecast run every time with the most recent IFS analysis during the day. Consequently, the hydrometeorological chain can provide updated forecasts during the entire event in a nowcasting framework.

7.2.3.3 The hydrological framework: RainFARM and Continuum

The hydrological framework is constituted by a rainfall downscaling model and a hydrological model both widely described in previous publications [Silvestro et al. (2011); Laiolo et al. (2014); Silvestro et al. (2016)]. Continuum is continuous and distributed hydrological model, developed by Silvestro et al. (2013, 2015) while the configuration adopted in this work is described in Davolio et al. (2017) together with its calibration, particularly focused on floods and flow peak events. Table 13 reports the main characteristics of the implementation for three basins, affected by the considered events and where streamflow observations were

available; the table also reports the values of skill scores for the validation period [Davolio et al. (2017)]:

- Nash Sutcliffe (NS) coefficient (Nash and Sutcliffe, 1970):

$$NS = 1 - \frac{\sum_{t=1}^{t\max} \left(Q_m(t) - Q_o(t)\right)^2}{\sum_{t=1}^{t\max} \left(Q_0(t) - \overline{Q_o}\right)^2} \qquad \textbf{Eq 7.1}$$

$Q_m(t)$ and $Q_o(t)$ are the modelled and observed streamflows at time t. $\overline{Q_0}$ is the mean observed streamflow. T_{max} is the number of time steps of the entire simulation.

- Relative Error of High Flows (REHF)

$$\mathrm{REHF} = \frac{1}{\mathrm{Nvalues}} \left[\sum_{i=1}^{\mathrm{Nvalues}} \frac{\left|\mathrm{Q_m(t) - Q_o(t)}\right|}{\mathrm{Q_o(t)}} \right]_{\mathrm{Q>Qth}} \qquad \textbf{Eq 7.2}$$

where Q_{th} is chosen as the 99 percentile of the observed hydrograph along the considered period, Nvalues is the number of time steps where $Q>Q_{th}$.

Basin	Station	area [km^2]	spatial resol. Dx [m]	Time resol. [min]	Period of validation	NS	REHF
Bisagno	Passerella Firpo	92	480	60	01/01/2013 - 31/12/2014	0.26	0.16
Vara	Nasceto	202	480	60	01/01/2013 - 31/12/2014	0.83	0.1
Magra	Calamazza	960	480	60	01/01/2013 - 31/12/2014	0.81	0.14

Table 13: Characteristics of the considered basins, and of the spatial and time model implementation. The values of two skill scores calculated on validation period are also shown.

The state variables of the hydrological model at the beginning of each of the considered events were evaluated doing a seamless run from 01/01/2011 until 31/12/2014 feeding the model with gauges (rainfall, air temperature, solar radiation, air relative humidity, wind velocity) interpolated with a simple Kriging method.

The rainfall downscaling model (RainFARM, Rebora et al. (2006a, 2006b)) has been used in many applications [Silvestro and Rebora (2014)]. Its workflow follows, in brief, the following steps: i) the rainfall field predicted by the NWP model is aggregated at spatial and time scales (hereafter L_r and t_r) which are considered averagely reliable ii) the aggregated rainfall field is then downscaled to spatial and time scales which are generally equal or finer than those of NWP. iii) a stochastic component allows to produce an ensemble of equi-probable rainfall scenarios. Using these equi-probable rainfall scenarios as input to the hydrological model, an ensemble of equi-probable streamflow scenarios can be obtained.

RainFARM has two parameters estimated directly from the power spectrum of the predicted rainfall field, so that they can vary for each event; the L_r and t_r values are assumed as in Davolio et al. (2015, 2017): L_r=15 km and t_r=6 hours. Each rainfall scenario has a fine spatio-temporal coherent structure, which maintains the characteristics of the NWP rainfall field in terms of i) volume of precipitation ii) spatial and time structure at the scales L_r and t_r.

Since in this study a high resolution NWP is dealt with, RainFARM has the main role to manage the uncertainty in spatial and time structure of the original QPF, consequently the final spatial and time resolution of the rainfall field is the same of the NWP, Dx=1 km, Dt=1 hour.

7.2.4 Results and validation

The first part of this section compares the results of the 3DVAR operators for reflectivity/in situ observations and assess their performances with respect to the Open Loop simulation. The overarching goal is to identify the 3DVAR operator that allows obtaining the greater improvement in terms of forecasts skills with respect to the Open Loop run. The second part focuses on the evaluation of the impact on the hydrological forecast accuracy of the best 3DVAR-driven meteorological simulation for each case study.

7.2.4.1 Meteorological evaluation of the 3dvar sensitivity

For each event, the 24 hours QPFs provided by the Open Loop run and the 3DVAR operators in rapid refresh mode are compared with the available 24-hour accumulation QPE of raingauges and Settepani radar (only for the 2014 case). However, it is important to mention that the Genoa 2014 flash flood had a peculiar spatio-temporal evolution as it was characterized by two distinct phases: one in the morning and the second in the evening, respectively. It is noteworthy to remember that the second phase of the event was completely missed by the operational models and also by several WRF hindcast simulations in Open Loop mode [Fiori et al. (2017), Lagasio et al. (2017)]. Thus, for this case study, in addition to the 24-hous QPFs, have been evaluated also the 12-hours QPFs of the morning (00-12UTC) and the afternoon (12-24UTC). Chronologically, the first event to happen is the Cinque Terre flash flood on 25 October 2011, when up to 470 mm of rainfall were observed in 24 hours (Figure 33, Panel a). Figure 33 shows a general good agreement of all the simulations (as well as the Open Loop, in Panel b) with respect to the observed rain map, despite the forecasts misplaced and underestimated the precipitation peak recorded.

To offer a quantitative estimation of the sensitivity experiments performances, a spatial and statistical evaluation is performed through the use of MODE (see Chapter 5): two rainfall accumulations thresholds, respectively of 72 mm and 96 mm over 24 hours, are adopted to compare the QPE and the QPFs. The use of the rainfall thresholds allows to isolate the intense part of the precipitation pattern and to obtain a set of comparable objects for each threshold, one in the observation field and the second in each forecast field (Figure 34).

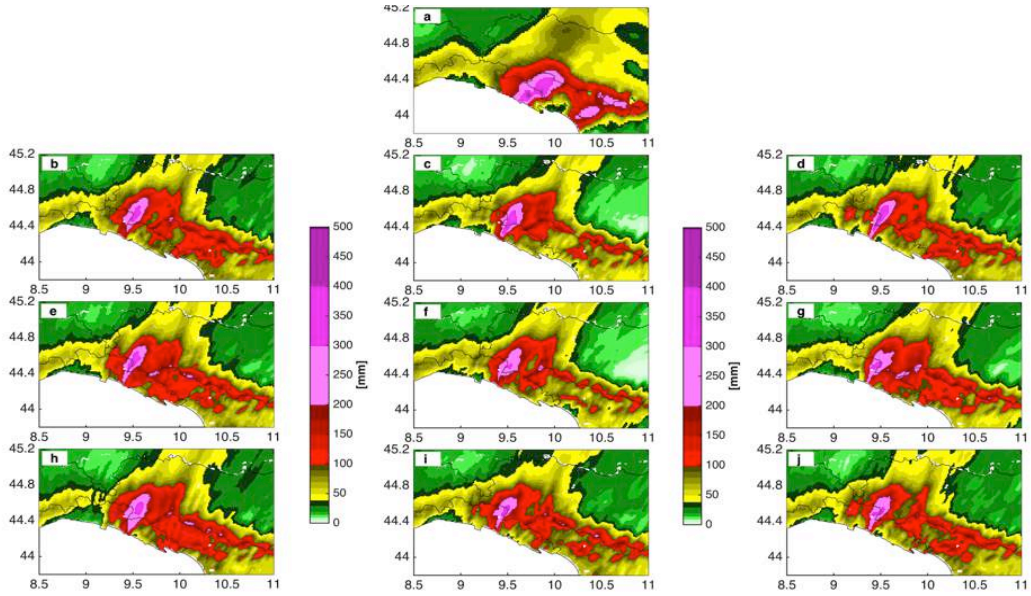

Figure 33: Comparison among the 25 October 2011 24 hours QPE from raingauges interpolation (Panel a), the Open Loop QPF (Panel b) and the QPF of each member of the sensitivity: ALL-direct (Panel c), ALL-indirect (Panel d), ALL-indirect-rqv (Panel e), Radar-direct (Panel f), Radar-direct-modif (Panel g), Radar-indirect (Panel h), Radar-indirect-rqv (Panel i) and Stations-only (Panel j).

The objects overlapping (Figure 34) confirms the general agreement between the QPFs and the QPE but highlights also the misplacing of the most intense precipitation core, located too close to the coastline by some experiments (and more prominently for the 96 mm threshold, second column in Figure 34), such as the Open Loop in Panel b, the run with indirect methods in Panels d, f, h, n, p and with stations-only data assimilation, Panel r. These first considerations are confirmed by the statistical and spatial scores calculated by MODE and

reported in Table 14. The MODE results confirm the good quality of the Open Loop run that has a PODY of about 75% for the 72 mm threshold and reveal that in general the 3DVAR best performance is obtained with the modified operator for the direct data assimilation (Radar-direct-modif) achieving the best result in 13 out of 26 scores (summing the scores for the 72 mm and the 96 mm thresholds, Table 15) followed by the ALL-direct simulation with best values in 6 scores. In this case the change in the direct reflectivity operator allowed obtaining a rainfall pattern with better shape-related parameters (CENT DIST, ANGLE DIFF, SYMM DIFF), a better agreement between forecasted rainfall points and the observed ones (CSI, HK, HSS) and a good FAR.

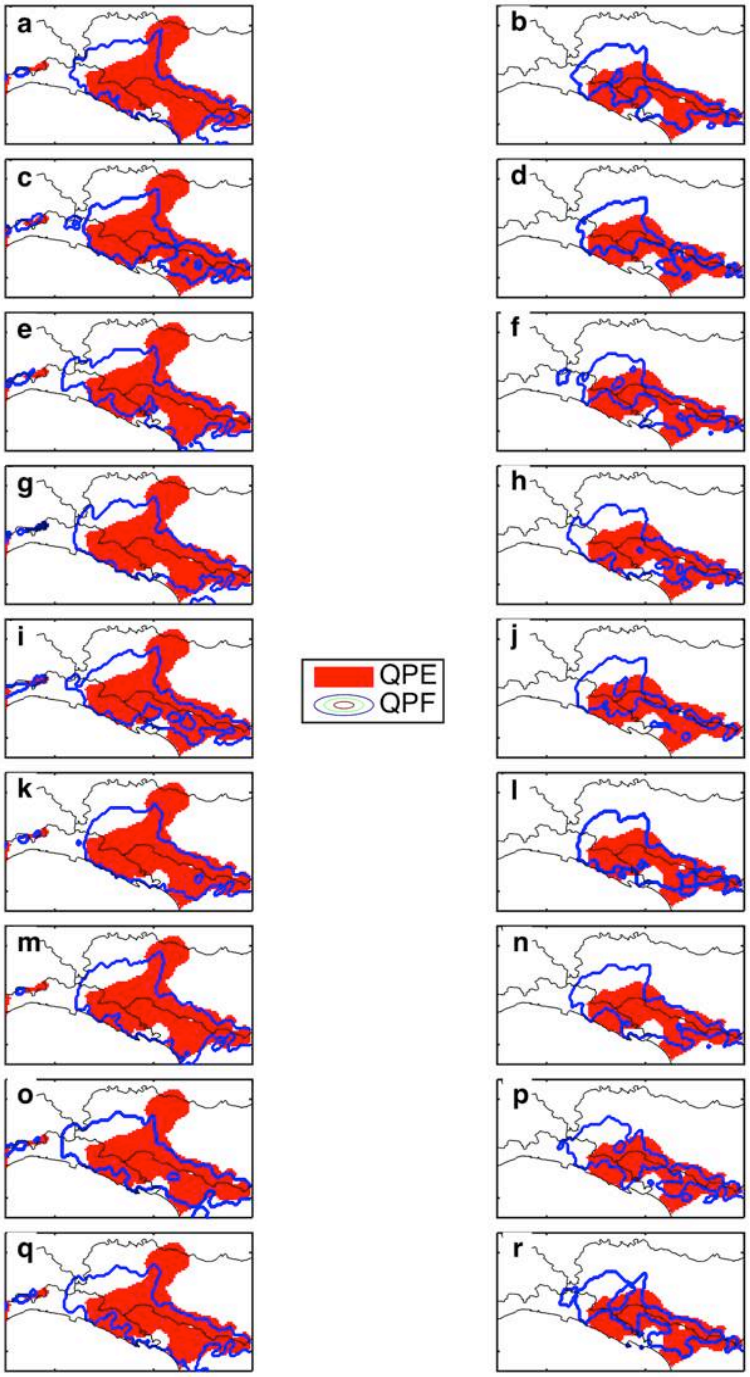

Figure 34: Representation of the objects obtained through the MODE application for the 72 mm threshold (first column) and the 96 mm threshold (second column) for the 25 October 2011, comparing in each panel the object obtained from the QPE (in solid red) with the QPFs (blue contour) for each simulation: Open Loop (Panels a, b), ALL-direct (Panels c, d), ALL-indirect (Panels e, f), ALL-indirect-rqv (Panels g, h), Radar-direct (Panels i, j), Radar-direct-modif (Panels k, l), Radar-indirect (Panels m, n), Radar-indirect-rqv (Panels o, p) and Stations-only (Panels q, r).

72mm													
run	CENTROID DIST	ANGLE DIFF	AREA RATIO	SYMMETRIC DIFF	INTERSECTION AREA	UNION AREA	P90 RATIO	FBIAS	PODY	FAR	CSI	HK	HSS
ALL-direct	9.73	2.34	0.82	1381	**1873**	3254	0.75	0.83	0.68	0.18	0.59	0.64	0.68
ALL-indirect	7.24	6.85	0.92	1421	1462	2883	0.63	1.04	0.71	0.32	0.54	0.62	0.61
ALL-indirect-rqv	6.56	2.42	**1.00**	1003	1580	2583	0.73	1.05	0.75	0.29	0.58	0.66	0.65
Radar-direct	7.03	1.95	0.84	1160	1335	2495	0.75	0.85	0.67	0.22	0.56	0.62	0.65
Radar-direct-modif	**5.08**	**0.81**	0.95	**888**	1595	2483	**0.76**	0.92	0.73	**0.20**	**0.61**	**0.68**	**0.70**
Radar-indirect	5.42	1.30	0.96	1027	1618	2645	**0.76**	**1.01**	0.75	0.26	0.59	0.68	0.67
Radar-indirect-rqv	7.00	2.94	0.92	1366	1491	2857	0.68	1.05	0.73	0.31	0.55	0.64	0.63
Stations-only	7.07	6.43	0.92	1388	1481	2869	0.64	1.03	0.71	0.31	0.54	0.63	0.62
Open Loop	5.99	5.68	0.91	1218	1585	**2803**	0.69	1.05	**0.75**	0.28	0.58	0.67	0.66
	Best small	***Best small***	***Best=1***	***Best small***	***Best big***	***Best small***	***Best=1***	***Best=1***	***Best=1***	***Best=0***	***Best=1***	***Best=1***	***Best=1***
96mm													
run	CENTROID DIST	ANGLE DIFF	AREA RATIO	SYMMETRIC DIFF	INTERSECTION AREA	UNION AREA	P90 RATIO	FBIAS	PODY	FAR	CSI	HK	HSS
ALL-direct	11.69	**4.31**	0.73	1014	657	**1671**	**0.82**	0.72	0.50	**0.30**	0.41	0.47	0.53
ALL-indirect	**7.52**	7.23	0.85	923	784	1707	0.72	0.92	0.58	0.36	0.44	0.53	0.55
ALL-indirect-rqv	10.75	3.95	0.90	905	972	1877	0.68	1.07	**0.67**	0.37	0.48	0.62	0.60
Radar-direct	14.24	4.41	0.73	1162	586	1748	0.75	0.64	0.39	0.38	0.32	0.36	0.42
Radar-direct-modif	8.58	5.66	0.92	**841**	**988**	1829	0.70	**1.00**	0.67	0.33	**0.51**	**0.62**	**0.62**
Radar-indirect	9.40	5.61	0.87	980	960	1940	0.73	1.09	0.67	0.39	0.47	0.61	0.58
Radar-indirect-rqv	10.02	4.65	0.95	1008	812	1820	0.68	1.00	0.61	0.38	0.44	0.56	0.56
Stations-only	10.54	6.01	0.87	1067	729	1796	0.68	0.93	0.55	0.41	0.40	0.49	0.51
Open Loop	8.75	7.19	**0.99**	996	859	1855	0.69	0.99	0.62	0.38	0.45	0.56	0.56
	Best small	**Best small**	**Best=1**	**Best small**	**Best big**	**Best small**	**Best=1**	**Best=1**	**Best=1**	**Best=0**	**Best=1**	**Best=1**	**Best=1**

Table 14: Spatial and statistical indices calculated through MODE to evaluate the sensitivity forecasts with respect to the Open Loop run for the Cinque Terre extreme event of 25 October 2011. The best performance for each score is highlighted in bold.

72 mm	96mm	TOT	
1	4	5	ALL-direct
0	1	1	ALL-indirect
1	1	2	ALL-indirect-rqv
0	0	0	Radar-direct
8	**6**	**14**	Radar-direct-modif
2	0	2	Radar-indirect
0	0	0	Radar-indirect-rqv
0	0	0	Stations-only
2	1	3	Open Loop

Table 15: Summary of the sensitivity performances: the times in which each forecast has the best result for each score is counted for each threshold and summarized in a total count that is used to find the best simulation for the Cinque Terre 2011 event.

The second event here considered is the Genoa flash-flood of 4 November 2011 that recorded about 450 mm of precipitation in the central hours (9-15UTC) of the day (Figure 35, Panel a) on the Bisagno catchment (black bold contour in all Panels of Figure 35).

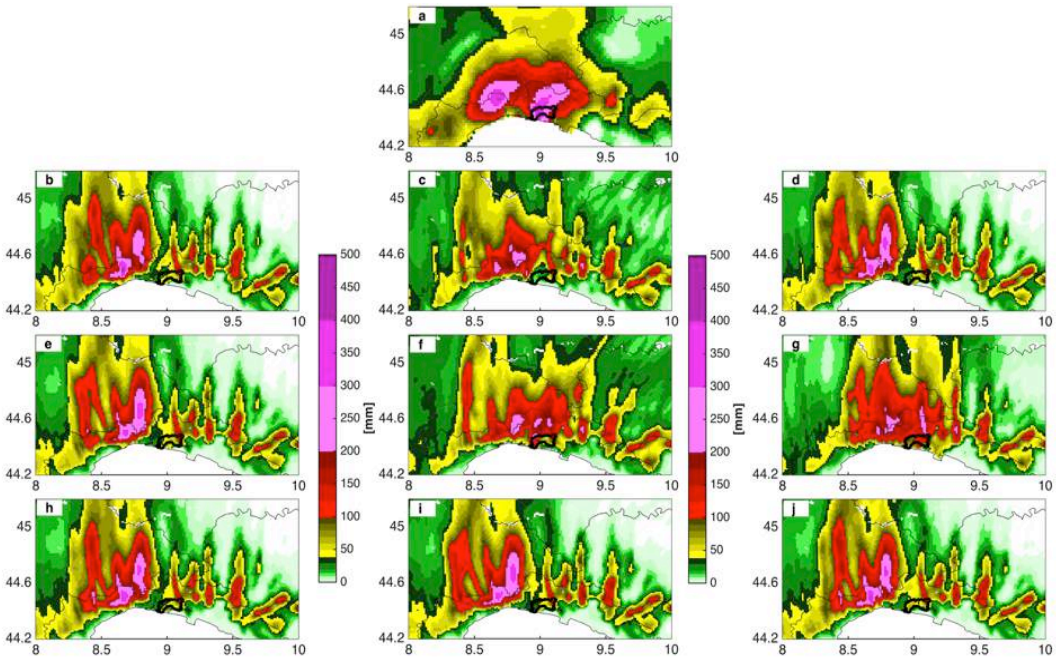

Figure 35: Comparison among the 4 November 2011 24 hours QPE from raingauges interpolation (Panel a), the Open Loop QPF (Panel b) and the QPF of each member of the sensitivity: ALL-direct (Panel c), ALL-indirect (Panel d), ALL-indirect-rqv (Panel e), Radar-direct (Panel f), Radar-direct-modif (Panel g), Radar-indirect (Panel h), Radar-indirect-rqv (Panel i) and Stations-only (Panel j). Black bold contour highlights the Bisagno catchment subjected to the flood.

In this case the Open Loop run (Figure 35, Panel b) shows a good agreement in terms of rainfall peaks but the most intense core of the precipitation pattern is again misplaced: the higher QPF value within the Bisagno catchment is less than 100 mm (dark yellow color). This behavior does not change with the stations-only sensitivity experiment (Figure 35, Panel j) nor using the indirect reflectivity operator (Figure 35, Panels d, h) also in combination with the in-cloud humidity operator (Figure 35, Panels e, i). Conversely, the use of the direct assimilation of radar reflectivity alone (Figure 35, panels f, g) improves the improves the rainfall pattern as the areal averaged QPF over the Bisagno catchment increases significantly of about 150-200 mm. These considerations are confirmed by the QPE and QPFs comparison using MODE with both 72 and 96 mm thresholds (Figure 36): indeed, the use of the direct data assimilation with radar alone allows to obtain a better localization (Figure 36, Panels i, j, k, l) of the precipitation maxima.

Furthermore, MODE statistical scores show that the direct assimilation with the modified reflectivity operator significantly enhanced the PODY and HSS, still ranking amongst the best performing experiments in terms of FAR (Table 16). The improvement is visible also in spatial scores such as CENT DIST (especially for the 96 mm threshold), AREA RATIO and INT AREA (Table 16). The summary in Table 17 upholds the first qualitative evaluation as the Radar-direct-modif achieved the best results on 15 out of 26 scores, while the others simulations equally shared the remainders.

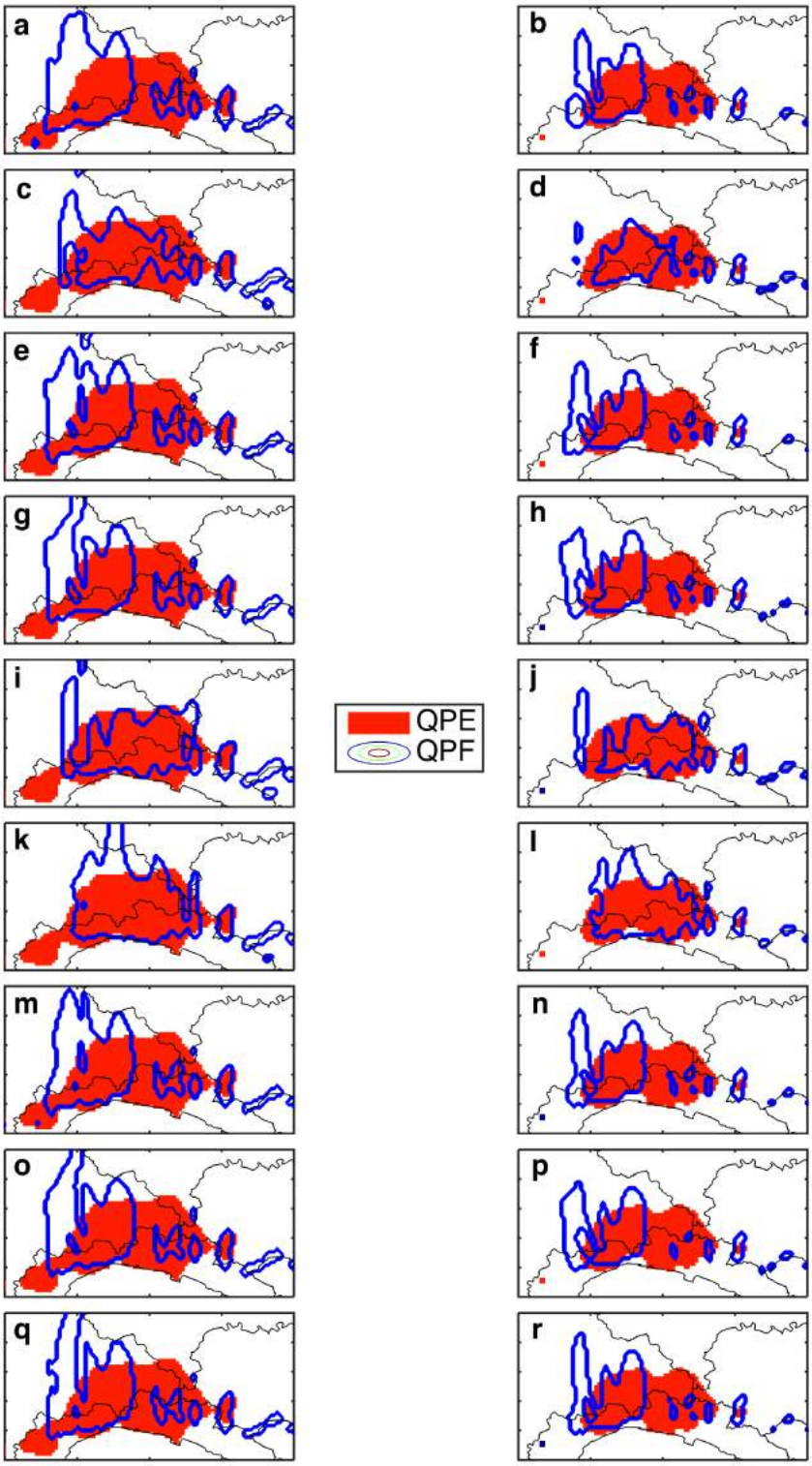

Figure 36: Representation of the objects obtained through the MODE application for the 72 mm threshold (first column) and the 96 mm threshold (second column) for the 4 November 2011 event, comparing in each panel the object obtained from the QPE (in solid red) with the QPFs (blue contour) for each simulation: Open Loop (Panels a, b), ALL-direct (Panels c, d), ALL-indirect (Panels e, f), ALL-indirect-rqv (Panels g, h), Radar-direct (Panels i, j), Radar-direct-modif (Panels k, l), Radar-indirect (Panels m, n), Radar-indirect-rqv (Panels o, p) and Stations-only (Panels q, r).

72mm													
run	CENTROID DIST	ANGLE DIFF	AREA RATIO	SYMMETRIC DIFF	INTERSECTION AREA	UNION AREA	P90 RATIO	FBIAS	PODY	FAR	CSI	HK	HSS
ALL-direct	**2.94**	20.99	0.65	740	628	**1368**	0.72	0.82	0.50	0.39	0.38	0.47	0.50
ALL-indirect	13.17	**3.58**	0.87	1141	655	1796	0.74	0.94	0.49	0.48	0.34	0.44	0.45
ALL-indirect-rqv	13.84	9.42	0.97	1320	628	1948	0.73	0.96	0.47	0.51	0.32	0.42	0.42
Radar-direct	4.31	16.44	0.76	**617**	757	1374	0.70	0.94	0.60	0.36	0.45	0.56	0.58
Radar-direct-modif	7.52	45.95	0.97	660	**858**	1518	0.67	1.06	**0.68**	**0.36**	**0.49**	**0.63**	**0.62**
Radar-indirect	12.84	9.20	0.96	1222	670	1892	0.73	0.94	0.50	0.46	0.35	0.45	0.47
Radar-indirect-rqv	13.95	10.36	**1.00**	1316	650	1966	0.74	**0.99**	0.49	0.51	0.33	0.43	0.43
Stations-only	11.77	44.03	0.86	1084	580	1664	**0.76**	0.94	0.49	0.48	0.33	0.43	0.44
Open Loop	12.64	3.87	0.92	1162	675	1837	0.72	0.98	0.51	0.48	0.35	0.45	0.46
	Best small	***Best small***	***Best=1***	***Best small***	***Best big***	***Best small***	***Best=1***	***Best=1***	***Best=1***	***Best=0***	***Best=1***	***Best=1***	***Best=1***
96mm													
run	CENTROID DIST	ANGLE DIFF	AREA RATIO	SYMMETRIC DIFF	INTERSECTION AREA	UNION AREA	P90 RATIO	FBIAS	PODY	FAR	CSI	HK	HSS
ALL-direct	2.98	11.12	0.53	529	355	884	0.71	0.61	0.44	**0.28**	0.37	0.43	0.52
ALL-indirect	9.13	9.31	0.67	701	327	1028	0.82	0.82	0.40	0.51	0.28	0.38	0.41
ALL-indirect-rqv	**2.16**	9.40	0.46	577	298	**875**	0.94	0.83	0.38	0.54	0.26	0.35	0.38
Radar-direct	9.21	9.15	0.68	430	464	894	0.69	0.86	0.58	0.32	0.46	0.56	0.60
Radar-direct-modif	2.16	13.11	**0.93**	**384**	**587**	971	**0.66**	**1.02**	**0.72**	0.29	**0.56**	**0.70**	**0.70**
Radar-indirect	8.98	10.11	0.69	679	340	1019	0.83	0.81	0.42	0.48	0.30	0.39	0.43
Radar-indirect-rqv	10.49	10.77	0.69	740	313	1053	0.86	0.86	0.39	0.55	0.26	0.36	0.38
Stations-only	9.37	10.66	0.67	680	335	1015	0.84	0.81	0.41	0.49	0.30	0.39	0.42
Open Loop	9.32	**8.07**	0.70	679	347	1026	0.80	0.83	0.43	0.48	0.31	0.40	0.44
	Best small	***Best small***	***Best=1***	***Best small***	***Best big***	***Best small***	***Best=1***	***Best=1***	***Best=1***	***Best=0***	***Best=1***	***Best=1***	***Best=1***

Table 16: Spatial and statistical indices calculated through MODE to evaluate the sensitivity forecasts with respect to the Open Loop run for the Genoa extreme event of 4 November 2011. The best performance for each score is highlighted in bold.

72 mm	96mm	TOT	
2	1	3	ALL-direct
1	0	1	ALL-indirect
0	2	2	ALL-indirect-rqv
1	0	1	Radar-direct
6	**9**	**15**	Radar-direct-modif
0	0	0	Radar-indirect
2	0	2	Radar-indirect-rqv
1	0	1	Stations-only
0	1	1	Open Loop

Table 17: Summary of the sensitivity performances: the times in which each forecast has the best result for each score is counted for each threshold and summarized in a total count that is used to find the best simulation for the Genoa 2011 event.

The third test case regards the Genoa 2014 flash flood, when again more than 400 mm of precipitation was recorded in a day. The QPE from Settepani radar is available for this event, and it is then used to gain a deeper understanding of the rainfall patterns over the sea [Fiori et al. (2017)]. From the rainfall daily accumulation it is possible to infer the significant underestimation of the Open Loop run (Figure 37, panel b). All the tested 3DVAR operators improve the precipitation volumes, despite in some cases the results are affected by an inland QPF overestimation downshear the Apennines (see upper right corner of Panels c, e, f and i in Figure 37).

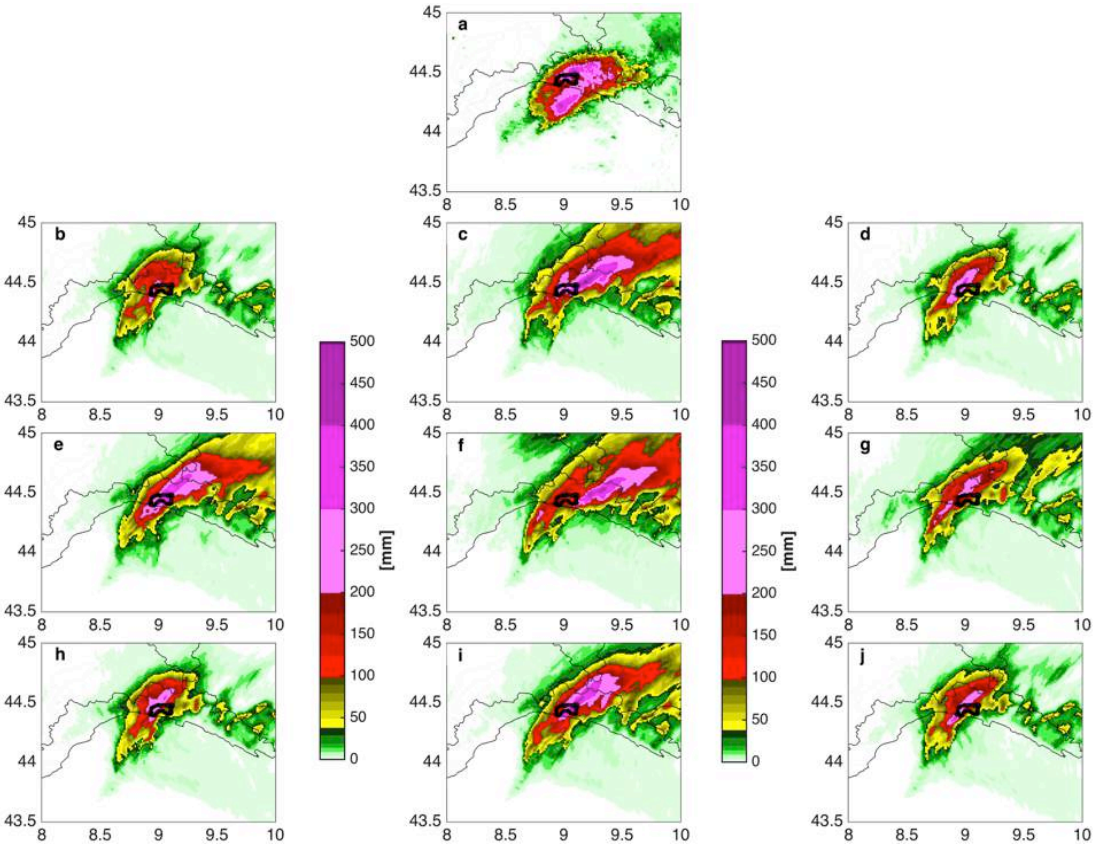

Figure 37: Comparison among the 9 October 2014 24 hours QPE from Settepani radar (Panel a), the Open Loop QPF (Panel b) and the QPF of each member of the sensitivity: ALL-direct (Panel c), ALL-indirect (Panel d), ALL-indirect-rqv (Panel e), Radar-direct (Panel f), Radar-direct-modif (Panel g), Radar-indirect (Panel h), Radar-indirect-rqv (Panel i) and Stations-only (Panel j). Black bold contour highlight the Bisagno catchment hit subjected to the flood.

When the two distinct phases of the event are addressed separately, both the object comparison (Figure 38) and MODE scores showed (Table 18) a general good agreement in terms of QPFs pattern and volumes for the 00-12 UTC period (Figure 39). Yet, a clearly better run does not stand out: for example, the Radar-indirect-rqv has a good POD but the ALL-indirect has the best FAR. Furthermore, Figure 38 reveals a slightly underestimation in term of spatial extent and orientation (major axis of the structure) by the majority of 3DVAR sensitivity experiments. This behavior is improved by Radar-indirect-rqv simulation (Figure 38, Panels o,p) that has the best CENT DIST for both thresholds and the best AREA RATIO for the 96 mm threshold (Table 18).

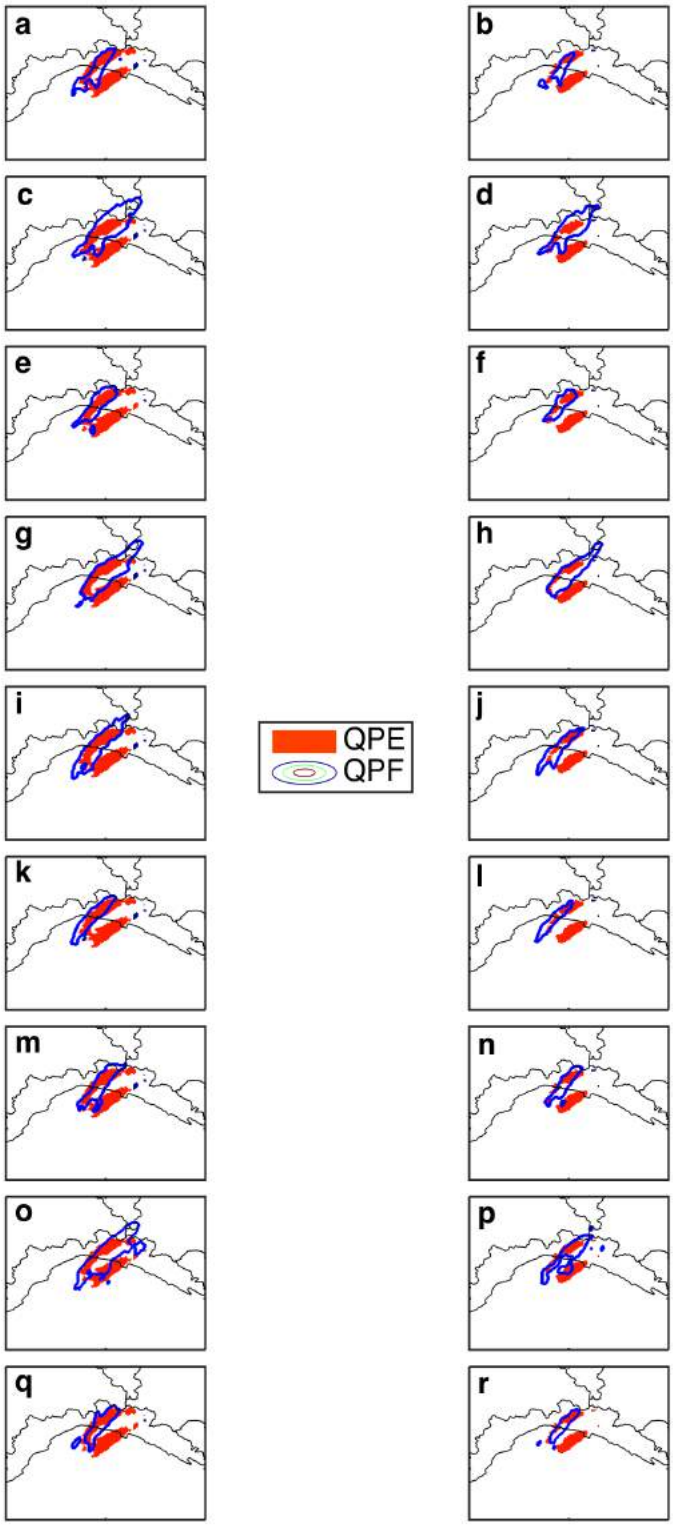

Figure 38: Representation of the objects obtained through the MODE application for the 72 mm threshold (first column) and the 96 mm threshold (second column) for the 00-12 UTC cumulated rainfall of 9 October 2014 event, comparing in each panel the object obtained from the QPE (in solid red) with the QPFs (blue contour) for each simulation: Open Loop (Panels a, b), ALL-direct (Panels c, d), ALL-indirect (Panels e, f), ALL-indirect-rqv (Panels g, h), Radar-direct (Panels i, j), Radar-direct-modif (Panels k, l), Radar-indirect (Panels m, n), Radar-indirect-rqv (Panels o, p) and Stations-only (Panels q, r).

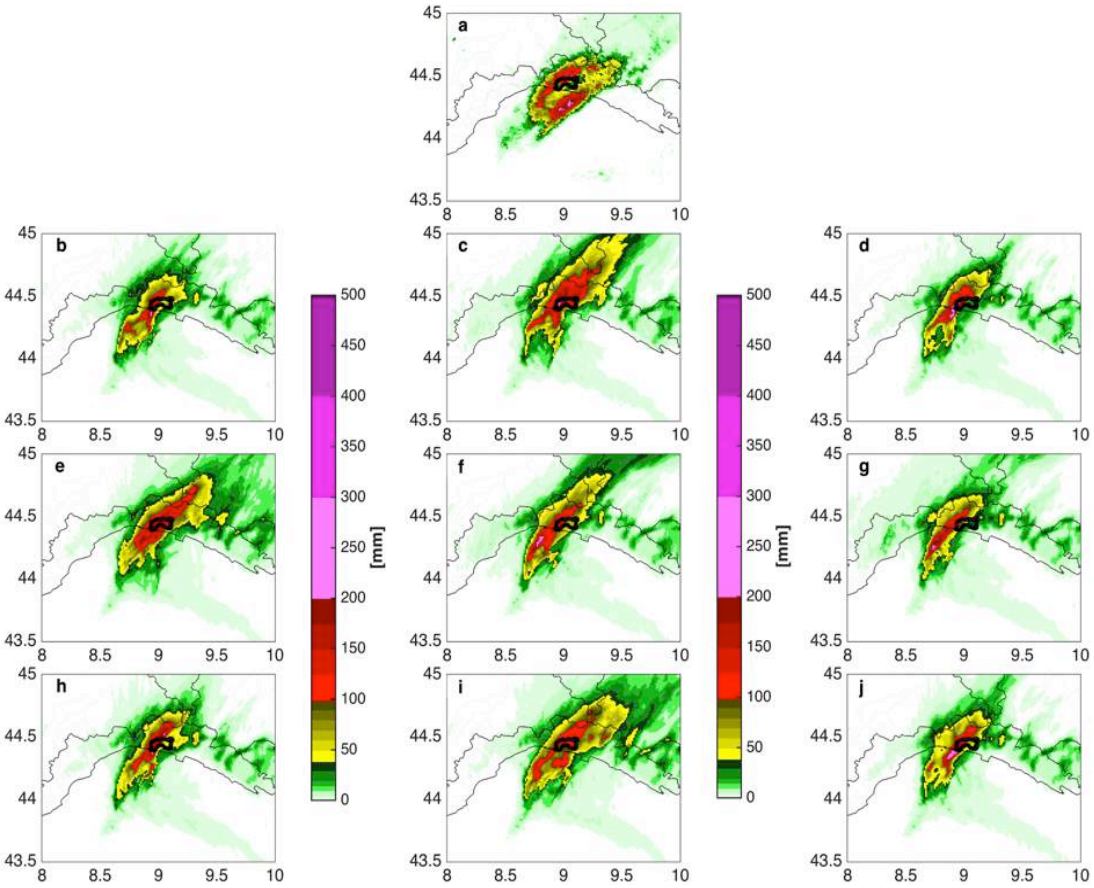

Figure 39: Comparison among the 9 October 2014 12 hours (00-12 UTC) QPE from Settepani radar (Panel a), the Open Loop QPF (Panel b) and the QPF of each member of the sensitivity: ALL-direct (Panel c), ALL-indirect (Panel d), ALL-indirect-rqv (Panel e), Radar-direct (Panel f), Radar-direct-modif (Panel g), Radar-indirect (Panel h), Radar-indirect-rqv (Panel i) and Stations-only (Panel j). Black bold contour highlight the Bisagno catchment hit subjected to the flood.

72mm													
run	CENTROID DIST	ANGLE DIFF	AREA RATIO	SYMMETRIC DIFF	INTERSECTION AREA	UNION AREA	P90 RATIO	FBIAS	PODY	FAR	CSI	HK	HSS
ALL-direct	15.80	7.44	0.81	1090	452	1542	1.01	1.18	0.48	0.59	0.29	0.48	0.44
ALL-indirect	8.96	4.00	0.53	**723**	350	1073	1.14	0.53	0.37	**0.29**	0.32	0.37	0.49
ALL-indirect-rqv	11.05	7.24	**0.93**	931	478	1409	0.94	**1.05**	0.51	0.51	0.33	0.51	0.50
Radar-direct	7.31	2.17	0.86	808	442	1250	0.88	0.84	0.47	0.44	**0.35**	0.47	**0.51**
Radar-direct-modif	10.60	4.22	0.52	769	292	1061	1.08	0.49	0.31	0.37	0.26	0.31	0.42
Radar-indirect	**6.73**	1.97	0.60	748	351	1099	**1.07**	0.58	0.38	0.35	0.31	0.37	0.47
Radar-indirect-rqv	7.90	5.48	0.82	1002	**505**	1507	0.72	1.26	**0.54**	0.57	0.32	**0.54**	0.48
Stations-only	7.56	1.92	0.48	695	315	**1010**	1.13	0.50	0.34	0.32	0.29	0.34	0.45
Open Loop	7.70	**0.36**	0.52	781	298	1079	0.92	0.50	0.32	0.37	0.27	0.32	0.42
	Best small	***Best small***	***Best=1***	***Best small***	***Best big***	***Best small***	***Best=1***	***Best=1***	***Best=1***	***Best=0***	***Best=1***	***Best=1***	***Best=1***

96mm													
run	CENTROID DIST	ANGLE DIFF	AREA RATIO	SYMMETRIC DIFF	INTERSECTION AREA	UNION AREA	P90 RATIO	FBIAS	PODY	FAR	CSI	HK	HSS
ALL-direct	14.12	23.71	0.70	770	**229**	999	0.95	1.40	**0.44**	0.68	0.23	**0.44**	0.37
ALL-indirect	9.35	19.46	0.62	**474**	172	646	1.08	0.61	0.33	**0.45**	0.26	0.33	0.41
ALL-indirect-rqv	11.77	25.05	0.78	745	206	951	0.89	1.26	0.40	0.68	0.21	0.40	0.35
Radar-direct	7.96	21.57	0.83	552	186	738	0.92	0.81	0.36	0.56	0.25	0.36	0.40
Radar-direct-modif	11.10	21.38	0.55	516	135	651	**1.01**	0.54	0.26	0.52	0.20	0.26	0.34
Radar-indirect	7.95	15.74	0.66	496	172	668	1.02	0.65	0.33	0.49	0.25	0.33	0.40
Radar-indirect-rqv	**5.60**	22.49	**0.99**	579	219	798	0.68	**1.02**	0.43	0.58	**0.27**	0.42	**0.42**
Stations-only	8.22	18.73	0.51	**474**	145	**619**	1.13	0.52	0.28	0.46	0.23	0.28	0.37
Open Loop	6.08	**7.36**	0.40	532	89	621	0.98	0.45	0.17	0.62	0.13	0.17	0.24
	Best small	***Best small***	***Best=1***	***Best small***	***Best big***	***Best small***	***Best=1***	***Best=1***	***Best=1***	***Best=0***	***Best=1***	***Best=1***	***Best=1***

Table 18 Spatial and statistical indices calculated through MODE to evaluate the sensitivity forecasts with respect to the Open Loop run for the first phase (00-12 UTC) of the Genoa extreme event of 9 October 2014. The best performance for each score is highlighted in bold.

In the second phase of the event (12-24 UTC) the different simulations show rather erratic performances (Figure 40). The Open Loop run (Figure 40, Panel b) does not reproduce the intensity nor the location of the event, as inside the Bisagno catchment the rainfall peak is about 70 mm with respect to the 250 mm observed. Instead, in 4 data assimilation options out of 8, there is a significant improvement in terms of QPF performances (Figure 40, Panels c - ALL-direct, e - ALL-indirect-rqv, f - Radar-direct e i - Radar-indirect-rqv) with even a good localization of the most intense part of event (Figure 40, Panels c - ALL-direct, i - Radar-indirect-rqv) and peaks of more than 200 mm within the Bisagno catchment. Yet an overestimation downshear the Apennines is more persisting in the ALL-direct and Radar-direct run than in the ALL-indirect-rqv and Radar-indirect-rqv (Figure 40, Panels c - ALL-direct, e - ALL-indirect-rqv, f - Radar-direct, i - Radar-indirect-rqv).

The object comparison (Figure 41) reveals that despite a significant improvement in QPF forecast for most of the 3DVAR sensitivity experiments of the inland portion of the rainfall, a reliable reproduction of the event over the sea area is still missed out, being the pattern more shifted landwards (Figure 41, Panels c, d - ALL-direct, g, h - ALL-indirect-rqv, i, j - Radar-direct, o, p - Radar-indirect-rqv). Nevertheless 3DVAR outperforms the Open Loop run that in turn does not exceed or even reach the 96 mm threshold in any point of the domain (Figure 41, Panel b). The reflectivity assimilation allowed to maintain a significant amount of precipitation on the coastline also when considering the 96 mm threshold, while the runs using the in-cloud humidity estimation (ALL-

indirect-rqv in Panels g, h and Radar-indirect-rqv in Panels o, p of Figure 41) largely decrease the overestimation downshear the Apennines.

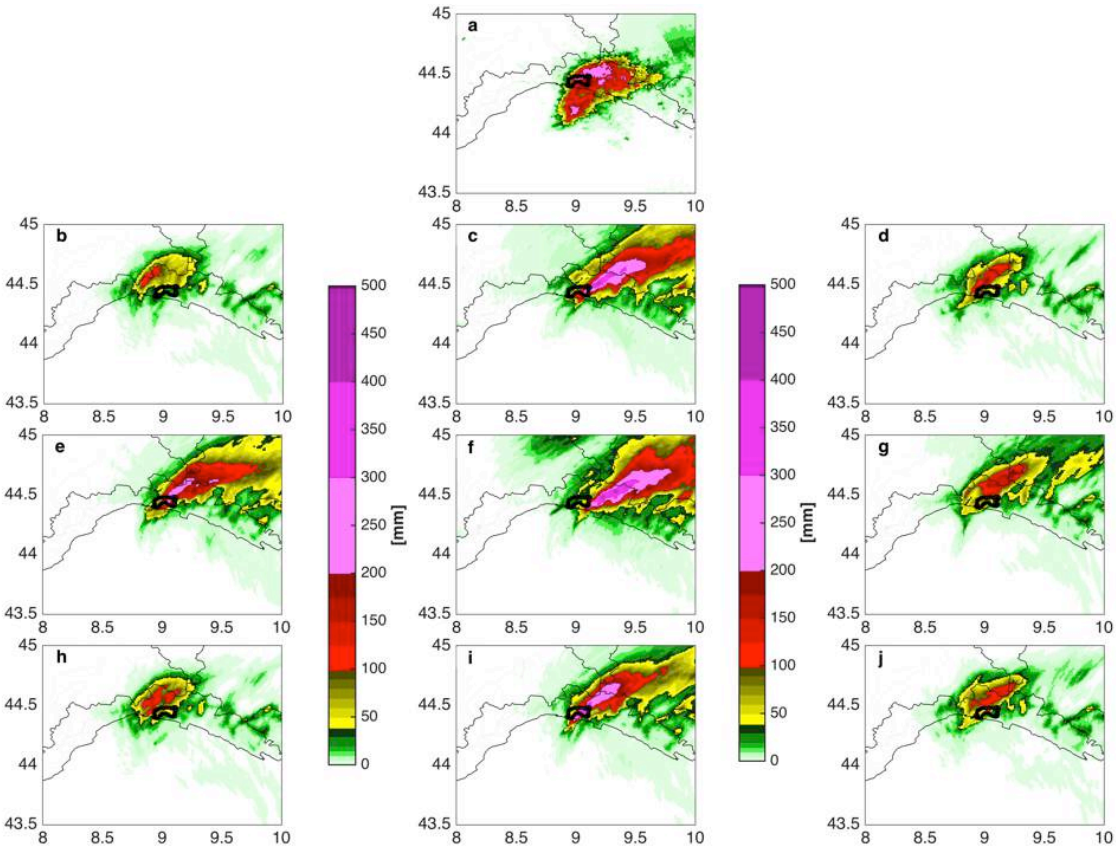

Figure 40: Comparison among the 9 October 2014 12 hours (12-24 UTC) QPE from Settepani radar (Panel a), the Open Loop QPF (Panel b) and the QPF of each member of the sensitivity: ALL-direct (Panel c), ALL-indirect (Panel d), ALL-indirect-rqv (Panel e), Radar-direct (Panel f), Radar-direct-modif (Panel g), Radar-indirect (Panel h), Radar-indirect-rqv (Panel i) and Stations-only (Panel j). Black bold contour highlight the Bisagno catchment hit subjected to the flood.

The qualitative considerations provided by the object maps comparison in Figure 41 is quantitatively confirmed by the scores computed by MODE (Table 19) where the Radar-indirect-rqv outperforms the others simulations especially in terms of statistical scores (POD, FAR, CSI, HK, HSS) for both thresholds (Table 19) with a good overlap of the objects area (INTER AREA, Table 19). Furthermore the reduced overestimation downshear the Apennines, and the

best localization of the precipitation pattern are confirmed by a lower FAR (Table 19).

Overall, considering the 24-hour cumulated rainfall (Figure 37), the Radar-indirect-rqv is the best performing experiment, particularly for the highest threshold (Table 20). Indeed, the objects comparison highlights that the Radar-indirect-rqv simulation better reproduces the event, both in terms of cumulated rainfall (Figure 37) and precipitation pattern orientation (Figure 42, Panels o, p) with respect to the Open Loop run (Figure 42, Panels a, b).

The Radar-indirect-rqv experiment has the best POD for the 96 mm threshold, providing the best localization for the most intense precipitation core. Furthermore, despite the overestimation on the Apennines, the Radar-indirect-rqv experiment has acceptable FAR values with respect to the run using the direct assimilation with the standard reflectivity operator. Conversely, the Radar-direct-modified experiment is the only one removing the large downshear overestimation that affects the other runs adopting direct method, i.e. it shows one of the lowest FAR for the second phase and a better FBIAS (Table 19). This consideration holds when considering the whole 24-hour cumulated rainfall (Table 20) even if the misplacing of the pattern in Figure 42 is to be accounted for the poor results of PODY and HSS with respect to the run using the indirect method, (Table 19, Table 20).

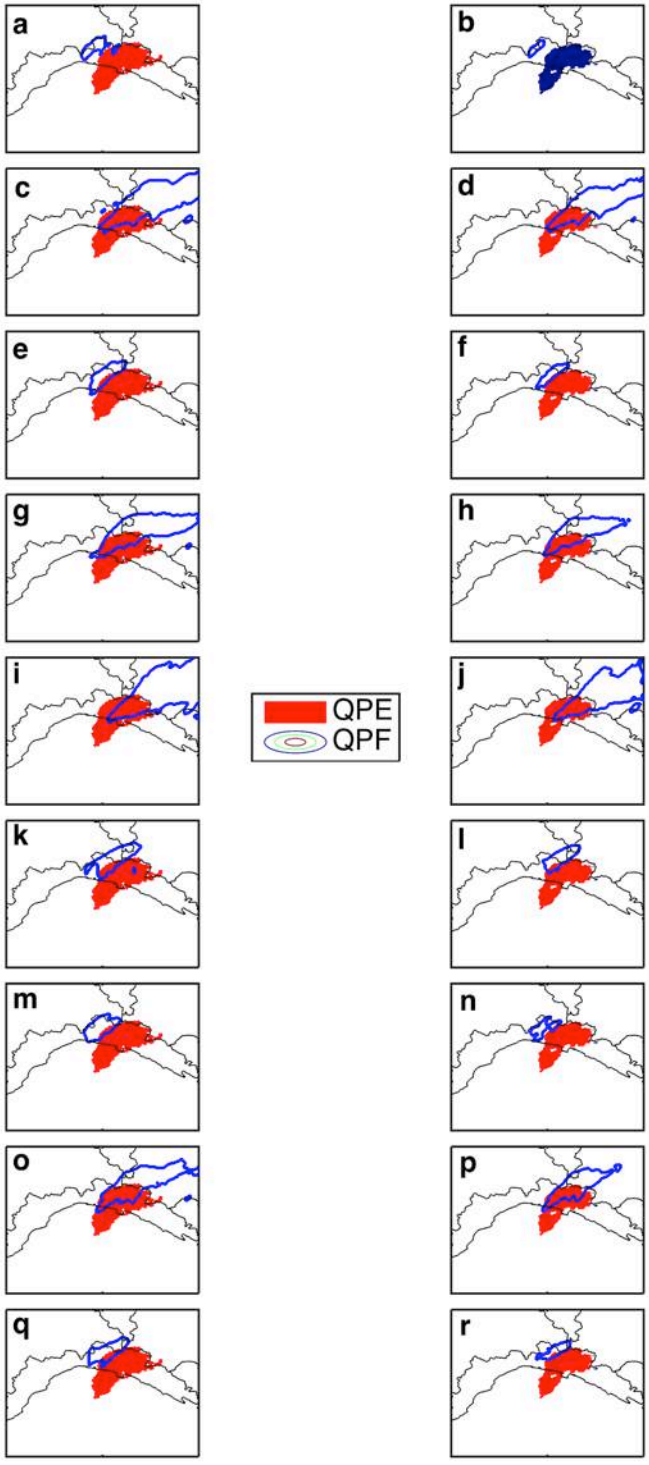

Figure 41: Representation of the objects obtained through the MODE application for the 72 mm threshold (first column) and the 96 mm threshold (second column) for the 12-24 UTC cumulated rainfall of 9 October 2014 event, comparing in each panel the object obtained from the QPE (in solid red) with the QPFs (blue contour) for each simulation: Open Loop (Panels a, b), ALL-direct (Panels c, d), ALL-indirect (Panels e, f), ALL-indirect-rqv (Panels g, h), Radar-direct (Panels i, j), Radar-direct-modif (Panels k, l), Radar-indirect (Panels m, n), Radar-indirect-rqv (Panels o, p) and Stations-only (Panels q, r).

72mm													
run	CENTROID DIST	ANGLE DIFF	AREA RATIO	SYMMETRIC DIFF	INTERSECTION AREA	UNION AREA	P90 RATIO	FBIAS	PODY	FAR	CSI	HK	HSS
ALL-direct	44.98	11.21	0.58	2981	528	3509	1.17	1.75	0.36	0.80	0.15	0.34	0.25
ALL-indirect	19.77	8.17	0.29	1734	91	1825	0.64	0.29	0.06	0.79	0.05	0.06	0.09
ALL-indirect-rqv	32.99	19.65	0.80	2380	482	2862	0.88	1.26	0.33	0.74	0.17	0.32	0.28
Radar-direct	49.34	7.41	0.49	3438	523	3961	1.16	2.07	0.35	0.83	0.13	0.34	0.22
Radar-direct-modif	21.82	**2.06**	0.45	1792	180	1972	0.71	0.45	0.12	0.73	0.09	0.12	0.16
Radar-indirect	22.32	3.83	0.32	1796	84	1880	0.58	0.32	0.06	0.83	0.04	0.05	0.08
Radar-indirect-rqv	32.84	14.82	**0.90**	2036	**546**	2582	**1.07**	**1.12**	**0.37**	**0.67**	**0.21**	**0.36**	**0.34**
Stations-only	20.91	4.11	0.33	1734	117	1851	0.55	0.33	0.08	0.76	0.06	0.08	0.11
Open Loop	**16.65**	8.47	0.02	**1456**	30	**1486**	0.39	0.18	0.02	0.89	0.02	0.02	0.03
	Best small	***Best small***	***Best=1***	***Best small***	***Best big***	***Best small***	***Best=1***	***Best=1***	***Best=1***	***Best=0***	***Best=1***	***Best=1***	***Best=1***

96mm													
run	CENTROID DIST	ANGLE DIFF	AREA RATIO	SYMMETRIC DIFF	INTERSECTION AREA	UNION AREA	P90 RATIO	FBIAS	PODY	FAR	CSI	HK	HSS
ALL-direct	43.05	20.39	0.62	2150	393	2543	1.21	1.59	0.35	0.78	0.15	0.34	0.26
ALL-indirect	**18.89**	**2.43**	0.20	1297	31	1328	0.67	0.20	0.03	0.87	0.02	0.03	0.04
ALL-indirect-rqv	28.28	22.63	**0.96**	1589	355	1944	**0.89**	**1.03**	0.31	0.70	0.18	0.31	0.30
Radar-direct	45.46	17.77	0.54	2477	372	2849	1.26	1.87	0.33	0.83	0.13	0.32	0.22
Radar-direct-modif	23.21	6.61	0.36	1390	72	1462	0.71	0.36	0.06	0.82	0.05	0.06	0.09
Radar-indirect	21.17	7.29	0.20	1330	14	1344	0.61	0.20	0.01	0.94	0.01	0.01	0.02
Radar-indirect-rqv	24.02	10.49	0.84	1285	**394**	1679	1.17	0.85	**0.35**	**0.59**	**0.23**	**0.34**	**0.37**
Stations-only	19.98	15.49	0.21	**1282**	39	**1321**	0.57	0.20	0.03	0.83	0.03	0.03	0.05
Open Loop	NaN	NaN	NaN	NaN	NaN	NaN	NaN	0.08	0.00	1.00	0.00	0.00	0.00
	Best small	***Best small***	***Best=1***	***Best small***	***Best big***	***Best small***	***Best=1***	***Best=1***	***Best=1***	***Best=0***	***Best=1***	***Best=1***	***Best=1***

Table 19: Spatial and statistical indices calculated through MODE to evaluate the sensitivity forecasts with respect to the Open Loop run for the second phase (12-24 UTC) of the Genoa extreme event of 9 October 2014. The best performance for each score is highlighted in bold.

72mm													
run	CENTROID DIST	ANGLE DIFF	AREA RATIO	SYMMETRIC DIFF	INTERSECTION AREA	UNION AREA	P90 RATIO	FBIAS	PODY	FAR	CSI	HK	HSS
ALL-direct	37.85	4.32	0.52	3699	1252	4951	0.86	1.94	0.59	0.70	0.25	0.57	0.39
ALL-indirect	14.21	15.40	0.51	1888	665	**2553**	0.84	0.51	0.31	0.39	0.26	0.31	0.41
ALL-indirect-rqv	28.72	7.51	**0.70**	2667	1250	3917	**0.86**	1.47	0.59	0.60	0.31	0.57	0.47
Radar-direct	41.01	**3.00**	0.44	4176	**1407**	5583	0.75	2.34	**0.66**	0.72	0.25	**0.64**	0.38
Radar-direct-modif	14.92	9.22	0.66	2159	684	2843	0.68	**0.66**	0.32	0.51	0.24	0.32	0.38
Radar-indirect	**14.13**	20.58	0.60	**1838**	781	2619	0.76	0.60	0.37	**0.39**	0.30	0.36	0.45
Radar-indirect-rqv	26.73	3.52	0.69	2512	1364	3876	0.86	1.49	0.64	0.57	**0.34**	0.63	**0.50**
Stations-only	15.42	14.84	0.57	2004	674	2678	0.72	0.57	0.32	0.45	0.25	0.31	0.40
Open Loop	15.09	20.18	0.64	1952	768	2720	0.53	0.64	0.36	0.43	0.28	0.36	0.43
	Best small	***Best small***	***Best=1***	***Best small***	***Best big***	***Best small***	***Best=1***	***Best=1***	***Best=1***	***Best=0***	***Best=1***	***Best=1***	***Best=1***

96mm													
run	CENTROID DIST	ANGLE DIFF	AREA RATIO	SYMMETRIC DIFF	INTERSECTION AREA	UNION AREA	P90 RATIO	FBIAS	PODY	FAR	CSI	HK	HSS
ALL-direct	34.25	14.26	0.58	2802	944	3746	0.94	1.72	0.54	0.68	0.25	0.53	0.39
ALL-indirect	14.88	7.67	0.44	1720	385	**2105**	0.87	0.44	0.22	0.50	0.18	0.22	0.30
ALL-indirect-rqv	24.76	13.00	0.80	2023	936	2959	0.92	1.26	0.54	0.57	0.31	0.53	0.47
Radar-direct	34.88	12.86	0.55	2930	965	3895	0.84	1.84	0.56	0.70	0.24	0.54	0.38
Radar-direct-modif	14.80	**2.08**	0.61	1889	443	2332	0.69	0.60	0.25	0.58	0.19	0.25	0.31
Radar-indirect	**14.56**	16.90	0.51	**1691**	470	2161	0.78	0.51	0.27	**0.47**	0.22	0.27	0.35
Radar-indirect-rqv	22.21	6.62	**0.84**	1832	**972**	2804	**0.95**	**1.20**	**0.56**	0.53	**0.34**	**0.55**	**0.50**
Stations-only	15.13	10.31	0.48	1709	425	2134	0.73	0.49	0.24	0.50	0.20	0.24	0.32
Open Loop	15.13	16.57	0.48	1715	424	2139	0.53	0.48	0.24	0.49	0.20	0.24	0.32
	Best small	***Best small***	***Best=1***	***Best small***	***Best big***	***Best small***	***Best=1***	***Best=1***	***Best=1***	***Best=0***	***Best=1***	***Best=1***	***Best=1***

Table 20: Spatial and statistical indices calculated through MODE to evaluate the sensitivity forecasts with respect to the Open Loop run for the daily accumulation (00-24 UTC) of the Genoa extreme event of 9 October 2014. The best performance for each score is highlighted in bold.

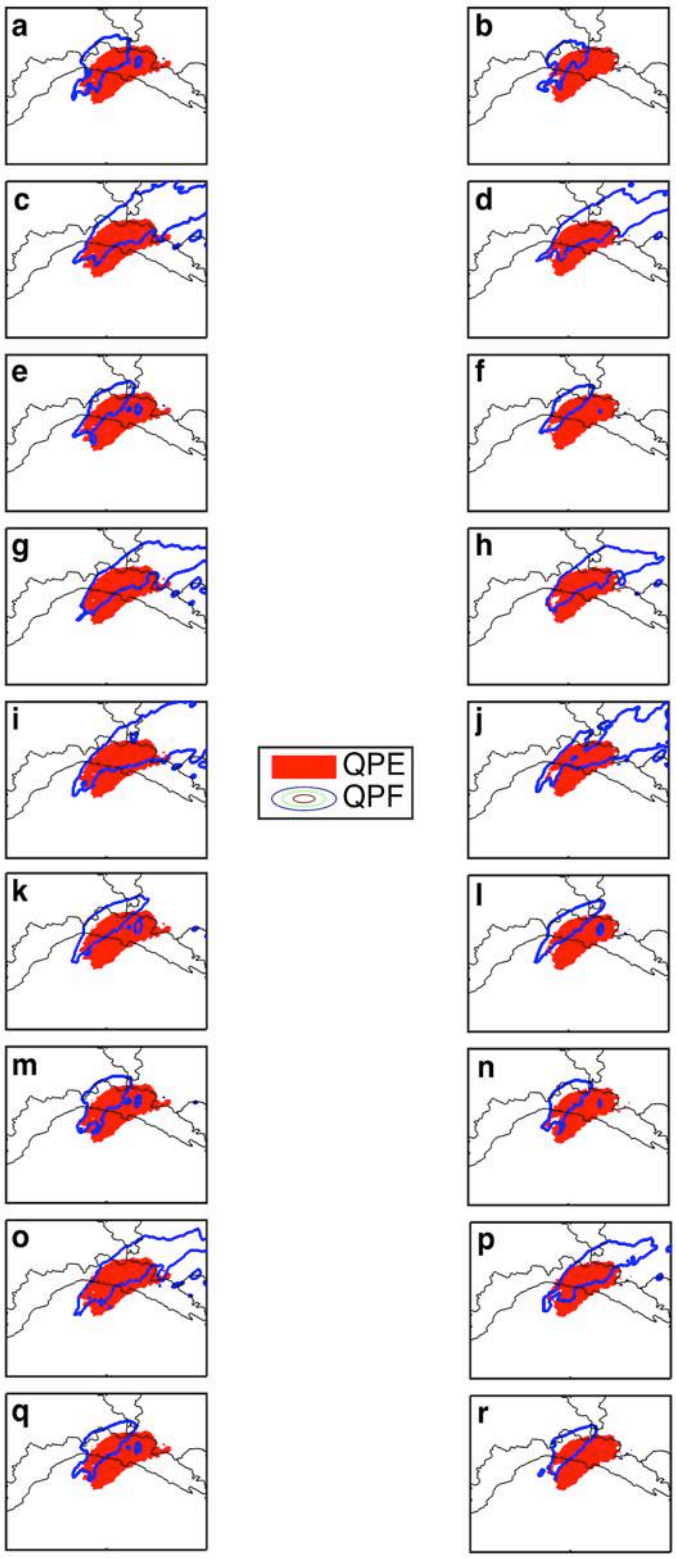

Figure 42: Representation of the objects obtained through the MODE application for the 72 mm threshold (first column) and the 96 mm threshold (second column) for the 00-24 UTC cumulated rainfall of 9 October 2014 event, comparing in each panel the object obtained from the QPE (in solid red) with the QPFs (blue contour) for each simulation: Open Loop (Panels a, b), ALL-direct (Panels c, d), ALL-indirect (Panels e, f), ALL-indirect-rqv (Panels g, h), Radar-direct (Panels i, j), Radar-direct-modif (Panels k, l), Radar-indirect (Panels m, n), Radar-indirect-rqv (Panels o, p) and Stations-only (Panels q, r).

Then, from the summary of the scores calculated for all the considered cumulated rainfall (Table 21), the Radar-indirect-rqv stands out as the best for the Genoa 2014 case.

72 mm	96mm	TOT	
0	2	2	ALL-direct
3	5	8	ALL-indirect
4	3	7	ALL-indirect-rqv
6	0	6	Radar-direct
2	2	4	Radar-direct-modif
5	3	8	Radar-indirect
14	**19**	**33**	Radar-indirect-rqv
1	4	5	Stations-only
4	1	5	Open Loop

Table 21: Summary of the sensitivity performances: the times in which each forecast has the best result for each score is counted for each threshold and summarized in a total count (summing Table 8, 9 and 10) that is used to find the best simulation for the Genoa 2014 event.

If a time frame during the second phase of the event (20 UTC) is considered, a deeper insight of the impact of the Radar-indirect-rqv data assimilation simulation with respect to the Open-Loop run (Figure 43) is gained.

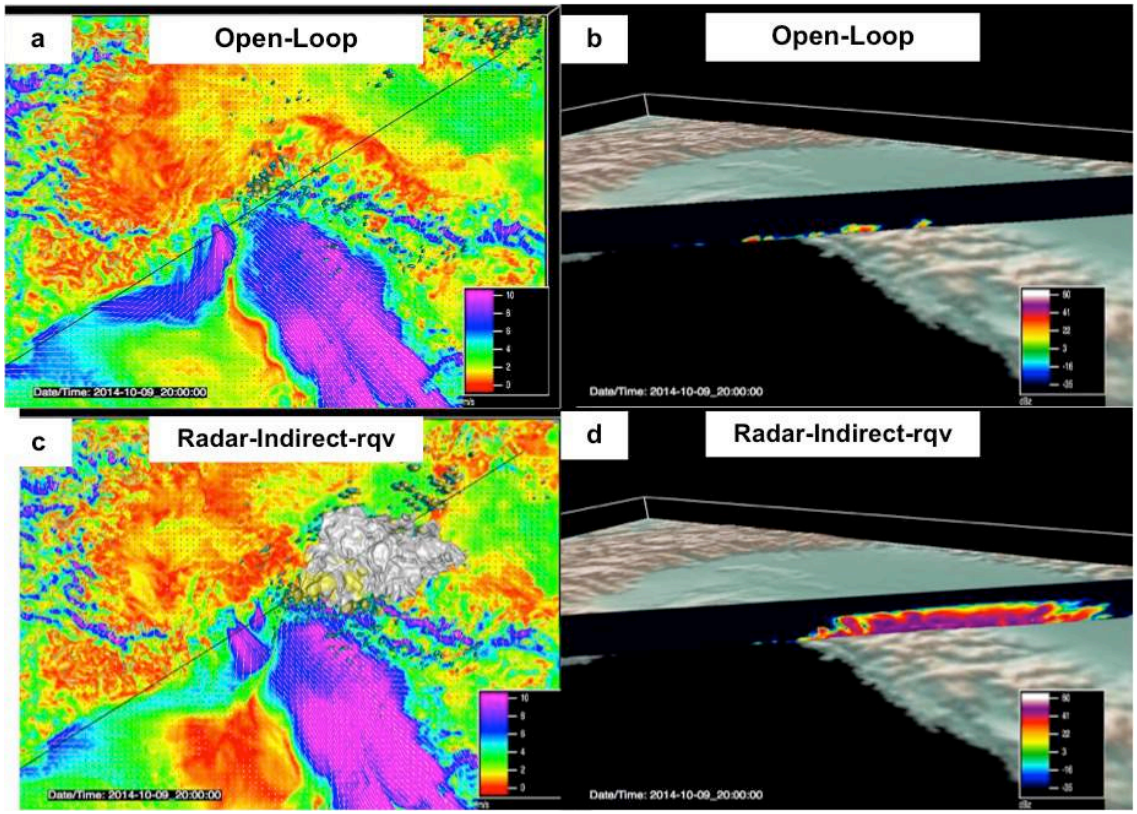

Figure 43: Comparison between the Open-Loop simulated structure with respect to the Radar-direct-rqv simulated structure at 20 UTC. Panels a and c report the 3D simulated structure composed by rainwater (cyano) graupel (yellow) and snow (grey) microphysics species respectively for Open Loop (a) and Radar-indirect-rqv (c) simulations with the horizontal 10m wind intensity for the Open Loop (a) and the Radar-indirect-rqv (c). The black line in Panels a and c indicates the location of the vertical section of the two structures to investigate the reflectivity values in the mean of the convective structure in Panels b (for Open-Loop) and d (for Radar-indirect-rqv)

The use of data assimilation actually provides an enhancement of the wind intensity (Figure 43, Panel c) supporting a more evident convergence line and in turn a more intense convection (Figure 43, Panel c). This results into the production of a widespread and more intense area of snow and graupel that were nearly absent in the Open-Loop (Figure 43, Panel a). Open-Loop (Figure 43, Panel b) has a shallower and more disorganized convective structure run while through the use of the reflectivity data assimilation (Figure 43, Panel d) a simulated deep moist and convective storm is in very good agreement with the observed one.

In conclusion, the best result for the two 2011 flash floods is achieved with the Radar-direct-modif since the modified operator takes into account also the ice species that are crucial in this kind of events [Fiori et al. (2017), Lagasio et al. (2017)]. In the 2014 flood too, this approach has a better score than standard direct assimilation. The reason might be that the isotherm was quite low-lying (about 2000-2500 m for the 2011 events and 4000 m for the 2014 flood) in comparison to the cloud top (up to 8000 m) thus the direct assimilation of the iced species actually played a role. Furthermore, for the 2014 flash flood the in-cloud humidity assimilation associated to the indirect method allows achieving the best performance both in terms of cumulated rainfall and pattern location. To better understand this difference in the results, the columnar contents of the different hydrometeors is computed with reference to a temporal snapshot during the respective main phase of these events (09 UTC for the 2011 cases and 20 UTC for the 2014 flood). Only radar reflectivity data assimilation operators are hereafter considered. The two use cases of 2011 are characterized by quite low-lying 0 °C isotherms (around 2000-2500 m). Thus, not surprisingly, for both the 25 October event (Figure 44) and the 4 November event (Figure 45), the Radar-direct-modif (Figure 44 and Figure 45 Panels c, h, m, r, w) simulations produce significant (around 8-10 mm) amounts of graupel columnar content (upshear) on the Tyrrhenian side of the Ligurian Apennines largely coinciding with large (around 4-5 mm) columnar rainwater content on the same area. The corresponding mixed-phase clouds experience a seeder-feeder mechanism in which the graupel and its falling crystals act as condensation nuclei for cloud water generation via heterogeneous nucleation, thus overall

increasing precipitating efficiency. The direct modified takes better account this phenomen with respect to the Radar_direct simulation which refers only to warm rain processes (Figure 44 and Figure 45 Panels b,g, l, q, v). The Radar-indirect (Figure 44 and Figure 45 Panels d, i, n, s, x) and Radar-indirect-rqv (Figure 44 and Figure 45 Panels e, j, o, t, y) are able to capture to some extent the same mechanism, but locate the structure in the wrong position (more evident for the 25 October event than in the 4 November case).

Concerning the 2014 event (Figure 46), the 0 °C isotherm is at about 4000 m so, thus resulting into a more “warm rain” case, at least in lower to middle troposphere, while the ice species are conversely located in the upper level of the convective anvil located downshear the Liguria Apennines. Consequently, the simulations using operators weighting more the liquid part of the structures (Radar_direct in Panels b, g, l,q, v and Radar_indirect_rqv in Panels e, j, o, t, y of Figure 46) are in a better position to capture the predominantly observed “warm rain” mechanisms. However, the Radar_direct simulation is still penalized by the aforementioned overestimation downshear that is mitigated by the use of the Radar_direct_modif (Figure 46 Panels c, h, m, r, w).

In the next section these best runs will be evaluated in terms of hydrological impact improvement with respect to their associated Open-Loop simulations.

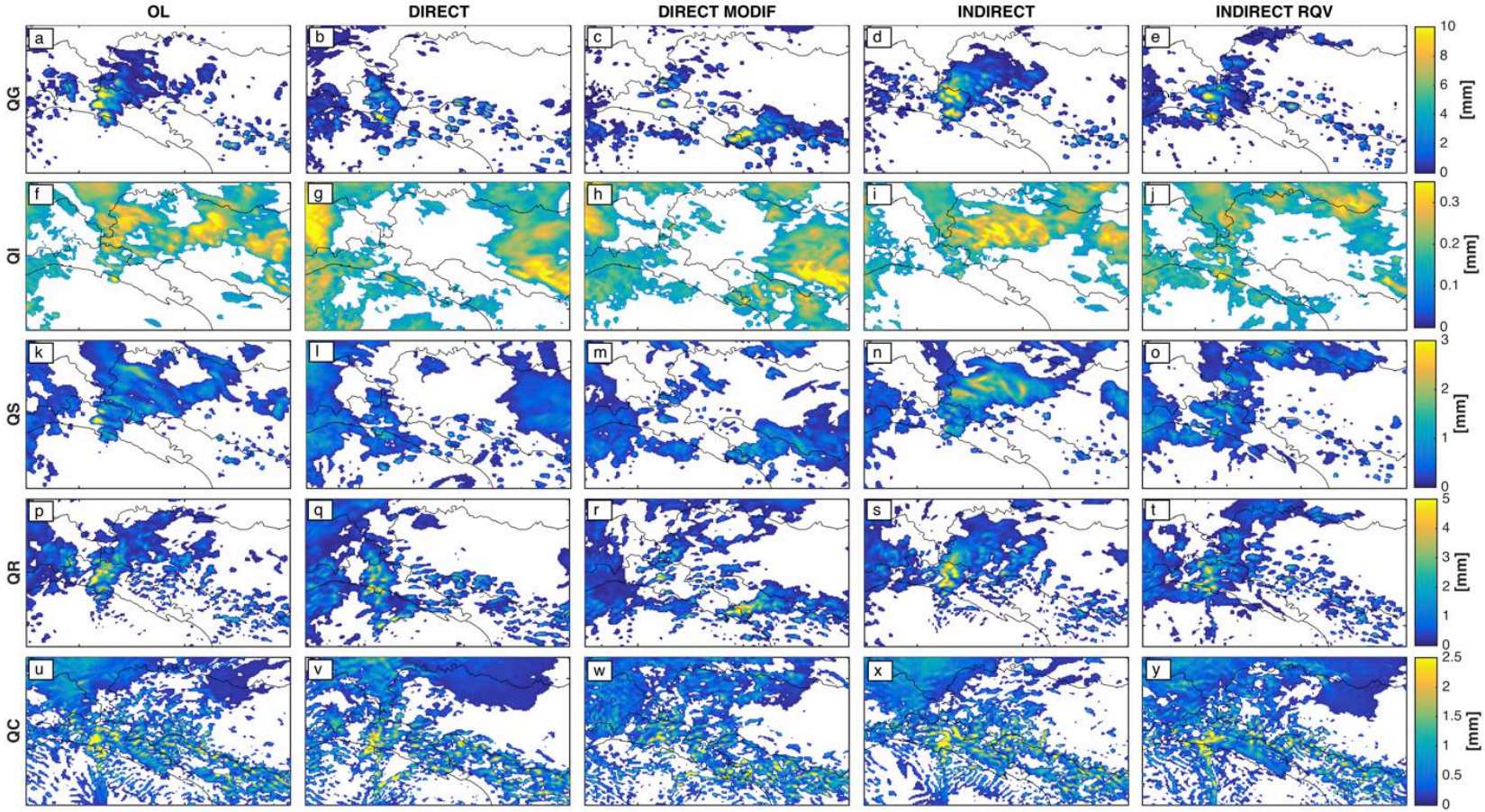

Figure 44: Columnar content analysis for 25 October 2011 at 09 UTC of graupel (QG) in first row, ice (QI) in second row, snow (QS) in third row, rain (QR) in fourth row and cloud water (QC) in the last row. Comparison between the open loop simulation (Panels a, f, k, p, u) and the results achieved with the different reflectivity operator: Radar-direct (Panels b, g, l, q, v), Radar-direct-modif (Panels c, h, m, r, w), Radar-indirect (Panels d, i, n, s, x) and Radar-indirect-rqv (Panels e, j, o, f, y).

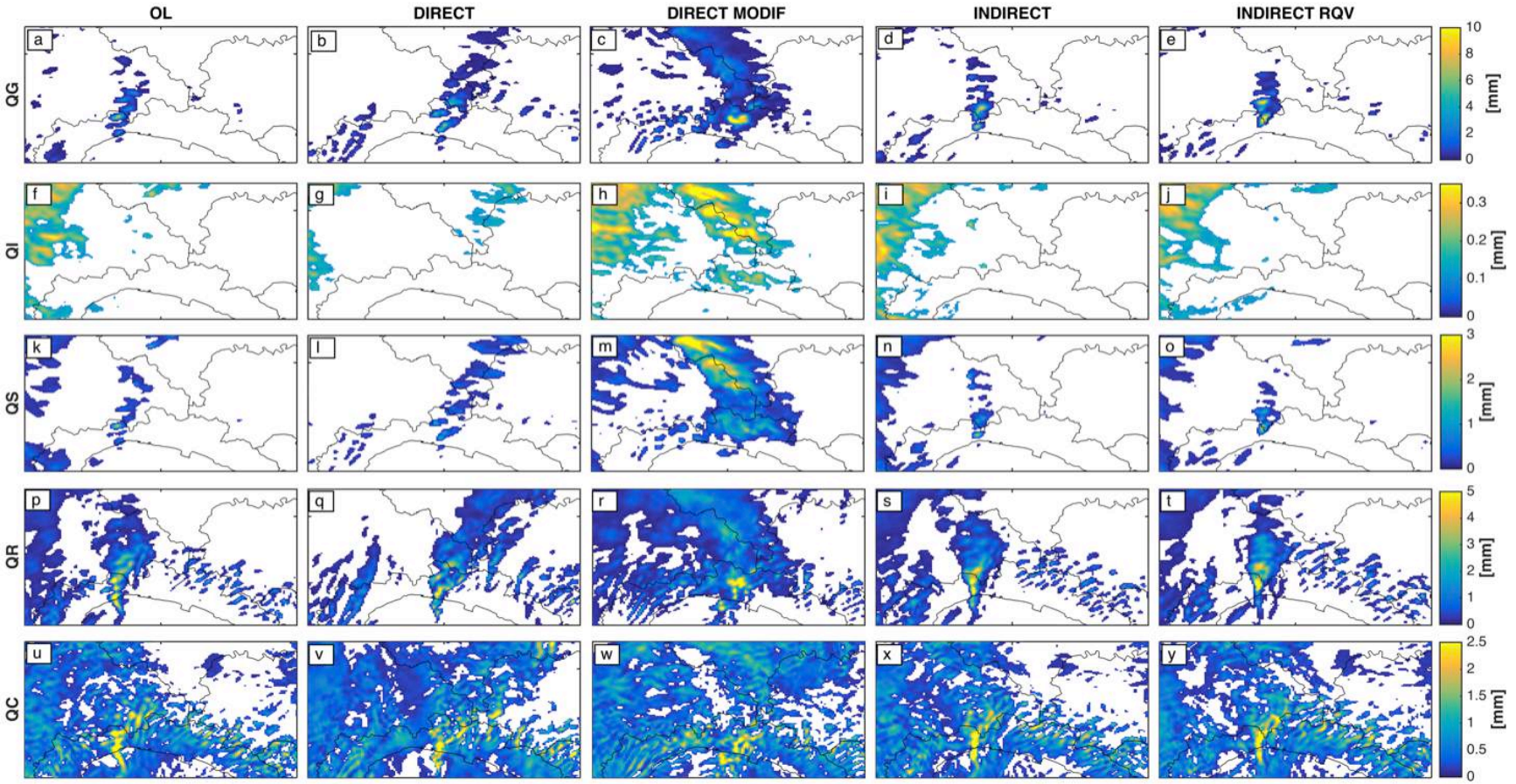

Figure 45: Columnar content analysis for 04 November 2011 at 09 UTC of graupel (QG) in first row, ice (QI) in second row, snow (QS) in third row, rain (QR) in fourth row and cloud water (QC) in the last row. Comparison between the open loop simulation (Panels a, f, k, p, u) and the results achieved with the different reflectivity operator: Radar-direct (Panels b, g, l, q, v), Radar-direct-modif (Panels c, h, m, r, w), Radar-indirect (Panels d, i, n, s, x) and Radar-indirect-rqv (Panels e, j, o, f, y).

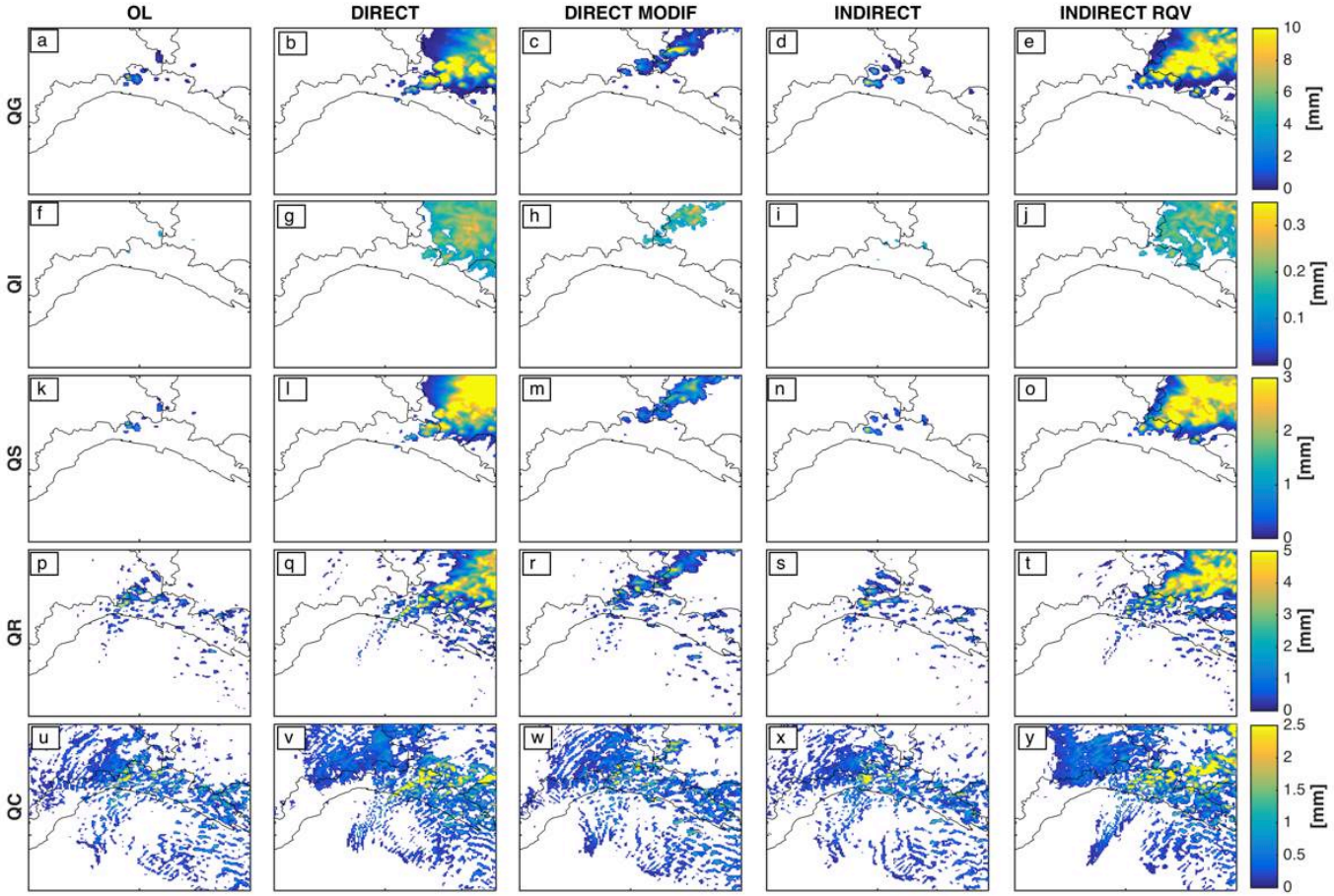

Figure 46: Columnar content analysis for 09 October 2014 at 09 UTC of graupel (QG) in first row, ice (QI) in second row, snow (QS) in third row, rain (QR) in fourth row and cloud water (QC) in the last row. Comparison between the open loop simulation (Panels a, f, k, p, u) and the results achieved with the different reflectivity operator: Radar-direct (Panels b, g, l, q, v), Radar-direct-modif (Panels c, h, m, r, w), Radar-indirect (Panels d, i, n, s, x) and Radar-indirect-rqv (Panels e, j, o, f, y).

7.2.4.2 *Hydrological impact of data assimilation*

To assess how in depth the best performing 3DVAR configuration affects the hydrological prediction (RainFARM+Continuum) the results are presented by means of a box plot of the peak flows. For the 2011 event in Cinqueterre, the most affected basin was Magra (Basin of 1686 km^2 crossing Toscana and Liguria regions): in this case, 3DVAR Radar-direct-modif operator does not enhance very much the streamflow prediction which is quite good also in the Open Loop configuration (Figure 47, Panel b). On the contrary on Vara basin (Figure 47, Panel d) the observed peak flow was not particularly severe, yet Open Loop configuration overestimated it. The data assimilation experiment helps in reducing the overestimation especially in 00 UTC and 06 UTC assimilation cycles. In Figure 47 red dots represent the observed peak while blue cross display the peak obtained with the hydrological model fed with observations.

Streamflow predictions for the Genoa 2011 also benefit from 3DVAR application (namely Radar-direct-modif) (Figure 47, Panel a), the 75% inter-quartile increases from about 180 to 220 m^3/s; similarly, the upper boundary of the distribution (whiskers) increases from 830 to more than 1000 m^3/s. In this case 3DVAR Radar-direct-modif operator cannot localize the intense rainfall core with high accuracy on the catchment, but the downscaling observed peaks are nonetheless included in the tail of the predicted peaks distribution through the application of the downscaling algorithm, a quite common circumstance when the basin targeted by the prediction is so small-sized [Siccardi et al. (2005)].

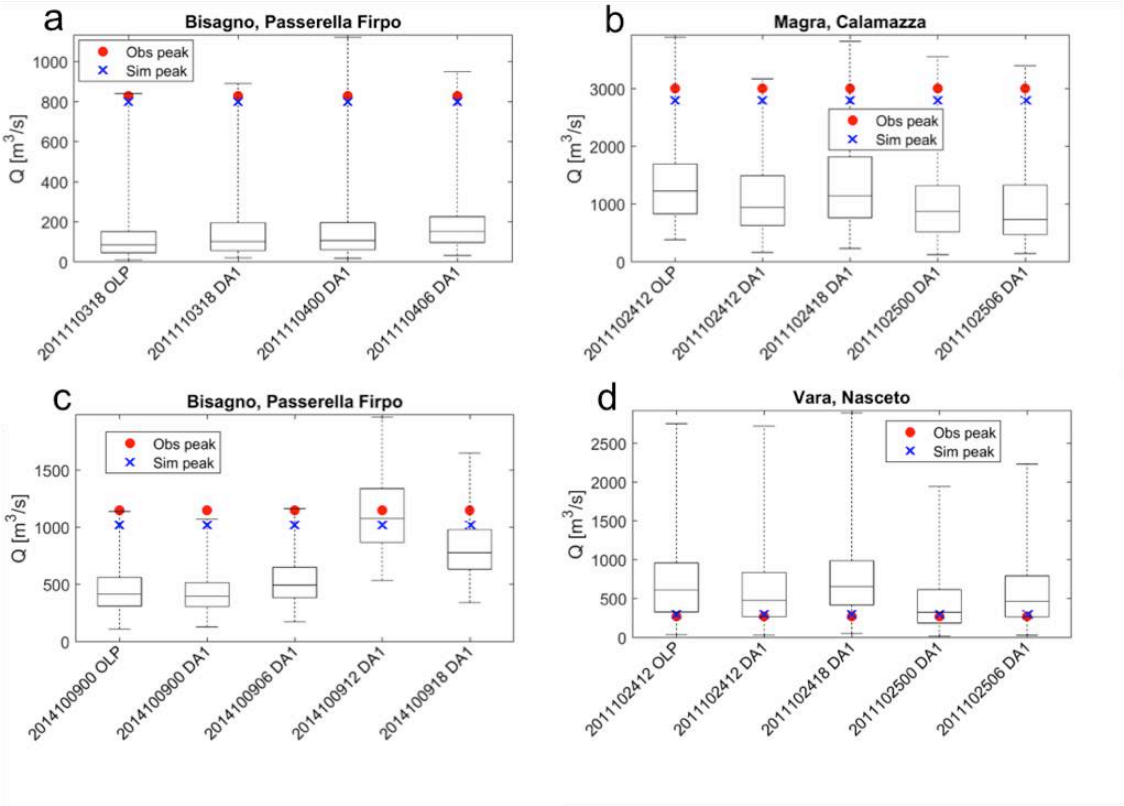

Figure 47: Results of hydrological verification in terms of peak flows. X axis reports the time of assimilation or the Open Loop NWPS run, y axes report peak flows. DA1 stands for data assimilation, OLP stands for Open Loop. Box plot represents the predicted peaks distribution, red dot the observed peak, blue cross the simulated peak obtained using observations as input to hydrological model. Each panel refers to a basin and to one of the considered events.

Figure 47, Panel c shows the results for the Genoa 2014 event again on Bisagno basin: the streamflow forecast obtained with WRF in open-loop configuration is compared with the ones obtained with 3DVAR Radar-indirect-rqv experiment performed every 6 hours. Black dots represent the observed peak while blue diamonds display the peak obtained with the hydrological model fed with observations. 3DVAR Radar-indirect-rqv experiment effect is negligible at 00 UTC while improves the prediction at 6 UTC and then at 12 UTC. These latter seem to be particularly good results, also from an operational standpoint, since both observed and simulated peak flow are inside the inter-quartile. The 18 UTC DA improves results but in this case we are really close to the observed peak, which occurred in the evening at 22 UTC.

The Genoa 9th October 2014 event was very challenging in terms of predictability of the rainfall intensity, the second phase of the event especially. Thus, for this event the whole hydrographs are analyzed after each assimilation cycle in order to evaluate the progressive improvement of the discharge forecast not only in terms of discharge peaks, as in the boxplots, but also addressing their time evolution (Figure 48). Results must be read accounting for the performance achieved in terms of precipitation (see Figure 39 and Figure 40).

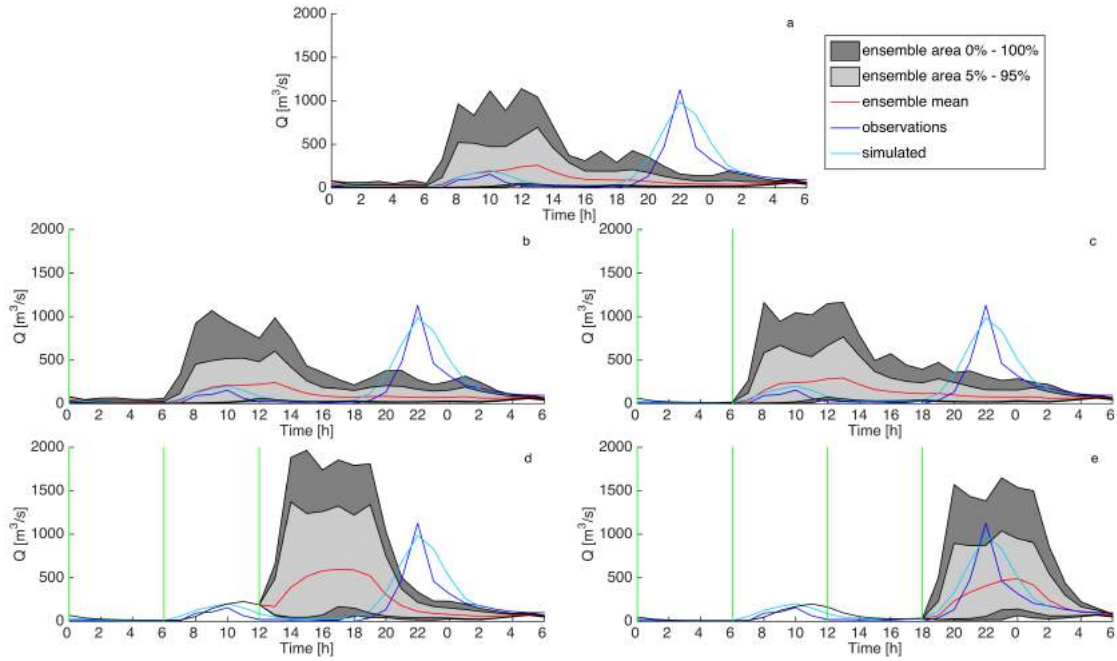

Figure 48: Hydrograph related to the Genoa 2014 event: Open-Loop in panel a, DA at 00 UTC in panel b, DA at 06 UTC in panel c, DA at 12 UTC in panel d, DA at 18 UTC in panel e. Dark gray represent the ensemble area between 0 and 100%, light grey represent the ensemble area between 5 and 95%, the red line refers to the ensemble mean, the blue line is the observation at Passerella Firpo station and the light blue line represents the streamflow computed using observed meteorological variables as input to the hydrological model.

At 00 and 06UTC DA is not impacting significantly on peak discharge timing, when compared with the Open Loop. In these cycles the forecast framework overestimates the rainfall between 00UTC and 12UTC and therefore the discharge peak. Looking at Figure 47, it is in fact evident that the time window

where the grey bands reach the higher values of streamflow (about 8:00 to 14:00 UTC) are similar in sub panels a, b and c.

DA performed at 12UTC, which would have been available from an operational point of view around 15 UTC, namely 5-6 hours earlier than the run forced with 12UTC analysis, improves significantly the rainfall prediction between 12UTC and 24UTC thus leading to an improvement of the discharge forecast accuracy. The 95-percentile is around 1200 m3/s and the average peak timing is around 18 UTC, much closer to the observed one, significantly improving also the finding of Parodi et al (2017).

Also DA at 18UTC, available from an operational point of view around 19UTC, would have been very important from a physically-based short-range nowcasting perspective allowing to understand the evolution in the next few hours during the most intense phases of the rainfall and discharge phenomena.

Generally, the application of the 3DVAR in cycling mode has, at least for this case study, a relevant impact on the hydro-meteorological results for the next 8-9 hours, lasting longer than in Davolio et al. (2017).

7.2.5 Concluding remarks

The back-building MCSs frequently affecting the Mediterranean coastal regions are very challenging from a predictive ability point of view. For this reason, this research activity addressed three back-building MCSs that occurred in Liguria between 2011 and 2014, causing 20 casualties and several hundreds of millions of euros of damage. The impact of a 6-hour cycling 3DVAR data assimilation scheme on the high resolution (1 km) WRF simulations feeding the Continuum hydrological model via the RainFARM stochastic downscaling has been evaluated.

The innovation of this work is represented by the use of different 3DVAR operators for the direct and indirect radar reflectivity data assimilation together with surface observations aiming to identify the best performing setup for MCSs prediction in terms of both QPF patterns and amounts. Subsequently the best performing QPF 3DVAR sensitivity experiments, evaluated through MODE, are fed into the RainFARM and the Continuum hydrological model to forecast peak discharge. The simulated discharge is used to validate the NWP performance at each assimilation step so as to highlight the added value of the use of a 6-hour cycling 3DVAR.

From a meteorological point of view, the 3DVAR assimilation of radar reflectivity has a greater impact on the forecasts in comparison to the use of surface observation data: radar data in fact provide information at many elevations within the troposphere, while the ground sensors data account for surface observations only. An additional advantage of radar observation is its geographical location: reflectivity observation cover the sea, where the convective cells develop, while ground sensors provide observational data only above land once the convective cells are developed. Furthermore, the modified direct operator allows achieving the best performance for the two study cases of 2011, improving the forecast made with standard direct operator. This positive impact is probably due to the fact that, the 0 °C isotherm was quite low-lying (850-900 hPa), thus supporting a relevant production of solid-phase hydrometeors.

For the Genoa 2014 case study the main challenge was the reproduction of the second phase of the event, completely missed by the operational Open-Loop simulation. The use of the indirect reflectivity operator, coupled with the in-cloud humidity retrieval, achieved the best performance providing an enhancement of

the kinematics, i.e. the prominent convergence line that triggered an even more intense deep convection in the second phase of the event.

The best meteorological simulations for each case study (Radar-direct-modif for both 2011 events and Radar-indirect-rqv for the 2014 event) were then fed into the Continuum hydrological model after the application of the RainFARM stochastic downscaling: peak discharge improves significantly even when the Open-Loop already provided a good forecast (like the Cinqueterre 2011 use case).

It is possible to conclude that the use of the hydro-meteorological framework coupling a high resolution WRF simulation including a 6-hour cycling 3DVAR of radar reflectivity, possibly using an ensemble of reflectivity operators, with the Continuum hydrological model can help to obtain more timely and accurate streamflow forecasts for back-building MCSs. Whenever there is not the possibility to use the full portfolio of 3DVAR radar reflectivity operators, the Radar-direct-modif setup turns out to be the best compromises solution. The result obtained in this research activity have been applied in an operational framework to implement a 3 hour cycling 3dvar followed by 48 hour forecast in the framework of the POR-FESR project founded by ARPAL and presented in the following section (7.3). Future works related with this research activity will be a further improvement of the operational forecasting WRF data assimilation (see section 7.3 hereafter) and the implementation of a fully coupled hydrometeorological chain (WRF+Continuum).

7.3 Operational application of WRF-3DVAR provided for regional forecast

The results obtained during the research activity presented above have been applied during the POR-FESR project where a 3-hour cycling 3DVAR is provided operationally to the ARPA-Liguria (ARPAL) regional forecasting center. The setup is the same used during the research activity with the modified direct operator but a different domains grid spacing is used (for operational constraints): in this application three nested domains of 22.5, 7.5 e 2.5 km and 50 vertical levels are used (Figure 49).

The global analyses are obtained from GFS (Global Forecasting System) with 0.25 resolution degrees and 3 hours time frequency for boundary conditions. The assimilation scheme provide two different forecast (Figure 50):

- Cycle 1: The WRF model is initialized with the 18 UTC GFS global model with a first 3DVAR assimilation of the Italian Radar Network and SYNOP stations. A WRF 3 hours forecast is performed until 21 UTC when another cycle of assimilation is performed with another 3 hour forecast and another assimilation cycle at 00 UTC. Then a 48 hour forecast is performed and is delivered to ARPAL within 3:30 UTC
- Cycle 2: In the second forecast the WRF model is initialized with the 06 UTC GFS global model with a first 3DVAR assimilation, again it is performed a 3 hour forecast and a second assimilation cycle at 09 UTC and a third assimilation at 12 UTC. Also in this case from 12 UTC it is run a forecast for 48 hours delivered to ARPAL within 15:30 UTC.

Figure 49: Nested domains for operational 3DVAR application

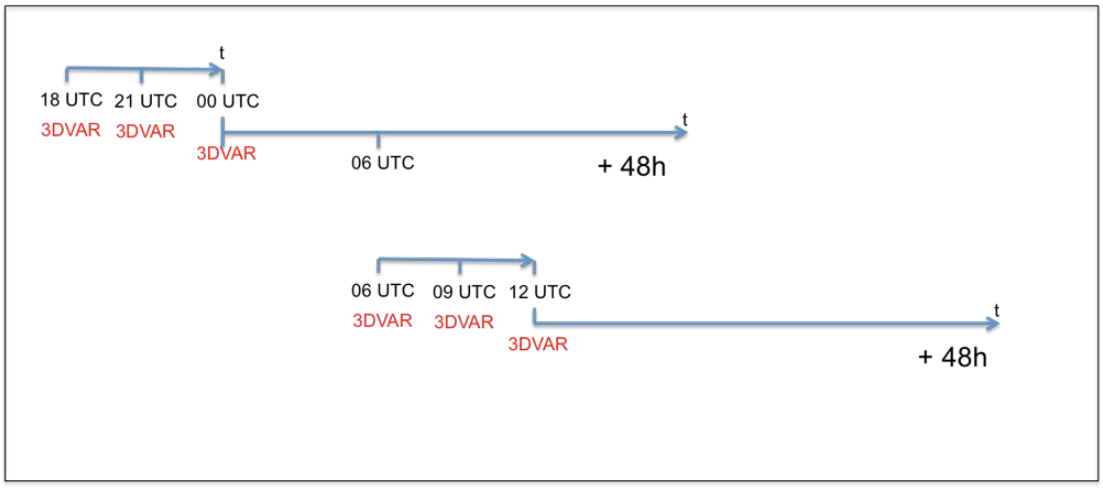

Figure 50: Operational assimilation scheme

Future work will concerns the improvement of the setup presented extending the innermost domain coverage to all Italy, maintaining the same resolution aforementioned, and incrementing the 3dvar cycling (1 hour cycling) before the 48 hours forecasts. The future assimilation scheme will be:

- Cycle 1: The WRF model will be initialized with the 18 UTC GFS global model with a first 3DVAR assimilation of the Italian Radar Network and SYNOP stations. A WRF 1 hour forecast will be performed until 19 UTC when another assimilation cycle will be performed with another 1 hour forecast and another assimilation cycle at 20 UTC and so forth until 00 UTC. Then a 48-hour forecast will be performed.
- Cycle 2: In the second forecast the WRF model will be initialized with the 06 UTC GFS global model with first 3DVAR assimilation, again will be performed a 1 hour forecast and a second assimilation cycle at 07 UTC, a third assimilation at 08 UTC and so forth until 12 UTC. Also in this case, from 12 UTC will be run a forecast for 48 hours.

8. Third research activity - satellite and non-conventional atmospheric observations data assimilation.

A first part of the work presented hereafter is currently under review:
Lagasio, M, Pulvirenti, L., Parodi, A., Boni, G., Pierdicca, N., Venuti, G., Realini, E., Gatti, A., Barindelli, S, & Rommen, B. Effect of the ingestion in the WRF model of different Sentinel-derived and GNSS-derived products: analysis of the forecasts of a high impact weather event. European Journal of Remote Sensing

8.1 The STEAM project

As already discussed, improving the forecast accuracy is a fundamental goal to limit social and economic damages. In this scenario the STEAM project (SaTellite Earth observation for Atmospheric Modeling) aims to respond to a specific question asked by the European Space Agency (ESA):

Can Sentinel satellites constellation weather observation data be used to better understand and predict with at higher spatial-temporal resolution the atmospheric phenomena that can lead to extreme events and intense atmospheric turbulence phenomena?

To assess this, STEAM has identified the WRF model as reference atmospheric modelling suite and has fed it, with variables observed by satellites of the Sentinel constellation such as humidity, soil and sea temperature, wind on the sea, the amount of water vapour in the atmospheric band closest to the earth. Usually all these data are not used in atmospheric forecasting models, conversely they are predominantly used for hydrological and marine modelling applications.

Along these lines STEAM has been articulated in two distinct but complementing components:

1) EO data provided by Sentinel as well as GNSS (Global Navigation Satellite System) water vapour data have been ingested for the first time

into cloud-resolving NWP experiments (down to 1 km grid spacing) to demonstrate the improvements in the predictive capability of severe weather events and to pave the way towards geosynchronous orbit synthetic aperture radar ideas;

2) LES experiments have been performed to gain a deeper understanding of the very fine-scale spatio-temporal properties tropospheric turbulence and spatial inhomogeneity of water vapor fields, thus resulting in the assessment of their effects on propagation parameters relevant for SatCom services, Radio Science and Radio Astronomy observation techniques.

In this work the results of the first point (1) are shown and analysed.

It can be expected that ingesting products derived from the aforementioned EO data into NWP models might significantly reduce weather forecast uncertainties. However, while some investigations on the assimilation in NWP models of low resolution (tens of km) EO derived products (e.g. soil moisture extracted from the Soil Moisture and Ocean Salinity mission data), are available in the literature (e.g. Muñoz Sabater et al. (2012)), very few studies were conducted on the ingestion of high-resolution EO products. To the best of our knowledge, only a couple of papers on the assimilation of water vapour maps derived from SAR data by applying the InSAR technique are available in the literature [Mateus et al. (2018); Pichelli et al. (2015)]. Data about the sea and land surfaces derived from Sentinel data were never used for weather forecast applications so far. The ingestion of high spatial or temporal resolution EO products in a NWP operating at cloud resolving grid represents the new contribution brought by this study.

Note that since, as discussed before, several model runs have to be accomplished to produce a complete set of results and each high-resolution run is very expensive from a computational point of view, the number of case

studies analysed throughout the whole duration of the STEAM project (18 months) should be forcedly limited to 2 events. Hence, the case studies have to be significant for an operational point of view (e.g. issues of weather alerts), so that it was decided to focus on high impact weather events (HIWEs). Thus, the experiments were conducted considering a flood event occurred in in the Livorno town (Tuscany, Central Italy) in September 2017 and a flood occurred in Silvi Marina (Abruzzo, South Italy) in November 2017.

8.2 Test cases

The first case study is the Livorno extreme weather event that took place in the night between 9 and 10 September 2017.

Starting from the afternoon-evening of Saturday September 9th a large trough deepens on the western Mediterranean (Figure 51), recalling an intense flow of currents from the south, mild and extremely humid, on all the Tyrrhenian sectors and on the part east of the Ligurian Sea (Figure 52).

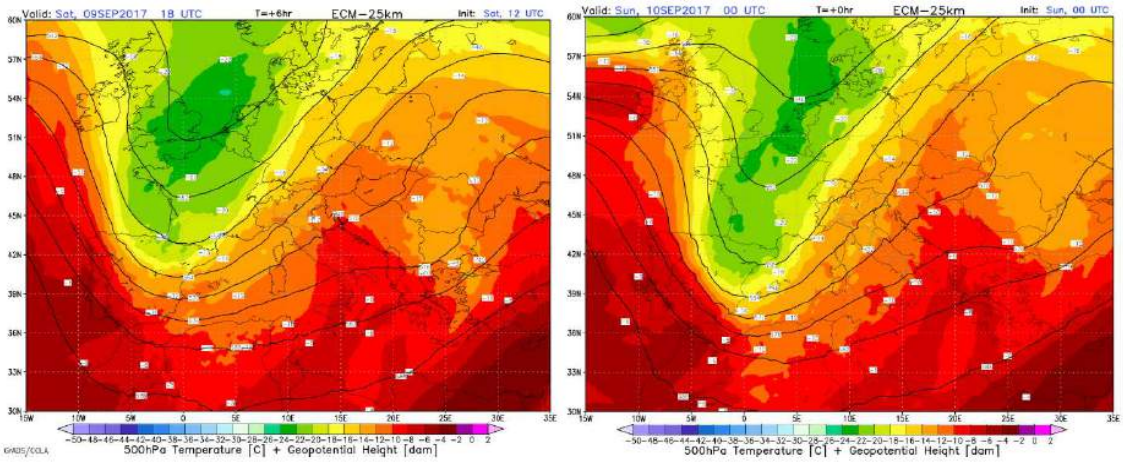

Figure 51: temperature and geopotential height (500 hPa) at 18UTC of 9 September (left) and 00UTC of 10 September 2017 (ECMWF 25 km run, 12UTC 9 September 2017).

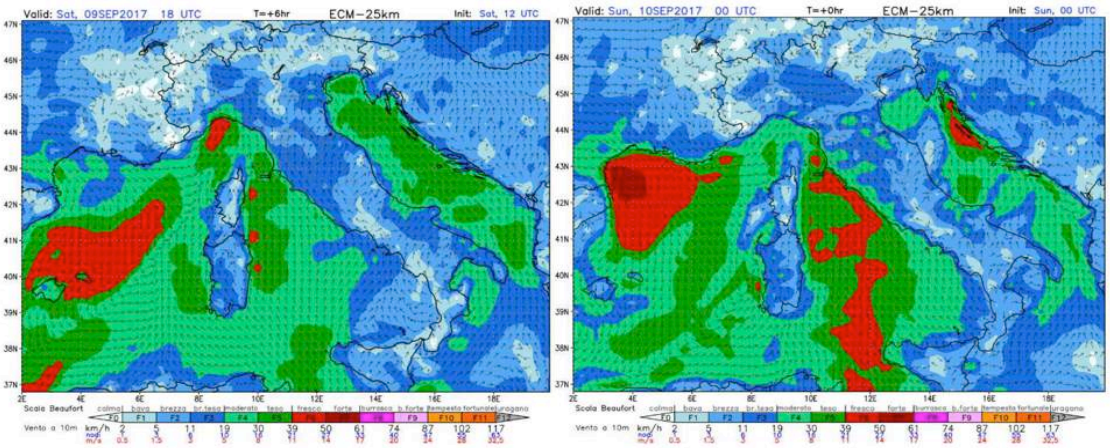

Figure 52: 10 m wind field at 18UTC of 9 September (left) and 00UTC of 10 September 2017 (ECMWF 25 km run, 12UTC 9 September 2017).

Significant amounts of precipitable water columnar content represent a condition potentially favourable of the triggering of very intense and efficient rainfall processes (Figure 53).

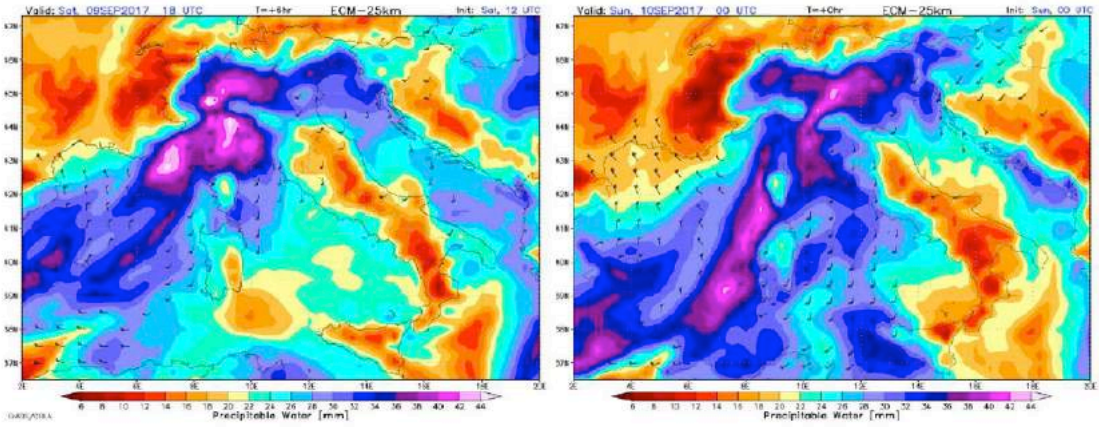

Figure 53: precipitable water columnar content at 18UTC of 9 September (left) and 00UTC of 10 September 2017 (ECMWF 25 km run, 12UTC 9 September 2017).

From the evening of Saturday 9 September, the freshest airflow associated with vorticity at 500 hPa was supportive of instability conditions on Tuscany region (Figure 54).

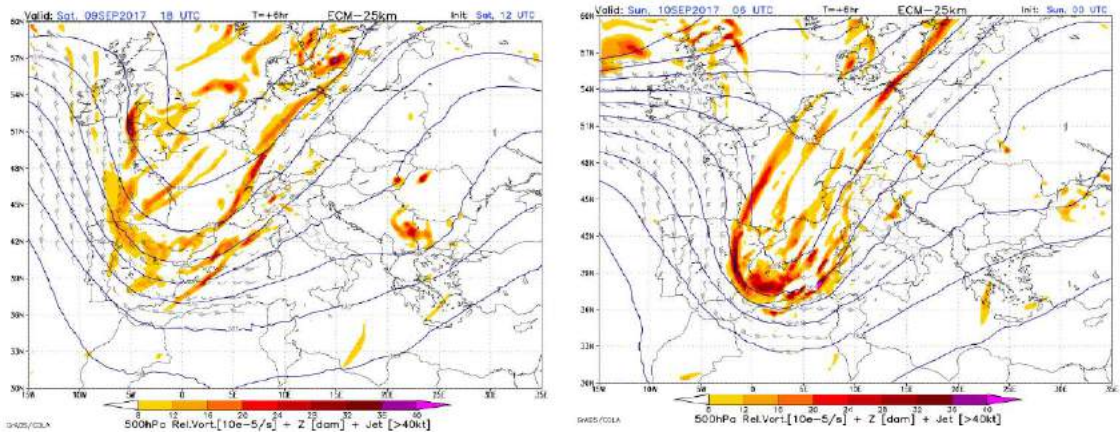

Figure 54: vorticity field (500 hPa) at 18UTC of 9 September (left) and 00UTC of 10 September 2017 (ECMWF 25 km run, 12UTC 9 September 2017).

The environment is also conducive to the development of intense local convective precipitation systems persistent, not only because of the slow evolution of the depression area, but also because of the shear of the winds (variation of the intensity and direction of the wind along the vertical column) well highlighted by the "deep level shear" (Figure 55) which determines a separation between the updraft area (rising currents that feed the storms) and that of downdraft (descending currents that generate the wind band), favouring locally stationary storms.

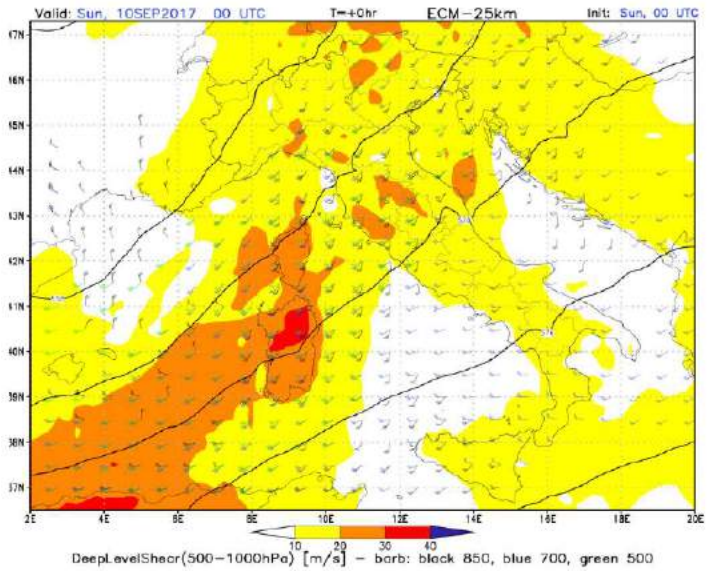

Figure 55: deep shear layer (500-1000 hPa) at 00UTC of 10 September 2017 (ECMWF 25 km run, 00UTC 10 September 2017).

However it is very important to consider, from a predictability standpoint, how the entire central Tyrrhenian sea, and large part of central Italy were prone to the potential occurrence of very intense, persistent, and self regenerating thunderstorm phenomena as confirmed by the values of the severe index: the Severe Weather Threat Index (SWEAT) measures thunderstorm potential by examining low-level moisture, convective instability, jet maxima, and warm advection (Figure 56).

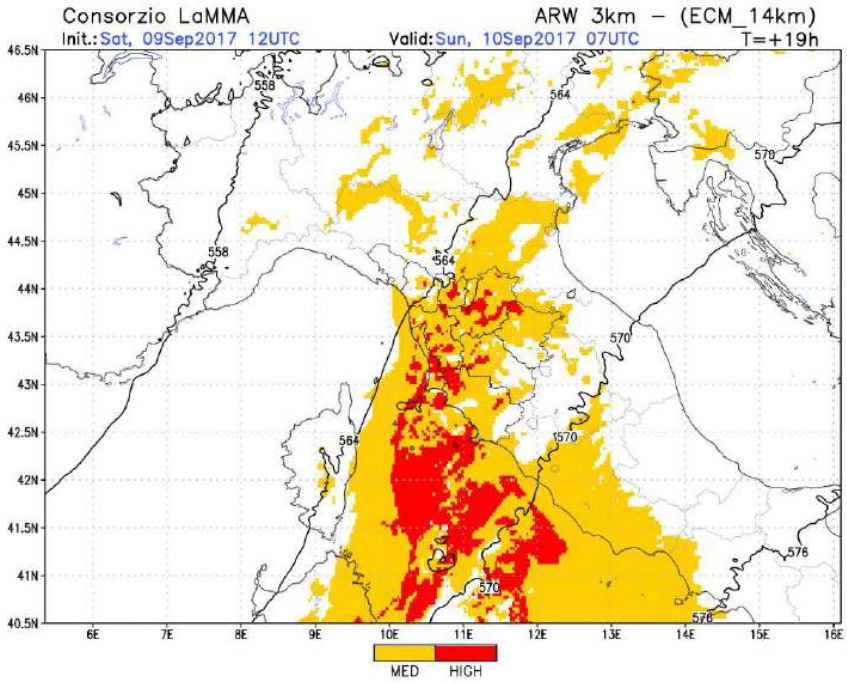

Figure 56: SWEAT index at 07UTC of 10 September 2017 (ECMWF 25 km run, 12UTC 9 September 2017).

The event according to the Molini et al (2011) criterion can be classified as: type II –short-lived (duration d < 12 hours) and very localized (less than AS = 50 × 50 km^2). These events correspond to the non-equilibrium convection, where a larger amount of CAPE is available, as a result of building up from large-scale processes over long time-scales, but the extent to which it produces convection and precipitation is restricted by theneed for a trigger sufficient to overcome the convective inhibition energy (CIN).

The resulting observed Quantitative Precipitation Estimate for the time period 18UTC 9 September 2017 – 06UTC 10 September 2017 is shown in the following map (Figure 57), using the raingauge data (courtesy of the Italian Civil Protection Department): an intense lightning activity was also in place (Figure 58).

Figure 57: Quantitative Precipitation Estimate using Italian raingauge data network for the time period 18UTC 9 September 2017 – 06UTC 10 September 2017 (courtesy of the Italian Civil Protection Department).

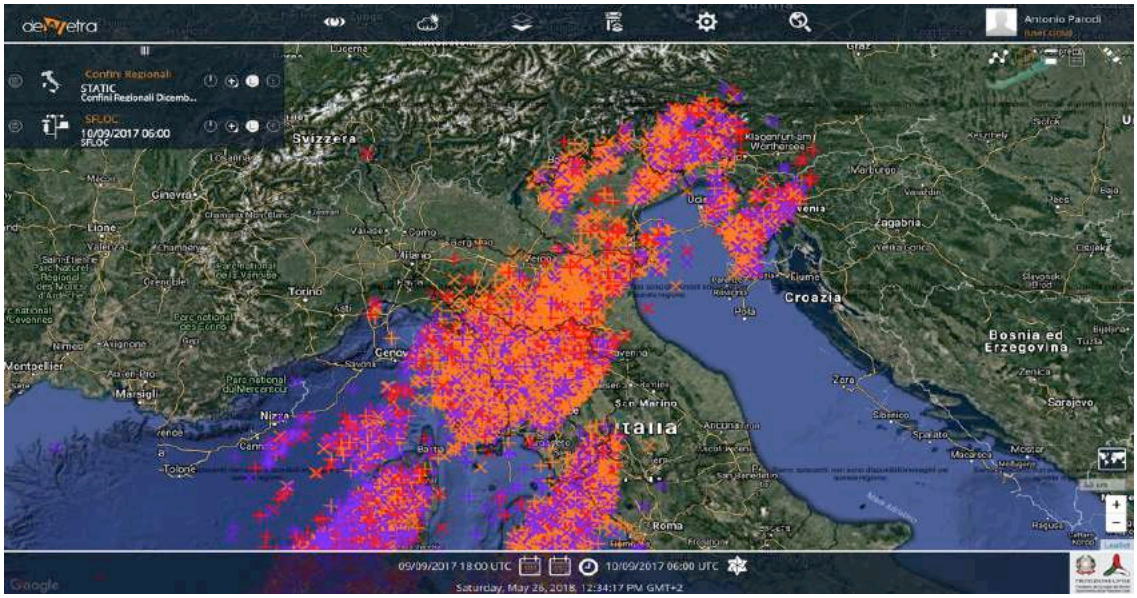

Figure 58: observed lightning strokes for the time period 18UTC 9 September 2017 – 06UTC 10 September 2017 (courtesy of the Italian Civil Protection Department).

The second case study is the Silvi-Marina extreme weather event that took place on 14-15 November 2017 in central Italy affecting mainly Abruzzo, Marche and Umbria regions.

On 14 November 2017 around 00UTC (500 hPa) an isolated trough is apparent over Italy peninsula, slowly moving, while shrinking, towards southern Italy 24 hours later (Figure 59). The synoptic scale system generates advection of moist and warm air in the lower troposphere (850 hPa) from Africa towards Apennines mountains range in Central Italy (Figure 60).

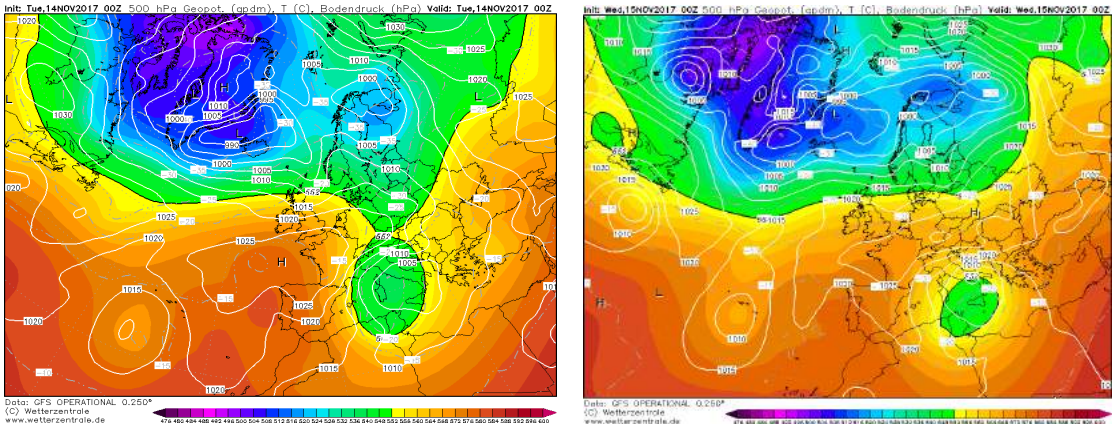

Figure 59: Geopotential at 500 hPa (GFS, 14 and 15 November 00UTC).

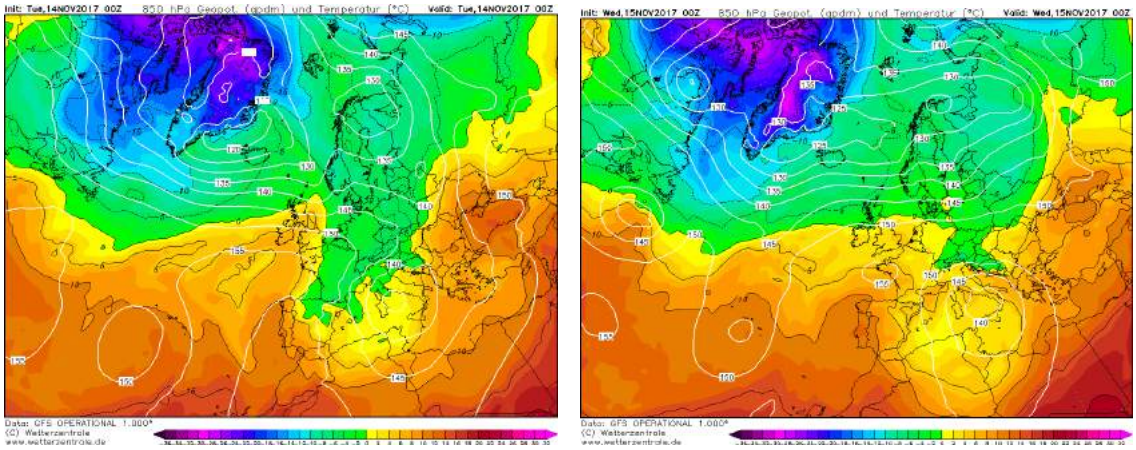

Figure 60: Temperature at 850 hPa (GFS, 14 and 15 November 00UTC).

The event according to the Molini et al (2011) criterion can be classified as: type I –long-lived (duration d ≥ 12 hours) and spatially distributed (more than AS = 50 × 50 km2). These events correspond to the equilibrium convection, where it is assumed that production of CAPE by large-scale processes is nearly balanced by its consumption by convective phenomena, and thus CAPE values stay small: this is confirmed by the CAPE values (around 1000 J/kg) at 12 UTC on 14 and 15 November 2017 (Figure 61). In this case the overall size, location and intensity of the precipitating region is determined by the large-scale flow.

The resulting observed Quantitative Precipitation Estimate respectively for the 24 hours of 14 and 15 November 2017 are shown in the following map (Figure 62 and Figure 63), using the raingauge data (courtesy of the Italian Civil Protection Department).

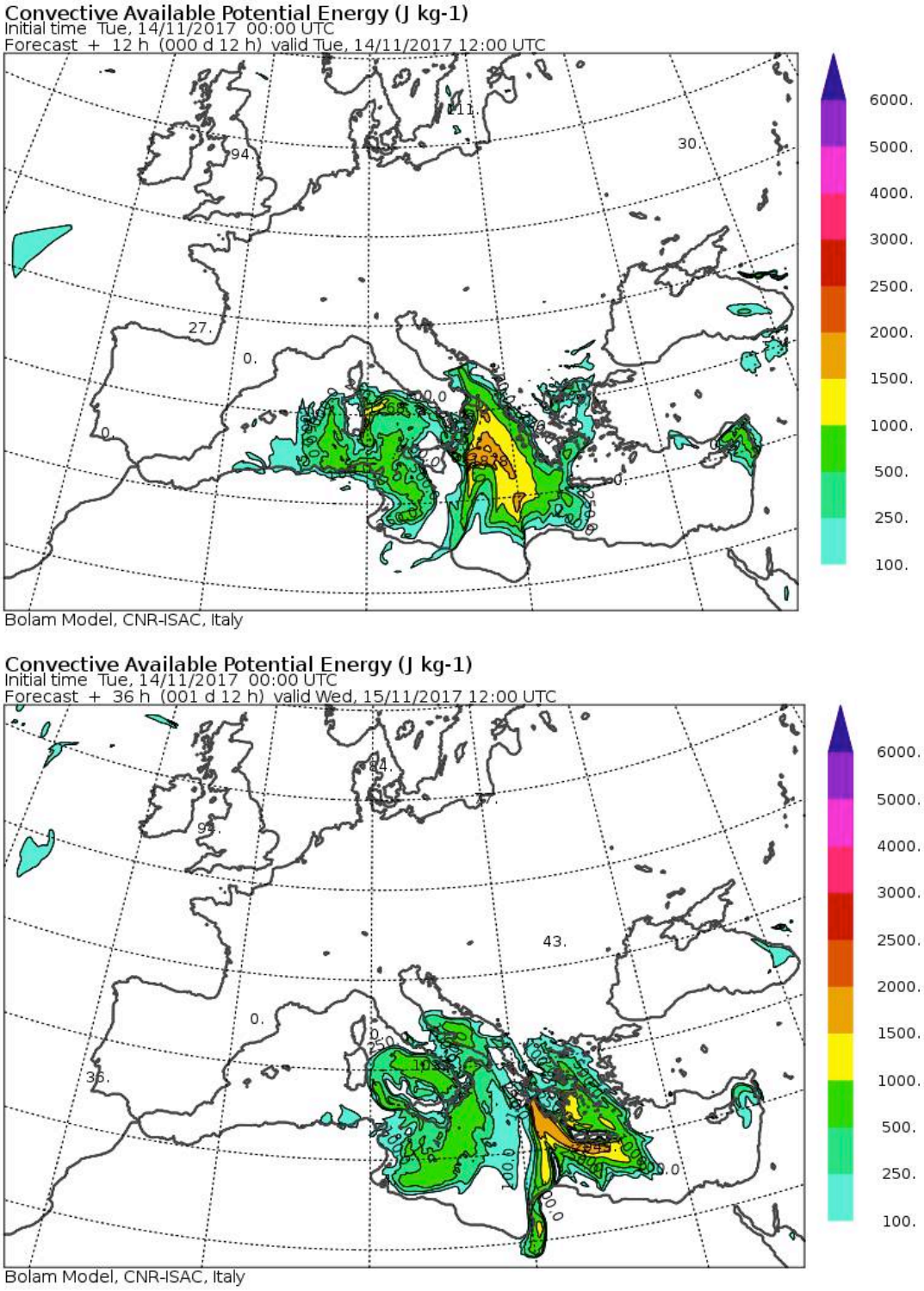

Figure 61: Convective Available Potential Energy (CAPE) at 12UTC on 14 and 15 November 2017 (BOLAM model, 00UTC)

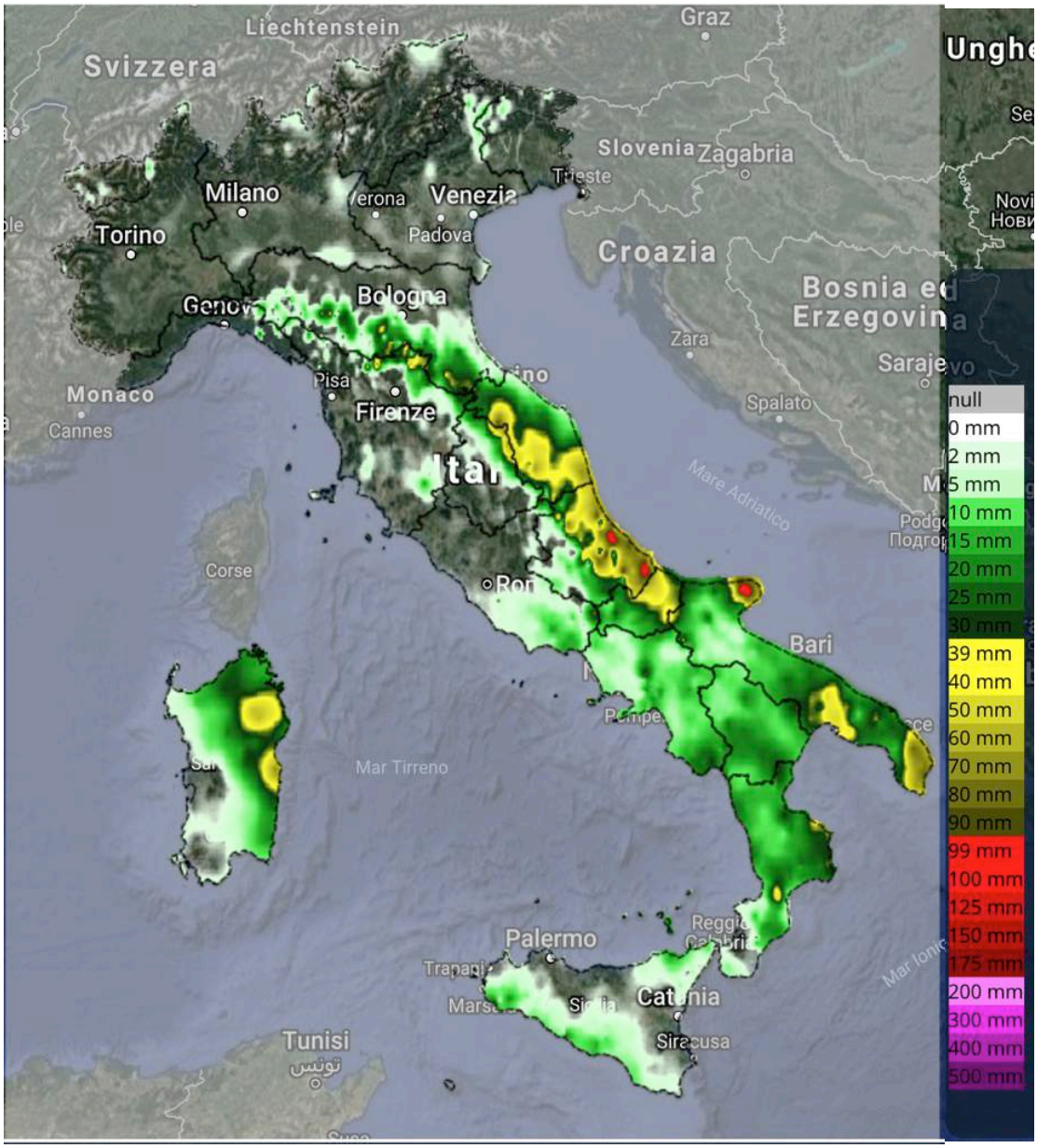

Figure 62: QPE 24 hours on 14 November 2017.

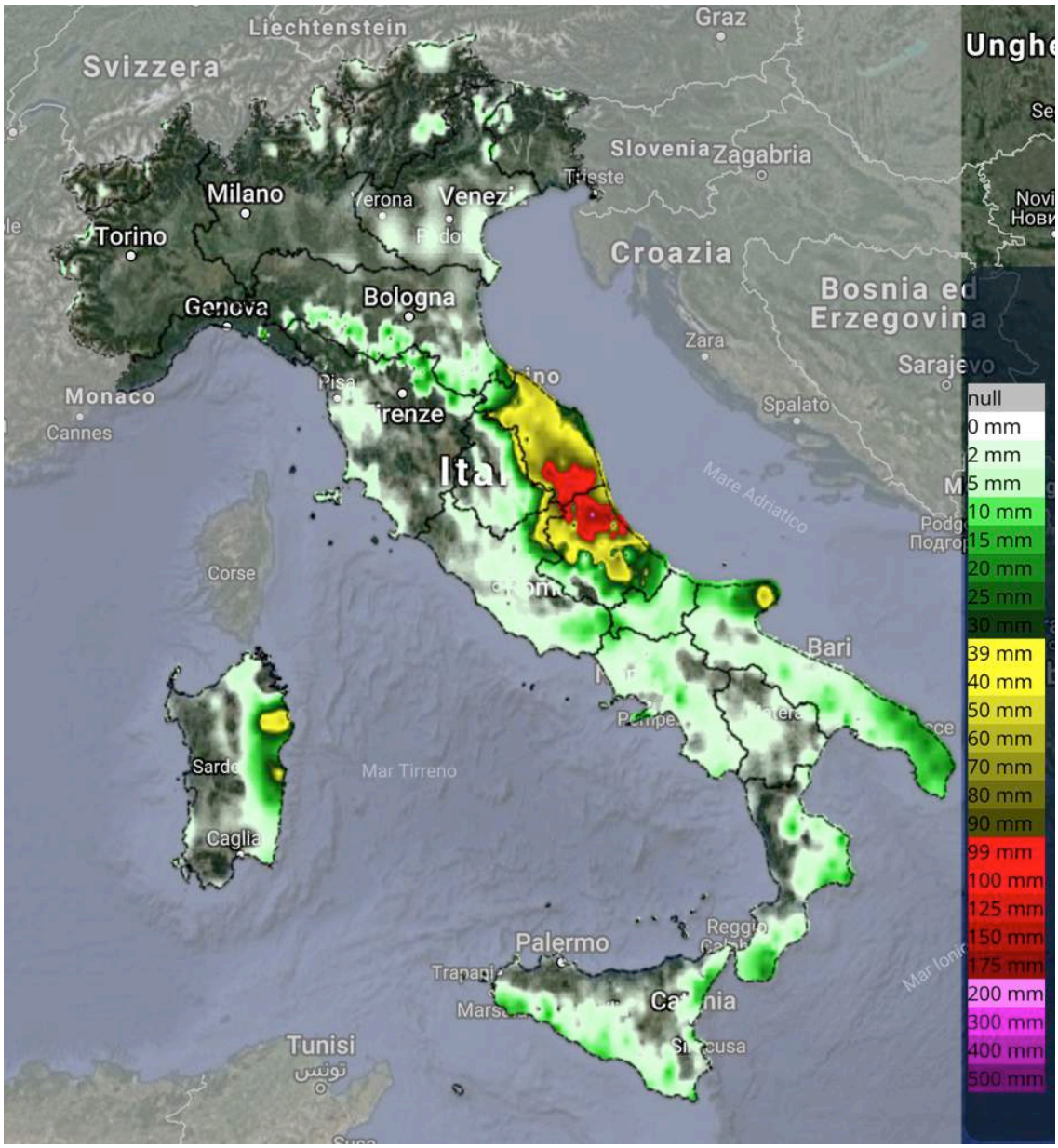

Figure 63: QPE 24 hours on 15 November 2017.

Some stations (Penna Sant'Andrea in Abruzzo and Sarnano in Marche) registered more than 200 mm of rainfall in 48 hours, with rainfall phenomena persisting for 30-36 hours and 15 minutes rain rate less than 10 mm, thus confirming that this event belongs to the type I –long-lived and spatially distributed category. In this respect also the number of lightning strokes observed during the two days of the event was negligible.

Figure 64: Penna Sant'Andrea (Abruzzo) rainfall data station.

8.3 Observational data description

8.3.1 Livorno test case

The following maps show the available EO observational data, the corresponding Sentinel source, and the acquisition time.

Soil Moisture: Sentinel 1, 18UTC 8 September 2017 (

Figure 65**).** The area corresponding to the observed QPE maxima is well captured by the Sentinel data and it corresponds to SM values around 0.3. In previous literature investigation it was found that accuracy of SM retrieval from SAR ranges between 0.04 m^3/m^3 (bare soils) and 0.14 m^3/m^3 (densely vegetated soils).

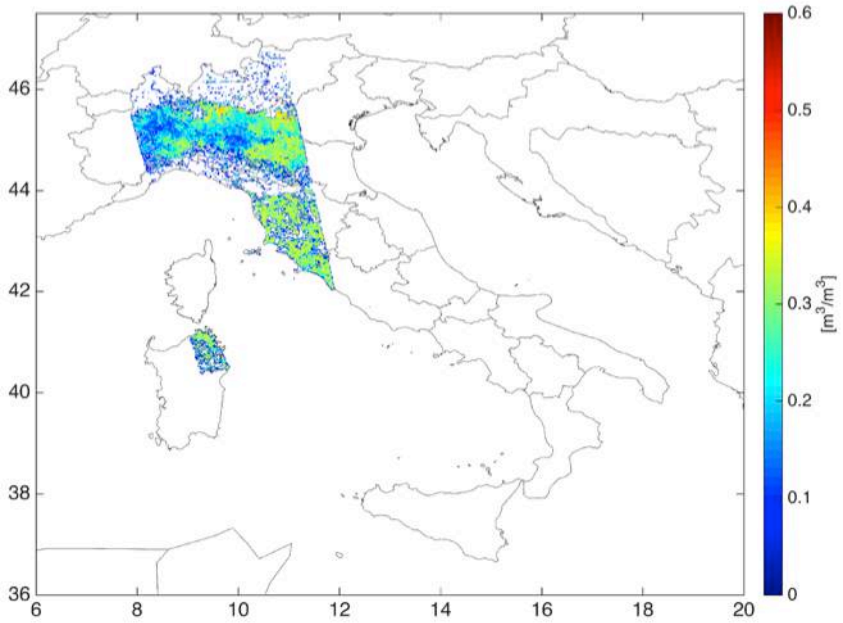

Figure 65: Soil Moisture Sentinel 1, 18UTC 8 September 2017.

Wind over the ocean: Sentinel 1, 18UTC 8 September 2017 (Figure 66**).** A significant Scirocco wind is blowing along southern Tuscany and northern Lazio coastline, while the wind over the sea pattern in front of northern Tuscany coastlines appear more disorganized and chaotic. Additionally a intense wind jet is apparent nearby the Strait of Bonifacio, in between Corsica and Sardinia. Using Sentinel-1A data, Monaldo et al. [JSTARS 2015] found that wind speed retrievals agree with ASCAT data better than 2 m/s in standard deviation for wind speeds less that 20 m/s.

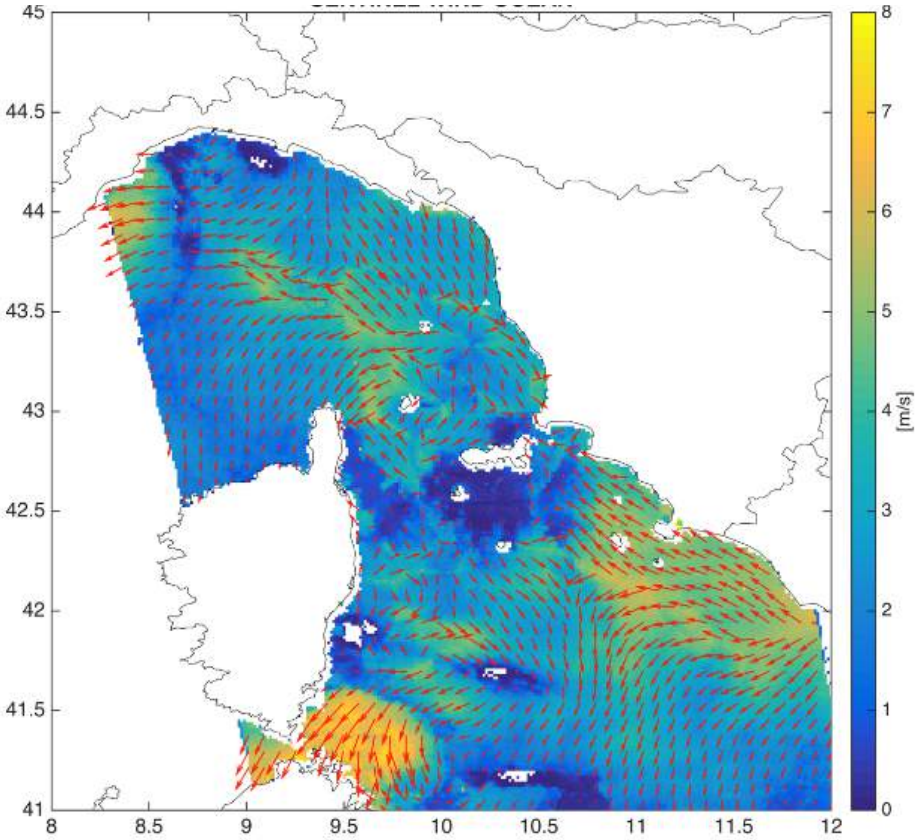

Figure 66: Wind over the ocean: Sentinel 1, 18UTC 8 September 2017.

Sea Surface Temperature: Sentinel 3, 21UTC 9 September 2017 (Figure 67)

The map shows valid values mainly on the swat southern part around Sicily island, while not valid observations are available in front of the Tuscany coastlines.

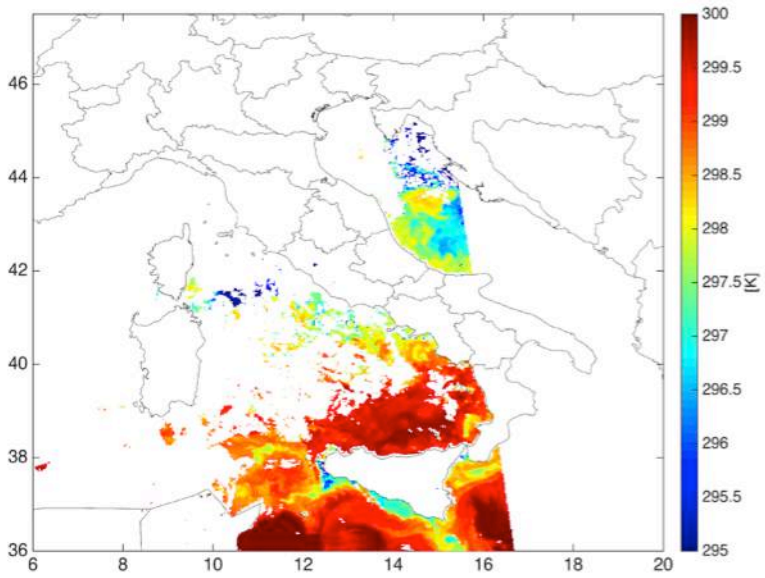

Figure 67: Sea Surface Temperature: Sentinel 3, 21UTC 9 September 2017

The SST Theoretical Uncertainty included in each level2 product is presented in Figure 68, showing values below 1.5 K.

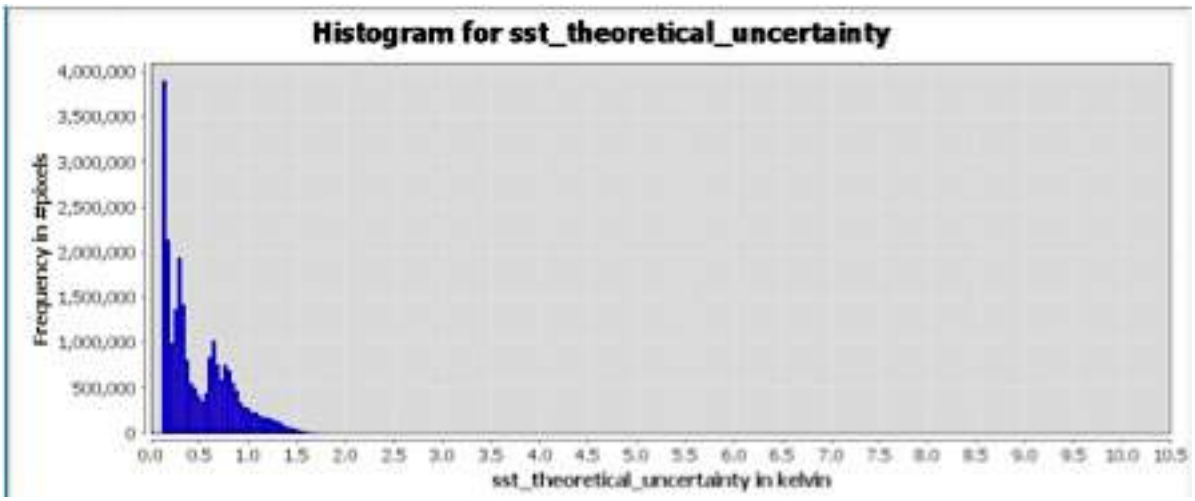

Figure 68: SST Theoretical Uncertainty included in each level2 product

Land Surface Temperature: Sentinel 3, 10UTC 9 September 2017 (Figure 69**).** The swat covers most of central Italy. The northern part of Tuscany near the area mostly affected by the observed torrential rainfall phenomena shows a land surface temperature significantly lower than surrounding areas, especially Adriatic coastlines, and eastern portion of Pianura Padana.

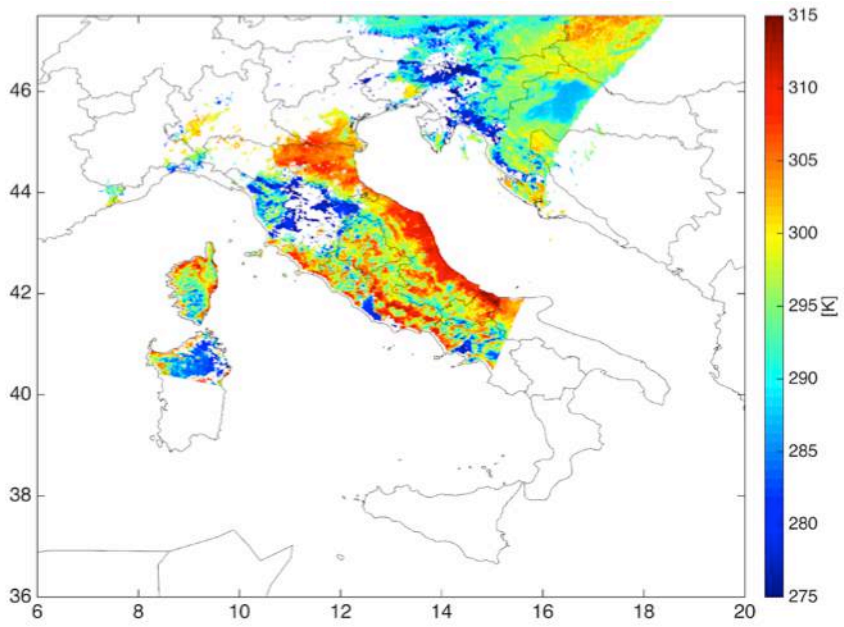

Figure 69: Land Surface Temperature: Sentinel 3, 10UTC 9 September 2017.

The LST Theoretical Uncertainty included in each level2 product is presented in Figure 70, showing values below 0.180 K.

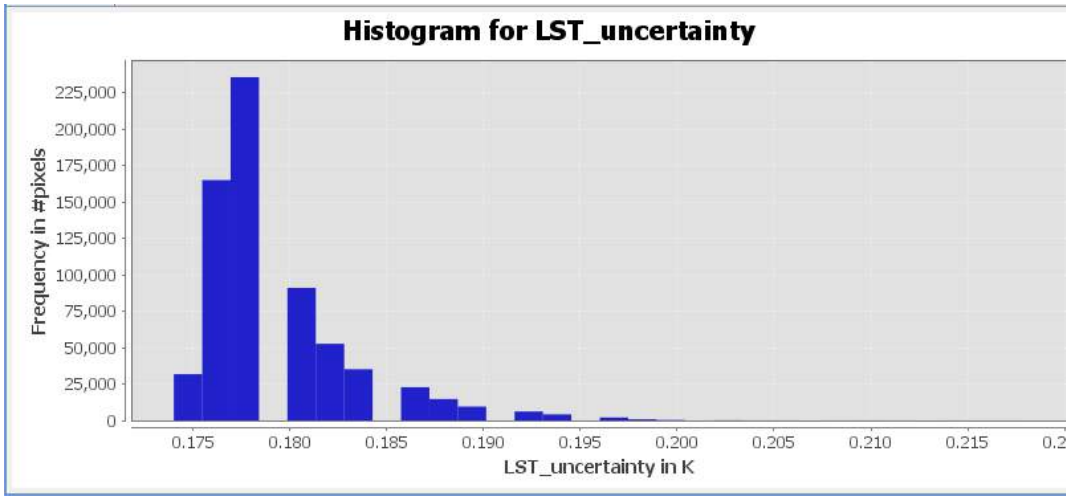

Figure 70: SST LST Theoretical Uncertainty included in each level2 product.

Zenith Total Delay: 375 GNSS stations. Zenith Total Delay (ZTD) time series were estimated starting from GNSS observations retrieved by 375 stations within the area of interest. Of these, 44 stations belong to the European Permanent Network (EPN), the remaining 331 to several Italian nation-wide and region-wide networks that publish 30-second GNSS observations for free (Figure 71).

The ZTD was estimated by a joint least squares adjustment of undifferenced phase observations (the so-called “PPP batch” approach), as implemented by GReD in the goGPS open source software. The processing settings included the use of the Vienna Mapping Function (VMF) to map slant delays to the zenith, and VMF grids to compute the a-priori values for the tropospheric delay. One tropospheric delay parameter was estimated per epoch (i.e. one every 30 seconds), with a constraint set to 1.5 cm/hour. North and East tropospheric delay gradients were estimated.

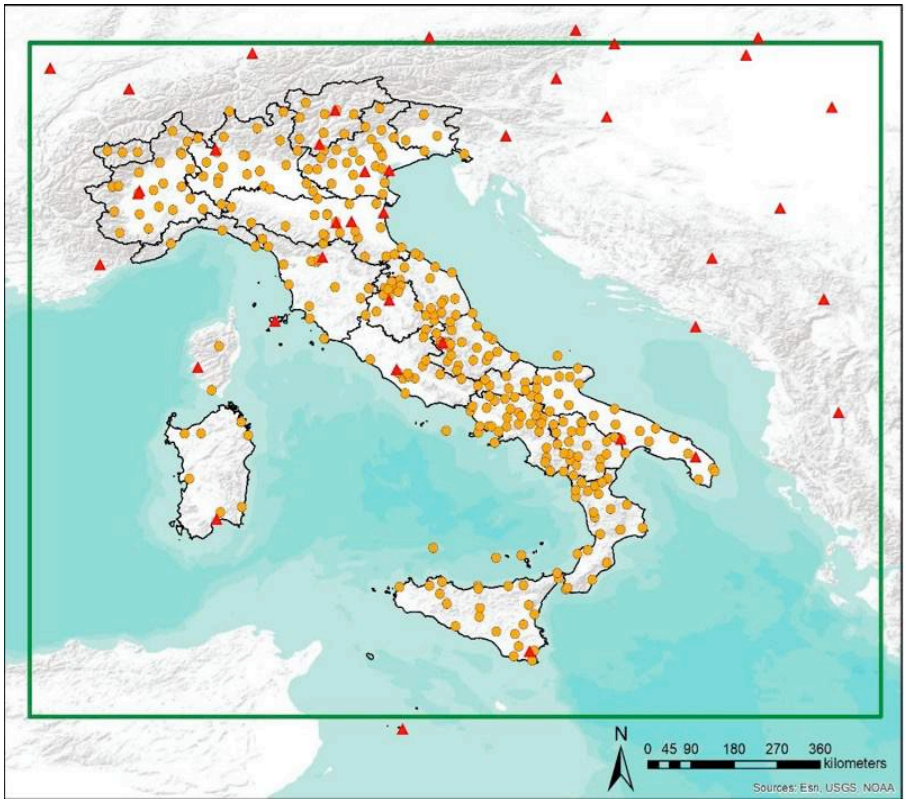

Figure 71: 375 GNSS stations used in the Livorno case study.

The resulting ZTD time series were validated by comparison with radiosondes, using the 8 available radiosonde launch sites in Italy, and considering the GNSS station nearest to the radiosonde launch site. This comparison resulted in ZTD differences with mean of 3 mm and standard deviation of 15 mm. A validation of the ZTD estimated from all stations was done by comparison with the ZTD computed by the online service GACOS (http://ceg-research.ncl.ac.uk/v2/gacos/), which uses a high-resolution ECMWF weather model. This comparison confirmed the statistics obtained with respect to radiosounding data, with a mean difference of 4 mm and standard deviation of 15 mm.

8.3.2 Silvi Marina test case

The following maps show the available EO observational data, the corresponding Sentinel source, and the acquisition time.

Soil Moisture: Sentinel 1, 05:10 UTC and 1704 UTC on 14 November 2017 (Figure 72**).** The area corresponding to the observed QPE maxima, over March and Abruzzo Apennines is well captured by the Sentinel data and it corresponds to SM values around 0.3. In previous literature investigation it was found that accuracy of SM retrieval from SAR ranges between 0.04 m^3/m^3 (bare soils) and 0.14 m^3/m^3 (densely vegetated soils).

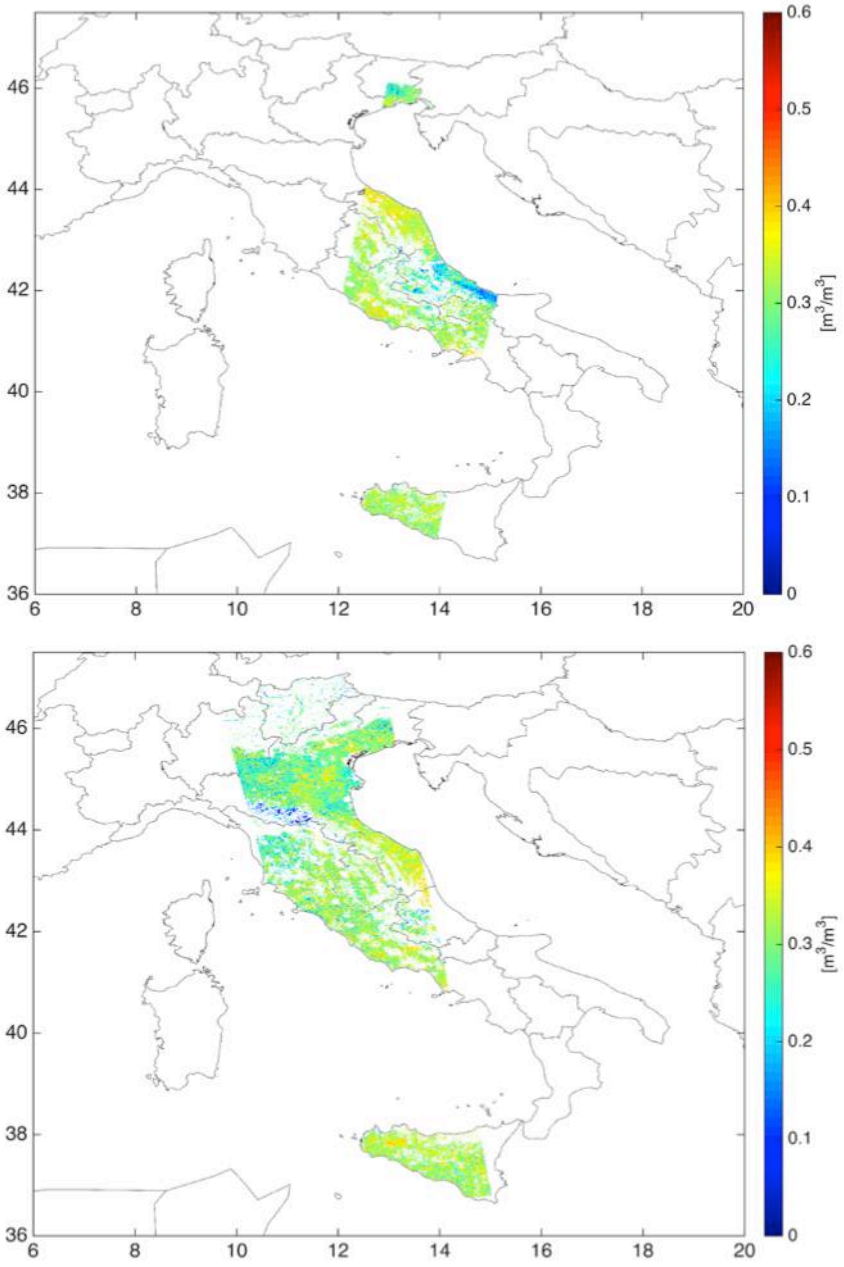

Figure 72: Soil Moisture: Sentinel 1, 05:04 (upper panel) and 17:10 (lower panel) UTC 14 November 2017.

Wind over the ocean: Sentinel 1, 05:10UTC and 17:04 14 November 2017

(Figure 73**)**

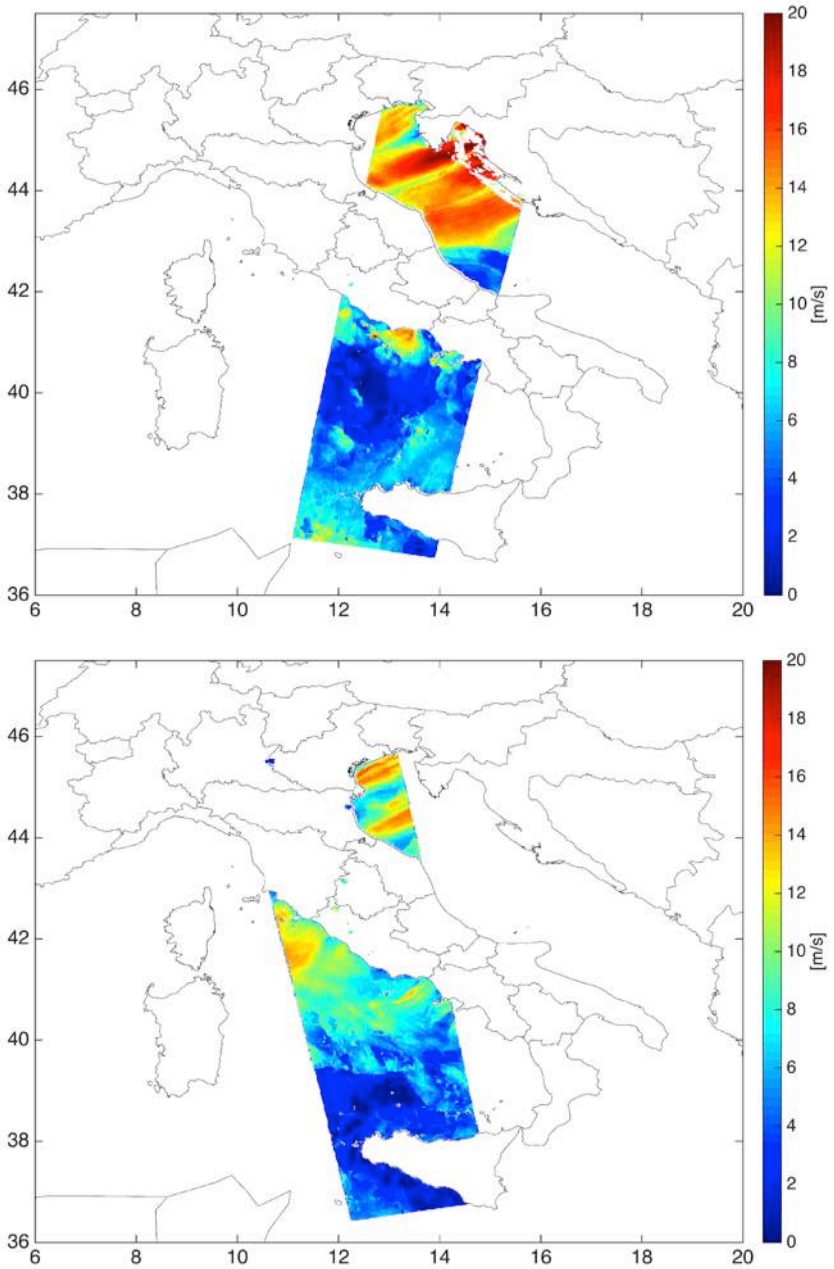

Figure 73: Wind over the ocean Sentinel 1, 05:04 (upper panel) and 17:10 (lower panel) UTC 14 November 2017.

Sea Surface Temperature: Sentinel 3, 19:36UTC 12 November 2017 (Figure 74**).** The map shows valid values only two days ahead the observed event, mainly on the swat southern part on the Ionian sea, as well as in front of the Abruzzo and Marche coastlines.

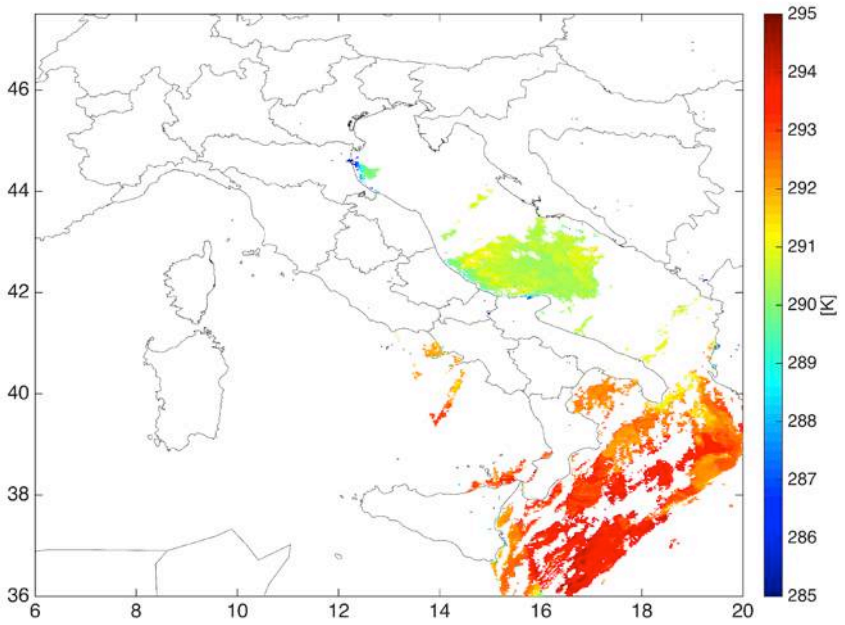

Figure 74: Sea Surface Temperature Sentinel 3, 19:36 UTC 12 November 2017.

Zenith Total Delay: 376 GNSS stations

Similarly to the Livorno case, ZTD time series were estimated starting from GNSS observations retrieved by 376 stations within the area of interest. Of these, 45 stations belong to the European Permanent Network (EPN), the remaining 331 to the Italian nation-wide and region-wide networks (Figure 75).

The ZTD was estimated following the same procedure as in the Livorno case. Validation was done with respect to radiosondes, yielding a mean difference of -2.6 mm and standard deviation of 19 mm.

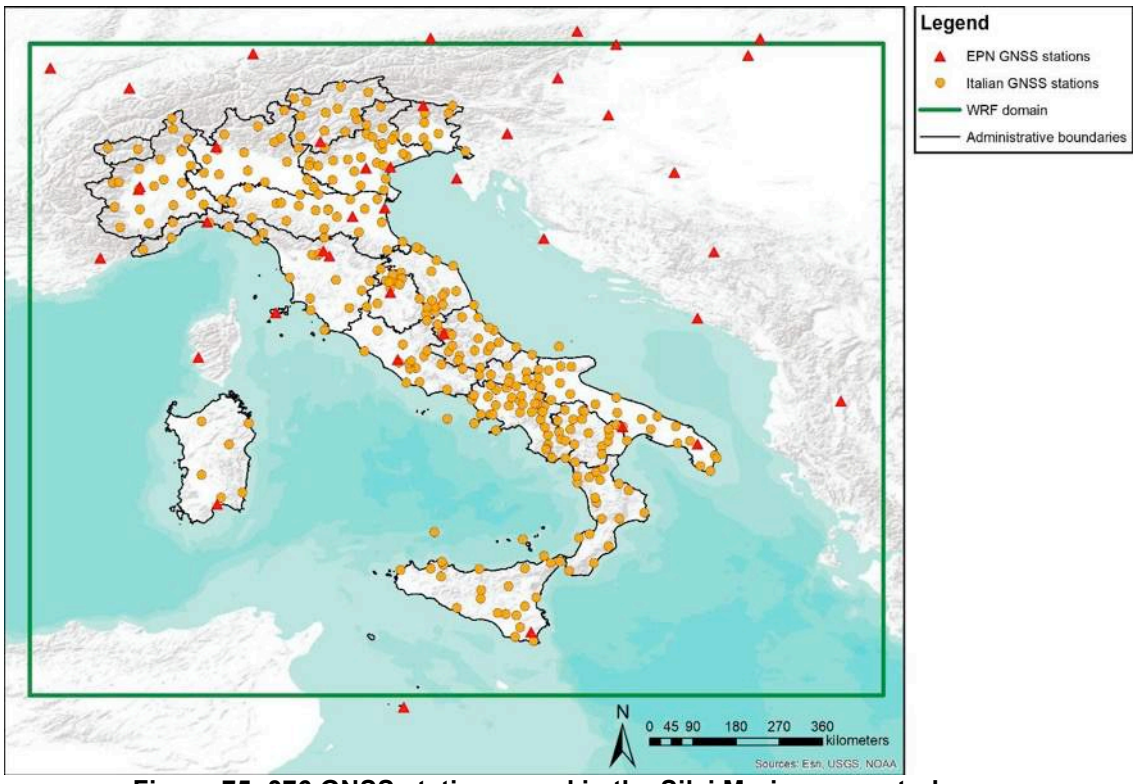

Figure 75: 376 GNSS stations used in the Silvi Marina case study.

SAR Atmospheric phase screen

49 Sentinel-1 images have been downloaded, ingested in TRE ALTAMIRA processing chain, and processed to obtain atmospheric products.

Dataset	
Number of Images	49
First Image	18 May 2017
Last Image	14 March 2018
Image Dimensions [pixels]	67395 x 12141
AOI [Km]	340 x 200

Atmospheric products have been subsampled, roughly at 100 x 100 [m] and delivered to other partners, after geocoding, in GeoTIFF format. In Figure 76 is

shown the incoherent mean of all the 49 images, depicting the Area of Interest (AOI), and in Figure 77 an example of the derived atmospheric product.

Along with the APS products have been generated a digital terrain model of the Area of Interest used in data processing and an incidence angle map, to allow the projection of the data along the zenith local direction.

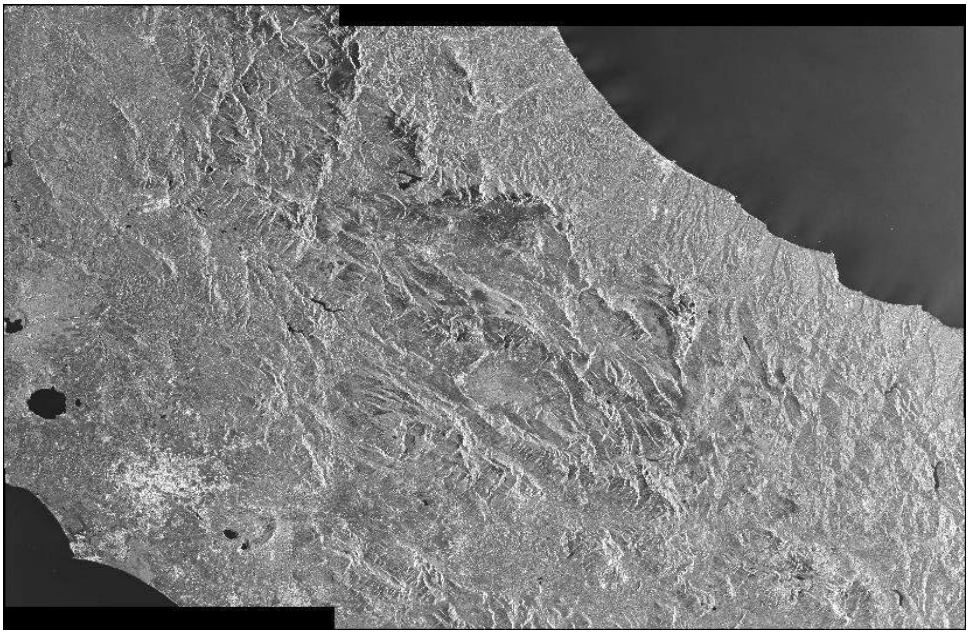

Figure 76: Silvi Marina AOI– incoherent mean of all the 49 processed images

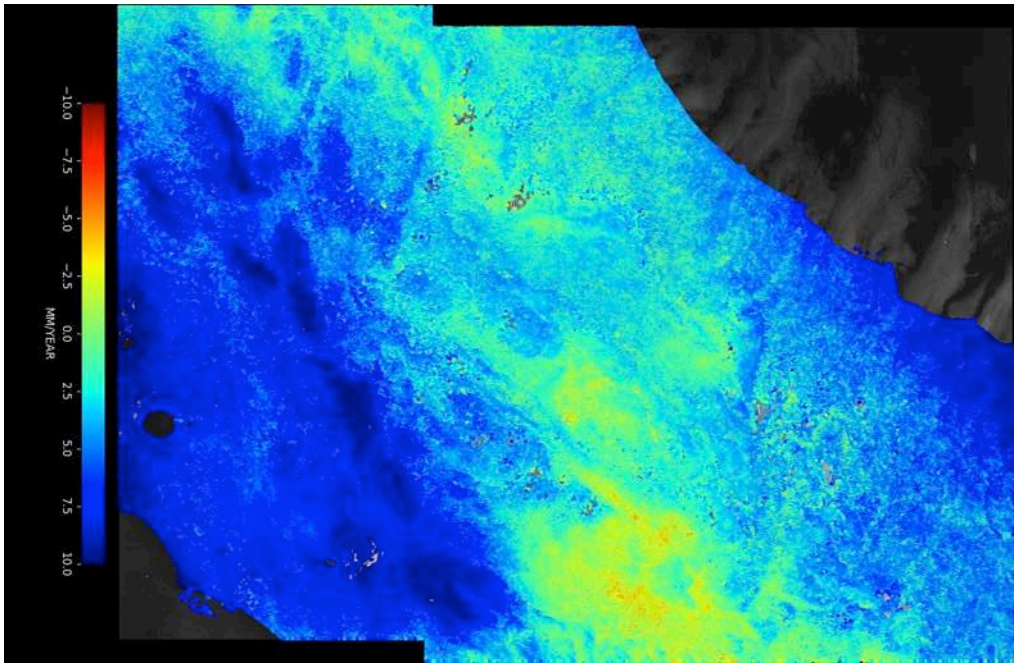

Figure 77: Silvi Marina AOI– Example of Atmospheric Phase Screen [mm/year].

The characteristics of the APS maps are summarized in the next table. Note that the temporal resolution does not comply with the OSCAR requirements for the IWV variable and the same applies for the timeliness. Nonetheless, SAR is the only instrument that permits achieving a horizontal (spatial) resolution that complies the OSCAR one at goal level. Hence, it is worthwhile to use the InSAR technique to produce IPWV maps.

SAR APS	SENTINEL-1
Spatial Resolution	100 x 100 [m]
Temporal Resolution	6 days
Timeliness	24 hours from image delivery
Coverage	250 x 210 [Km]
Thematic Accuracy	Millimetric precision on LOS delay
Availability	TRE ALTAMIRA Data Center
Notes	None

APS maps show relative variations of tropospheric delay along the satellite line-of-sight (LOS) with respect to a “master image”. In order to reconstruct an “absolute” zenithal tropospheric delay, which can be then assimilated by WRF, a calibration procedure is needed. This consists in the following steps:

- retrieval of ZTD maps from a NWP model, corresponding to the area covered by SAR maps, at the time of each acquisition (in this work we used GACOS maps from http://ceg-research.ncl.ac.uk/v2/gacos/);
- computation of relative variation of GACOS data with respect to the same time of the SAR master image;
- mapping of zenithal relative GACOS delay onto the LOS, using the cosine of the given incidence angle (obtaining the so-called “GACOS APS”);

- estimation of a plane fitting the difference between GACOS APS and SAR APS; this is done to consider orbital and ionosphere-induced errors;
- the estimated plane is removed from the SAR APS maps, and these are then mapped back to the zenithal direction;
- the zenithal SAR APS are then averaged over time, to produce a “mean SAR APS map”; the same is done also for the GACOS absolute zenithal maps;
- the mean SAR APS map is removed from each zenithal SAR APS, and the mean GACOS absolute zenithal map is added; this finalizes the calibration procedure, reconstructing the correct absolute zenithal tropospheric delay maps.

8.4 Result and validation

The data ingestion has been performed according to 3 different methodologies: direct insertion, nudging, and finally 3DVAR assimilation.

Direct insertion is meant hereafter as the substitution of a given variable in the NWM fields with the corresponding one retrieved by EO sensors.

Nudging is the simplest form of data assimilation that adjusts, via basic netwonian relaxation techniques, a given dynamical variables of NWM using EO data to provide a realistic representation of the atmosphere at a given time.

3DVAR is a variational data assimilation procedure that produces improved initial conditions by statistically merging one-time observations and forecast field at the same time. Variational data assimilation is based on a physical constraint derived from the forward model (forecast) so that the assimilation problem is formulated as an iterative process whose aim is to minimize the gap between observations and model states. The 3DVAR problem solution is given by the analysis state that minimizes the cost function which represents the a

posteriori maximum likelihood estimate of the true state of the atmosphere, combining the two sources of data: observations and background. The mapping between the observational data sources and the corresponding data ingestion methodologies for the two case studies is presented in the following table.

Event data	Event name	Ingestion methodology		
		Direct insertion	Nudging	3DVAR
9-10 September 2017	Livorno	LST, SST	SM	GNSS, WIND OVER OCEAN
14-15 November 2017	Silvi Marina	LST, SST	SM	INSAR, GNSS, WIND OVER OCEAN

Table 22: cases studies and related ingestion methodologies for the different data sources.

The analysis of the different NWM experiments results is performed in terms of comparison between observed and predicted rainfall depth fields.

The comparison has been performed by using the Method for Object Based Evaluation (MODE) approach. MODE resolves objects in both the forecast and observed fields. Object attributes are calculated and compared, and are used to associate (merge) objects within a single field, as well as to match objects between the forecast and observed fields. Finally, summary statistics describing the objects and object pairs are produced. These statistics can be used to identify correlations and differences among the objects, leading to insights concerning forecast strengths and weaknesses.

8.4.1 Livorno test case

The NWM experiments performed for this case study are driven respectively by IFS and GFS global circulation models with initialization at 18 UTC on 8 September 2017, 3 hours update of the boundary conditions, and 48 hours forecasting time interval.

The following table summarizes the methodology and timing for the ingestion of the different data sources (alone or their combinations)

Data source	Ingestion methodology	Timing
LST	Direction insertion	10 UTC 09/09/2017
SST	Direction insertion	21 UTC 09/09/2017
SM	Nudging	18 UTC 08/09/2017
GNSS/ZTD	3DVAR	multiple (down to 3 hour resolution)
WIND OVER OCEAN	3DVAR	18 UTC 08/09/2017
WIND OVER OCEAN + SM+ZTD	NUDGING, 3DVAR	variable

The maps to be directly inserted into the corresponding NWM fields have been obtained by an inverse square distance weighting interpolation of the Sentinel data on the WRF domains computational grids. The native WRF model data have been substituted by the EO derived ones, where available, while the native WRF model data have been maintained elsewhere. This approach has been applied to LST and SST variables and the results are provided in the following figures, referring to the innermost domain at 1.5 km grid spacing. Figure 78 and Figure 80 refer to GFS driven cases (LST and SST), while Figure 79 and Figure 81 refer to IFS driven cases (LST and SST).

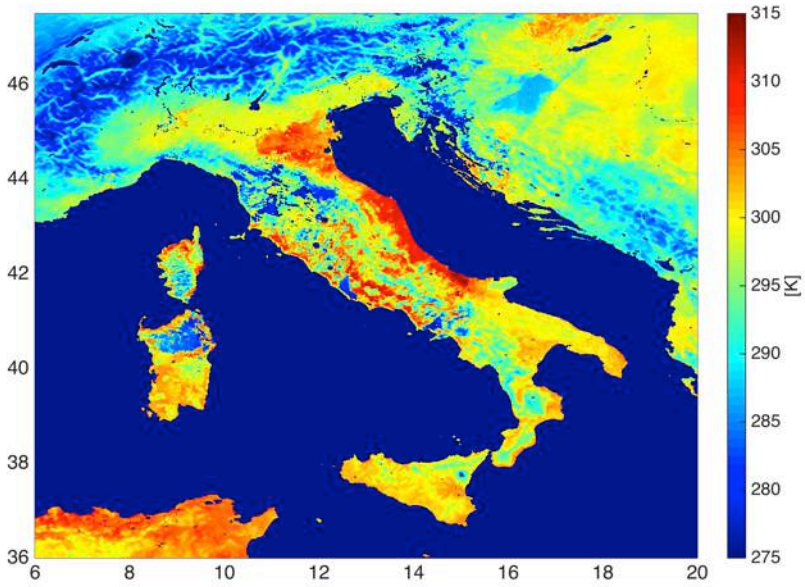

Figure 78: GFS driven cases. LST map passed to the WRF model via direction insertion at 10 UTC 09/09/2017.

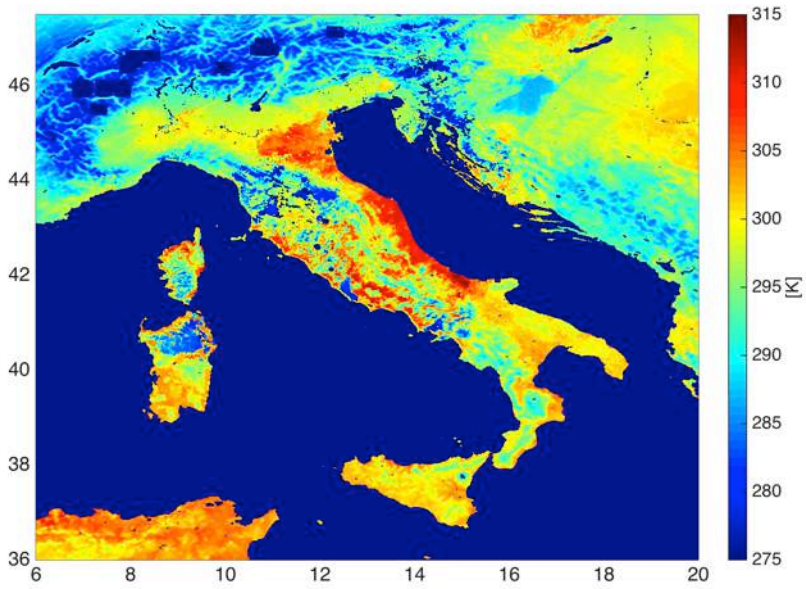

Figure 79: IFS driven cases. LST map passed to the WRF model via direction insertion at 10 UTC 09/09/2017.

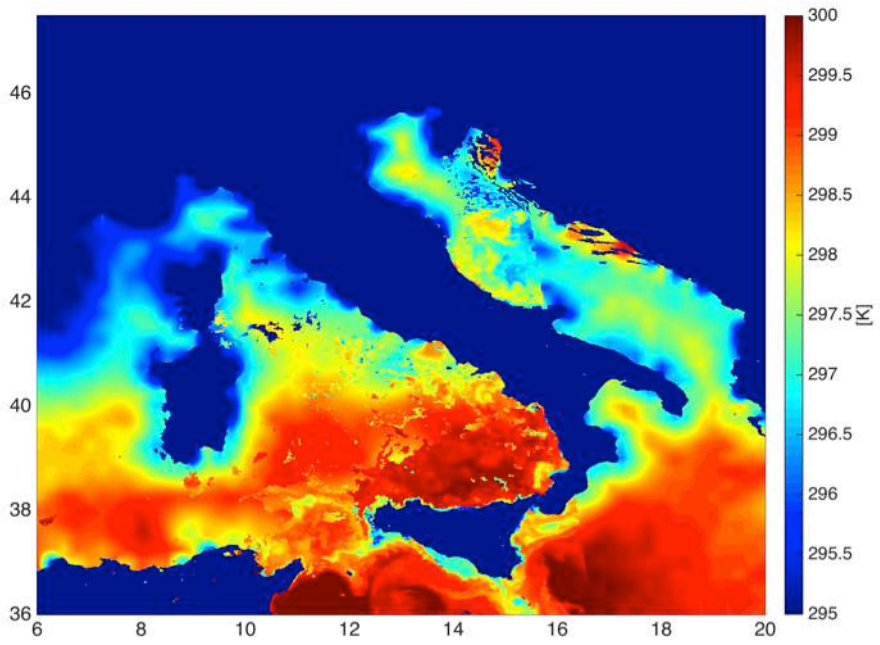

Figure 80: IFS driven cases. SST map passed to the WRF model via direction insertion at 21 UTC 09/09/2017.

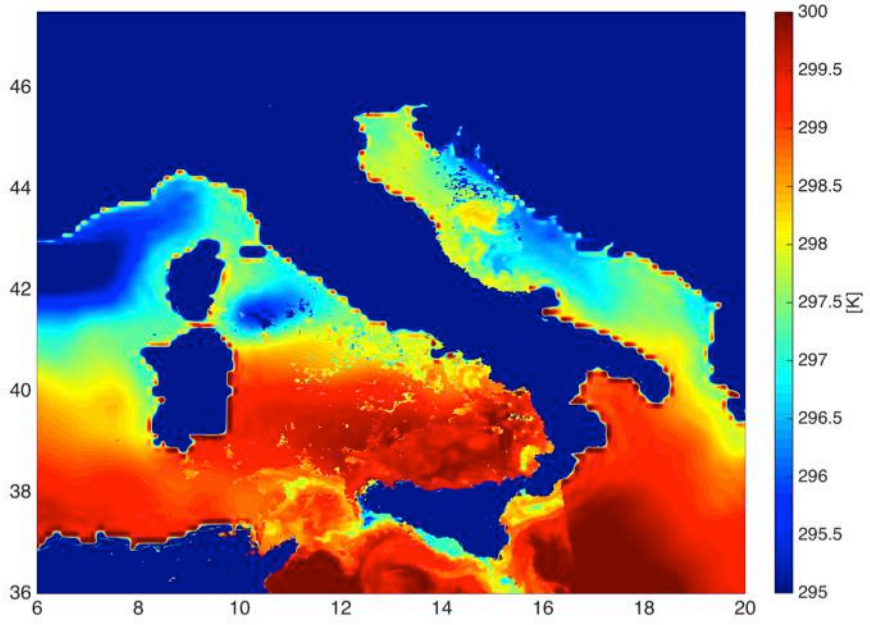

Figure 81: IFS driven cases. SST map passed to the WRF model via direction insertion at 21 UTC 09/09/2017.

The SM data preparation has been slightly more complex and inspired by a nudging like approach described hereafter: the difference map between Sentinel retrieved SM and the WRF SM field at the surface is computed; the resulting difference map is interpolated and smoothed back on the WRF model computational grids (one for each parent and/or nested domain); subsequently the direct insertion in the corresponding WRF surface layer SM field is made; finally, a vertical profile correction through linear interpolation of the difference between the Sentinel surface observation and the model one assuming zero difference at deepest level is performed. The resulting maps for each soil model layer (six in case of the adopted soil model) are presented in the following figures. Figure 82 refers to GFS driven cases, while Figure 83 refers to IFS driven cases.

Concerning the wind over ocean (Sentinel 1) data, they have been interpolated by an inverse square distance weighting interpolation over the WRF domains computational grids and have been assimilated using the WRF 3DVAR technique as 10m wind observations.

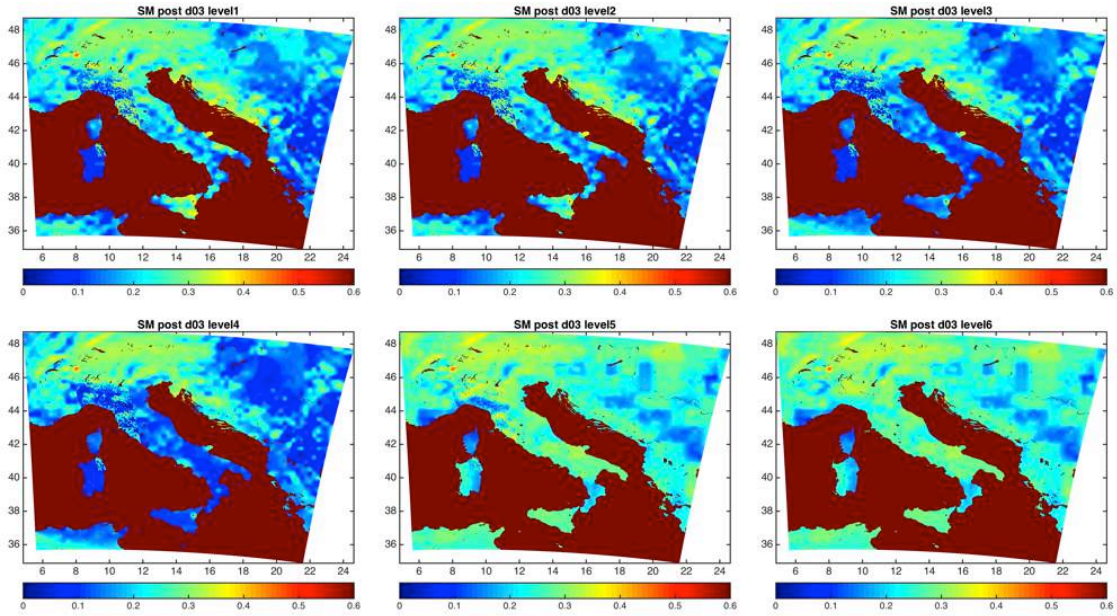

Figure 82: GFS driven cases. SM maps for each soil model layer passed to the WRF model via direction insertion at 18 UTC 09/09/2017.

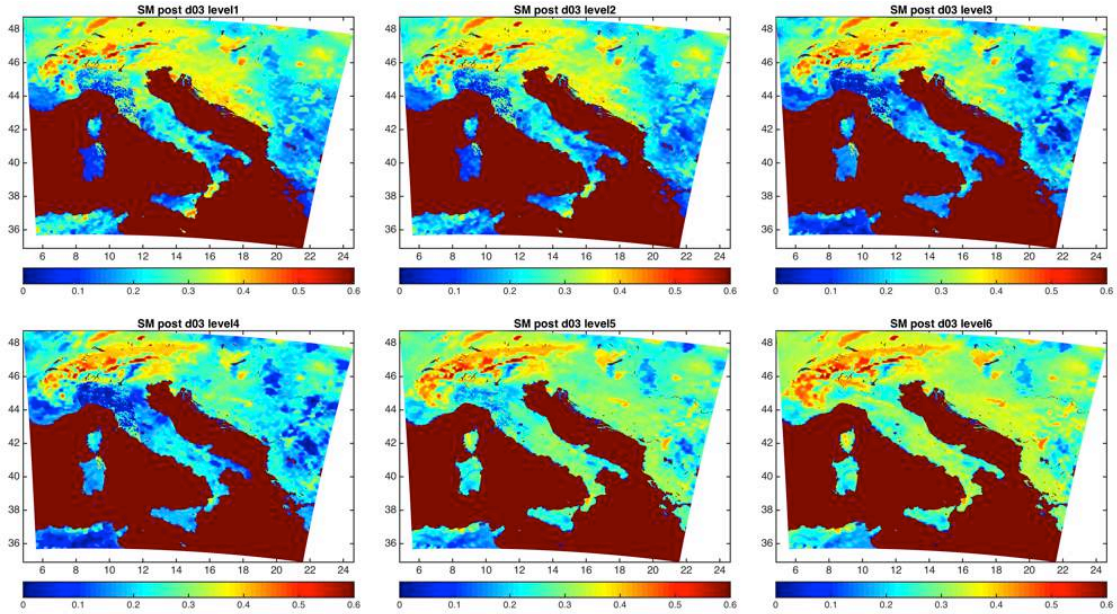

Figure 83: IFS driven cases. SM maps for each soil model layer passed to the WRF model via direction insertion at 18 UTC 09/09/2017.

The following pictures summarizes the QPF values provided by the different modelling experiments for the 12 hours time period from 18UTC on 9 September 2017 to 06UTC on 10 September 2017, where a=LST (direct insertion), b=SST (direct insertion), c=SM (nudging), d=WIND (3DVAR at the analysis time), e=ZTD3h (3DVAR 3h cycling with all the 1-minute ZTD observations available over a 30 minutes time window at the analysis time), f=ZTD3h_1ist (3DVAR 3h cycling with the 1-minute ZTD observations temporally nearest to the analysis time,), g=WIND+SM+ZTD (3DVAR wind at the analysis time, SM direction insertion at the analysis time, 3DVAR 3h cycling with the 1-minute ZTD observations temporally nearest to the analysis time), h=WIND+SM+ZTD (3DVAR wind at the analysis time, SM direction insertion at the analysis time, 3DVAR with the 1-minute ZTD observations temporally nearest to 18UTC), i=OBS, j=Open Loop (OL). Figure 84 refers to GFS driven cases, while Figure 85 refers to IFS driven cases.

The MODE analysis has been performed for three different rainfall thresholds namely 24, 48 and 72 mm: the results are presented in Table 23, Table 24, and Table 25. The main goal of this meteorological validation, from a QPF standpoint, is to select the best meteorological forecast out of the whole set of the sensitivity experiments. The most reliable meteorological forecast is selected as in Lagasio et al. (2017): all the indices and statistical scores described above are calculated for each sensitivity experiment, then the times in which a simulation has been the best for each score is counted. Finally, the run ranking as the best for the higher number of times is identified.

Based on this approach, in the case of the GFS driven experiments, the best performing run is WIND+SM+ZTD (3DVAR wind at the analysis time, SM direction insertion at the analysis time, 3DVAR 3h cycling with the 1-minute ZTD observations temporally nearest to the analysis time) with a total of 15 best scores. Conversely, in the case of the IFS driven experiments, the best performing one is WIND (3DVAR at the analysis time, namely 18 UTC on 08/09/2018), with a total of 16 best scores. Looking at the higher thresholds (48 and 72 mm, Table 24 and Table 25), for GFS driven simulations the assimilation of wind, soil moisture and ZTD (WIND+SM+ZTD) observations improve the OL predictive capability both in terms of POD and FAR, while the WIND only assimilation achieves the best result in terms of FBIAS. Furthermore in terms of structure location and shape WIND+SM+ZTD experiment provides the minimum CENTROID DIST, the maximum AREA RATIO and the best SYMMETRIC DIFF for the most intense core of precipitation (72 mm thresholds, Table 25).

Concerning the simulations driven by IFS, the best results in terms of POD and FBIAS is reached with the WIND only assimilation while the best FAR is

reached with the WIND+SM+ZTD experiment. In terms of spatial pattern, in this case the WIND only assimilation gives the best AREA RATIO, SYMMETRIC DIFF and INTERSERSECTION AREA revealing a good localization of precipitation pattern.

The rather heterogeneous response to the assimilated Sentinel and GNSS derived variables by the GFS and IFS driven experiments it is most probably due to the difference in their respective initial conditions fields. For sake of clarification and exemplification, the reader is referred to Figure 82 and Figure 83, where the comparison between SM analysis fields, outside the direct insertion/assimilation areas suggests quite prominent differences between GFS and IFS values, namely IFS soil layers look definitely drier than GFS ones. Then, this difference can lead to different response to the assimilation of the same observation.

It is also worth to notice that the assimilation of wind, soil moisture and ZTD all together (WIND+SM+ZTD and WIND+SM+ZTD_18UTC experiments) ranks well for both driving GCMs Thus, for operational purpose, this can be a recommended assimilation setup possibly with a 3-hour cycling 3dvar.

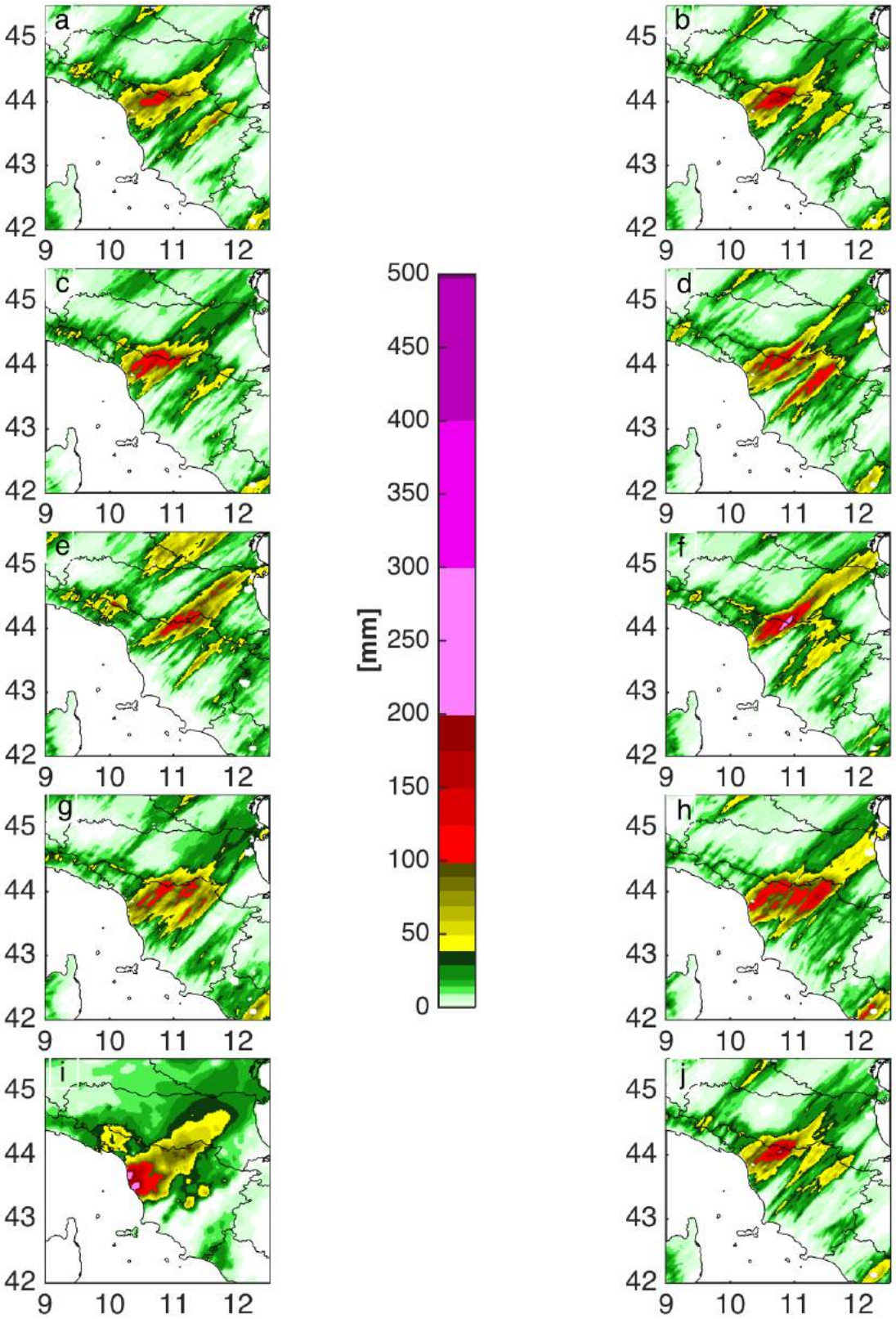

Figure 84: GFS driven cases. QPF values for the 12 hours time period from 18UTC on 9 September 2017 to 06UTC on 10 September 2017, where a=LST, b=SST, c=SM, d=WIND, e=ZTD3h, f=ZTD3h_1ist, g=WIND+SM+ZTD, h=WIND+SM+ZTD_18UTC (only 18UTC), i=OBS, j=Open Loop (OL). For details about the 3DVAR approaches the reader is referred to the main text.

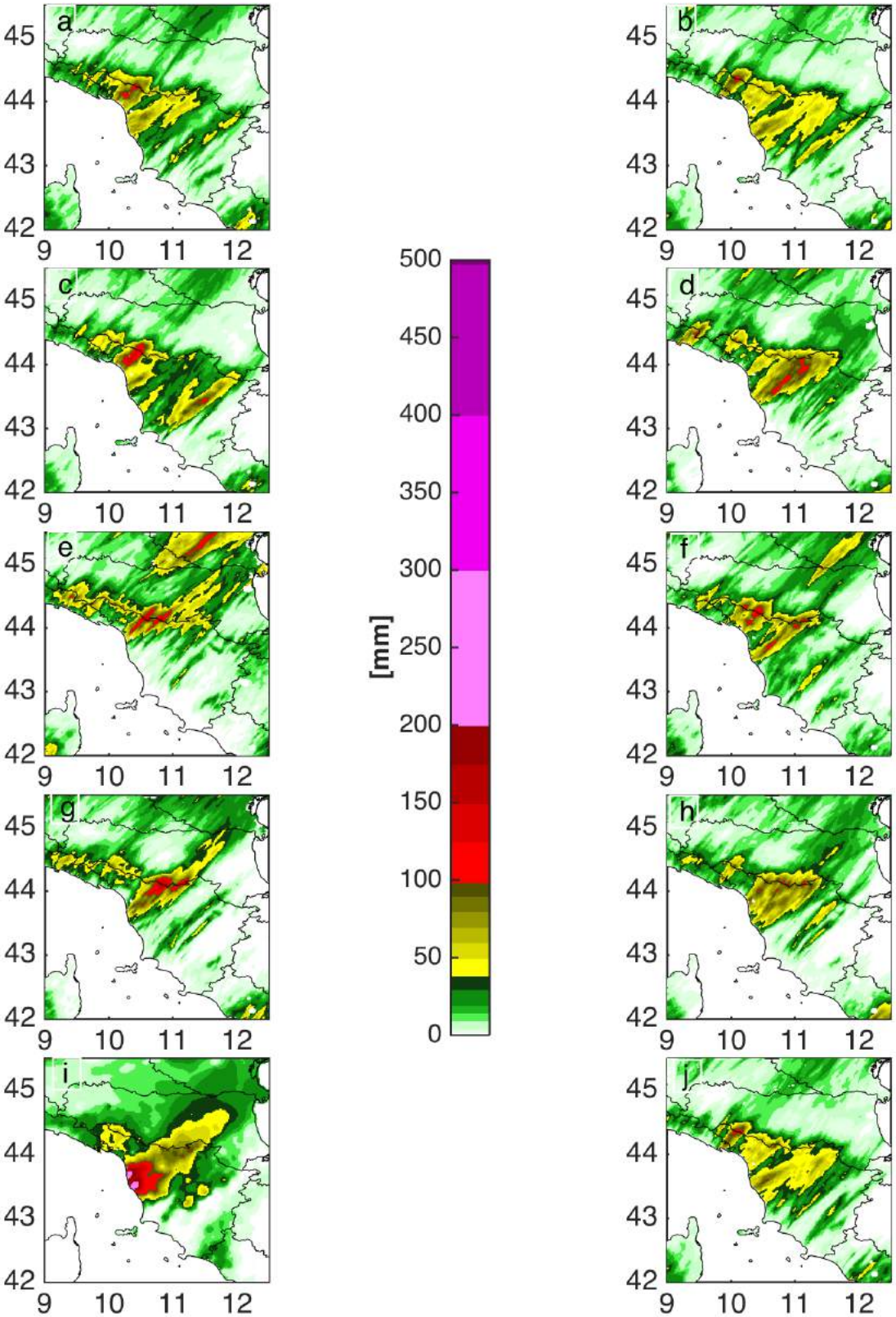

Figure 85: IFS driven cases. QPF values for the 12 hours time period from 18UTC on 9 September 2017 to 06UTC on 10 September 2017, where a=LST, b=SST, c=SM, d=WIND, e=ZTD3h, f=ZTD3h_1ist, g=WIND+SM+ZTD, h=WIND+SM+ZTD_18UTC (only 18UTC), i=OBS, j=Open Loop (OL). For details about the 3DVAR approaches the reader is referred to the main text.

24 mm (GFS)													
run	CENTROID DIST	ANGLE DIFF	AREA RATIO	SYMMETRIC DIFF	INTERSECTION AREA	UNION AREA	P90 RATIO	FBIAS	PODY	FAR	CSI	HK	HSS
OL	5.34	4.15	0.73	3027.00	3395.00	6422.00	0.95	0.86	0.59	0.31	**0.47**	**0.48**	**0.50**
LST	5.88	23.10	0.70	3440.00	3202.00	6642.00	0.93	0.82	0.54	0.34	0.43	0.43	0.46
SM	**4.73**	12.86	0.72	3536.00	3209.00	6745.00	0.93	0.77	0.55	**0.29**	0.45	0.46	0.49
SST	4.97	5.64	0.73	**2959.00**	3450.00	**6409.00**	0.92	0.88	**0.60**	0.32	**0.47**	**0.48**	0.50
WIND	7.63	7.50	0.79	3902.00	3228.00	7130.00	0.88	0.92	0.55	0.40	0.41	0.40	0.41
WIND+SM+ZTD	9.44	8.17	**0.83**	3683.00	**3470.00**	7153.00	**0.98**	**0.93**	0.59	0.37	0.44	0.45	0.46
WIND+SM+ZTD_18UTC	14.09	12.80	0.78	3411.00	3429.00	6840.00	0.82	0.91	0.58	0.36	0.44	0.45	0.46
ZTD3h	6.58	22.54	0.76	4019.00	3067.00	7086.00	0.95	**1.07**	0.52	0.51	0.34	0.30	0.29
ZTD3h_1ist	7.70	**2.89**	0.80	3741.00	3329.00	7070.00	0.92	0.88	0.57	0.36	0.43	0.44	0.45
	Best small	***Best small***	***Best=1***	***Best small***	***Best big***	***Best small***	***Best=1***	***Best=1***	***Best=1***	***Best=0***	***Best=1***	***Best=1***	***Best=1***

24 mm (IFS)													
Run	CENTROID DIST	ANGLE DIFF	AREA RATIO	SYMMETRIC DIFF	INTERSECTION AREA	UNION AREA	P90 RATIO	FBIAS	PODY	FAR	CSI	HK	HSS
OL	18.77	65.31	0.76	3323.00	3418.00	6741.00	0.96	0.77	**0.59**	0.24	**0.50**	**0.51**	**0.55**
LST	15.33	40.81	0.70	3484.00	3192.00	6676.00	0.96	0.80	0.54	0.32	0.43	0.44	0.47
SM	16.99	50.12	0.77	3474.00	3295.00	6769.00	0.97	0.82	0.57	0.31	0.46	0.47	0.50
SST	15.88	47.68	0.76	3152.00	**3434.00**	6586.00	0.94	0.80	**0.59**	0.26	0.49	**0.51**	0.54
WIND	**11.28**	40.31	0.56	**3105.00**	2875.00	**5980.00**	0.82	0.69	0.50	0.27	0.43	0.43	0.47
WIND+SM+ZTD	16.52	10.32	0.66	3985.00	2875.00	6860.00	**0.98**	0.78	0.49	0.37	0.38	0.37	0.40
WIND+SM+ZTD_18UTC	11.52	24.46	0.62	3234.00	3138.00	6372.00	0.91	0.66	0.53	**0.19**	0.48	0.48	0.54
ZTD3h	24.91	**2.59**	**0.95**	5522.00	3271.00	8793.00	0.93	**1.09**	0.56	0.49	0.36	0.34	0.33
ZTD3h_1ist	10.65	14.09	0.73	4058.00	2961.00	7019.00	**0.98**	0.75	0.50	0.32	0.41	0.40	0.44
	Best small	***Best small***	***Best=1***	***Best small***	***Best big***	***Best small***	***Best=1***	***Best=1***	***Best=1***	***Best=0***	***Best=1***	***Best=1***	***Best=1***

Table 23: Spatial and statistical indices calculated through MODE (24 mm rainfall depth threshold) to evaluate the sensitivity forecasts (driven by GFS and IFS respectively) with respect to the Open Loop run for the time interval 18UTC 09/10/2017 – 06UTC 10/09/2017. The best performance for each score is highlighted in bold.

48 mm (GFS)													
Run	CENTROID DIST	ANGLE DIFF	AREA RATIO	SYMMETRIC DIFF	INTERSECTION AREA	UNION AREA	P90 RATIO	FBIAS	PODY	FAR	CSI	HK	HSS
OL	6.93	12.37	0.58	1653.00	760.00	2413.00	0.97	0.68	0.37	0.46	0.28	0.33	0.39
LST	7.07	21.42	0.67	**1225.00**	987.00	**2212.00**	0.90	0.81	0.48	0.40	0.36	0.45	0.49
SM	9.95	21.70	0.61	1456.00	817.00	2273.00	0.96	0.62	0.41	0.35	0.33	0.38	0.46
SST	8.09	23.04	0.63	1623.00	750.00	2373.00	0.92	0.65	0.36	0.44	0.28	0.33	0.39
WIND	**3.80**	28.05	**0.98**	1833.00	1022.00	2855.00	**0.99**	1.08	0.50	0.54	0.31	0.43	0.42
WIND+SM+ZTD	6.68	25.38	**0.98**	1325.00	1276.00	2601.00	0.98	**1.06**	0.62	**0.41**	0.43	0.57	0.56
WIND+SM+ZTD_18UTC	5.78	13.95	0.89	1256.00	**1410.00**	2666.00	0.87	1.22	**0.69**	0.44	**0.45**	**0.63**	**0.57**
ZTD3h	30.67	**2.35**	0.69	1629.00	809.00	2438.00	**0.99**	1.18	0.43	0.64	0.24	0.34	0.32
ZTD3h_1ist	29.33	2.38	0.80	2042.00	700.00	2742.00	0.95	0.91	0.35	0.62	0.22	0.28	0.30
	Best small	***Best small***	***Best=1***	***Best small***	***Best big***	***Best small***	***Best=1***	***Best=1***	***Best=1***	***Best=0***	***Best=1***	***Best=1***	***Best=1***

48 mm (IFS)													
run	CENTROID DIST	ANGLE DIFF	AREA RATIO	SYMMETRIC DIFF	INTERSECTION AREA	UNION AREA	P90 RATIO	FBIAS	PODY	FAR	CSI	HK	HSS
OL	13.39	80.17	0.44	1731.00	537.00	2268.00	0.74	0.67	0.29	0.57	0.21	0.25	0.29
LST	7.06	13.13	0.30	1354.00	570.00	**1924.00**	0.75	0.59	0.32	0.46	0.25	0.29	0.35
SM	23.40	41.72	0.31	2147.00	186.00	2333.00	**0.98**	0.62	0.14	0.78	0.09	0.08	0.10
SST	8.41	48.21	0.53	1873.00	533.00	2406.00	0.73	0.67	0.30	0.56	0.21	0.25	0.30
WIND	**1.19**	18.00	**0.76**	1171.00	1105.00	2276.00	0.92	**0.88**	**0.56**	0.36	0.43	**0.53**	0.56
WIND+SM+ZTD	6.78	**8.92**	0.47	1226.00	795.00	2021.00	**0.98**	0.56	0.41	**0.27**	0.36	0.39	0.49
WIND+SM+ZTD_18UTC	6.99	16.59	0.72	**1040.00**	**1130.00**	2170.00	0.92	0.81	**0.56**	0.31	**0.45**	**0.53**	**0.58**
ZTD3h	12.97	19.91	0.49	1757.00	550.00	2307.00	0.83	1.13	0.30	0.74	0.16	0.20	0.19
ZTD3h_1ist	13.91	41.69	0.58	1812.00	685.00	2497.00	0.93	0.75	0.33	0.56	0.24	0.29	0.32
	Best small	***Best small***	***Best=1***	***Best small***	***Best big***	***Best small***	***Best=1***	***Best=1***	***Best=1***	***Best=0***	***Best=1***	***Best=1***	***Best=1***

Table 24: Spatial and statistical indices calculated through MODE (48 mm rainfall depth threshold) to evaluate the sensitivity forecasts (driven by GFS and IFS respectively) with respect to the Open Loop run for the time interval 18UTC 09/10/2017 – 06UTC 10/09/2017. The best performance for each score is highlighted in bold.

72 mm (GFS)													
run	CENTROID DIST	ANGLE DIFF	AREA RATIO	SYMMETRIC DIFF	INTERSECTION AREA	UNION AREA	P90 RATIO	FBIAS	PODY	FAR	CSI	HK	HSS
OL	12.32	9.93	0.54	1201.00	227.00	1428.00	**0.97**	0.55	0.21	0.61	0.16	0.19	0.25
LST	11.47	20.60	0.53	1118.00	263.00	1381.00	0.92	0.61	0.25	0.59	0.18	0.23	0.28
SM	11.57	20.55	0.64	1115.00	322.00	1437.00	0.93	0.65	0.30	0.53	0.23	0.28	0.34
SST	12.52	10.44	0.54	1213.00	221.00	1434.00	0.96	0.55	0.21	0.62	0.15	0.19	0.24
WIND	11.49	15.39	0.66	1078.00	352.00	1430.00	**0.97**	**1.06**	0.33	0.69	0.19	0.29	0.28
WIND+SM+ZTD	**9.11**	13.49	**0.78**	**755.00**	577.00	**1332.00**	0.95	**1.06**	0.54	**0.49**	**0.36**	0.51	**0.50**
WIND+SM+ZTD_18UTC	11.50	22.88	0.71	1217.00	**681.00**	1898.00	**0.97**	1.53	**0.64**	0.58	0.34	**0.59**	0.47
ZTD3h	38.14	2.82	0.70	1298.00	262.00	1560.00	0.95	0.84	0.25	0.71	0.15	0.21	0.23
ZTD3h_1ist	20.16	**0.06**	0.68	1317.00	242.00	1559.00	0.90	0.71	0.23	0.68	0.15	0.20	0.23
	Best small	***Best small***	***Best=1***	***Best small***	***Best big***	***Best small***	***Best=1***	***Best=1***	***Best=1***	***Best=0***	***Best=1***	***Best=1***	***Best=1***

72 mm (IFS)													
run	CENTROID DIST	ANGLE DIFF	AREA RATIO	SYMMETRIC DIFF	INTERSECTION AREA	UNION AREA	P90 RATIO	FBIAS	PODY	FAR	CSI	HK	HSS
OL	14.53	**0.84**	0.09	973.00	99.00	**1072.00**	0.87	0.23	0.09	0.60	0.08	0.09	0.13
LST	12.49	13.28	0.05	1021.00	51.00	**1072.00**	0.82	0.29	0.05	0.83	0.04	0.03	0.05
SM	16.38	4.69	0.04	1031.00	41.00	**1072.00**	0.85	0.48	0.04	0.92	0.03	0.01	0.02
SST	15.03	1.67	0.08	989.00	84.00	1073.00	0.85	0.21	0.08	0.62	0.07	0.07	0.12
WIND	8.37	0.94	**0.62**	**783.00**	**477.00**	1260.00	0.93	**0.73**	**0.45**	0.38	**0.35**	**0.43**	**0.50**
WIND+SM+ZTD	11.23	6.73	0.49	914.00	344.00	1258.00	0.98	0.51	0.32	**0.36**	0.27	0.31	0.41
WIND+SM+ZTD_18UTC	9.82	21.93	0.58	996.00	348.00	1344.00	0.87	0.63	0.33	0.48	0.25	0.31	0.38
ZTD3h	16.77	19.09	0.33	1371.00	30.00	1401.00	**0.99**	0.70	0.03	0.96	0.02	-0.01	-0.01
ZTD3h_1ist	**8.10**	3.48	0.25	872.00	233.00	1105.00	0.91	0.48	0.22	0.54	0.17	0.21	0.27
	Best small	**Best small**	**Best=1**	**Best small**	**Best big**	**Best small**	**Best=1**	**Best=1**	**Best=1**	**Best=0**	**Best=1**	**Best=1**	**Best=1**

Table 25: Spatial and statistical indices calculated through MODE (72 mm rainfall depth threshold) to evaluate the sensitivity forecasts (driven by GFS and IFS respectively) with respect to the Open Loop run for the time interval 18UTC 09/10/2017 – 06UTC 10/09/2017. The best performance for each score is highlighted in bold.

24 mm	48 mm	72 mm	TOT	GFS DRIVEN CASES
3	0	1	4	OL
0	2	0	2	LST
2	0	0	2	SM
5	0	0	5	SST
0	3	2	5	WIND
4	3	**8**	**15**	**WIND+SM+ZTD**
0	**5**	4	9	WIND+SM+ZTD_18UTC
1	1	0	2	ZTD3h
1	0	1	2	ZTD3h_1ist

Table 26: Summary of the sensitivity performances (GFS driven cases). The times in which each forecast has the best result for each score is counted for each threshold and summarized in a total count (summing Tables 1, 2 and 3) that is used to find the best simulation.

24 mm	48 mm	72 mm	TOT	IFS DRIVEN CASES
4	0	2	6	OL
0	1	1	2	LST
0	1	1	2	SM
3	0	0	3	SST
3	5	**8**	**16**	**WIND**
1	3	1	5	WIND+SM+ZTD
1	**6**	0	7	WIND+SM+ZTD_18UTC
3	0	1	4	ZTD3h
1	0	1	2	ZTD3h_1ist

Table 27: Summary of the sensitivity performances (IFS driven cases). The times in which each forecast has the best result for each score is counted for each threshold and summarized in a total count (summing Tables 1, 2 and 3) that is used to find the best simulation.

To gain a deeper insight in the modelling experiments for the best performing IFS driven case, namely the WIND one, a reference timestep at 02UTC on 10/09/2017, corresponding to the most intense phase of the observed event, has been considered. Then, using the VAPOR (Visualization and Analysis Platform for Ocean, Atmosphere, and Solar Researchers, www.vapor.ucar.edu) software, the atmospheric flow field has been analysed for the OL experiment, corresponding to the QPF in panel J (Figure 85).

Over the same scene (Figure 86), 3D isosurfaces (5*10-5 kg/kg) for the rainwater, snow and graupel variables have been rendered in combination with the wind field at 10 m in case of the OL (panel A) and IFS 3DVAR-WIND case (panel C). The results show that over the area interested by the most intense observed rainfall phenomena (blue circle) the OL run is not able to produce any significant convective phenomena, while the IFS 3DVAR-WIND does it. This reflects in the vertical cross sections of the reflectivity field for the two modelling experiments (green circles panels B and D): while reflectivity is nearly absent nearby the Tuscany coastlines (Livorno area) for the OL experiment (panel B), conversely strong activity is apparent in panel D over the Livorno area and downshear the main convective system, with values peaking up to 50-55 dBz.

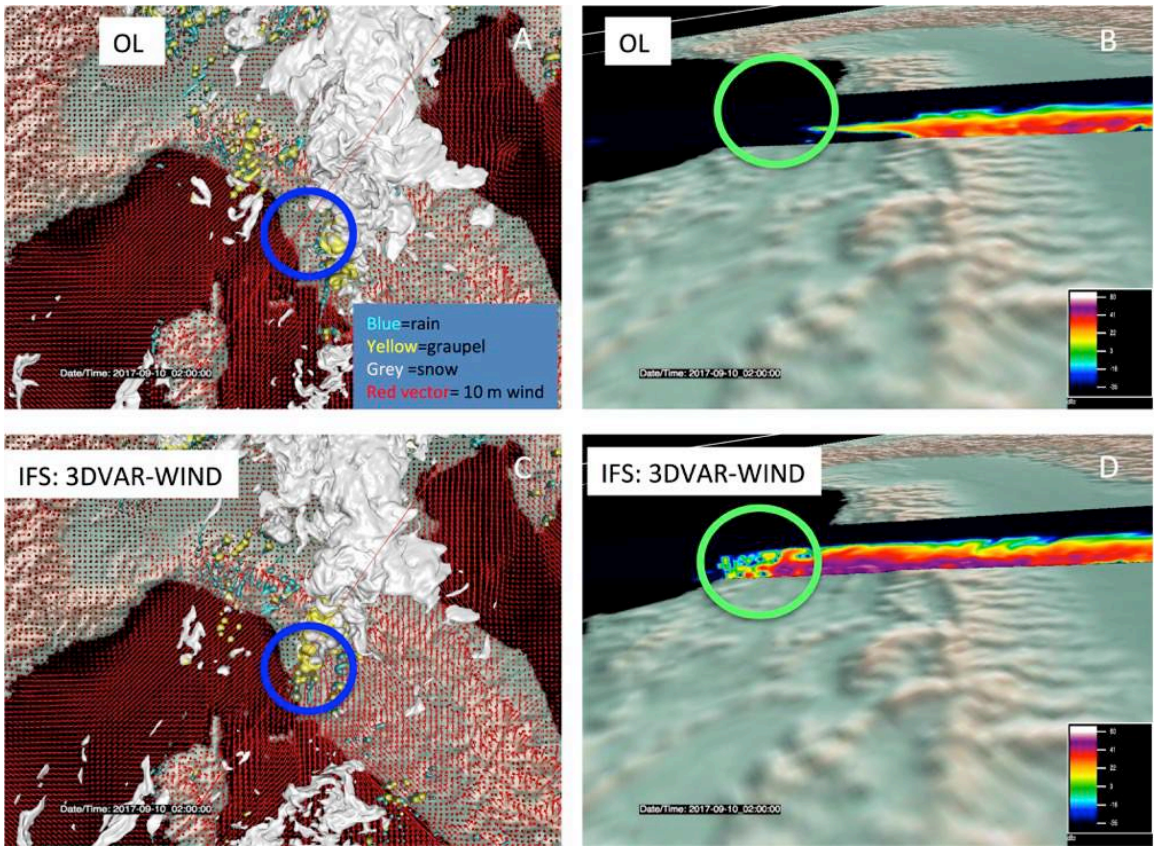

Figure 86: Comparison between the Open-Loop simulated structure with respect to the 3DVAR-WIND simulated structure at 02 UTC of 10 September 2017. Panels a and c report the 3D simulated structure composed by rainwater (cyano) graupel (yellow) and snow (grey) microphysics species respectively for Open Loop (a) and 3DVAR-WIND (c) simulations with the horizontal 10m wind intensity represented by red vectors. The red line in Panels a and c indicates the location of the vertical section of the two structures to investigate the reflectivity values in the middle of the convective structure in Panels b (for Open-Loop) and d (for 3DVAR-WIND).

8.4.2 Silvi Marina test case

The NWM experiments performed for this case study are driven respectively by IFS and GFS global circulation models with initialization at 00 UTC on 14 November 2017, 3 hours update of the boundary conditions, and 48 hours forecasting time interval.

The following table summarizes the methodology and timing for the ingestion of the different data sources (alone or their combinations)

Data source	Ingestion methodology	Timing
SM (Sentinel 1)	Nudging	05 UTC and 17UTC 14/11/2017
SMAP_S1 (SMAP and Sentinel 1)	Nudging	05 UTC and 17UTC 14/11/2017
SMAP	Nudging	05 UTC and 17UTC 14/11/2017
SST	Direction insertion	00 UTC 14/11/2017
WIND OVER OCEAN	3DVAR	05 UTC and 17UTC UTC 14/11/2017
ZTD3h_1ist	3DVAR	3-hour cycling
ZTD-INSAR	3DVAR	05 UTC 14/11/2017
WIND+SM+INSAR_only5	NUDGING, 3DVAR	05 UTC 14/11/2017

As in the case of Livorno, the maps to be directly inserted into the corresponding NWM fields have been obtained by an inverse square distance weighting interpolation of the Sentinel data on the WRF domains computational grids. The native WRF model data have been substituted by the EO derived ones, where available, while the native WRF model data have been maintained elsewhere. This approach has been applied to SST variable and the results are provided in the following figures, referring to the innermost domain at 1.5 km grid spacing. Figure 87 refers to GFS driven case, while Figure 88 refers to IFS one.

The SM data preparation has been based on a nudging like approach, described in the previous section for the Livorno case study. For the Silvi Marina case, the direct insertion of SM data has not been based only on Sentinel 1 data sources but it has involved also Soil Moisture Active Passive (SMAP) observations and SMAP-Sentinel 1 combination.

The resulting maps for each soil model layer (six in case of the adopted soil model) are presented in the following figures. Figure 89 and Figure 91 refer to GFS driven cases (05UTC and 17UTC on 14/11/2017), while Figure 90 and Figure 92 refer to IFS driven cases, when SM-Sentinel 1 are directly inserted. Conversely SM-SMAP data are directly inserted into GFS and IFS driven cases

respectively at 16UTC on 14/11/2017 (Figure 93 and Figure 94). The effect of the combined SMAP-Sentinel SM product is finally explored via direct insertion at 05UTC on 14/11/2017 (Figure 95 and Figure 96).

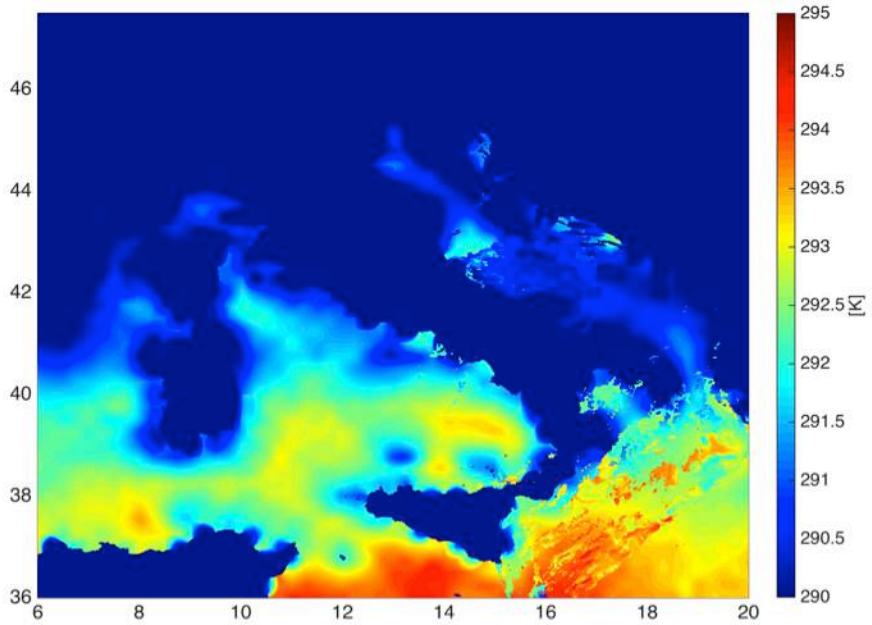

Figure 87: GFS driven cases. SST map passed to the WRF model via direction insertion at 00 UTC 14/11/2017.

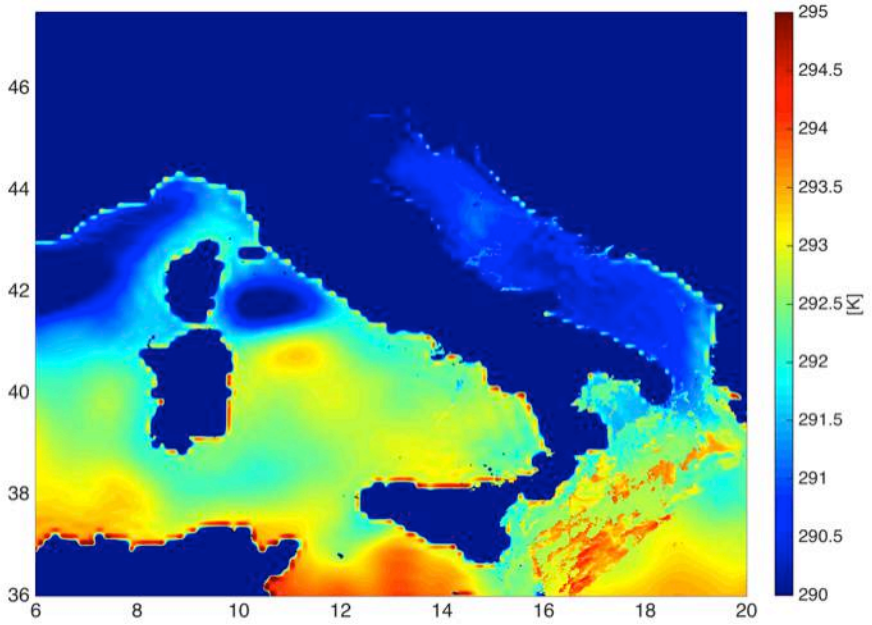

Figure 88: IFS driven cases. SST map passed to the WRF model via direction insertion at 00 UTC 14/11/2017.

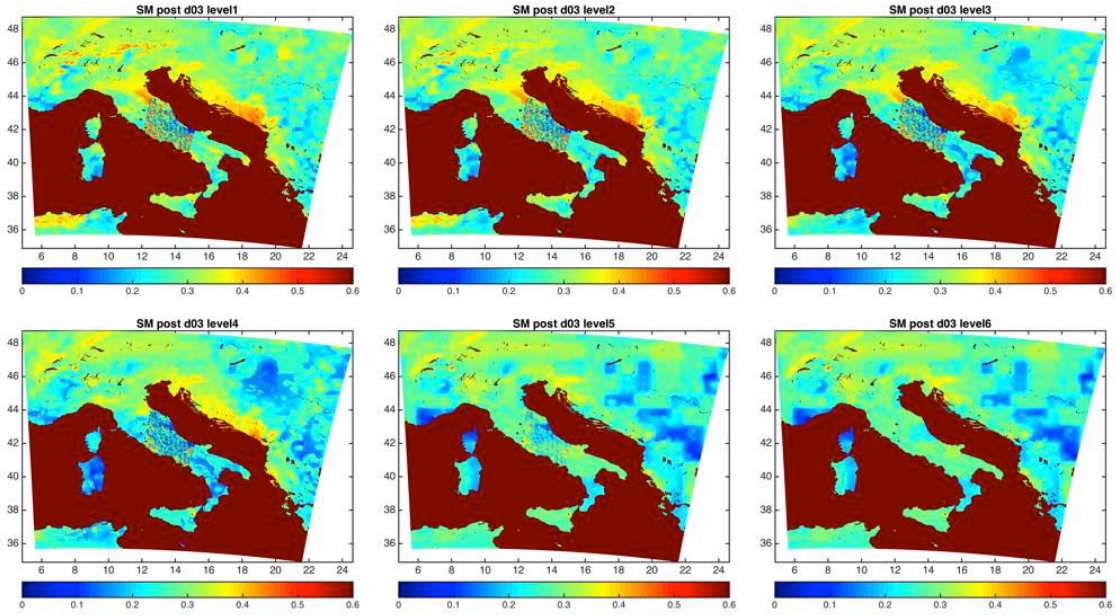

Figure 89: GFS driven cases. SM-Sentinel 1 maps for each soil model layer passed to the WRF model via direction insertion at 05 UTC 14/11/2017.

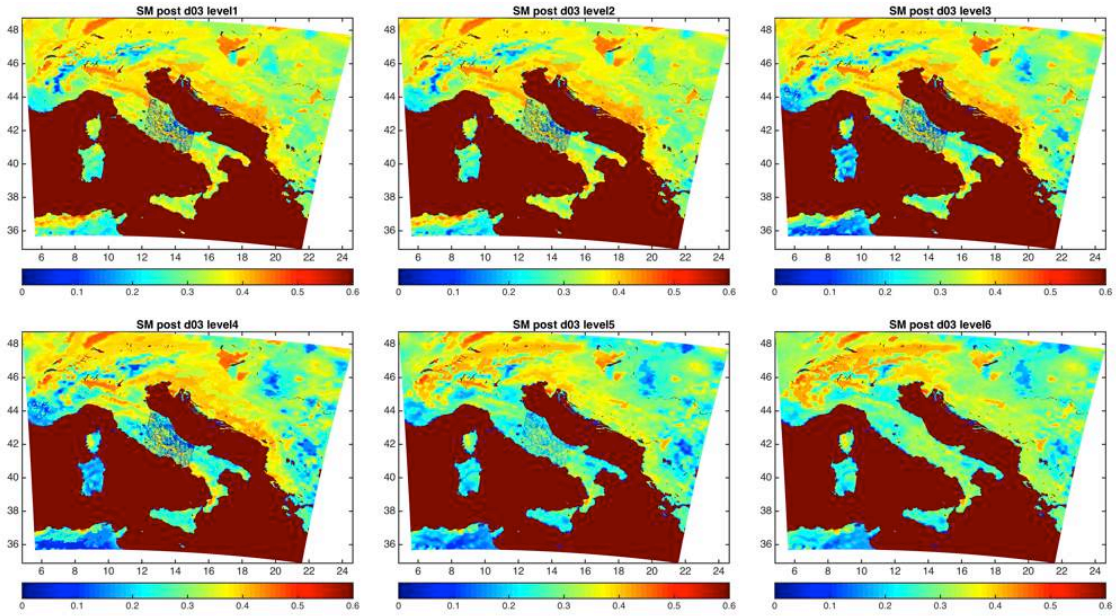

Figure 90: IFS driven cases. SM-Sentinel 1 maps for each soil model layer passed to the WRF model via direction insertion at 05 UTC 14/11/2017.

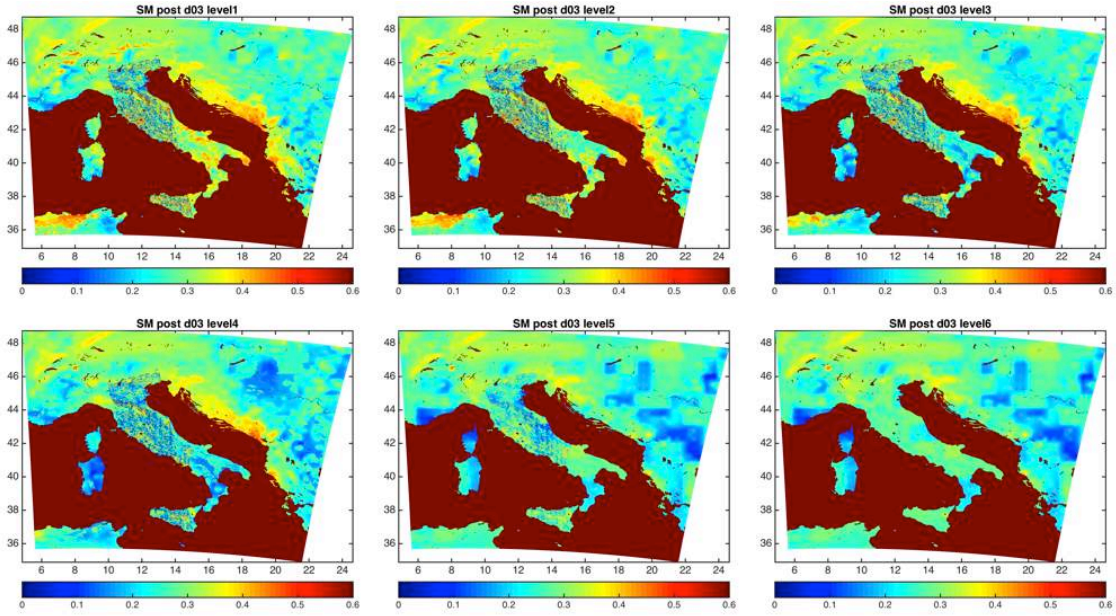

Figure 91: GFS driven cases. SM-Sentinel 1 maps for each soil model layer passed to the WRF model via direction insertion at 17 UTC 14/11/2017.

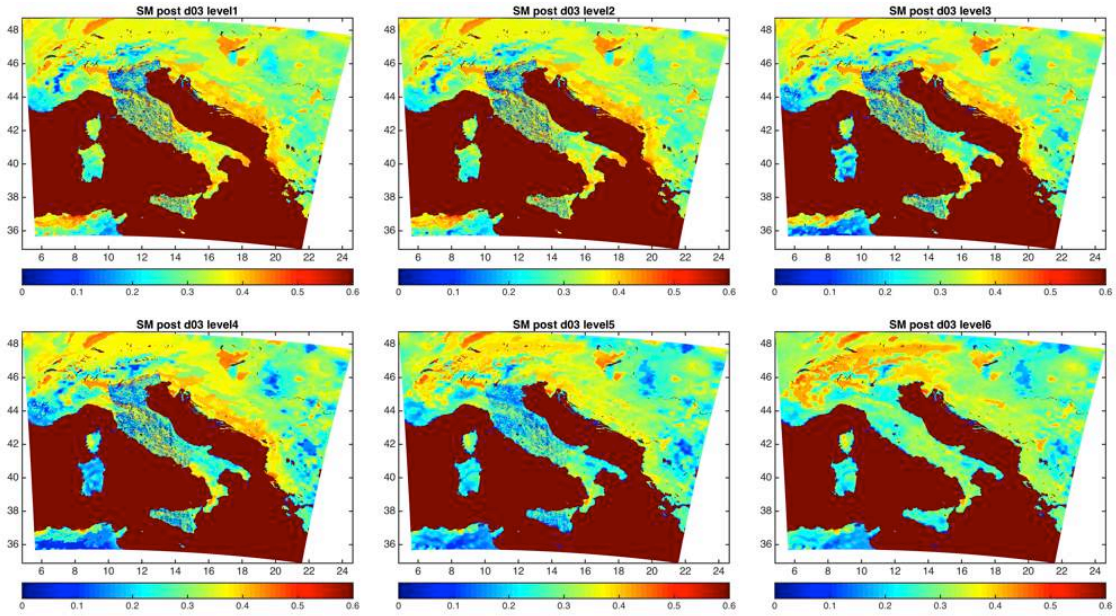

Figure 92: IFS driven cases. SM-Sentinel 1 maps for each soil model layer passed to the WRF model via direction insertion at 17 UTC 14/11/2017.

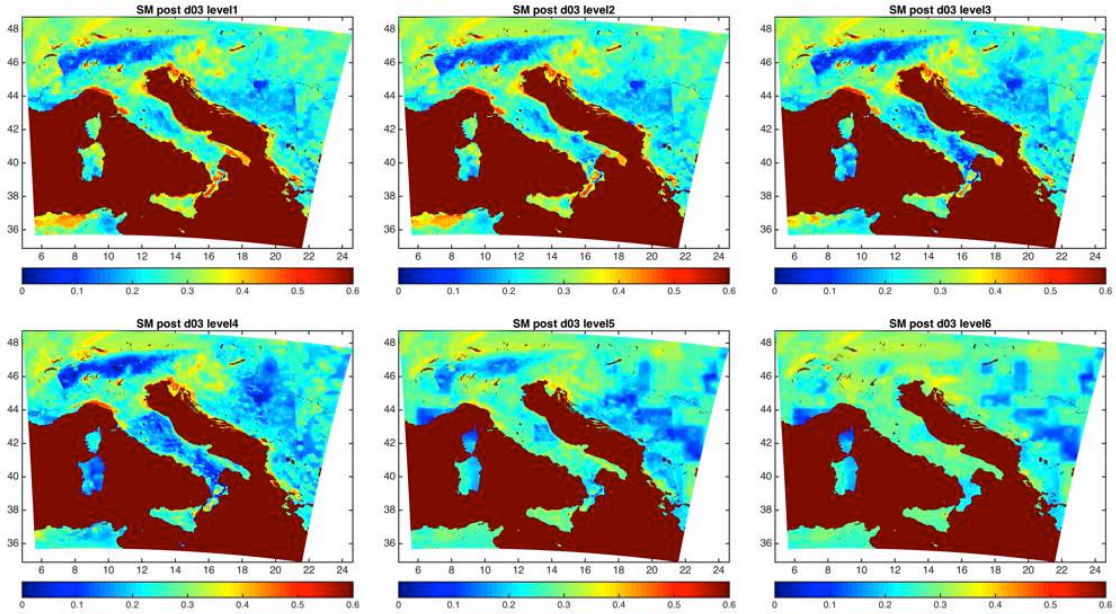

Figure 93: GFS driven cases. SM-SMAP 1 maps for each soil model layer passed to the WRF model via direction insertion at 16 UTC 14/11/2017.

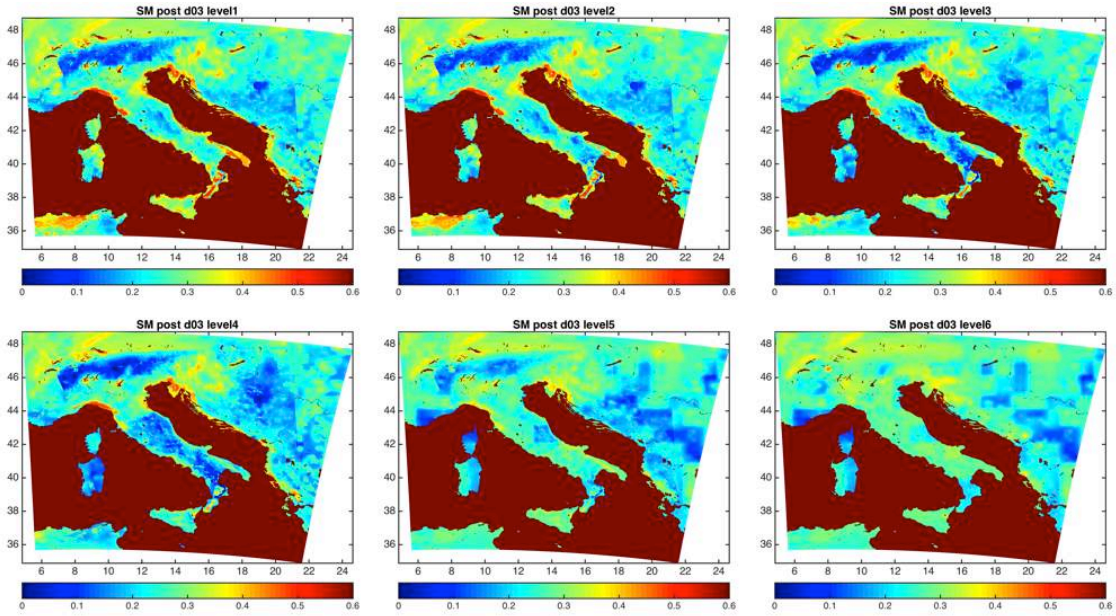

Figure 94: IFS driven cases. SM-SMAP maps for each soil model layer passed to the WRF model via direction insertion at 16 UTC 14/11/2017.

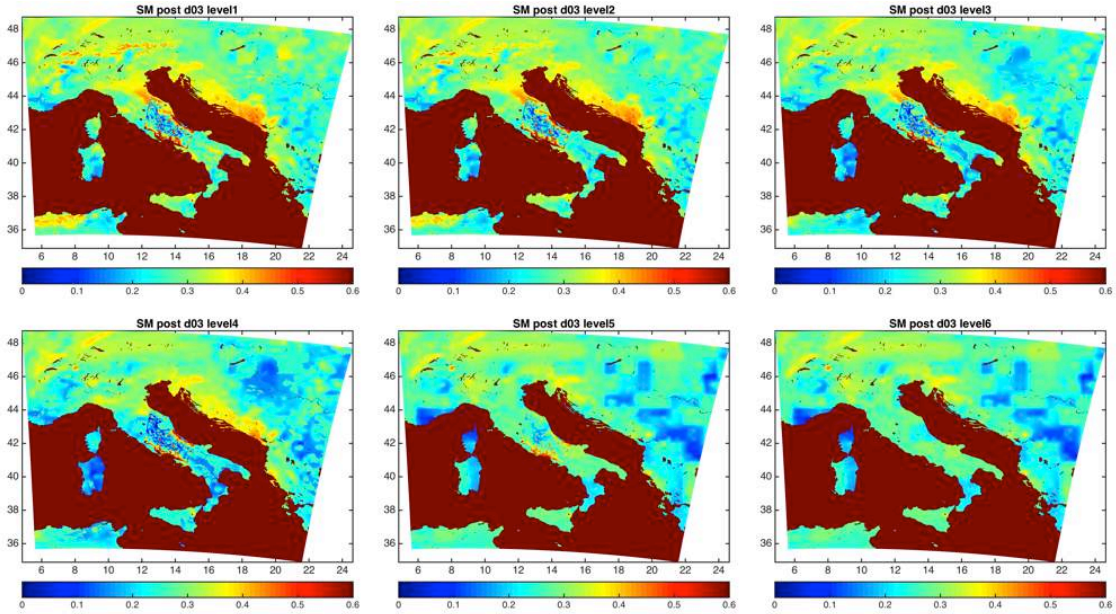

Figure 95: GFS driven cases. SM-SMAP/Sentinel 1 maps for each soil model layer passed to the WRF model via direction insertion at 05 UTC 14/11/2017.

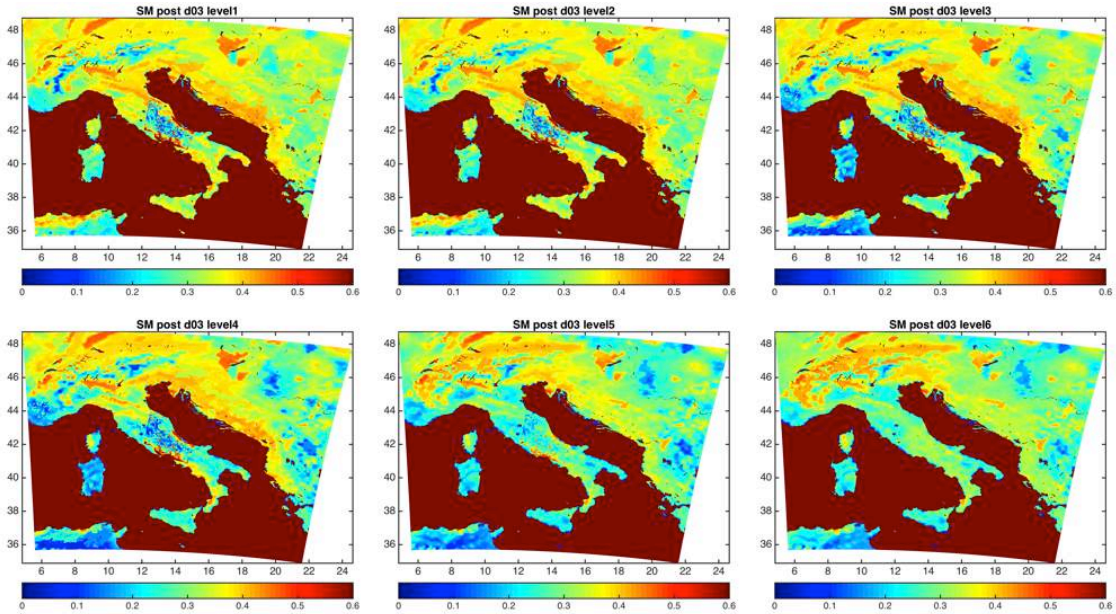

Figure 96: IFS driven cases. SM-SMAP/Sentinel 1 maps for each soil model layer passed to the WRF model via direction insertion at 05 UTC 14/11/2017.

The following pictures summarizes the QPF values provided by the different modelling experiments for the 24 hours time period from 00UTC on 15 November 2017 to 00UTC on 16 November 2017, where a=Open Loop, b=SST (direct insertion), c=SM-Sentinel 1 (nudging), d=SM-SMAP/Sentinel 1 (nudging), e=SM-SMAP (nudging), f=WIND (3DVAR at the analysis time), g=ZTD-INSAR (3DVAR at the analysis time), h=ZTD3h_1ist (3DVAR 3h cycling with the 1-minute ZTD observations temporally nearest to the analysis time), i=WIND+SM+ZTD-INSAR (SM direction insertion, 3DVAR wind and ZTD-INSAR at 05UTC 14/11/2017), j=OBS. Figure 97 refers to GFS driven cases, while Figure 98 refers to IFS driven cases.

The MODE analysis has been performed for three different rainfall thresholds namely 24, 48 and 72 mm: the results are presented in Table 28, Table 29, and Table 30. The main goal of this meteorological validation, from a QPF standpoint, is to select the best meteorological forecast out of the whole set of the sensitivity experiments. The most reliable meteorological forecast is selected as in Lagasio et al. (2017): all the indices and statistical scores described above are calculated for each sensitivity experiment, then the times in which a simulation has been the best for each score is counted. Finally, the run ranking as the best for the higher number of times is identified. Based on this approach the best performances, especially for the IFS driven experiments, are achieved with the ZTD assimilation whether from GNSS and InSAR observations. More specifically, the best performance is achieved with the 3-hour cycling 3dvar of GNSS observations providing the best POD with a FAR still be good (around 20-30% depending on thresholds) and the best FBIAS in particular for 72 mm threshold. The assimilation of ZTD from InSAR observation allow to achieve the second best result for the IFS driven experiment providing

the best FAR, CSI, HK and HSS scores for the 24 mm thresholds and obtaining good results also in the spatial pattern evaluation indices. Furthermore, with GFS the second best result is achieved with the SMAP_SM ingestion that has the best CENTROID DIST and AREA RATIO for the 24 mm thresholds, the best SYMM DIFF, CSI, HK and HSS values in the 48 mm thresholds and maintain same results also for the 72 mm thresholds. Finally, the simulation performed coupling SM, ZTD-InSAR and WIND data assimilation at 05 UTC of 14/11/2017 does not further improves the results obtained with the single variables even if it allows to improve the FAR for the 48 mm thresholds (both IFS and GFS) and 72 mm thresholds (IFS only).

It is worth to notice that this event, contrary to the Livorno use case, according to the Molini et al (2011) criterion can be classified as: type I –long-lived (duration d ≥ 12 hours) and spatially distributed (more than AS = 50 × 50 km^2). This can be the reason why a constant update of the ZTD every 3 hours from GNSS during the entire event allowed to obtain the best result with respect to a single update performed with the Sentinel observations. Furthermore, in this test case both the OL simulations have already a very good performance, thus it is more difficult to obtain a significant improvement from data assimilation.

Bearing in mind the of the overarching question of the STEAM project, namely if the Sentinel satellites constellation weather observation data can be used to better understand and predict with at higher spatial-temporal resolution the atmospheric phenomena resulting in severe weather events, the coupled variables data assimilation (SM+ZTD_INSAR+WIND) has been performed not looking at the best results obtained from the single variables standalone, but using in combination all the Sentinel derived observations that positively influenced the forecast.

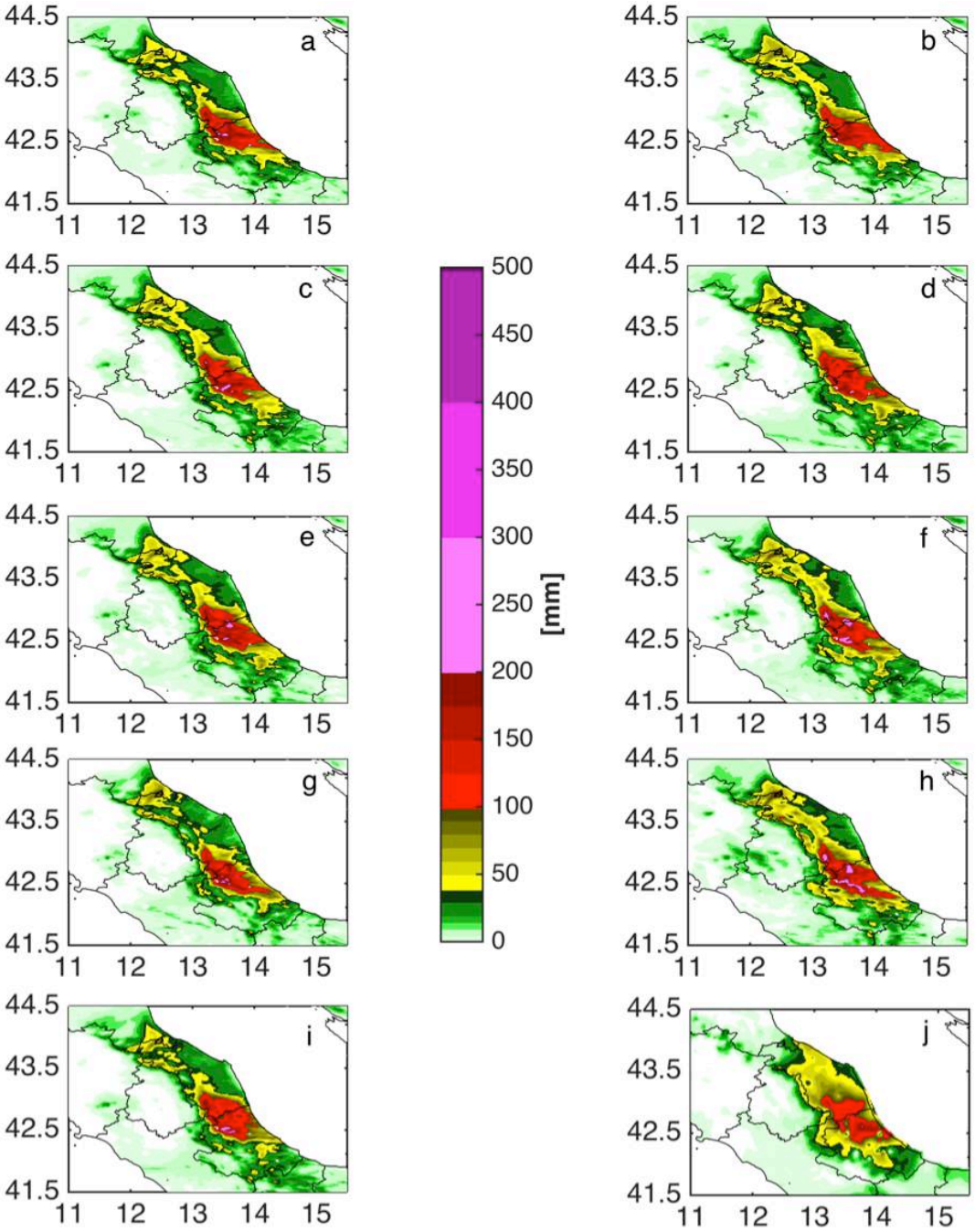

Figure 97: GFS driven cases. QPF values for the 24 hours time period from 00UTC on 15 November 2017 to 00UTC on 16 November 2017, where a=Open Loop, b=SST, c=SM-Sentinel 1, d=SM-SMAP/Sentinel 1, e=SM-SMAP, f=WIND, g=ZTD-INSAR, h=ZTD3h_1ist, i=WIND+SM+ZTD-INSAR, j=OBS. For details about the 3DVAR approaches the reader is referred to the main text.

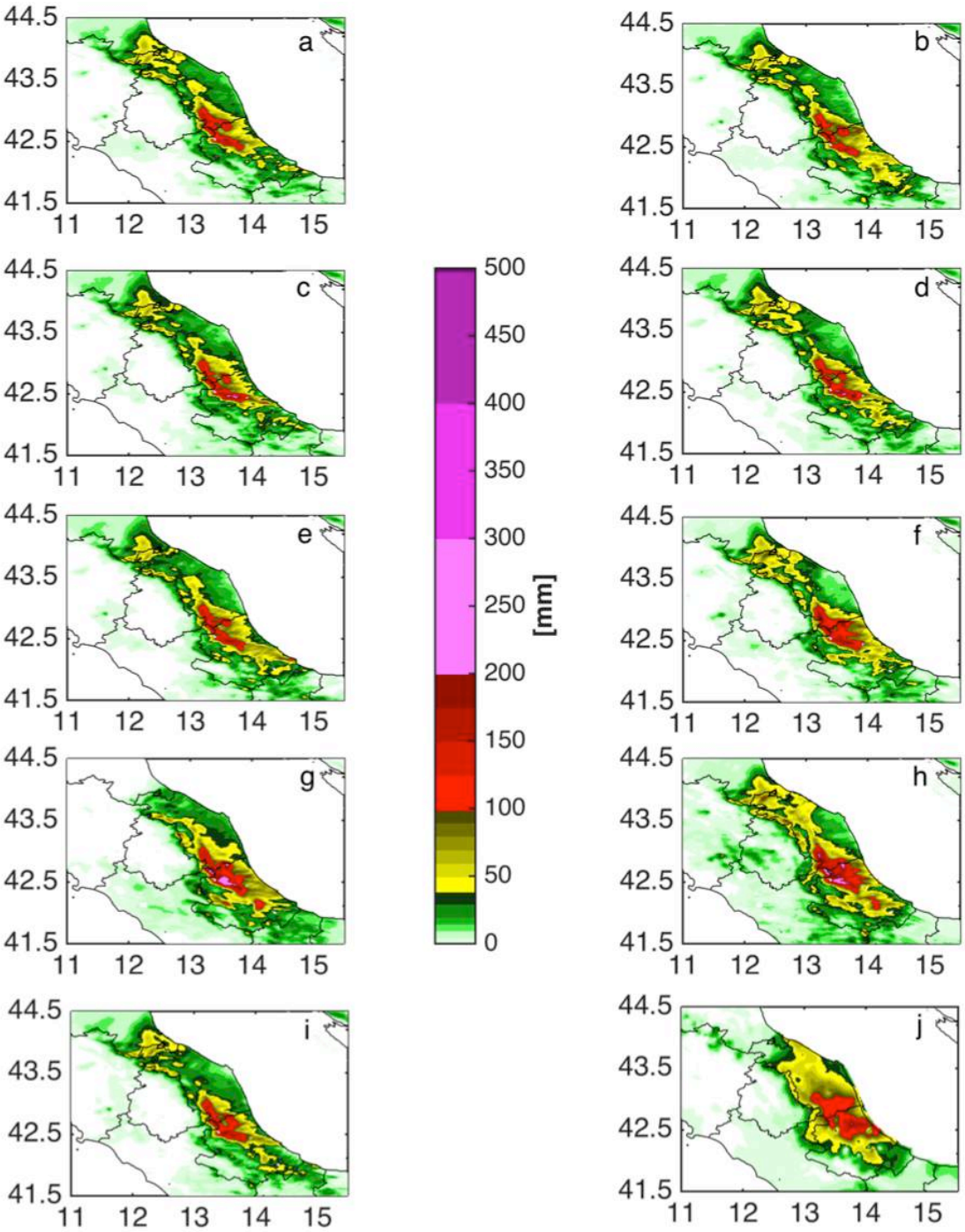

Figure 98: IFS driven cases. QPF values for the 24 hours time period from 00UTC on 15 November 2017 to 00UTC on 16 November 2017, where a=Open Loop, b=SST, c=SM-Sentinel 1, d=SM-SMAP/Sentinel 1, e=SM-SMAP, f=WIND, g=ZTD-INSAR, h=ZTD3h_1ist, i=WIND+SM+ZTD-INSAR, j= OBS. For details about the 3DVAR approaches the reader is referred to the main text.

24 mm (GFS)													
run	CENTROID DIST	ANGLE DIFF	AREA RATIO	SYMMETRIC DIFF	INTERSECTION AREA	UNION AREA	P90 RATIO	FBIAS	PODY	FAR	CSI	HK	HSS
OL	10.55	5.70	0.87	2534.00	3533.00	6067.00	0.81	0.91	0.72	0.21	0.60	0.65	0.67
SM	8.78	4.12	0.95	2246.00	3891.00	6137.00	0.84	1.01	0.79	0.22	0.65	0.71	0.71
SMAP_S1	**6.99**	3.54	**0.99**	2347.00	3993.00	6340.00	0.87	1.07	0.81	0.24	0.65	0.72	0.71
SMAP	11.38	4.50	0.95	2164.00	3912.00	6076.00	0.85	**1.00**	0.79	**0.20**	0.66	0.72	0.73
SST	12.29	5.04	0.95	2322.00	3833.00	6155.00	0.86	0.99	0.78	0.21	0.64	0.71	0.71
WIND	9.05	**2.58**	**0.99**	2333.00	3989.00	6322.00	0.89	1.06	0.81	0.24	0.65	0.72	0.71
WIND+SM+ZTD ZTD3h_1ist	11.03	4.70	0.95	**1874.00**	**4342.00**	6216.00	**0.96**	1.13	**0.88**	0.22	**0.71**	**0.80**	**0.76**
ZTD-INSAR	11.50	5.21	0.82	2618.00	3366.00	**5984.00**	0.83	0.86	0.68	0.21	0.58	0.62	0.65
WIND+SM+INSAR_only5	7.14	3.82	0.91	2777.00	3503.00	6280.00	0.80	0.95	0.71	0.25	0.57	0.63	0.64
	Best small	***Best small***	***Best=1***	***Best small***	***Best big***	***Best small***	***Best=1***	***Best=1***	***Best=1***	***Best=0***	***Best=1***	***Best=1***	***Best=1***

24 mm (IFS)													
Run	CENTROID DIST	ANGLE DIFF	AREA RATIO	SYMMETRIC DIFF	INTERSECTION AREA	UNION AREA	P90 RATIO	FBIAS	PODY	FAR	CSI	HK	HSS
OL	12.85	6.96	0.86	3068.00	3250.00	6318.00	0.77	0.90	0.66	0.27	0.53	0.58	0.59
SM	12.40	6.78	0.85	3051.00	3226.00	6277.00	0.74	0.90	0.65	0.27	0.53	0.57	0.59
SMAP_S1	11.84	5.01	0.88	3075.00	3299.00	6374.00	0.77	0.93	0.67	0.28	0.53	0.58	0.59
SMAP	8.47	6.76	0.87	3127.00	3234.00	6361.00	0.78	0.93	0.66	0.30	0.51	0.56	0.57
SST	**5.88**	6.03	**0.90**	3326.00	3212.00	6538.00	0.80	0.95	0.65	0.31	0.50	0.55	0.56
WIND	12.22	5.44	0.89	2733.00	3488.00	6221.00	0.86	**0.96**	0.71	0.26	0.57	0.62	0.63
WIND+SM+ZTD ZTD3h_1ist	9.11	**2.01**	0.90	2857.00	**3985.00**	6842.00	**0.89**	1.17	**0.81**	0.31	0.60	0.68	0.65
ZTD-INSAR	10.27	3.48	0.81	**1770.00**	3771.00	**5541.00**	0.88	0.87	0.77	**0.12**	**0.69**	**0.73**	**0.76**
WIND+SM+INSAR_only5	11.57	6.08	0.82	3343.00	2995.00	6338.00	0.74	0.87	0.61	0.30	0.48	0.52	0.54
	Best small	***Best small***	***Best=1***	***Best small***	***Best big***	***Best small***	***Best=1***	***Best=1***	***Best=1***	***Best=0***	***Best=1***	***Best=1***	***Best=1***

Table 28: Spatial and statistical indices calculated through MODE (24 mm rainfall depth threshold) to evaluate the sensitivity forecasts (driven by GFS and IFS respectively) with respect to the Open Loop run for the time interval 00UTC 15/11/2017 – 00UTC 16/11/2017. The best performance for each score is highlighted in bold.

48 mm (GFS)													
run	CENTROID DIST	ANGLE DIFF	AREA RATIO	SYMMETRIC DIFF	INTERSECTION AREA	UNION AREA	P90 RATIO	FBIAS	PODY	FAR	CSI	HK	HSS
OL	10.87	14.91	0.53	1775.00	1401.00	**3176.00**	0.75	0.60	0.48	**0.20**	0.43	0.46	0.55
SM	10.50	11.80	0.59	1649.00	1567.00	3216.00	0.82	0.70	0.54	0.23	0.47	0.51	0.58
SMAP_S1	13.76	9.89	0.67	**1452.00**	1787.00	3239.00	0.80	0.81	0.61	0.24	**0.52**	**0.58**	**0.63**
SMAP	10.28	12.31	0.61	1631.00	1594.00	3225.00	0.76	0.74	0.55	0.26	0.46	0.51	0.58
SST	11.89	12.09	0.60	1790.00	1499.00	3289.00	0.82	0.74	0.52	0.31	0.42	0.47	0.53
WIND	8.33	9.53	0.65	1724.00	1613.00	3337.00	0.88	0.84	0.55	0.34	0.43	0.50	0.54
WIND+SM+ZTD ZTD3h_1ist	**8.07**	**6.82**	**0.96**	2213.00	**1833.00**	4046.00	**0.97**	**0.99**	**0.63**	0.37	0.46	0.57	0.57
ZTD-INSAR	16.37	14.49	0.50	1923.00	1285.00	3208.00	0.80	0.62	0.44	0.29	0.37	0.41	0.48
WIND+SM+INSAR_only5	13.80	14.14	0.55	1539.00	1558.00	**3097.00**	0.72	0.64	0.54	**0.17**	0.48	0.52	0.61
	Best small	***Best small***	***Best=1***	***Best small***	***Best big***	***Best small***	***Best=1***	***Best=1***	***Best=1***	***Best=0***	***Best=1***	***Best=1***	***Best=1***

48 mm (IFS)													
Run	CENTROID DIST	ANGLE DIFF	AREA RATIO	SYMMETRIC DIFF	INTERSECTION AREA	UNION AREA	P90 RATIO	FBIAS	PODY	FAR	CSI	HK	HSS
OL	**5.65**	6.44	0.41	2008.00	1117.00	3125.00	0.95	0.51	0.38	0.25	0.34	0.36	0.45
SM	10.54	6.84	0.39	1971.00	1103.00	**3074.00**	0.94	0.48	0.38	**0.21**	0.34	0.36	0.46
SMAP_S1	14.22	**6.32**	0.42	2020.00	1115.00	3135.00	0.95	0.53	0.38	0.28	0.33	0.36	0.44
SMAP	17.44	13.27	0.48	2133.00	1155.00	3288.00	**0.99**	0.56	0.40	0.30	0.34	0.37	0.45
SST	15.64	9.28	0.50	2036.00	1236.00	3272.00	**0.99**	0.59	0.43	0.29	0.36	0.39	0.47
WIND	9.61	9.37	0.53	1990.00	1303.00	3293.00	0.93	0.69	0.45	0.35	0.36	0.40	0.46
WIND+SM+ZTD ZTD3h_1ist	5.83	6.34	**0.74**	1843.00	**1687.00**	3530.00	0.97	**0.91**	**0.58**	0.36	0.44	0.52	0.54
ZTD-INSAR	14.86	9.79	0.62	**1817.00**	1528.00	3345.00	0.96	0.68	0.53	0.23	**0.46**	**0.50**	**0.57**
WIND+SM+INSAR_only5	12.62	9.66	0.38	1971.00	1082.00	**3053.00**	0.89	0.47	0.37	**0.21**	0.34	0.35	0.45
	Best small	***Best small***	***Best=1***	***Best small***	***Best big***	***Best small***	***Best=1***	***Best=1***	***Best=1***	***Best=0***	***Best=1***	***Best=1***	***Best=1***

Table 29: Spatial and statistical indices calculated through MODE (48 mm rainfall depth threshold) to evaluate the sensitivity forecasts (driven by GFS and IFS respectively) with respect to the Open Loop run for the time interval 00UTC 15/11/2017 – 00UTC 16/11/2017. The best performance for each score is highlighted in bold.

72 mm (GFS)													
run	CENTROID DIST	ANGLE DIFF	AREA RATIO	SYMMETRIC DIFF	INTERSECTION AREA	UNION AREA	P90 RATIO	FBIAS	PODY	FAR	CSI	HK	HSS
OL	7.09	12.62	0.72	716.00	964.00	1680.00	0.84	0.74	0.64	**0.13**	0.58	0.63	0.72
SM	5.28	7.73	0.73	678.00	993.00	1671.00	0.82	0.77	0.66	0.14	0.60	0.65	0.73
SMAP_S1	5.74	6.67	**0.89**	**559.00**	**1173.00**	1732.00	**0.94**	0.94	**0.78**	0.16	**0.68**	**0.77**	**0.79**
SMAP	**5.15**	8.57	0.75	625.00	1028.00	**1653.00**	0.77	0.79	0.69	0.14	0.62	0.68	0.75
SST	7.92	13.03	0.74	753.00	957.00	1710.00	0.83	0.79	0.64	0.19	0.55	0.62	0.69
WIND	7.20	9.17	0.74	783.00	943.00	1726.00	0.83	0.81	0.63	0.22	0.53	0.61	0.67
WIND+SM+ZTD ZTD3h_1ist	8.58	**5.21**	**0.89**	922.00	990.00	1912.00	0.81	**1.01**	0.66	0.35	0.49	0.63	0.62
ZTD-INSAR	9.06	8.92	0.65	968.00	784.00	1752.00	0.84	0.70	0.52	0.26	0.44	0.51	0.59
WIND+SM+INSAR_only5	**4.56**	7.79	0.84	585.00	1119.00	1704.00	0.90	0.87	0.75	0.14	0.66	0.73	0.78
	Best small	***Best small***	***Best=1***	***Best small***	***Best big***	***Best small***	***Best=1***	***Best=1***	***Best=1***	***Best=0***	***Best=1***	***Best=1***	***Best=1***

72 mm (IFS)													
Run	CENTROID DIST	ANGLE DIFF	AREA RATIO	SYMMETRIC DIFF	INTERSECTION AREA	UNION AREA	P90 RATIO	FBIAS	PODY	FAR	CSI	HK	HSS
OL	7.59	1.12	0.44	1035.00	587.00	1622.00	0.96	0.45	0.39	**0.13**	0.37	0.39	0.52
SM	7.42	3.47	0.44	1034.00	588.00	1622.00	0.98	0.45	0.39	**0.13**	0.37	0.39	0.52
SMAP_S1	7.58	**0.36**	0.44	1035.00	586.00	**1621.00**	0.97	0.46	0.39	0.15	0.36	0.38	0.51
SMAP	8.02	2.94	0.43	1090.00	549.00	1639.00	**0.99**	0.47	0.37	0.22	0.33	0.36	0.47
SST	**6.13**	1.79	0.47	996.00	629.00	1625.00	0.95	0.50	0.42	0.16	0.39	0.41	0.54
WIND	6.30	7.20	0.57	**893.00**	758.00	1651.00	0.91	0.62	0.51	0.19	**0.45**	0.50	**0.60**
WIND+SM+ZTD ZTD3h_1ist	9.08	1.30	**0.74**	1009.00	**832.00**	1841.00	0.85	**0.81**	**0.56**	0.32	0.44	**0.53**	0.58
ZTD-INSAR	8.26	5.76	0.59	969.00	737.00	1706.00	0.90	0.70	0.49	0.30	0.41	0.48	0.55
WIND+SM+INSAR_only5	7.26	1.99	0.44	997.00	609.00	**1606.00**	0.93	0.46	0.41	**0.12**	0.38	0.40	0.53
	Best small	***Best small***	***Best=1***	***Best small***	***Best big***	***Best small***	***Best=1***	***Best=1***	***Best=1***	***Best=0***	***Best=1***	***Best=1***	***Best=1***

Table 30: Spatial and statistical indices calculated through MODE (72 mm rainfall depth threshold) to evaluate the sensitivity forecasts (driven by GFS and IFS respectively) with respect to the Open Loop run for the time interval 00UTC 15/11/2017 – 00UTC 16/11/2017. The best performance for each score is highlighted in bold.

24 mm	48 mm	72 mm	TOT	GFS DRIVEN CASES
0	0	1	1	OL
0	0	0	0	SM
2	4	**8**	14	SMAP_S1
2	0	1	3	SMAP
2	0	0	2	SST
2	1	0	3	WIND
TBD	TBD	TBD	TBD	WIND+SM+ZTD
7	**7**	3	**17**	ZTD3h_1ist
2	0	0	2	ZTD-INSAR
0	2	1	3	WIND+SM+INSAR_only5

Table 31: Summary of the sensitivity performances (GFS driven cases). The times in which each forecast has the best result for each score is counted for each threshold and summarized in a total count (summing Tables 1, 2 and 3) that is used to find the best simulation.

24 mm	48 mm	72 mm	TOT	IFS DRIVEN CASES
0	1	0	1	OL
0	1	0	1	SM
0	1	1	2	SMAP_S1
0	1	1	2	SMAP
2	1	1	4	SST
1	0	3	4	WIND
TBD	TBD	TBD	TBD	WIND+SM+ZTD
4	4	**5**	**13**	ZTD3h_1ist
6	4	0	10	ZTD-INSAR
0	2	2	4	WIND+SM+INSAR_only5

Table 32: Summary of the sensitivity performances (IFS driven cases). The times in which each forecast has the best result for each score is counted for each threshold and summarized in a total count (summing Tables 1, 2 and 3) that is used to find the best simulation.

8.5 Concluding remarks

In the framework of the STEAM projects two sets of experiments have been presented in this work trying to answer to the project overarching question if Sentinel satellites constellation weather observation data can be used to better understand and predict severe weather events. For this purpose two different events have been chosen. The first event is the Livorno flood that according to the Molini et al (2011) criterion can be classified as: type II–short-lived (duration d < 12 hours) and very localized (less than AS = 50 × 50 km^2). The second one is the Silvi Marina flood that can be classified as: type I–long-lived (duration d ≥ 12 hours) and spatially distributed (more than AS = 50 × 50 km^2) (Molini et al. 2011). For each event two groups of experiments have been performed, the first one driven by IFS global model and the second by GFS. For each group a sequence of sensitivity experiments has been executed through the assimilation (with different techniques) of single sets of observed (from Sentinel or GNSS) variables. Finally, building on the results of the assimilation experiments driven by Sentinel or GNSS standalone observations, a simulation assimilating all the most influencing observations together has been performed. As expected, given their different nature, the two project case studies showed different responses to the same type of assimilated observations. In particular, the 3-hour cycling 3DVAR of GNSS ZTD offers good results in both Livorno and Silvi-Marina cases but it is not fundamental in the type II Livorno event that significantly benefits also from the adjustment of the wind field with high-resolution Sentinel observation. Conversely, the type I Silvi Marina case takes mostly advantage from a 3-hour cycling update of ZTD and the single time Sentinel observations are more penalized because they allow correcting the model only the day before the event. Furthermore, IFS and GFS driven experiments revealed

sometimes significantly different responses to the same assimilated variable: this is most probably due to the difference in their respective initial conditions fields. For example comparing the SM analysis fields for the Livorno case, there is a quite prominent difference between GFS and IFS values, namely IFS soil layers look definitely drier than GFS ones. This can lead to different response to the same SM observation. In general the assimilation of Sentinel and GNSS derived variables always resulted into an improvement in the weather forecast, even if sometimes relatively small for some variables (like SST or LST). Thus, it worth to further explore the synergy between Sentinel observation and weather modeling maybe in different test cases and geographical context trying to exploit the spatial high resolution nature of Sentinel data. These results also pave the way to further explore the impact on hydro-meteorological predictive capability of data provided by the potential next-generation Earth Explorer geostationary InSAR satellite (Geosynchronous –Continental Land-Atmosphere Sensing System, G-CLASS), currently under evaluation by ESA.

Future works will be developed to consolidate the results achieved during the STEAM project in different frameworks. First of all CIMA Foundation will lead the Pilot 2 of E-SHAPE H2020 project in which it will be exploit the new capacities for designing and delivering innovative services for extreme-scale hydro-meteorological modeling, using Copernicus data directly ingested through the Copernicus Open Access Hub APIS, and the DIAS platform paving the way towards a more operational assimilation of Copernicus satellite data. Furthermore, different test cases will be analysed also in Africa in the framework of the TWIGA H2020 project. Finally, as aforementioned, further specifics experiments will be performed assimilating water vapour from InSAR to contribute to G-CLASS activities for science and requirement consolidation.

9. Conclusion

This thesis presents three different research lines cooperatively tackling the reduction of uncertainty in the severe rainfall phenomena prediction.

The first activity has been developed to exploit the interplay between extreme convective rainfall phenomena and severe lightning activity for back-building MCSs occurring in north-western Mediterranean (Varazze, 4th October 2010, Cinqueterre, 25th October 2011, Genoa, 4th November 2011 and Genoa, 9th October 2014, Nice, 3rd October 2015 and so forth) and to use the LPI to provide further insight into the vertical thermodynamical structure of the predicted convective flow field.

An effective methodology for the rainfall and lightning activity forecasting and evaluation is presented to improve the probability of predicting events like the one occurred in Genoa in 2014 by applying both the Price and Rind (1992) lightning parameterization and the Lightning Potential Index (LPI) approaches to a microphysics driven ensemble modelling approach, at cloud-resolving grid spacing (1 km). This activity identifies the LPI as a tool helping in the forecasting phase to discriminate between scenarios leading to (very) deep moist convective, heavily precipitating, and persistent storms and ones resulting in shallower and more disorganized convective situations, thus not producing significant ground effects. Building on the results of the first part of this thesis, the LPI is currently used in an operational open loop version of the WRF model executed at 1.5 km grid spacing over the entire Italy by CIMA Research Foundation, in the framework of the cooperation with the Italian Civil Protection Department and Ligurian Regional Environmental Protection Agency (ARPAL). Furthermore, the model outputs with LPI have been provided during the

EXAEDRE measurement campaign that took place in September 2018 in the framework of HyMeX project.

Thought the use of a LPI is helpful both in forecasting and hindcast phase, the study highlights that the main source of uncertainty in the forecast of high impact weather events is linked to the correct reproduction of the deep moist convective phenomena. Consequently, the second research activity proposes a hydro-meteorological forecasting chain combining a high resolution WRF model instance including a 3DVAR data assimilation cycle - with the fully distributed Continuum hydrological model. The use of data assimilation is the value added to previous research results achieved with such hydrometeological chain in the framework of the DRIHM project. The main goal is to gain a further insight on the prediction of back-building MCSs investigating the influence of different reflectivity forward operators on the overall hydro-meteorological predictive capability. Although no data assimilation setup stands out as giving the best results for all the three cases, the study highlights the systematic benefit of radar data assimilation for the prediction of heavy precipitating events. Furthermore, the proposed modified radar data assimilation operator has showed a significant potential for the improvement of rainfall and streamflow forecasts. As an output of this research activity the complete hydro-meteorological chain including the modified direct operator is currently under implementation in the framework of the Italian Civil Protection Department and CIMA Research Foundation agreement for the period 2019-2021. Moreover an operational version of WRF model executed at 2.5 km grid spacing over the northern and central and including the modified data assimilation radar operator is maintained by CIMA Research Foundation on behalf of ARPAL and currently under upgrade, as aforementioned in Section 7.3. In all these applications the

first and the second research activities results are coupled together with the LPI forecast provided also by the operational WRF run with data assimilation. This will allow highlighting the possible value added of reflectivity data assimilation for lighting activity forecast.

This second research line has also paved the way to two further evolutions: on one side to explore the possible added-value of unconventional weather observation data assimilation (personal weather stations, Internet of Things) such as pressure sensors on mobile phones or temperature sensors on cars; on the other side to investigate the potential improvement in the forecast obtained with data assimilation will be investigated in terms of renewable energy production prediction (EC report).

The third research activity is developed in the framework of the STEAM project trying to investigate new areas of synergy between atmospheric models and data from spaceborne systems. Along this line, a cloud resolving model is fed with observational data provided by Sentinel satellites constellation, such as humidity, soil and sea temperature, wind on the sea, the amount of water vapour in the atmospheric band closest to the earth. The results presented in this manuscript encourage the use of these ESA Sentinel satellites products for the forecast of highly precipitating severe weather events. During the thesis the data assimilation experiments have been applied on a Mediterranean region. An on-going work is the application of zenith total delay assimilation both from InSAR and GNSS stations over other geographical areas such as Africa in the framework of H2020 TWIGA (Transforming Weather Water data into value-added Information services for sustainable Growth in Africa) project. This activity is also the starting point to investigate the possible automation of the procedures here presented demonstrating their possible added value as

operational service. In fact, the E-SHAPE H2020 project will be exploit the new capacities for designing and delivering innovative services for extreme-scale hydro-meteorological modelling, using Copernicus data and core services directly ingested through the Copernicus Open Access Hub APIS, and the DIAS platform. Furthermore, the results presented in this thesis can represent an important basis for a methodological framework to assess the possible impact on hydro-meteorological predictive capability of data provided by a next-generation geostationary InSAR satellite (Geosynchronous –Continental Land-Atmosphere Sensing System, G-CLASS) currently under evaluation by ESA.

References

Adamo, C., S. Goodman, A. Mugnai, and J.A. Weinman (2009), Lightning measurements from satellites and significance for storms in the Mediterranean, in Betz HD, Schumann U, Laroche P (eds) Lightning: principles, instruments and applications. Review of modern lightning research, pp. 309–329, Springer, Berlin.

Al-Momar, S., W. Deierling, J. K. Williams, and E. G. Hoffman, (2015). Examining in-cloud convective turbulence in relation to total lightning and the 3D wind field of severe thunderstorms. In AMS 17th Conference on Aviation, Range, and Aerospace Meteorology, Paper (Vol. 5).

Andersson, E., and J. N. Thépaut, (2008), "ECMWF's 4D-Var data assimilation system–the genesis and ten years in operations." ECMWF Newsletter 115 8-12.

Angevine, W. M., H. Jiang, and T. Mauritsen, (2010), Performance of an eddy diffusivity–mass flux scheme for shallow cumulus boundary layers. Mon. Wea. Rev., 138, 2895–2912.

Arakawa, A., (2004), The cumulus parameterization problem: past, present and future, J. Clim., 17, 2493-2525, doi: 10.1175/1520-0442(2004)017<2493:RATCPP>2.0.CO;2.

Baldauf, M., A. Seifert, J. Förstner, D. Majewski, M. Raschendorfer, and T. Reinhardt (2011), Operational convective-scale numerical weather prediction with the COSMO model: Description and sensitivities, Mon.Weather Rev., 139(12), 3887–3905, doi:10.1175/MWR-D-10-05013.1.

Ball, J. T., I. E. Woodrow, and J. A. Berry, (1987), A model predicting stomatal conductance and its contribution to the control of photosynthesis under

different environmental conditions. Progress in Photosynthesis Research, I. Biggins, Ed., Martinus Nijhoff, 221–224.

Barker, D.M., W. Huang, Y.R. Guo, and Q.N. Xiao, (2004), A Three-Dimensional (3DVAR) Data Assimilation System For Use With MM5: Implementation and Initial Re-sults. Mon. Wea. Rev., 132, 897-914.

Barker, D., Huang, X. Y., Liu, Z., Auligné, T., Zhang, X., Rugg, S., ... & Demirtas, M. (2012), The weather research and forecasting model's community variational/ensemble data assimilation system: WRFDA. Bulletin of the American Meteorological Society, 93(6), 831-843.

Barthe, C., W. Deirling, M.C. Barth (2010), Estimation of total lightning from various storm parameters: a cloud-resolving model study, J. Geophys. Res., 115 (D24), D24202.

Bauer, P., Thorpe, A., & Brunet, G., (2015), The quiet revolution of numerical weather prediction. Nature, 47, 525(7567).

Bechtold, P., M. Köhler, T. Jung, M. Leutbecher, M. Rodwell, F. Vitart and G. Balsamo, (2008), Advances in predicting atmospheric variability with the ECMWF model, From synoptic to decadal time-scales. Quart. J. Roy. Meteor. Soc. 134, 1337-1351.

Beljaars, A.C.M., (1994), The parameterization of surface fluxes in large-scale models under free convection, Quart. J. Roy. Meteor. Soc., 121, 255–270.

Benjamin, Stanley G., Georg A. Grell, John M. Brown, and Tatiana G. Smirnova, (2004), Mesoscale weather prediction with the RUC hybrid isentropic-terrain-following coordinate model. Mon. Wea. Rev., 132, 473-494.

Benoit, R., et al. (2002), The real-time ultrafinescale forecast support during the special observing period of the map, Bull. Am. Meteorol. Soc., 83(1), 85–109.

Bergthorsson, P.,and B. Döös, (1955), Numerical weather map analysis, Tellus 7, 329-340.

Bjerknes, V., (1904), Das Problem der Wettervorhersage, betrachtet vom Standpunkte der Mechanik und der Physik, Meteor. Zeit. 21, 1–7, Translation by Y.

Blanchard, D.C., Progress in Oceanography, vol. 1 (Pergamon Press, Elmsford, 1963)

Bougeault, P., and P. Lacarrère, (1989), Parameterization of orography induced turbulence in a mesobeta-scale model. Mon. Wea. Rev., 117, 1872–1890.

Bouttier F. and P. Courtier, (1999), Data assimilation concepts and methods. Technical report, European Centre for Medium-Range Weather Forecasts (ECMWF), Meteorological / Training Course Lecture Series.

Bretherton, C.S., Park, S., (2009), A new moist turbulence parameterization in the community atmosphere model. J. Clim. 22, 3422–3448. http://dx.doi.org/10.1175/2008JCLI2556.1.

Bryan, G. H., Wyngaard, J. C., & Fritsch, J. M. (2003). Resolution requirements for the simulation of deep moist convection. *Monthly Weather Review*, *131*(10), 2394-2416.

Bryan, G. H., and H. Morrison, (2012), Sensitivity of a simulated squall line to horizontal resolution and parameterization of microphysics. Mon. Wea. Rev., 140, 202–225, doi:10.1175/ MWR-D-11-00046.1.

Bryson A. E. and Y. C. Ho, (1990), Applied Optimal Control, Hemisphere

Publishing Corporation, Washington DC, USA.

Carter, A. E., and R.E. Kidder (1976), Lightning in relation to precipitation, J. Atmos. Terr. Phys., 39, 139–148.

Cassola, F., F. Ferrari, and A. Mazzino, (2015), Numerical simulations of Mediterranean heavy precipitation events with the WRF model: A verification exercise using different approaches. Atmos. Res., 164-165, 210–225, doi:10.1016/j.atmosres.2015.05.010.

Charney, J. G., Fjørtoft, R., and von Neuman, J., (1950), Numerical integration of the barotropic vorticity equation. Tellus 2, 237-254.

Charney, J. G., (1951), Dynamical forecasting by numerical process. Compendium of meteorology. American Meteorological Society, Boston, MA.

Chen, S.-H., and W.-Y. Sun, (2002), A one-dimensional time dependent cloud model. J. Meteor. Soc. Japan, 80, 99–118.

Chou M.-D., and M. J. Suarez, (1994), An efficient thermal infrared radiation parameterization for use in general circulation models. NASA Tech. Memo. 104606, 3, 85pp.

Clark, P., N. Roberts, H. Lean, S. P. Ballard, and C. Charlton-Perez, (2016), Convection-permitting models: a step-change in rainfall forecasting. Meteorological Applications, 23(2), 165-181.

Collins, W.D. et al. (2004), Description of the NCAR Community Atmosphere Model (CAM 3.0), NCAR Technical Note, NCAR/TN-464+STR, 226pp.

Coniglio, M.C., Correia, J., Marsh, P.T., Kong, F., (2013), Verification of convection-allowing WRF model forecasts of the planetary boundary

layer using sounding observations. Weather Forecast. 28, 842–862. http://dx.doi.org/10.1175/WAF-D-12-00103.1.

Courtier, P., J.-N. Thépaut, and A. Hollingsworth, (1994), A strategy for operational implementation of 4D-Var, using an incremental approach. Quart. J. Roy. Meteor. Soc., 120, 1367–1387.

Dahl, J. M. L., H. Holler, and U. Schumann (2011), Modeling the flash rate of thunderstorm. Part I: Framework, Mon. Wea. Rev., 139, 3093-3111, doi:http://dx.doi.org/10.1175/MWR-D-10-05031.1.

Daley, R., (1991), Atmospheric Data Analysis. Cambridge Atmospheric and Space Science Series, Cambridge Uni- versity Press. ISBN 0-521-38215-7, 457 pages.

Das, M. K., M. A. M. Chowdhury, S. Das, S. K. Debsarma and S. Karmakar, (2015), Assimilation of Doppler weather radar data and their impacts on the simulation of squall events during premonsoon season. Nat. Hazards, 77, 901–931, https://doi.org/10.1007/s11069-015-1634-9.

Davis, A. C., B. Brown, and R. Bullock, (2006a), Object-based verification of precipitation forecasts. Part I: Methodology and application to mesoscale rain areas. *Mon. Weather Rev.*, **134**, 1772–1784.

Davis, A. C., B. Brown, and R. Bullock, (2006b), Object-based verification of precipitation forecasts. Part II: Application to convective rain system. *Mon. Weather Rev.*, **134**, 1785–1795.

Davolio, S., F. Silvestro, and P. Malguzzi (2015), Effects of Increasing Horizontal Resolution in a Convection Permitting Model on Flood Forecasting: The 2011 Dramatic Events in Liguria (Italy), Journal of

Hydrometeorology, 16, 1843-1856, doi: http://dx.doi.org/10.1175/JHM-D-14-0094.1.

Davolio, S., F. Silvestro and T. Gastaldo, (2017), Impact of Rainfall Assimilation on High-Resolution Hydrometeorological Forecasts over Liguria, Italy. *J. Hydrometeor.*, ***18*****(10)**, 2659-2680.

Dauhut, T., J.-P. Chaboureau, J.Escobar, and P.Mascart, (2015), Largeeddy simulations of Hector the convector making the stratosphere wetter. Atmos. Sci. Lett., 16, 135–140, doi:10.1002/asl2.534.

Dawson, D. T., II, M. Xue, J. A. Milbrandt, and M. K. Yau, (2010), Comparison of evaporation and cold pool development between single-moment and multimoment bulk microphysics schemes in idealized simulations of tornadic thunderstorms. Mon.Wea. Rev., 138, 1152–1171, doi:10.1175/2009MWR2956.1.

De Leonibus, L., D. Biron, M. Sist, D. Labate, F. Zauli, and D. Melfi (2010), Wind intensity reconstruction over Italy through lampinet lightning data, paper presented at 3rd International Lightning Meteorology Conference, Orlando, Florida.

Deardorff, J. W. (1970), A numerical study of three-dimensional turbulent channel flow at large Reynolds numbers. *J. Fluid Mech.***41**, 453–480.

Deardorff, J. W. (1972), Numerical investigation of neutral and unstable planetary boundary layers. *Journal of the Atmospheric Sciences*, *29*(1), 91-115.

Defer, E., Lagouvardos, K., & Kotroni, V. (2005). Lightning activity in the eastern Mediterranean region. *Journal of Geophysical Research: Atmospheres*, *110*(D24).

Deierling, W. and Petersen W.A (2008), Total lightning activity as an indicator of updraft characteristics, J. Geophys. Res., 113, D16210, doi:10.1029/2007JD009598.

Dharssi, I., A. C. Lorenc, and N. B. Ingleby, (1992), Treatment of gross errors using maximum probability theory. Quart. J. Roy. Meteor. Soc., 118, 1017–1036.

Dirmeyer, P. A., et al. (2012), Simulating the diurnal cycle of rainfall in global climate models: Resolution versus parametrization, Clim. Dyn., 39, 399–418.

Dickinson, R. E. (1983), Land surface processes and climate—Surface albedos and energy balance. Advances in geophysics, 25, 305-353.

Dickinson, R. E., Shaikh, M., Bryant, R., & Graumlich, L. (1998). Interactive canopies for a climate model. Journal of Climate, 11(11), 2823-2836.

Done, J., C. A. Davis, and M. Weisman (2004), The next generation of NWP: Explicit forecasts of convection using the Weather Research And Forecasting (WRF) model, Atmos. Sci. Lett., 5(6), 110–117.

Dowell, D. C., Wicker, L. J., & Snyder, C. (2011), Ensemble Kalman filter assimilation of radar observations of the 8 May 2003 Oklahoma City supercell: Influences of reflectivity observations on storm-scale analyses. *Monthly Weather Review*, *139*(1), 272-294.

Ducrocq, V., I. Braud, S. Davolio, R. Ferretti, C. Flamant, A. Jansa, ... & S. Belamari, (2014), HyMeX-SOP1: The field campaign dedicated to heavy precipitation and flash flooding in the northwestern Mediterranean. Bull. Amer. Meteor. Soc., 95(7), 1083-1100, https://doi.org/10.1175/BAMS-D-12-00244.1.

Dudhia, J., (1989), Numerical study of convection observed during the winter monsoon experiment using a mesoscale two-dimensional model, J. Atmos. Sci., 46, 3077–3107.

Dudhia, J., Hong, S. Y., & Lim, K. S. (2008), A new method for representing mixed-phase particle fall speeds in bulk microphysics parameterizations. *Journal of the Meteorological Society of Japan. Ser. II*, *86*, 33-44.

Dyer, A. J., and B. B. Hicks, (1970), Flux-gradient relationships in the constant flux layer, Quart. J. Roy. Meteor. Soc., 96, 715–721.

Fels, S. B. and M. D. Schwarzkopf, (1975), The Simplified Exchange Approximation: A New Method for Radiative Transfer Calculations, J. Atmos. Sci., 32, 1475–1488.

Fiori, E., Parodi, A., & Siccardi, F. (2010). Turbulence closure parameterization and grid spacing effects in simulated supercell storms. *Journal of the Atmospheric Sciences*, *67*(12), 3870-3890.

Fiori, E., Parodi, A., & Siccardi, F. (2011). Uncertainty in prediction of deep moist convective processes: Turbulence parameterizations, microphysics and grid-scale effects. *Atmospheric research*, *100*(4), 447-456.

Fiori, E., Comellas, A., Molini, L., Rebora, N., Siccardi, F., Gochis, D. J., Tanelli, S., and Parodi, A. (2014), Analysis and hindcast simulations of an extreme rainfall event in the Mediterranean area: The Genoa 2011 case, Atmos. Res., 138, 13-29, doi:10.1016/j.atmosres.2013.10.007

Fiori, E., M. Lagasio, A. Parodi, R. Procopio, A. Smorgonskiy, F. Rachidi, and G. Diendorfer (2016), Implementation and Performance Analysis of the Lightning Potential Index as a Forecasting Tool, paper presented at 33rd

International Conference on Lightning Protection (ICLP), Estoril, Portugal.

Fiori, E., L. Ferraris, L. Molini, F. Siccardi, D. Kranzlmueller, and A. Parodi, (2017), Triggering and evolution of a deep convective system in the Mediterranean Sea: Modelling and observations at a very fine scale. Q. J. R. Meteorol. Soc., 143, 927–941, doi:10.1002/qj.2977.

Foresti L, Panziera L, Mandapaka PV, Germann U, Seed A. (2013), Retrieval of analogue radar images for ensemble nowcasting of orographic rainfall. Meteorol. Appl. DOI: 10.1002/met.1416.

Foresti L, Seed A. (2015), On the spatial distribution of rainfall nowcasting errors due to orographic forcing. Meteorol. Appl. 22: 60–74, DOI: 10.1002/met.1440.

Gao, J. and D. J. Stensrud, (2012), Assimilation of reflectivity data in a convective-scale, cycled 3DVAR framework with hydrometeor classification. J. Atmos. Sci., 69(3), 1054-1065.

Gatlin, P. N., and S. J. Goodman (2010), A Total Lightning Trending Algorithm to Identify Severe Thunderstorms, J. Atmos. Oceanic Technol., 27, 3–22, doi:http://dx.doi.org/ 10.1175/2009JTECHA1286.1.

Gauthier, P., & Thepaut, J. N. (2001), Impact of the digital filter as a weak constraint in the preoperational 4DVAR assimilation system of Météo-France. *Monthly weather review*, *129*(8), 2089-2102.

Gent, P.R., Danabasoglu, G., Donner, L.J., Holland, M.M., Hunke, E.C., Jayne, S.R., Lawrence, D.M., Neale, R.B., Rasch, P.J., Vertenstein, M., Worley, P.H., Yang, Z.L., Zhang, M., (2011), The community climate system model version 4. J. Clim. 24, 4973–4991. http://dx.doi.org/10.1175/2011JCLI4083.1.

Giannaros, T. M., V. Kotroni, and K. Lagouvardos (2015), Predicting lightning activity in Greece with the Weather Research and Forecasting (WRF) model, Atmos. Res., 156, 1-13, doi: 10.1016/j.atmosres.2014.12.009.

Giannaros, T. M., Lagouvardos, K., & Kotroni, V. (2016), Performance evaluation of an operational lightning forecasting system in Europe. Natural Hazards, 1-18, 2016, doi: 10.1007/s11069-016-2555-y.

Gilmore, M. S., J. M. Straka, and E. N. Rasmussen, (2004), Precipitation and evolution sensitivity in simulated deep convective storms: Comparisons between liquid-only and simple ice and liquid phase microphysics. Mon. Wea. Rev., 132, 1897–1916.

Grell, G., L. Schade, R. Knoche, A. Pfeiffer, and J. Egger (2000), Nonhydrostatic climate simulations of precipitation over complex terrain, J. Geophys. Res., 105, 29,595–29,608.

Gustafsson, N., (1992), Use of a digital filter as weak constraint in variational data assimilation. *Proc. Workshop on Variational Assimilation with Special Emphasis on Three-dimensional Aspects,* Reading, United Kingdom, European Centre for Medium-Range Weather Forecasts, 327–338.

Ha, J.-H., H.-W. Kim, and D.-K. Lee, (2011), Observation and numerical simulations with radar and surface data assimilation for heavy rainfall over central Korea, Adv. Atmos. Sci., 28, 573–590, https://doi.org/10.1007/s00376-010-0035-y.

Hally, A., O. Caumont, L. Garrote, E. Richard, A. Weerts, F. Delogu,... & M. Ivković, (2015), Hydrometeorological multi-model ensemble simulations of the 4 November 2011 flash flood event in Genoa, Italy, in the

framework of the DRIHM project. *Natural Hazards and Earth System Sciences*, **15(3)**, 537-555.

Hayden, C. M., and R. J. Purser, (1995), Recursive filter objective analysis of meteorological fields: Applications to NESDIS operational processing. J. Appl. Meteor., 34, 3–15.

Holtslag, A. A. M. and B. A. Boville, (1993), Local versus non-local boundary layer diffusion in a global climate model, J. Climate, 6, 1825–1842.

Hong, S.-Y., and H.-L. Pan, (1996), Nonlocal boundary layer vertical diffusion in a medium-range forecast model, Mon. Wea. Rev., 124, 2322–2339.

Hong, S.-Y., J. Dudhia, and S.-H. Chen, (2004), A Revised Approach to Ice Microphysical Processes for the Bulk Parameterization of Clouds and Precipitation, Mon. Wea. Rev., 132, 103–120.

Hong, S.-Y., and J.-O. J. Lim, (2006), The WRF Single-Moment 6-Class Microphysics Scheme (WSM6), J. Korean Meteor. Soc., 42, 129–151.

Hong, S.-Y., and Y. Noh, and J. Dudhia, (2006), A new vertical diffusion package with an explicit treatment of entrainment processes. Mon. Wea. Rev., 134, 2318–2341.

Hong, S.-Y., (2007), Stable Boundary Layer Mixing in a Vertical Diffusion Scheme. The Korea Meteor. Soc., Fall conference, Seoul, Korea, Oct. 25-26.

Hong, S. Y., Lim, K. S. S., Lee, Y. H., Ha, J. C., Kim, H. W., Ham, S. J., & Dudhia, J. (2010), Evaluation of the WRF double-moment 6-class microphysics scheme for precipitating convection. Advances in Meteorology.

Huang, X.Y., Q. Xiao, D.M. Barker, X. Zhang, J. Michalakes, W. Huang, T. Henderson, J. Bray, Y. Chen, Z. Ma, J. Dudhia, Y. Guo, X. Zhang, D.J.

Won, H.C. Lin, and Y.H. Kuo, (2009), Four-Dimensional Variational Data Assimilation for WRF: Formulation and Preliminary Results. Mon. Wea. Rev., 137, 299–314.

Iacono, M. J., J. S. Delamere, E. J. Mlawer, M. W. Shephard, S. A. Clough, and W. D. Collins, (2008), Radiative forcing by long–lived greenhouse gases: Calculations with the AER radiative transfer models. J. Geophys. Res., 113, D13103.

Ide, K., P. Courtier, M. Ghil, and A. C. Lorenc, (1997), Unified notation for data assimilation: Operational, sequential and variational. J. Meteor. Soc. Japan, 75, 181–189.

Janjic, Z. I., (1990), The step-mountain coordinate: physical package, Mon. Wea. Rev., 118, 1429–1443.

Janjic, Z. I., (1994), The step-mountain eta coordinate model: further developments of the convection, viscous sublayer and turbulence closure schemes, Mon. Wea. Rev., 122, 927–945.

Janjic, Z. I., (1996), The surface layer in the NCEP Eta Model, Eleventh Conference on Numerical Weather Prediction, Norfolk, VA, 19–23 August; Amer. Meteor. Soc., Boston, MA, 354–355.

Janjic, Z. I., (2002), Nonsingular Implementation of the Mellor–Yamada Level 2.5 Scheme in the NCEP Meso model, NCEP Office Note, No. 437, 61 pp.

Janjic ZI. (2003), A non-hydrostatic model based on a new approach. Meteorol. Atmos. Phys. 82: 271–285.

Kain, J.S., S.J. Weiss, J.J. Levit, M.E. Baldwin, and D.R. Bright (2006), Examination of convection-allowing configurations of the WRF model for

the prediction of severe convective weather: the SPC/NSSL Spring Program 2004, Weather Forecast, 21, 167-181, doi:http://dx.doi.org/10.1175/WAF906.1.

Kain, J.S, S.J. Weiss, D.R. Bright, M.E. Baldwin, J.J. Levit, G.W. Carbin, C.S. Schwartz, M.L. Weismann, K.K. Droegemeier, D.B. Weber, and K.W. Thomas (2008), Some pratical considerations regarding horizontal resolution in the first generation of operational convection-allowing NWP, Weather Forecast, 23, 931-952.

Kalnay, E., (2002), Atmospheric Modeling Data Assimilation and Predictability, Cambridge University Press.

Kessler, E., (1969), On the distribution and continuity of water substance in atmospheric circulation, Meteor. Monogr., 32, Amer. Meteor. Soc., 84 pp

Kosović, B., & Curry, J. A. (2000), A large eddy simulation study of a quasi-steady, stably stratified atmospheric boundary layer. Journal of the atmospheric sciences, 57(8), 1052-1068.

Krehbiel, P. R., Brook, M., & McCrory, R. A. (1979), An analysis of the charge structure of lightning discharges to ground. *Journal of Geophysical Research: Oceans*, *84*(C5), 2432-2456.

Lacis, A. A., and J. E. Hansen, (1974), A parameterization for the absorption of solar radiation in the earth's atmosphere. J. Atmos. Sci., 31, 118–133

Lagasio, M., A. Parodi, R. Procopio, F. Rachidi, and E. Fiori (2017), Lightning Potential Index performances in multimicrophysical cloud-resolving simulations of a back-building mesoscale convective system: The Genoa 2014 event, J. Geophys. Res. Atmos., 122, doi:10.1002/2016JD026115.

Laiolo, P., S. Gabellani, N. Rebora, R. Rudari, L. Ferraris, S. Ratto, H. Stevenin

and M. Cauduro, (2014), Validation of the Flood-PROOFS probabilistic forecasting system. Hydrol. Process., 28: 3466–3481. doi: 10.1002/hyp.9888

Langhans, W., J. Schmidli, and C. Schar, (2012), Bulk convergence of kilometer-scale simulations of moist convection over complex terrain. J.Atmos. Sci., 69, 2207–2228, doi:10.1175/JAS-D-11-0252.1.

Latham, J., A.M Blyth, H.J Christian Jr., W. Deierling, and A.M. Gadian (2004), Determination of precipitation rates and yields from lightning measurements, Journal of Hydrology, 288, 13-19, doi:10.1016/j.jhydrol.2003.11.009.

Lean, H. W., P. A. Clark, M. Dixon, N. M. Roberts, A. Fitch, R. Forbes, and C. Halliwell (2008), Characteristics of high-resolution versions of the Met Office unified model for forecasting convection over the United Kingdom, Mon. Weather Rev., 136(9), 3408–3424,doi:10.1175/2008MWR2332.1.

Lee, J.-H., H.-H. Lee, Y. Choi, H.-W. Kim, and D.-K. Lee, (2010), Radar data assimilation for the simulation of mesoscale convective systems. Adv. Atmos. Sci., 27, 1025–1042, https://doi.org/10.1007/s00376-010-9162-8.

Lilly, D. K. (1967), The representation of small-scale turbulence in numerical simulation experiments. *Proc. IBM Sci. Comput. Symp. Environm. Sci. (Yorktown Heights, Nov. 14th to 15th 1966)*, pp. 195–210. Thomas J. Watson Res. Center, Yorktown Heights, N.Y.

Lim, K.-S. S., and S.-Y. Hong (2010), Development of an effective double-moment cloud microphysics scheme with prognostic cloud condensation nuclei (CNN) for weather and climate models, Mon. Wea. Rev., 138, 1587-1612.

Lin, Y.-L., R. D. Farley, and H. D. Orville, (1983), Bulk parameterization of the snow field in a cloud model. J. Climate Appl. Meteor., 22, 1065–1092.

Liu, J., M. Bray, and D. Han, (2013), A study on WRF radar data assimilation for hydrological rainfall prediction, Hydrol. Earth Syst. Sci., 17, 3095–3110, https://doi.org/10.5194/hess-17-3095-2013.

Lorenc, A. C., and Coauthors, (2000), The Met. Office global three-dimensional variational data assimilation scheme. Quart. J. Roy. Meteor. Soc., 126, 2991–3012.

Lorenc, A. C., (2003), Modelling of error covariances by 4D-Var data assimilation. Quart. J. Roy. Meteor. Soc., 129, 3167–3182.

Lorenz, A., (1986), Analysis methods for numerical weather prediction. Quart. J. Roy. Meteor. Soc., 112, 1177-1194.

Lynch, P., and X.-Y. Huang, (1992), Initialization of the HIRLAM model using a digital filter. Mon. Wea. Rev., 120, 1019–1034.

Lynch, P., (2008), The origins of computer weather prediction and climate modelling. *Journal of Computational Physics.,* **97**, 3431-3444.

Lynn, B., and Y. Yair (2008), Lightning Potential Index: A new tool for predicting the lightning density and the potential for ex- treme rainfall, Geophys. Res. Abstracts, paper presented at EGU General Assembly, Vienna, Vol. 10, EGU2008-A-01571, SRef-ID: 1607-7962/gra/EGU2008-A-01571.

Lynn, B., and Y. Yair (2010), Prediction of lightning flash density with the WRF model, Adv. Geosci., 23, 11-16, doi:10.5194/adgeo-23-11-2010.

Maiello, I., S. Gentile, R. Ferretti, L. Baldini, R. Nicoletta, E. Picciotti,… & S.M. Frank, (2017), Impact of multiple radar reflectivity data assimilation on the numerical simulation of a flash flood event during the HyMeX

campaign. Hydrology and Earth System Sciences, 21(11), 5459-5476. doi:http://dx.doi.org/10.5194/hess-21-5459-2017.

Mansell, E. R., C. L. Ziegler, and E. C. Bruning, (2010), Simulated electrification of a small thunderstorm with two–moment bulk microphysics. J. Atmos. Sci., 67, 171–194.

Mateus, P., Miranda, P.M.A., Nico, G., Catalão, J., Pinto, P., Tomé, R., (2018), Assimilating InSAR Maps of Water Vapor to Improve Heavy Rainfall Forecasts: A Case Study With Two Successive Storms. J. Geophys. Res. Atmos. 123, 3341–3355. https://doi.org/10.1002/2017JD027472.

Mass, C., D. Ovens, K. Westrick, and B. Colle (2002), Does increasing horizontal resolution produce more skillful forecasts? The results of two years of real-time numerical weather prediction over the Pacific Northwest, Bull. Am. Meteorol. Soc., 83, 407–430.

Mazzarella, V., I. Maiello, V. Capozzi, G. Budillon, and R. Ferretti, (2017), Comparison between 3D-var and 4D-var data assimilation methods for the simulation of a heavy rainfall case in central italy. Advances in Science and Research, 14, 271-278. doi:http://dx.doi.org/10.5194/asr-14-271-2017

McCaul, E.W., S.J. Goodman, K.M. LaCasse, and D.J. Cecil (2009), Forecasting lightning threat using cloud-resolving model simulations, Weather Forecasting, 24, 709–729, doi:10.1175/2008WAF2222152.1.

McCumber, M., W.-K. Tao, J. Simpson, R. Penc, and S.-T. Soong, 1991: Comparison of icephase microphysical parameterization schemes using numerical simulations of tropical convection, J. Appl. Meteor., 30, 985–1004.

Mellor, G. L., & Yamada, T. (1982), Development of a turbulence closure model for geophysical fluid problems. *Reviews of Geophysics*, *20*(4), 851-875.

Mintz (1999), The problem of weather forecasting as a problem in mechanics and physics. Los Angeles, 1954. Reprinted in Shapiro and Grønas, 1–4.

Mlawer, E. J., Taubman, S. J., Brown, P. D., Iacono, M. J., & Clough, S. A. (1997), Radiative transfer for inhomogeneous atmospheres: RRTM, a validated correlated-k model for the longwave. *Journal of Geophysical Research: Atmospheres*, *102*(D14), 16663-16682.

Molini, L., Parodi, A., Rebora, N., & Craig, G. C. (2011), Classifying severe rainfall events over Italy by hydrometeorological and dynamical criteria. Quarterly Journal of the Royal Meteorological Society, 137(654), 148-154.

Morrison, H., J. A. Curry, and V. I. Khvorostyanov, (2005), A new double-moment microphysics parameterization for application in cloud and climate models, Part I: Description. J. Atmos. Sci., 62, 1665–1677.

Morrison, H., and J. O. Pinto, (2006) Intercomparison of bulk microphysics schemes in mesoscale simulations of springtime Arctic mixed-phase stratiform clouds. Mon. Wea. Rev., 134, 1880–1900.

Morrison, H., Thompson, G., & Tatarskii, V. (2009). Impact of cloud microphysics on the development of trailing stratiform precipitation in a simulated squall line: Comparison of one-and two-moment schemes. Monthly Weather Review, 137(3), 991-1007.

Muñoz Sabater, J., Fouilloux, A., De Rosnay, P., (2012), Technical implementation of SMOS data in the ECMWF integrated forecasting system. IEEE Geosci. Remote Sens. Lett. 9, 252–256. https://doi.org/10.1109/LGRS.2011.2164777

Nash, J. E., and J. V. Sutcliffe, (1970), River flood forecasting through conceptual models. Part I: a discussion of principles, J. Hydrol., 10, 282-290.

Niu, G. Y., & Yang, Z. L. (2004), Effects of vegetation canopy processes on snow surface energy and mass balances. Journal of Geophysical Research: Atmospheres, 109(D23).

Niu, G.-Y., Z.-L. Yang, R. E. Dickinson, L. E. Gulden, and H. Su (2007), Development of a simple groundwater model for use in climate modelsand evaluation with Gravity Recovery and Climate Experiment data,J. Geophys. Res., 112, D07103, doi:10.1029/2006JD007522.

Niu, G.-Y., et al. (2011), The community Noah land surface model with multiparameterization options (Noah-MP): 1. Model description and evaluation with local-scale measurements. J. Geophys. Res., 116, D12109, doi: 10.1029/2010JD015139.

NOAA, cited 2001: National Oceanic and Atmospheric Administration Changes to the NCEP Meso Eta Analysis and Forecast System: Increase in resolution, new cloud microphysics, modified precipitation assimilation, modified 3DVAR analysis.

Noh, Y., W.G. Cheon, S.-Y. Hong, and S. Raasch, (2003), Improvement of the K-profile model for the planetary boundary layer based on large eddy simulation data. Bound.-Layer Meteor., 107, 401–427.

Panofsky, H., (1949), Objective weather-map analysis. J. Appl. Meteor. 6, 386-392.

Parodi, A., & Emanuel, K. (2009), A theory for buoyancy and velocity scales in deep moist convection. Journal of the Atmospheric Sciences, 66(11), 3449-3463.

Parodi, A., & Tanelli, S. (2010), Influence of turbulence parameterizations on high-resolution numerical modeling of tropical convection observed during the TC4 field campaign. Journal of Geophysical Research: Atmospheres, 115(D10).

Parodi, A., Foufoula-Georgiou, E., & Emanuel, K. (2011), Signature of microphysics on spatial rainfall statistics. Journal of Geophysical Research: Atmospheres, 116(D14).

Parodi, A., G. Boni, L. Ferraris, F. Siccardi, P. Pagliara, E. Trovatore, and D. Kranzlmueller, (2012), The “perfect storm”: From across the Atlantic to the hills of genoa. *EOS Trans. AGU*, **93(24)**, 225–226, doi:10.1029/2012EO240001.

Parodi, A., Ferraris, L., Gallus Jr, W. A., Maugeri, M., Molini, L., Siccardi, F., & Boni, G. (2017), Ensemble cloud-resolving modelling of a historic back-building mesoscale convective system over Liguria: the San Fruttuoso case of 1915. Climate of the Past, 13(5), 455

Parodi, A., G. Boni, L. Ferraris, F. Siccardi, P. Pagliara, E. Trovatore, and D. Kranzlmueller (2012), The “perfect storm”: From across the Atlantic to the hills of Genoa, Eos, Transactions American Geophysical Union, 93(24), 225-226, doi:10.1029/2012EO240001.

Parodi, A., Kranzlmüller, D., Clematis, A., Danovaro, E., Galizia, A., Garrote, L., ... & Siccardi, F. (2017), DRIHM (2US): An e-Science Environment for

Hydrometeorological Research on High-Impact Weather Events. Bulletin of the American Meteorological Society, 98(10), 2149-2166.

Parrish, D. F., and J. C. Derber, (1992), The National Meteorological Center's Spectral Statistical Interpolation analysis system. Mon. Wea. Rev., 120, 1747–1763.

Paulson, C. A., (1970), The mathematical representation of wind speed and temperature profiles in the unstable atmospheric surface layer. J. Appl. Meteor., 9, 857–861.

Petersen, W.A., S.A. Rutledge, and R.E. Orville (1996), Cloud-to-ground lightning observations to TOGA COARE: Selected results and lightning location algorithm, Mon. Weather Rev., 124(4), 602 – 620.

Petersen, W.A., S.A. Rutledge, R.C. Cifelli, B.S. Ferrier, and B.F. Smull (1999), Shipborne Dual-Doppler operations during TOGA COARE: Integrated observations of storm kinematics and electrification, Bull. Am. Meteorol. Soc., 80(1), 81 – 96.

Pieri, A. B., von Hardenberg, J., Parodi, A., & Provenzale, A. (2015), Sensitivity of Precipitation Statistics to Resolution, Microphysics, and Convective

Pichelli, E., Ferretti, R., Cimini, D., Panegrossi, G., Perissin, D., Pierdicca, N., Rocca, F., Rommen, B., (2015), InSAR Water Vapor Data Assimilation into Mesoscale Model MM5: Technique and Pilot Study. IEEE J. Sel. Top. Appl. Earth Obs. Remote Sens. 8, 3859–3875. https://doi.org/10.1109/JSTARS.2014.2357685.

Pineda, N., J. Bech, T. Rigo, and J. Montanyà (2011), A Mediterranean nocturnal heavy rainfall and tornadic event. Part II: Total lightning analysis, Atmos. Res., 100:4, 638-648. doi:10.1016/j.atmosres.2010.10.027.

Pleim, J. E., (2006), A simple, efficient solution of flux-profile relationships in the atmospheric surface layer, J. Appl. Meteor. and Clim., 45, 341–347.

Pleim, J. E. and A. Xiu, (1995), Development and testing of a surface flux and planetary boundary layer model for application in mesoscale models. J. Appl. Meteor., 34, 16–32.

Pleim, J. E., (2007), A combined local and non-local closure model for the atmospheric boundary layer. Part 1: Model description and testing, J. Appl. Meteor. and Clim., 46, 1383–1395.

Powers, J. G., Klemp, J. B., Skamarock, W. C., Davis, C. A., Dudhia, J., Gill, D. O., ... & Grell, G. A. (2017), The weather research and forecasting (WRF) model: overview, system efforts, and future directions. Bulletin of the American Meteorological Society, (2017).

Prein, A. F., G. J. Holland, R. M. Rasmussen, J. Done, K. Ikeda, M. P. Clark, and C. H. Liu (2013b), Importance of regional climate model grid spacing for the simulation of heavy precipitation in the Colorado headwaters, J. Clim., 26(13), 4848–4857.

Price, C., and D. Rind, (1992), A simple lightning parameterization for calculating global lightning distributions, J. Geophys. Res., 97 (D9), 9919-9933.

Price, C., Y. Yair, A. Mugnai, K. Lagouvardos, M.C. Llasat, S. Michaelides, S. Dietrich, E. Galanti, L. Garrote, D. Katsanos, V. Kotroni, M. Llasat-Botija, L. Mediero, E. Morin, K. Nicolaides, K. Savvidou, B. Ziv, (2011 a). The FLASH project: using lightning data to better understand and predict flash floods. Special Edition of Environmental Science & Policy "Climate Change and Water", 898-911.

Price, C., Y. Yair, A. Mugnai, K. Lagouvardos, M. C. Llasat, S. Michaelides, U. Dayan, S. Dietrich, F. Di Paola, E. Galanti, L. Garrote, N. Harats, D. Katsanos, M. Kohn, V. Kotroni, M. Llasat-Botija, B. Lynn, L. Mediero, E. Morin, K. Nicolaides, S. Rozalis, K. Savvidou, B. Ziv, (2011 b). Using Lightning Data to Better Understand and Predict Flash Floods in the Mediterranean. Surv Geophys 32:733–751, DOI 10.1007/s10712-011-9146-y.

Price, C. G. (2013). Lightning applications in weather and climate research.Surveys in Geophysics, 34(6), 755-767.

Pu, Z., & Lin, C. (2015), Evaluation of double-moment representation of ice hydrometeors in bulk microphysical parameterization: comparison between WRF numerical simulations and UND-Citation data during MC3E. Geoscience Letters, 2(1), 1.

Purser, R. J., W.-S. Wu, D. F. Parrish, and N. M. Roberts, (2003a), Numerical aspects of the application of recursive filters to variational statistical analysis. Part I: Spatially homogeneous and isotropic Gaussian covariances. Mon. Wea. Rev., 131, 1524–1535.

Pytharoulis, I., S. Kotsopoulos, I. Tegoulias, S. Kartsios, D. Bampzelis, and T. Karacostas, (2016). Numerical modeling of an intense precipitation event and its associated lightning activity over northern Greece. Atmospheric Research, 169, 523-538.

Rajeevan, M., Kesarkar, A., Thampi, S. B., Rao, T. N., Radhakrishna, B., & Rajasekhar, M. (2010). Sensitivity of WRF cloud microphysics to simulations of a severe thunderstorm event over Southeast India. In Annales geophysicae: atmospheres, hydrospheres and space sciences (Vol. 28, No. 2, p. 603).

Rakov, V. A. and Uman, M. A. (2003), Lightning. Physics and Effects, Cambridge University Press, Cambridge.

Rebora, N., L. Ferraris, J. H. Hardenberg and A. Provenzale, (2006a), Rainfall downscaling and flood forecasting: a case study in the Mediterranean area. Nat. Hazards and Earth Syst. Sci., 6, 611-619.

Rebora, N., L. Ferraris, J. H. Hardenberg and A. Provenzale, (2006b), The RainFARM: Rainfall Downscaling by a Filtered Auto Regressive Model. J. Hydrometeor., 7(4), 724-738.

Rebora, N., L. Molini, E. Casella, A. Comellas, E. Fiori, F. Pignone, F. Siccardi, F. Silvestro, S. Tanelli, and A. Parodi, (2013), Extreme rainfall in the Mediterranean: What can we learn from observations?, *J. Hydrometeor.*, **11**, 906–922, doi:10.1175/JHM-D-12-083.1.

Rotunno, R., Y. Chen, W. Wang, C. Davis, J. Dudhia, and G. J. Holland, (2009), Large-eddy simulation of an idealized tropical cyclone. Bull. Amer. Meteor. Soc., 90, 1783–1788, doi:10.1175/ 2009BAMS2884.1.

Richard, E., A. Buzzi, and G. Zängl (2007), Quantitative precipitation forecasting in the Alps: The advances achieved by the mesoscale alpine programme, Q. J. R. Meteorol. Soc., 133(625), 831–846.

Ricard,D.,C. Lac, S. Riette,R. Legrand, and A.Mary, (2013), Kinetic energy spectra characteristics of two convection-permitting limited-area models AROME and Meso-NH. Quart. J. Roy. Meteor. Soc., 139, 1327–1341, doi:10.1002/qj.2025.

Richardson, L. F., (1922), Weather prediction by numerical process. Cambridge University Press, Cambridge. Reprinted by Dover(1965,NewYork) with a new introduction by Sydney Chapman.

Roberts, R. E., J. E. A. Selby, and L. M. Biberman, (1976), Infrared continuum absorption by atmospheric water-vapor in 8–12 um window. Applied Optics, 15 (9), 2085–2090.

Rodgers, C. D., (1968), Some extensions and applications of the new random model for molecular band transmission. Quart. J. Roy. Meteor. Soc., 94, 99–102.

Rutledge, S. A., and P. V. Hobbs, (1984), The mesoscale and microscale structure and organization of clouds and precipitation in midlatitude cyclones. XII: A diagnostic modeling study of precipitation development in narrow cloud-frontal rainbands. J. Atmos. Sci., 20, 2949–2972.

Sakurai, N., S. Shimizu, Y. Shusse, S. I. Suzuki, T. Maesaka, K. Kieda, and K. Iwanami (2015), Relationships between Updraft Characteristics and Cloud-to-Ground Lightning Activity in Warm-Season Convective Storms in the Kanto Region, Japan. SOLA, 11, 177-180.

Sasamori, T., J. London, and D. V. Hoyt, (1972), Radiation budget of the Southern Hemisphere. Meteor. Monogr., 13, No. 35, 9–23.

Saunders C. P. R., (2008), Charge separation mechnisms in clouds, Space Sci. Rev., 137(1–4), 335–354, doi:10.1007/s11214-008-09345-0.

Schwartz, C. S., J. S. Kain, S. J. Weiss, M. Xue, D. R. Bright, F. Kong, K. W. Thomas, J. J. Levit, and M. C. Coniglio (2009), Next-day convection-allowing WRF model guidance: A second look at 2-km versus 4-km grid spacing, Mon. Weather Rev., 137(10), 3351–3372, doi:10.1175/2009MWR2924.1.

Schwarzkopf, M. D., and S. B. Fels, (1985), Improvements to the algorithm for computing CO2 transmissivities and cooling rates. J. Geophys. Res., 90 (ND6), 541–550.

Schwarzkopf, M. D., and S. B. Fels, (1991), The simplified exchange method revisited — An accurate, rapid method for computation of infrared cooling rates and fluxes. J. Geophys. Res., 96 (D5), 9075–9096.

Schultz, C.J., W.A. Petersen, and L.D. Carey (2009), Preliminary development and evaluation of lightning jump algorithms for the real-time detection of severe weather, J. Appl. Meteor., 48, doi:10.1175/2009JAMC2237.1.

Schultz, C.J., J. Christopher, W.A. Petersen, and L.D. Carey (2011), Lightning and Severe Weather: A Comparison between Total and Cloud-to-Ground Lightning Trends, Wea. Forecasting, 26, 744–755, doi:http://dx.doi.org/10.1175/WAF-D-10-05026.1

Shin, H. H., and S.-Y. Hong, (2011), Intercomparison of planetary boundary-layer parameterizations in the WRF Model for a single day from CASES-99. Bound.-Layer Meteor., 139, 261–281.

Shin, H. H., & Dudhia, J. (2016). Evaluation of PBL parameterizations in WRF at subkilometer grid spacings: Turbulence statistics in the dry convective boundary layer. Monthly Weather Review, 144(3), 1161-1177.

Siccardi, F., Boni, G., Ferraris, L., and Rudari, R. (2005), A reference framework for probabilistic flood forecast, J. Geophys. Res., 110, D05 101, doi:10.1029/2004JD005 314,.

Silvestro, F., N. Rebora, and L. Ferraris, (2009), An algorithm for real-time rainfall rate estimation using polarimetric radar: RIME, J. Hydrometeor., 10, 227–240, doi:10.1175/2008JHM1015.1.

Silvestro, F., N. Rebora and L. Ferraris, (2011), Quantitative flood forecasting on small and medium size basins: a probabilistic approach for operational purposes. J. Hydrometeor, 12(6), 1432-1446.

Silvestro, F. and N. Rebora, (2014), Impact of precipitation forecast uncertainties and initial soil moisture conditions on a probabilistic flood forecasting framework. Journal of Hydrology, 519, 1052–1067.

Silvestro, F., S. Gabellani, F. Delogu, R. Rudari, P. Laiolo, G. Boni, (2015), Uncertainty reduction and parameter estimation of a distributed hydrological model with ground and remote-sensing data. Hydrol. Earth Syst. Sci., 19, 1727-1751, doi:10.5194/hess-19-1727-2015

Silvestro, F., N. Rebora, G. Cummings, and L. Ferraris, (2015b), Experiences of dealing with flash floods using an ensemble hydrological nowcasting framework: Implications of communication, accessibility and distribution of the results. J. Flood Risk Manage., doi:10.1111/jfr3.12161.

Silvestro, F., N. Rebora, F. Giannoni, A. Cavallo, L. Ferraris, (2016), The flash flood of the Bisagno Creek on 9th October 2014: an “unfortunate” combination of spatial and temporal scales. Journal of Hydrology, 541, Part A, 50–62, doi:10.1016/j.jhydrol.2015.08.004

Skamarock, W. C., and Coauthors, (2008), A description of the Advanced Research WRF version 3. NCAR Tech Note NCAR/TN-475+STR, 113 pp. [Available online at www.mmm.ucar.edu/wrf/users/docs/arw_v3.pdf.]

Skamarock WC, Klemp JB. (2008), A time-split non-hydrostatic atmospheric model for weather research and forecasting applications. J. Comput. Phys. 227: 3465–3485.

Smirnova, T. G., J. M. Brown, and S. G. Benjamin, (1997), Performance of different soil model configurations in simulating ground surface temperature and surface fluxes. Mon. Wea. Rev., 125, 1870–1884.

Smirnova, T. G., J. M. Brown, S. G. Benjamin, and D. Kim, (2000), Parameterization of cold season processes in the MAPS land-surface scheme. J. Geophys. Res., 105 (D3), 4077–4086.

Smith, P. L., Jr., C. G. Myers, and H. D. Orville, (1975), Radar reflectivity factor calculations in numerical cloud models using bulk parameterization of precipitation processes. J. Appl. Meteor., 14, 1156–1165.

Sommeria, G. (1976), Three-dimensional simulation of turbulent processes in an undisturbed trade wind boundary layer. *Journal of the Atmospheric Sciences*, *33*(2), 216-241.

Soula, S., and S. Chauzy (2001), Some aspects of the correlation between lightning and rain activities in thunderstorms, Atmos. Res., 56, 355–373, doi:10.1016/S0169-8095(00)00086-7.

Stephens, G. L., (1978), Radiation profiles in extended water clouds. Part II: Parameterization schemes, J. Atmos. Sci., 35, 2123–2132.

Stolzenburg, M., Kreisberg, N., & Hering, S. (1998), Atmospheric size distributions measured by differential mobility optical particle size spectrometry. *Aerosol Science and Technology*, *29*(5), 402-418.

Stough, S.M., L.D. Carey, and C.J. Schultz (2014), Total lightning as an indicator of mesocyclone behavior, Conference Proceedings 15th International Conf. on Atmospheric Electricity, Norman, OK.

Sugimoto, S., N. A. Crook, J. Sun, Q. Xiao, D. M. Barker, (2009), An Examination of WRF 3DVAR Radar Data Assimilation on Its Capability in Retrieving Unobserved Variables and Forecasting Precipitation through Observing System Simulation Experiments, American Meteorological Society, 137, 4011-4029. DOI: 10.1175/2009MWR2839.1

Sukoriansky, S., B. Galperin, and V. Perov, (2005), Application of a new spectral theory of stably stratified turbulence to the atmospheric boundary layer over sea ice. Bound.-Layer Meteor., 117, 231–257, doi:10.1007/s10546-004-6848-4.

Sun, J. and Crook, N. A., (1997), Dynamical and Microphysical Retrieval from Doppler RADAR Observations Using a Cloud Model and Its Adjoint, Part I: Model Development and Simulated Data Experiments, J. Atmos. Sci., 54, 1642–1661.

Talagrand, O., (1997), Assimilation of observations, an introduction,J. Met. Soc. Japan Special Issue, 75, 1B, 191-209.

Tao, W.-K., J. Simpson, and M. McCumber (1989), An ice-water saturation adjustment, Mon. Wea. Rev., 117, 231–235.

Tao, W.-K., and J. Simpson, (1993), The Goddard cumulus ensemble model. Part I: Model description. Terr. Atmos. Oceanic Sci., 4, 35–72.

Tao, W.-K,, J. Simpson, D. Baker, S. Braun, M.-D. Chou, B. Ferrier, D. Johnson, A. Khain, S. Lang, B. Lynn, C.-L. Shie, D. Starr, C.-H. Sui, Y. Wang, and P. Wetzel, (2003), Microphysics, radiation and surface processes in the Goddard Cumulus Ensemble (GCE) model. Meteor. and Atmos. Phys., 82, 97–137.

Thompson, G., R. M. Rasmussen, and K. Manning, (2004), Explicit forecasts of winter precipitation using an improved bulk microphysics scheme. Part I: Description and sensitivity analysis. Mon. Wea. Rev., 132, 519–542.

Tapia, A., J. Smith, and M. Dixon (1998), Estimation of convective rainfall from lightning observations, J. Appl. Meteorol., 37, 1497–1509.

Thompson, G., P.R. Field, R.M. Rasmussen, and W.D. Hall (2008), Explicit Forecast of Winter Precipitation Using an Improved Bulk Microphysics Scheme. Part II: Implementation of a New Snow Parameterization, Mon. Wea. Rev., 136, 5095-5115, doi:10.1175/2008MWR2387.1.

Uccellini, L. W., and D. R. Johnson, (1979), The Coupling of Upper and Lower Tropospheric Jet Streaks and Implications for the Development of Severe Convective Storms. Mon. Wea. Rev. 107, 682–703. Willis, E.P., W.H. Hooke: 2006 Cleveland Abbe and American meteorology, 1871–1901, Bull. Am. Met. Soc. 87, 315–326.

Van Den Broeke, M.S., D.M. Schultz, R.H. Johns, J.S. Evans, and J.E. Hales (2005), Cloud-to-ground lightning production in strongly forced, low-instability convective lines associated with damaging wind, Weather and forecasting, 20(4), 517-530.

Veersé, F., and J.-N. Thépaut, (1998), Multi-truncation incremental approach for four-dimensional variational data assimilation. Quart. J. Roy. Meteor. Soc., 124, 1889–1908.

Verelle, A., D. Ricard, and C. Lac, (2014), Sensitivity of highresolution idealized simulations of thunderstorms to horizontal resolution and turbulence parameterization. Quart. J. Roy. Meteor. Soc., 141, 433–448, doi:10.1002/qj.2363.

Vulpiani, G., P. Pagliara, M. Negri, L. Rossi, A. Gioia, P. Giordano, ... & F. S. Marzano, (2008), The Italian radar network within the national early-warning system for multi-risks management. Proc. of Fifth European Conference on Radar in Meteorology and Hydrology (ERAD 2008),184.

Wang, H., J. Sun, X. Zhang, X. Y Huang and T. Auligné, (2013), Radar data assimilation with WRF 4D-Var. Part I: System development and preliminary testing. Mon. Wea. Rev., 141(7), 2224-2244.

Wang, H., X. Y. Huang, J. Sun, D. Xu, M. Zhang, S. Fan and J. Zhong, (2014), Inhomogeneous background error modeling for WRF-Var using the NMC method. J. Appl. Meteor. Climatol., 53(10), 2287-2309.

Wang, X., Barker, D. M., Snyder, C., & Hamill, T. M. (2008), A hybrid ETKF–3DVAR data assimilation scheme for the WRF model. Part II: Real observation experiments. Monthly Weather Review, 136(12), 5132-5147.

Wang, W., C. Bruyere, M. Duda, J. Dudhia, D. Gill, M. Kavulich, ... & X. Zhang, (2016), WRF ARW-Version 3 Modelling System User's Guide January 2016. Boulder, Colorado, USA: National Center for Atmospheric Research.

Webb, E. K., (1970), Profile relationships: The log-linear range, and extension to strong stability, Quart. J. Roy. Meteor. Soc., 96, 67–90.

Wee, T. K., & Kuo, Y. H. (2004), Impact of a digital filter as a weak constraint in MM5 4DVAR: An observing system simulation experiment. *Monthly weather review*, *132*(2), 543-559.

Weisman, M. L., C. Davis, W. Wang, K. W. Manning, and J. B. Klemp (2008), Experiences with 0-36-h explicit convective forecasts with the WRF-ARW model, Weather Forecasting, 23(3), 407–437.

Weusthoff, T., F. Ament, M. Arpagaus, and M. W. Rotach (2010), Assessing the benefits of convection-permitting models by neighborhood verification: Examples from MAP D-PHASE, Mon.Weather Rev., 138(9), 3418–3433, doi:10.1175/2010MWR3380.1.

Wicker, L. J., and R. B. Wilhelmson, (1995), Simulation and analysis of tornado development and decay within a three-dimensional supercell thunderstorm. J. Atmos. Sci., 52, 2675–2703.

Williams, E. R., (1985), Large-scale charge separation in thunderclouds, J. Geophys. Res., 90, 6013-6025, doi:10.1029/JD090iD04p06013.

Willis, E.P., W.H. Hooke (2006), Cleveland Abbe and American meteorology, 1871–1901, Bull. Am. Met. Soc. 87, 315–326.

Wilson, C. T. R. (1916), On some determinations of the sign and magnitude of electric discharges in lightning flashes. *Proc. R. Soc. Lond. A*, *92*(644), 555-574.

Wong, J., Barth, M.C., Noone, D, (2013), Evaluating a lightning parameterization based on cloud-top height for mesoscale numerical model simolations, Geosci. Model Dev., 6, 429-443, doi:10.5194/gmd-6-429-2013.

Wu, W. -S., R. J. Purser, and D. F. Parrish, (2002), Three-Dimensional Variational Analysis with Spatially Inhomogeneous Covariances. Mon. Wea. Rev., 130, 2905–2916.

Wyngaard, J. C. (2004). Toward numerical modeling in the “Terra Incognita”. *Journal of the atmospheric sciences*, *61*(14), 1816-1826.

Xiao, Qingnong, and Juanzhen Sun, (2007), Multiple-radar data assimilation and short-range quantitative precipitation forecasting of a squall line observed during IHOP_2002. Mon. Wea. Rev., 135, 3381–3404.

Xiu, A. and J. E. Pleim, (2001), Development of a land surface model part I: Application in a mesoscale meteorology model. J. Appl. Meteor., 40, 192–209.

Yair, Y., B. Lynn, C. Price, V. Kotroni, K. Lagouvardos, E. Morin, A. Mugnai, and M. d. C. Llasat (2010), Predicting the potential for lightning activity in Mediterranean storms based on the Weather Research and Forecasting (WRF) model dynamic and microphysical fields, J. Geophys. Res., 115, D04205, doi:10.1029/2008JD010868

Yang, Z.-L., and G.-Y. Niu (2003), The versatile integrator of surface andatmosphere processes (VISA) part I: Model description, Global Planet.Change, 38, 175–189, doi:10.1016/S0921-8181(03)00028-6.

Zhang, D.-L., and R.A. Anthes, (1982), A high-resolution model of the planetary boundary layer– sensitivity tests and comparisons with SESAME–79 data. J. Appl. Meteor., 21, 1594–1609.

Zilitinkevich, S. S., (1995), Non-local turbulent transport: pollution dispersion aspects of coherent structure of convective flows, Air Pollution III — Volume I. Air Pollution Theory and Simulation, Eds. H. Power, N. Moussiopoulos and C.A. Brebbia. Computational Mechanics Publications, Southampton Boston, 53–60.

Zou, X., F. Vandenberghe, M. Pondeca, and Y.-H. Kuo, (1997), Introduction to adjoint techniques and the MM5 adjoint modeling system. NCAR Tech. Note NCAR/TN-435 1 STR, 110 pp. [Available from UCAR Communications, P.O. Box 3000, Boulder, CO, 80307.]